MODELING OF SHAPE MEMORY ALLOYS CONSIDERING RATE-INDEPENDENT AND RATE-DEPENDENT IRRECOVERABLE STRAINS

A Dissertation

by

DARREN J. HARTL

Submitted to the Office of Graduate Studies of
Texas A&M University
in partial fulfillment of the requirements for the degree of

DOCTOR OF PHILOSOPHY

December 2009

Major Subject: Aerospace Engineering

MODELING OF SHAPE MEMORY ALLOYS CONSIDERING RATE-INDEPENDENT AND RATE-DEPENDENT IRRECOVERABLE STRAINS

A Dissertation

by

DARREN J. HARTL

Submitted to the Office of Graduate Studies of
Texas A&M University
in partial fulfillment of the requirements for the degree of

DOCTOR OF PHILOSOPHY

Approved by:

Chair of Committee,	Dimitris C. Lagoudas
Committee Members,	Ibrahim Karaman
	J. N. Reddy
	James Boyd
	Arun Srinivasa
Head of Department,	Dimitris C. Lagoudas

December 2009

Major Subject: Aerospace Engineering

ABSTRACT

Modeling of Shape Memory Alloys Considering
Rate-Independent and Rate-Dependent Irrecoverable Strains. (December 2009)
Darren J. Hartl, B.S., Texas A&M University
Chair of Advisory Committee: Dr. Dimitris C. Lagoudas

This dissertation addresses new developments in the constitutive modeling and structural analysis pertaining to rate-independent and rate-dependent irrecoverable inelasticity in Shape Memory Alloys (SMAs). A new model for fully recoverable SMA response is derived that accounts for material behaviors not previously addressed. Rate-independent and rate-dependent irrecoverable deformations (plasticity and viscoplasticity) are then considered. The three phenomenological models are based on continuum thermodynamics where the free energy potentials, evolution equations, and hardening functions are properly chosen. The simultaneous transformation-plastic model considers rate-independent irrecoverable strain generation and uses isotropic and kinematic plastic hardening to capture the interactions between irrecoverable plastic strain and recoverable transformation strain. The combination of theory and implementation is unique in its ability to capture the simultaneous evolution of recoverable transformation strains and irrecoverable plastic strains. The simultaneous transformation-viscoplastic model considers rate-dependent irrecoverable strain generation where the theoretical framework is modified such that the evolution of the viscoplastic strain components are given explicitly. The numerical integration of the constitutive equations is formulated such that objectivity is maintained for SMA structures undergoing moderate strains and large displacements. Experimentally validated analysis results are provided for the fully recoverable model, the simultaneous transformation-plastic yield model, and the transformation-viscoplastic creep model.

To my parents, who raised me,
my wife Crissy, who supported me,
and my son Ian, who motivated me

ACKNOWLEDGMENTS

As this dissertation represents the culmination of a lifetime spent learning, it seems inappropriate to begin by acknowledging anyone other than my Creator and the two people chosen by Him to protect and guide me in my youth. I thank my parents for being the perfect team: my mother teaching me the focus of a good student and my father building in me the intuition of a good engineer. Above all else, I thank them for instilling in me the diligence to complete a task once started. Few tasks have been longer or more strenuous than the generation of this new body of knowledge.

My collegiate experience, from my junior year to my final hooding as a Ph.D., has been most profoundly affected by the words and deeds of my graduate advisor, Dr. Dimitris Lagoudas. As a "boss," he pushed this one-time undergraduate research assistant to achieve something new each week, from summer to winter and back again, while maintaining a "fellowship worthy" GPA. As an advisor, he taught me that I am rarely right the first five times, and that Americans can be just as good at math as those with more theoretical backgrounds. I have watched him move between the roles of Scientist, Mentor, and Administrator, and over the past eight years, have learned a great deal about how (and how not) to one day be all three.

I am also thankful for the input and influence of my graduate committee members. Dr. Jim Boyd was the first to teach me active materials in the formal sense, and gave me my first experience in the rigorous mathematical description of bodies that were more than just elastic. I am most thankful to Dr. Ibrahim Karaman for our regular research interactions, where I have had the opportunity to observe a young member of the faculty teach the world how it works. Dr. JN Reddy taught the first class where I can remember thinking, "I was meant to go to graduate school, and I am meant to study mechanics," and also fostered my appreciation for the power of

a properly-coded algorithm. Dr. Arun Srinivasa came into my academic life at just the right moment, when I was comfortable with my progress and thought I knew it all. His unique and outspoken perspectives challenged even the foundations of my work, and I thank him for that. Finally, I want to acknowledge Dr. Kalyana Nakshatrala for providing input during my preliminary exam. Dr. Amine Benzerga did the same during the final defense of this dissertation, and I thank him for his suggestions regarding its improvement.

From industry, I would like acknowledge the constant help and motivation provided by my Boeing collaborators, Frederick "Tad" Calkins of Boeing Commercial Aircraft and James "Jim" Mabe of Boeing Research and Technology. We have been in constant communication since before the first experimental plan for the Ni60Ti material, when I was a first year graduate student. I thank them for always being great engineers on the phone and great guys in person.

Of course I would not have even attempted graduate school without the love and support of my best friend and beautiful wife, Crissy. For all the many times that I suffered through homework, exams, derivations, and numerical disasters, she suffered with me. The last five years have been difficult, and I cannot thank her enough for her patience and belief in me. No amount of words within the page limit of this acknowledgment could ever explain how important it is to have the daily support of one's best friend.

My experience as a doctoral student has also been greatly enriched by those individuals who shared in the struggles of studying at Texas A&M. Many early and essential lessons were learned from the likes of Luke Penrod, Eric Vandygriff, and Pavlin Entchev. Olivier Bertacchini always brought life into any group gathering, and Luciano Machado was the best officemate I could ask for. Bjoern Kiefer will never really know how much I enjoyed watching him think and listening to him

expound on the intricate details of thermodynamics. The graduation of Luciano and Bjoern represented a monumental shift in the make-up of the S.M.A.R.T. team, but new members such as Brent Volk, Krishnendu Haldar, Francis Phillips, and Justin Schick helped us to move forward. I want to especially thank Brent for being my sounding board as I began to make my own unique contributions, and also for being patient with my weak grasp of college athletics. Undergraduate assistants like Jesse Mooney helped to multiply my productivity times over, while Tony Menn always kept me laughing. Many hours were also spent in lively conversation with members of the "nano" team, including Piyush Thakre, Amnaya Awasthi, and in particular Gary Don Seidel, who was always there to initiate an afternoon football game or lend an ear as I tried to determine what to do with my life after graduation.

Finally, I must conclude by thanking my friend and colleague of the past eight years, Parikshith Kumar. Almost every significant experience I have had as a graduate student has been shared with him. He understands and enjoys technical subjects that remain nebulous to me, and he has always been gracious in sharing what he has learned about the science with those who do the math. I have always tried to reciprocate, and having done so, feel that the two of us worked together as a great and productive team (his work in characterizing the HTSMA alloy described in this work for the purposes of calibrating the model was pivotal to its success). When I recall proposals and conferences and the authoring of a textbook, I remember that it was Kumar in particular who helped to make each both valuable and enjoyable. Thank you.

NOMENCLATURE

$\boldsymbol{\alpha}$	Effective thermal expansion coefficient tensor (1-D form: α)
$\boldsymbol{\alpha}^A$	Thermal expansion coefficient tensor for austenite ($\boldsymbol{\alpha}^M$ for martensite)
$\boldsymbol{\beta}$	Plastic back stress tensor (1-D form: β)
$\boldsymbol{\beta}_0$	Plastic back stress tensor in the reference configuration
$\boldsymbol{\varepsilon}$	Total strain tensor (1-D form: ε)
$\boldsymbol{\varepsilon}^p$	Plastic strain tensor (1-D form: ε^p)
$\overline{\epsilon}^p$	Effective plastic strain
$\overline{\epsilon}^p{}_{crit}$	Critical effective plastic strain for prevention of transformation
$\boldsymbol{\varepsilon}^t$	Transformation strain tensor (1-D form: ε^t)
$\boldsymbol{\varepsilon}^{th}$	Thermal strain tensor
$\boldsymbol{\varepsilon}^{tp}$	TRIP strain tensor (1-D form: ε^{tp})
$\boldsymbol{\varepsilon}^{t-r}$	Transformation strain tensor at transformation reversal
$\boldsymbol{\varepsilon}^{vp}$	Viscoplastic strain tensor (1-D form: ε^{vp})
$\boldsymbol{\Lambda}^p$	Plastic direction tensor (1-D form: Λ^p)
$\boldsymbol{\Lambda}^t$	Transformation direction tensor (1-D form: Λ^t)
$\boldsymbol{\Lambda}^{tp}$	TRIP direction tensor (1-D form: Λ^{tp})
$\boldsymbol{\Lambda}^{vp}$	Viscoplastic direction tensor (1-D form: Λ^{vp})
λ^{vp}	Viscoplastic strain rate function
ν^A	Poisson's ratio of austenite (ν^M for martensite)
Φ^p	Plastic yield function
Φ^t	Transformation function
Φ^{vp}	Viscoplastic creep/relaxation function
π^p	Thermodynamic driving force for plastic yield
π^t	Thermodynamic driving force for transformation
ρ	Density of material (assumed equal for austenite and martensite)

$\boldsymbol{\sigma}$	Applied stress tensor (1-D form: σ)
$\boldsymbol{\sigma}'$	Deviatoric stress tensor
σ^*	Reference stress for the measurement of slopes C^A and C^M
$\overline{\sigma}$	Mises equivalent stress
$\overline{\sigma}_{crit}$	Critical stress level below which no transformation strain is generated
$\boldsymbol{\sigma}_p^{eff}$	Effective stress tensor for plastic yield (1-D form: σ_p^{eff})
$\boldsymbol{\sigma}_t^{eff}$	Effective stress tensor for transformation (1-D form: σ_t^{eff})
σ_i	Uniaxial constant applied stress level
ξ	Martensitic volume fraction
ξ_{irr}	Irrecoverable martensitic volume fraction
ξ^r	Martensitic volume fraction at transformation reversal
$\boldsymbol{\zeta}^p$	Set of internal variables related to plastic yielding
$\boldsymbol{\zeta}^t$	Set of internal variables related to transformation
A_f	Austenitic finish temperature at zero applied stress
A_s	Austenitic start temperature at zero applied stress
C^A	Stress influence coefficient for transformation into austenite (C^M for martensite)
C_H	Plastic hardening coefficient
$\boldsymbol{\mathcal{C}}$	Effective stiffness tensor
c	Effective specific heat (assumed equal for austenite and martensite)
D	Stress coefficient corresponding to the condition $C^A \neq C^M$
E	Effective Young's modulus
E^A	Young's modulus of austenite (E^M for martensite)
f_A^p	Plastic hardening function for pure austenite (f_M^p for martensite)
f^t	Transformation hardening function
f^{tp}	TRIP strain magnitude function
f^{vp}	Viscoplastic hardening function
G	Specific Gibbs free energy potential of total material

G^A	Specific Gibbs free energy potential of pure austenite (G^M for martensite)
G^{mix}	Specific Gibbs free energy potential due to mixing of phases
g^p	Viscoplastic hardening energy
g^p_A	Plastic hardening energy in pure austenite (g^p_M in martensite)
g^t	Transformation hardening energy
H^{cur}	Current maximum transformation strain
$H_{\max}$	Highest magnitude of full transformation strain for all applied stress levels
$H_{\min}$	Full transformation strain at zero applied stress
k	Solution iteration counter
K^A_β	Kinematic hardening modulus of pure austenite (K^M_β for martensite)
$\boldsymbol{\mathcal{L}}$	Continuum tangent modulus (or tangent stiffness) tensor
M_f	Martensitic finish temperature at zero applied stress
M_s	Martensitic start temperature at zero applied stress
n	Load (or time) increment counter
N_a	Power law creep exponent
n_i	Transformation hardening smoothness coefficients ($i = 1 \ldots 4$)
p	Effective viscoplastic strain
Q	Activation energy for viscoplastic creep
$\boldsymbol{\mathcal{Q}}$	Orthogonal rotation tensor for objective (Hughes-Winget) integration
$\mathbf{q}$	Heat conduction vector
$\mathbf{R}$	Inelastic strain residual (i.e., associated with transformation, plastic, or viscoplastic strain)
R	Gas constant
r	Rate of internal heat generation
$\mathcal{S}$	Effective compliance tensor
$\mathcal{S}^A$	Compliance tensor of austenite ($\mathcal{S}^M$ for martensite)
s	Effective specific entropy
s_0	Effective specific entropy at the reference state

T	Current temperature
T_0	Temperature at reference configuration
u	Effective specific internal energy
u_0	Effective specific internal energy at the reference state
$\tilde{x}$	For any quantity x, the difference between x^M and x^A
Y^p	Critical thermodynamic force for plastic yield (yield stress)
Y^t	Critical thermodynamic force for transformation
Y_0^t	Critical thermodynamic force for transformation at zero applied stress

TABLE OF CONTENTS

CHAPTER Page

CHAPTER Page

LIST OF TABLES

LIST OF FIGURES

FIGURE Page

FIGURE Page

FIGURE Page

FIGURE Page

FIGURE Page

CHAPTER I

INTRODUCTION

It is often the goal of engineers and designers to increase the multifunctionality of various system components as a means of maximizing overall system performance. Active materials such as piezoelectrics, shape memory polymers, and shape memory alloys (SMAs) provide possible solutions to this design challenge [2]. SMAs are alloys that are able to recover seemingly permanent strains via a stress-induced or temperature-induced phase transformation between *martensite*, the low temperature phase, and *austenite*, the high temperature phase [3, 4, 1]. These materials are particularly attractive as single-component actuators because the inelastic strains can be recovered under the presence of substantial loads.

As the variety of SMA applications increases in the aerospace [5, 6, 7], medical [8, 9, 10], and oil industries [11], among others, the need to accurately account for the response of SMAs subjected to a wider range of loading paths has become increasingly important. Many applications include torsional [12] or bending [13, 14] components, some exploiting localized buckling behavior [15], and the analysis of each of these must include the capability to account for large rotations. Monolithic SMA bodies, whether rod or tube or beam, must be formed and eventually fastened, and these actions can induce stress concentrations and irrecoverable plastic yield in the SMA material. The interactions between irrecoverable plastic strains and recoverable transformation strains must be considered in all of these instances. In the case of *high temperature shape memory alloys* (HTSMAs), the operating temperatures and stresses imposed promote the initiation and evolution of rate-dependent *viscoplas-*

The journal model is International Journal of Engineering Science.

tic deformation during transformation. The description of such behavior requires the development of a theoretical framework able to capture both rate-independent transformation and the rate-dependent creep.

This dissertation addresses each of these three topics: *i*) increased fidelity in the modeling and analysis of SMA components undergoing the conventional (fully recoverable) martensitic phase transformation and utilized in applications of increasing complexity; *ii*) modeling and analysis of SMA components containing material regions undergoing martensitic transformation as well as plastic yielding induced by high stresses, in some cases simultaneously; and *iii*) modeling and analysis of SMA and HTSMA components containing material regions undergoing martensitic transformation and viscoplastic yielding (e.g., creep or relaxation), perhaps simultaneously in the case of HTSMAs.

A. Improved SMA Model for Analysis of Complex Structures

The unique properties of SMAs, especially their potential for implementation as material actuators, have led to their proposed use in a number of applications, many of them intended for the aerospace industry[1] [7]. One of the earliest applications was a coupling for hydraulic lines in F-14 fighter jets in 1970's [16]. In the 1990's, researchers applied the unique properties of SMAs to active structures. The DARPA "Smart Wing" project [12, 17] examined the use of shape memory alloys and other active materials to warp and deform aircraft wings from within. This application is illustrated in Fig. 1a. Likewise, the SAMPSON project probed the feasibility of tailoring jet engine intake and exhaust geometries using SMA elements in various

[1]Portions reprinted from *Proceedings of the Institution of Mechanical Engineers, Part G: Journal of Aerospace Engineering*, Vol. 221, No. 4, DOI 10.1243/09544100JAERO211, Hartl, D. and Lagoudas, D., pp. 535–552, Copyright 2007, with permission from Professional Engineering Publishing

forms, including large bundles of SMA wires used to pivot the inlet cowl [18]. The SAMPSON is shown in Fig. 1b after installation in a wind tunnel for testing.

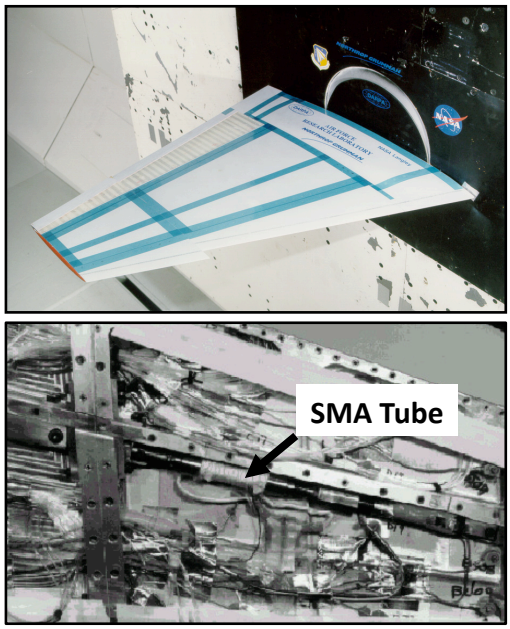

(a) The DARPA Smart Wing (with torque tube cutaway) [12]

(b) The SAMPSON active inlet cowl [18]

Fig. 1. Two aircraft applications of SMAs investigated by researchers.

Regarding helicopter applications, SMAs have provided engineering solutions for actuators placed within confined geometric spaces and undergoing high dynamic loads [19, 20]. Spacecraft applications have also been developed or considered [6], including release mechanisms for very small "micro" satellites [21]. A rotary example of such an actuator is shown in Fig. 2a, where SMA springs act as active elements. Another popular example of a space-based application is the construction of active hinges from an SMA material for use in solar panel deployment. The final design was known as the *lightweight flexible solar array* (LFSA) [15], and it can be seen in Fig. 2b. Inflatable space structures using SMA components as collapsable structural

members have also been studied [22].

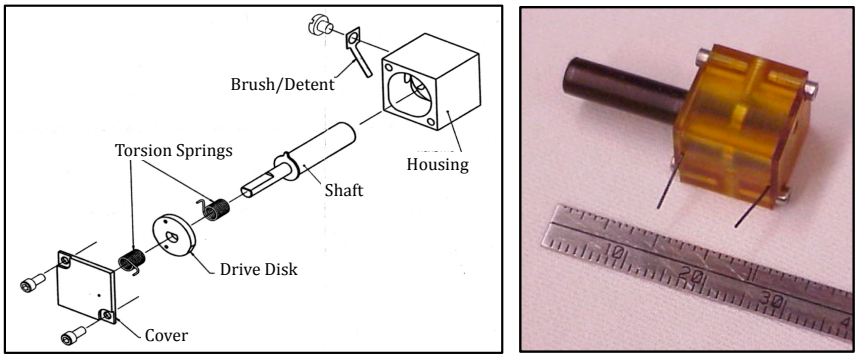

(a) Rotary actuator for micro-satellites [21]

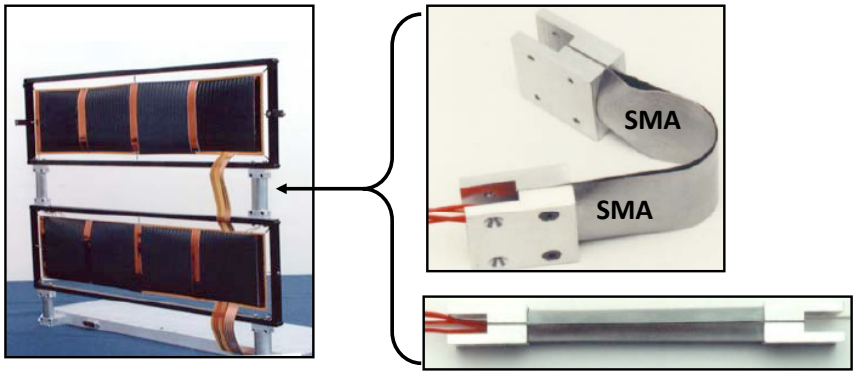

(b) SMA hinges for solar panel deployment (LFSA) [15]

Fig. 2. Two spacecraft applications of SMAs investigated by researchers.

Currently, research is being performed on a completely new set of aerospace actuation applications [23]. One example is the Boeing *variable geometry chevron* (VGC) [24], which is a multicomponent extension of the engine thrust reverser sleeve secondary structure and is intended to reduce engine noise. The VGC, designed, fabricated, and flight tested by Boeing Research and Technology [24, 25], represents an adaptable system and includes active SMA beams (or flexures) encased in a composite structure with a complex 3-D configuration. The VGC is shown in

Fig. 3. Such multi-component applications incorporating SMA forms subjected to non-homogeneous loading and experiencing potentially large structural deformations illustrate the need for powerful analysis tools including accurate constitutive models and capable numerical implementations.

Fig. 3. The Boeing *variable geometry chevron* (VGC). Configuration of single chevron and placement on aircraft are both illustrated.

Due to unusual material behavior and exciting potential applications like the VGC, constitutive modeling of SMAs has attracted the attention of many researchers since the discovery of the most common alloy, NiTi (or *Nitinol*), in the 1960's [26]. While a number of intricacies have yet to be addressed, the modeling of the reversible martensitic transformation at the macro-scale under the most common loading conditions (i.e., proportional loading) has been well-established. Combination, alteration, and permutation of established methods of mechanics, especially those related to rate-independent inelastic phenomena, have served to provide the community with a plethora of modeling options for the conventional transformation response. SMA modeling is often divided into two broad categories [27, 28]. *Micromechanical* mod-

els seek to model martensitic regions or individual grains as unique subdomains and then apply homogenization techniques to predict the response of the bulk material, and are given this name because they account for material microstructure directly. Those that directly capture experimental observations of the bulk material behavior at the macro-scale are known as *phenomenological* models, and these often rely on thermodynamics to motivate their mathematical structures. Various micromechanical models for SMAs have been summarized in the literature [29]. This dissertation addresses new phenomenological models, and thus this second category will be briefly reviewed, though more detailed descriptions can be found elsewhere [1, 27, 28].

The first known phenomenological model specifically proposed for SMAs was that described by Bertram in 1982 [30], though this fact is missed by many researchers. The earliest one-dimensional (1-D) phenomenological models had more impact on the scientific and engineering communities [31, 32, 33], though they were limited to capturing only martensitic transformation. Other 1-D modeling options [34, 35] capture both the reorientation of martensite and the martensite-austenite transformation and remain popular for engineering analysis. Three-dimensional models are necessary to capture the response of SMA components beyond simple tensile loading. These often employ the methodology of classical plasticity assuming an infinitesimal strain formulation [36, 37, 38, 39], where the differences in tensile and compressive response (asymmetry) have also been addressed [40]. The reorientation of martensite in 3-D systems has been captured [41, 42], and the methods of statistical thermodynamics have also been applied to SMA modeling [43]. Note that none of these phenomenological models is intended to capture irrecoverable material behaviors, and such an extension is the focus of the current dissertation. Further, each is formulated using infinitesimal strains and implemented for the analysis of small structural deformations.

The extension of conventional SMA modeling to account for large deformations has also been addressed in the literature. Most of these models, motivated by finite strain (crystal) plasticity, multiplicatively decompose the current total deformation gradient into an elastic and transformation part [44, 45, 46, 47, 48], while another explicitly considers the concept of multiple reference configurations [49][2].The motivation for the finite deformation models is commonly noted to be the analysis of large structural rotations [48] or large distortions [47]. However, martensitic transformation induces only moderate recoverable strains (i.e., 5–8% [1]), thus finite strain models are not necessary for the engineering analysis of SMA components unless additional effects such as large plastic distortions are considered. The need to consider large structural deformations, especially rotations, *does* apply to many SMA applications. As an alternative to finite strain formulations, methods exist whereby local "rigid body" rotations can be accounted for objectively in the incremental implementation of small strain models [50, 51, 52]. These methods are known as *incrementally objective*.

This dissertation will investigate the improvement of current 3-D constitutive models for SMAs by revisiting the proposed evolution equations and hardening laws and by updating the numerical implementation to account for large local rotations caused by large structural deformations using incrementally objective methods. With regard to the evolution equations, this work investigates how the magnitude of the transformation strain generated in the loading direction changes with the magnitude in the applied load. In other models in the literature, older [34, 31] and newer [53, 51], the magnitude of transformation strain is taken to be a constant. Experimental

[2]Note that the work by Ziolkowski [47] also describes the "known concept of multiplicative decomposition" as another method of considering multiple natural or reference configurations.

results, on the other hand, indicate that this is not often the case [54, 55]. This effect is considered in the 3-D model and numerically implemented. The discussion of the transformation hardening follows from recently published work [56], and here the model relations developed elsewhere are again implemented numerically in 3-D. The combination of evolution equation and hardening improvements increases predictive accuracy of the constitutive model across a wide range of SMA material systems.

B. Rate-Independent Plastic Deformations in SMAs

In the literature, the extension of SMA modeling to account for irrecoverable strains commonly assumes that one of two distinct phenomena is occuring. The first is known as *transformation-induced plasticity* (TRIP) while the second is associated with slip mechanisms common in metals which initiate at sufficiently high stresses (i.e., *yield stresses*). TRIP accounts for irrecoverable strain generated due to the cyclic thermo-mechanical transformation of shape memory alloys during which dislocations, grain boundary mismatches, and other effects can accumulate [57, 58, 59]. A noticeable, cumulative, and permanent macroscopic deformation (relative to the original reference configuration) is observed. Modeling of this plastic behavior does not include the conventional notion of a yield surface, but rather proposes evolution equations for the plastic variables which are directly dependent on the number of transformation cycles completed. However, to model plastic yielding initiated directly by high applied stresses (e.g., during monotonic loading), phenomenological SMA models have been combined with conventional metal plastic deformation models, and 1-D [60, 61] and 3-D [62, 63, 64] models have been proposed. These models, especially as implemented in the literature, are restricted to plastic yield which is active when phase transformation is not (i.e., they assume that the processes of martensitic transfor-

mation and plastic slip do not occur simultaneously [62]). In one example, it is specifically postulated that the criteria for plastic strain generation is the completion of phase transformation [64]. Simultaneous phase transformation and yield have been considered in a micromechanics-based model formulated for iron-based shape memory alloys [65], though the implementation is limited to 1-D. The analysis of simultaneous transformation and yield in conventional 3-D NiTi bodies is not considered in the literature and is a major contribution of this body of research.

Experimental evidence and the growing number of engineering applications of SMAs motivates the development and implementation of models that address simultaneous phase transformation and plastic yield in SMAs, including conventional NiTi-based alloy systems [66]. This simultaneous behavior is observed in SMA materials subjected to two loading paths in particular, as illustrated in the phase diagram of Fig. 4.[3] Path 1 represents loading from austenite into stress-induced martensite at temperatures sufficient to drive the critical stress for transformation up to the critical stress for plastic slip (see discussions in [67, 68]), while Path 2 represents heating from reoriented martensite into austenite while applying kinematic constraints (e.g., the total strain is held constant). In this condition, the recovery of transformation strain causes an opposing change in the elastic strain, and thus can drive the stress up through the critical level for yield. As yield progresses, the peak recovery stress (or *blocking stress*, the highest stress attainable during thermally-induced transformation) may be reached (see [69], especially Table 8.1). Path 1 can correspond to

[3]The phase diagram is a graphical representation of the various thermomechanical (stress-temperature) regimes where different processes occur or pure phases exist. Throughout this dissertation, such schematic diagrams will be used to illustrate pure austenitic states, pure martensitic states, states of transformation from austenite to martensite (*forward* transformation), and states of transformation from martensite to austenite (*reverse* transformation). In addition, thermomechanical conditions sufficient for the progression of plastic yield and viscoplastic creep/relaxation processes are also indicated. For a more detailed explanation, see [1].

fabrication of SMA forms or the utilization of an SMA-based application at high temperatures. For example, the use of an SMA application based on the pseudoelastic effect (e.g., such as a vibration isolation device [70]) at temperatures that far exceed A^f, intentionally or otherwise, can lead to such simultaneous yielding and stress-induced transformation in the SMA components. Path 2 corresponds to local kinematic constraints and resulting stress concentrations in SMA bodies that provide thermally-induced actuation. For example, the installation of fasteners in monolithic SMA components can cause such stress concentrations due to the large property mismatch between the SMA material and conventional fastener materials. Compared to the the SMA component, which can sustain substantial recoverable deformation, a steel fastener is nearly rigid, resulting in local kinematic constraints of the kind illustrated in Path 2. As an example, the Boeing VGC [24] uses steel fasteners threaded directly into thick SMA beams.

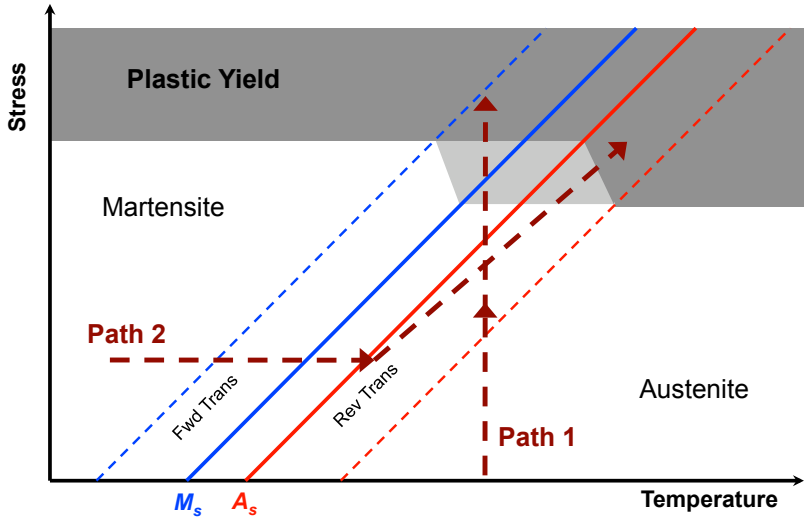

Fig. 4. Schematic illustration of two possible thermomechanical loading paths leading to simultaneous transformation and plastic slip.

To put the work described in this dissertation into context, it is also worth re-

viewing the concept of the material characteristic temperature "M_d." In short, this temperature is defined throughout the literature on SMAs as: "the temperature above which martensite cannot be stress-induced" [71] (see also [72]). It is understood that above this temperature, transformation stresses reach such a level that the irrecoverable plastic yielding becomes dominant. But the definition of this critical temperature is not described in the literature beyond this qualitative understanding, so Fig. 5 has been provided to give a schematic illustration with respect to the phase diagram.

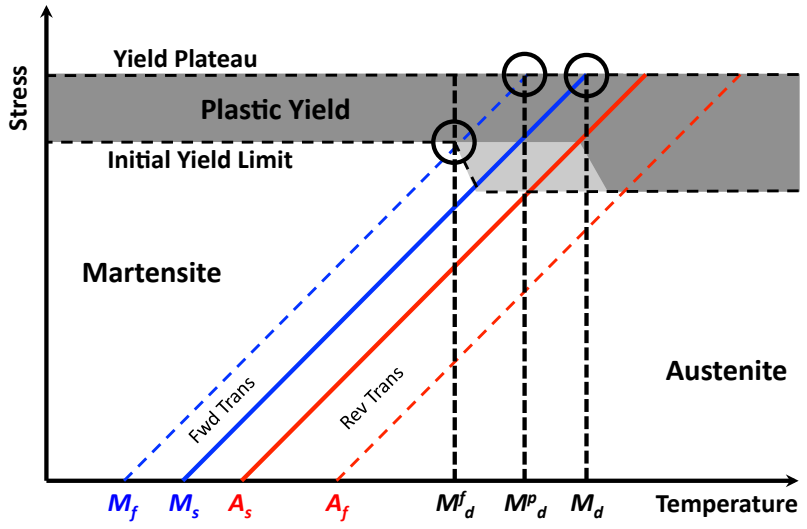

Fig. 5. Schematic illustration of temperature ranges for isothermal loading over which various transformation and yielding responses are observed (cf. Fig. 6).

Figure 5 expands upon Fig. 4 by describing both the initial yield limit (deviation from linear behavior) and the plastic yield plateau (or ultimate tensile strength [73]), and by focusing in more detail on possible isothermal paths. The definitions of the initial yield limit and yield plateau are illustrated in Fig. 6a. Maintaining the common definition of A_f, we then introduce two higher temperatures: M_d^c is given (schematically) by the intersection of the martensitic finish line with the initial yield limit of

martensite, while M_d^p is given by the intersection of the martensitic finish line with the yield plateau. Given these definitions, we can then consider the stress-strain *loading* response in three temperature ranges: $A_f \leq T \leq M_d^c$, $M_d^c < T \leq M_d^p$, and $M_d^p < T$. In the first range ($A_f \leq T \leq M_d^c$), the stress-induced forward transformation of martensite is able to *complete* prior to the initiation of plastic yield. This is seen in Fig. 6a. In the second range ($M_d^c < T \leq M_d^p$), yielding may initiate prior to transformation, but the stress-induced forward transformation of martensite is able to *complete* before the plastic yield plateau is reached. This is seen in Fig. 6b. At temperatures above M_d^p, stress-induced martensitic transformation may be initiated, but can only longer be *partially* completed before the material reaches the plastic yield plateau. This is seen in Fig. 6c. The temperature at which the material reaches the yielding plateau *prior* to beginning transformation is then denoted M_d, as martensite can no longer be stress-induced and only plastic dislocations are formed. The stress-strain response at a temperature above M_d is shown in Fig. 6d.[4] This work provides a model that captures isothermal material behavior over this entire range, from A_f to M_d, where transformation and plastic yield may occur simultaneously.

However, while the consideration of simultaneous transformation and plasticity is key to this work, there are also many other situations in which plastic yielding will occur in an SMA material *apart* from transformation (e.g., when a pure phase undergoes plastic deformation). The new model also makes contributions in this area by accounting for the effects that generated plastic strains have on subsequent phase transformation. Just as the installation of fasteners partially motivates the modeling of simultaneous effects, other processes motivate accurate modeling of pure phase yielding and effects on subsequent transformation. A common example of pure phase

[4]Given this illustration, it is clear that a possible alternative definition for M_d is "the temperature below which the plastic yielding of pure austenite is not possible."

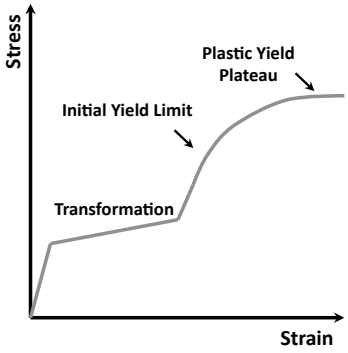

(a) $A_s \leq T \leq M_d^c$

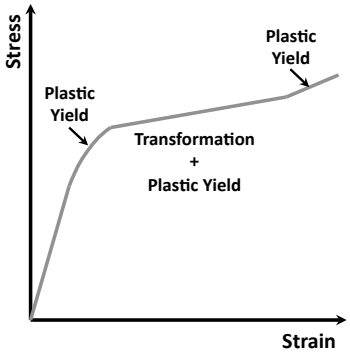

(b) $M_d^c < T \leq M_d^p$

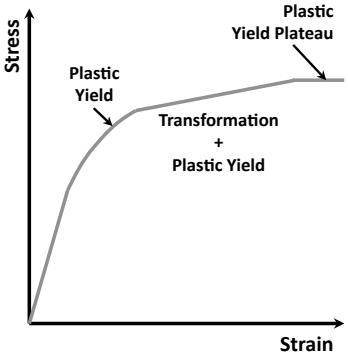

(c) $M_d^p < T \leq M_d$ (transformation not completed)

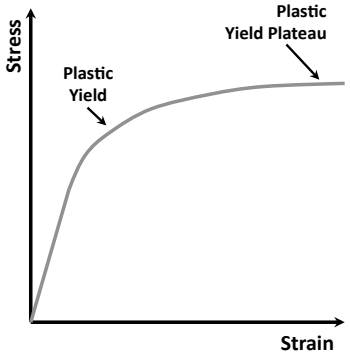

(d) $M_d < T$ (transformation not initiated)

Fig. 6. Schematic illustration of the stress-strain response during isothermal *loading* of austenite in one of four different temperature ranges (cf. Fig. 5).

yielding is found in the study of indentation in SMAs. New tribological applications also have the capability to both create and utilize plastic strains in SMAs [74, 75]. With regard to indentation, localized stress concentrations near the indenter, which may be of the spherical [76], Vickers [77], or Berkovich [78] configuration, lead to the formation of plastic strains in the martensitic phase after stress-induced martensitic transformation or detwinning process has completed. It has been shown that, provided the proper training techniques are applied, a two-way thermally-induced

deformation can be observed in these indents as heating causes recovery of some (but not all) of the indent depth. Subsequent cooling causes the indent to become deeper once again, and the process is repeatable [79].

A model that seeks to address any of the examples above and accurately account for plastic deformation in SMAs must consider the interaction between the two processes, and specifically the effects of plastic strain on subsequent transformation. Numerous experimental studies have been performed to assess these effects in detail. Studies on TRIP [80] indicated that irrecoverable strains generated during cyclic transformation continue to decrease both the critical stress for transformation and the recoverable strain. More pertinent to this dissertation, several studies, including the early works of Miyazaki and Shaw, have examined the transformation behavior of SMAs after subjecting specimens to loads sufficient to cause yielding due to slip [67, 68, 81]. Each of these studies noted a loss in recoverable deformation due to the generation of plastic dislocations in the austenitic parent phase. This loss of recoverable deformation has been attributed to a loss of recoverable martensite, and a linear relationship has been proposed between the amount of plastic strain generated and the amount of martensite retained [62]. Other studies of NiTi behavior by Liu and Favier showed that, in addition to a loss in recoverable strain, plastic strains generated in the material caused a change in both subsequent transformation temperatures and development of TWSME [82].

This dissertation will combine a rate-independent SMA model as described in Section A with the rate-independent models of classical plasticity assuming both isotropic and kinematic hardening. The derivation will be influenced by the laws of thermodynamics applied at the engineering scale, including the proposition of a suitable free energy potential. This approach has been used often in SMA modeling [37] and has also been discussed in the development of plasticity models [83].

C. Rate-Dependent Viscoplastic Deformations in SMAs

By modifying the methods discussed in the previous section, a whole new class of irrecoverable deformations in SMAs can be considered. These deformations are the rate-dependent, diffusion-driven viscoplastic strains induced by the motion of vacancies or dislocations [83], such as climb or climb-assisted gliding of dislocations [84]. Such strains appear and evolve in metals subjected to sufficiently high temperatures (greater than roughly one-third the absolute melting temperature). The need to account for these effects in shape memory alloys arises from one of the following two engineering problems:

1. Assessment of the change in thermomechanical state, internal and observed, and change in actuation behavior for a conventional SMA material (transformation temperatures below 100 °C) that has been exposed to high temperatures and sufficient forces due to shape-setting, hot rolling, or other processes (see Fig. 7a), or

2. Assessment of the coupled transformation-viscoplastic yielding response of an HTSMA with transformation temperatures sufficiently high to induce viscoplastic yielding[5] (see Fig. 7b).

The processing, shape setting, and application of conventional SMAs is an established subject with a long history. However, the effects that high temperature excursions might have on subsequent behaviors in these materials have not been modeled, and consideration of these is an important contribution of this dissertation. Further, the area of HTSMAs is relatively new, with potential HTSMA applications being in-

[5]The term *viscoplastic yielding* is used throughout the dissertation and is intended to capture both the processes of viscoplastic creep and relaxation, as well as any other process arising from the evolution of rate-dependent irrecoverable strains.

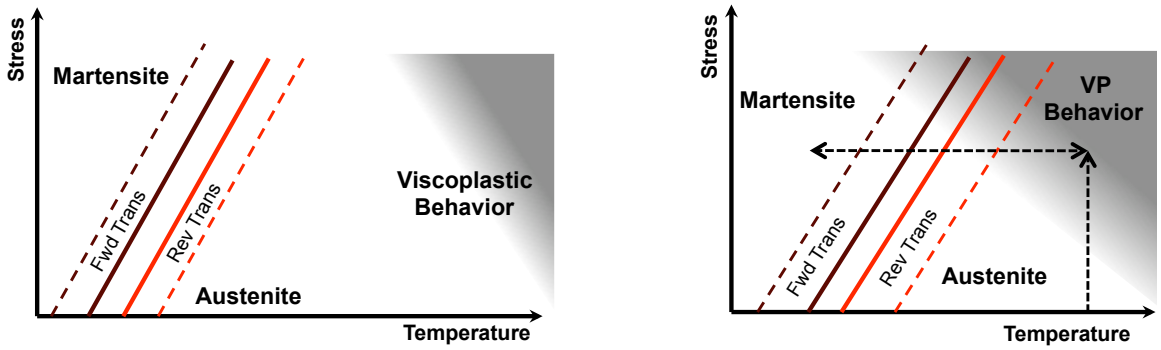

(a) Conventional SMAs (b) HTSMAs

Fig. 7. Schematic illustration of the relationship between transformation and viscoplastic regimes in conventional SMAs and HTSMAs.

vestigated for the oil and aerospace industries. For example, jet engine chevrons have been proposed for installation in the engine core region, where the high temperatures of engine exhaust gases require transformation temperatures far above that observed in conventional SMAs [85]. In such an application, it is important to understand how the high ambient temperatures will affect the operation of the active structure, and how that might change over time or over actuation cycles. Therefore, the ability to capture the coupled processes (transformation and viscoplastic creep/relaxation) simultaneously is becoming increasingly important, especially to predict the actuation loss that can occur in these materials due to the irrecoverable rate-dependent strains.

It is worth noting that the rate-dependency of SMAs is not limited to high temperature behaviors. Throughout the history of SMA research, investigations of various types of rate-dependency have been discussed. In studying the effects of loading rate on the stress-strain response, some works have considered tensile testing at rates exceeding conventional quasi-static levels [68], while others have investigated dynamic loading conditions (i.e., impact loading) [86, 87, 88]. The results of these studies in-

dicate that martensitic reorientation (or the detwinning of martensite) is effectively a rate-independent phenomenon analogous to conventional metal plasticity [66].[6] The stress-strain response during austenite-martensite transformation, however, is rate-dependent, and this is almost exclusively attributed to the coupling between the latent heat of martensitic transformation, the rate-dependent process of transferring heat into and out of a material system, and the variation of transformation stress with temperature. It is not related to classical metal viscoplasticity.

The rate-dependent viscoplastic behavior of conventional SMA compositions such as equiatomic and nearly-equiatomic NiTi exposed to high temperatures has been experimentally studied, and creep has been observed and quantified given both tensile [90, 91, 92] and compressive loads [93]. But the utility of this research is limited to the topics of metal forming, processing, and shape-setting; it is not applicable to actuator development and analysis. This is because the temperatures required to induce such diffusion-driven rate-dependency far exceed the useful actuation or pseudoelastic temperature range of conventional SMA materials. More recently, however, the entire range of SMA research topics, from alloy development [94] to basic material characterization [95, 96] to application design [85] has found a new focus in HTSMAs. To predict the structural response of both conventional SMAs at elevated temperatures and the newer HTSMA compositions providing actuation, a new constitutive model coupling transformation to the rate-dependent viscoplastic creep must be developed and implemented.

In the literature, the only SMA models proposed to capture rate-dependent behavior are intended to account for the time-dependent thermal effects associated with

[6] In one notable exception, [89] showed that the martensitic reorientation in a NiTiCu alloy system could progress over time given a constant applied load, though such a result is not commonly reported.

the latent heat of transformation, as discussed above. In several models, this rate-dependency results from coupling the balance of energy (and constitutive heat transfer assumptions) with the proposed thermomechanical constitutive equations [37, 97, 98]. In other models, rate-dependent thermomechanical equations are postulated directly (without explicit recourse to the balance of energy), though motivation by thermal effects is often qualitatively invoked [99, 100, 101, 53]. The statistical thermodynamics approach to conventional SMA modeling [43] is also formulated in a rate-dependent manner, though the relaxation time parameter is set to a low value consistent with the short time scales of of the diffusionless phase transformation mechanisms. Regardless of the motivation or formulation, not one of the models just mentioned is applicable to the problem of rate-dependent generation of irrecoverable (i.e., viscoplastic) strains. Rather, these formulations apply only to the physical process of phase transformation and, because they describe the formation and recovery of *martensite* as a rate-dependent process, they include only elastic and *recoverable* transformation strains.

As with rate-independent plasticity, this dissertation will describe the combination of a rate-independent SMA model (Section A) with models of viscoplasticity based on thermodynamics as discussed by Chaboche [83, 102, 103], and Arnold [104]. Each of these sources begins their derivations by assuming a free energy potential, where Arnold and Saleeb describe this approach as *generalized viscoplasticity with potential structure* (GVIPS). This methodology is compatible with the approach to SMA modeling used by [37] and extended herein. It is worth mentioning that other possible methods exist for the modeling of transformation and viscoplasticity. For example, the class of models that attempts to unify plastic and viscoplastic phenomena [84, 103] could be used to unify the transformation and viscoplastic behaviors. However, the two processes of transformation and creep/relaxation are known to arise

from very different underlying physical mechanisms (i.e., diffusionless phase transformation and climb-assisted dislocation motion, respectively). Given this, *unification* of the inelastic strains, one recoverable and one not, is considered unnecessary, while the *coupling* of the two differing effects is taken to be the goal of this work. By expanding upon the work on rate-*independent* plasticity in SMAs described in this dissertation and coupling the models in a similar way, the implementation of the new rate-dependent coupled model proceeds in a straightforward manner. This is because the key relations for viscoplastic yield can be written in a form that is analogous to those for conventional plasticity (see, for example, the work of [105], especially Section 2.3). The final implementation in an FEA framework (as with the conventional and transformation-plasticity models) then allows for the analysis of complex active structures experiencing localized viscoplastic yielding, either due to processing at temperatures well above the transformation range (i.e., in conventional SMAs), or during transformation at high temperatures (i.e., in HTSMAs).

D. Summary of the Dissertation

In summary, this dissertation is organized as follows:

- Chapter II describes a constitutive model for conventional SMAs undergoing martensitic transformation whereby a fully-recoverable inelastic transformation strain is evolved. This model represents an extension from the models found in the literature, and experimental data is provided that motivates its new features.

- Chapter III continues the discussion of the SMA model for fully-recoverable deformations by describing the method by which the model is implemented in a numerical (finite element) framework. Example analyses are used to demon-

strate the effectiveness of the new modeling tool, where predictions are compared to independently-obtained experimental data.

- Chapter IV expands upon the work of the previous two chapters by considering the effects of rate-independent plastic deformations generated in an SMA material, where the two processes can be coupled. Both the mathematical model and the numerical implementation are described. Experimental calibration and computational analysis examples are provided, including experimental validation of analysis predictions.

- Chapter V again expands on Chapters I and II but considers rate-dependent irrecoverable deformations occurring in SMAs, especially in HTSMAs. Again, the mathematical model, numerical implementation, and analysis examples are provided. The results from multiple examples are compared to experimental data.

- Chapter VI provides a summary of this body of work and discusses possible future research efforts stemming from it.

CHAPTER II

IMPROVED SMA MODEL FOR ANALYSIS OF COMPLEX STRUCTURES

This chapter begins the dissertation by motivating, deriving, and demonstrating the effectiveness of a baseline model onto which further extensions (rate-independent plasticity, rate-dependent viscoplasticity) are added. The baseline model itself extends upon other models found in the literature to more accurately capture various aspects of the transformation response described herein. To begin, Section A describes the experimental motivation for improving upon the models in the literature and forming the new baseline SMA phase transformation model, Section B outlines the improvements themselves, and Section C describes the derivation of the mathematical model itself using continuum thermodynamics. To conclude the chapter, Section D includes model calibration and the simulation of experiments, and demonstrates the unique capabilities and accuracy of the proposed model.

A. Experimental Motivation for SMA Model Improvement

The improvements that comprise the new constitutive model for SMA thermoelastic and transformation response were in large part motivated by an experimental study of a particular composition of SMA proposed for use in aerospace applications [25, 106]. It can be seen throughout the literature, however, that the pertinent behaviors can also be observed in other SMA compositions [55, 54]. The new study and its results are described in the following sections.

1. Material composition and experimental setup

Although the most popular shape memory alloy composition is near-equiatomic NiTi (or *Nitinol*) with a composition of $Ni_{55}Ti_{45}$ wt% ($Ni_{50}Ti_{50}$ at%), the material considered here has a composition of $Ni_{60}Ti_{40}$ wt% ($Ni_{55}Ti_{45}$ at%), which is hereafter referred to as "Ni60Ti". Recent work has established nickel-rich NiTi as a viable shape memory alloy material for aerospace applications [24]. These alloys have only been available commercially for the last 10 years; however, research into the effect of increasing the nickel content in NiTi alloys above the equiatomic composition has been under investigation for decades [107, 108, 109, 110, 111]. The Boeing Phantom Works (now *Boeing Research and Technology*) Flight Sciences organization has done extensive testing on NiTi properties for actuator development [25, 112]. Among all NiTi alloys, nickel-rich compositions were shown to provide several advantages in aerospace application design. Among other advantageous traits, this material shows excellent repeatability of response (thermomechanical stability) after a relatively small number of training cycles, especially when compared to the equiatomic NiTi composition.

All actuators and test specimens considered in this study (both Chapter II and Chapter III) were fabricated from a single billet of Ni60Ti which had been hot rolled into a plate with a nominal thickness of 0.25 in (6.35 mm). The specimens used for tensile characterization were formed via water jet and wire *Electrical Discharge Machining* (EDM) cutting. ASTM standard subsized tensile coupons [113] were then EDM cut from smaller plates for thermomechanical testing. The actuator flexures for the VGC discussed later in Chapter III, Section B were also cut from the same original plate, with both the tensile specimens and the flexures cut with their long dimensions aligned with the rolling direction.

The characterization described in this section was performed at the Material

and Structures Laboratory in the Department of Aerospace Engineering at Texas A&M University. Thermomechanical loading was performed on an MTS 880 loading frame (100 kip (445 kN) load cell, Epsilon brand 1.0 in (25.4 mm) gauge length extensometer, MTS control suite). Active heating was provided by Omega resistive heating strips and cooling was provided by a custom designed liquid nitrogen dispersal system. Thermal control and thermal data acquisition were accomplished via a custom National Instruments (NI) LabView program coupled with an NI SCB-68 data acquisition board.

The quasi-static material characterization of the material actuation behavior involved the imposition of a series of isobaric (constant stress) thermal cycles applied to the newly trained specimen. The results of these tests would provide information about two important relationships:

- how the critical temperatures for transformation varied with applied stress, and
- how the amount of recoverable transformation strain generated varied with applied stress.

Understanding these two relationships (in addition to assessing the thermoelastic behavior of the material) was the goal of the characterization steps described herein. The constant stress levels were 30, 60, 90, 120, 150, 200, 250, and 300 MPa.

To perform such testing, the environmental chamber surrounding the SMA sample was configured for slow thermal cycling. Heat strips mounted to the wall of the chamber were used to slowly and evenly heat the entire environment surrounding the sample. During cooling, liquid nitrogen was forced through tubing mounted within the chamber along its upper edge. Liquid/gaseous nitrogen was thereby introduced into the chamber environment from the top and drifted downwards. This led to slow, uniform cooling of the entire chamber. The characteristic time needed to both heat

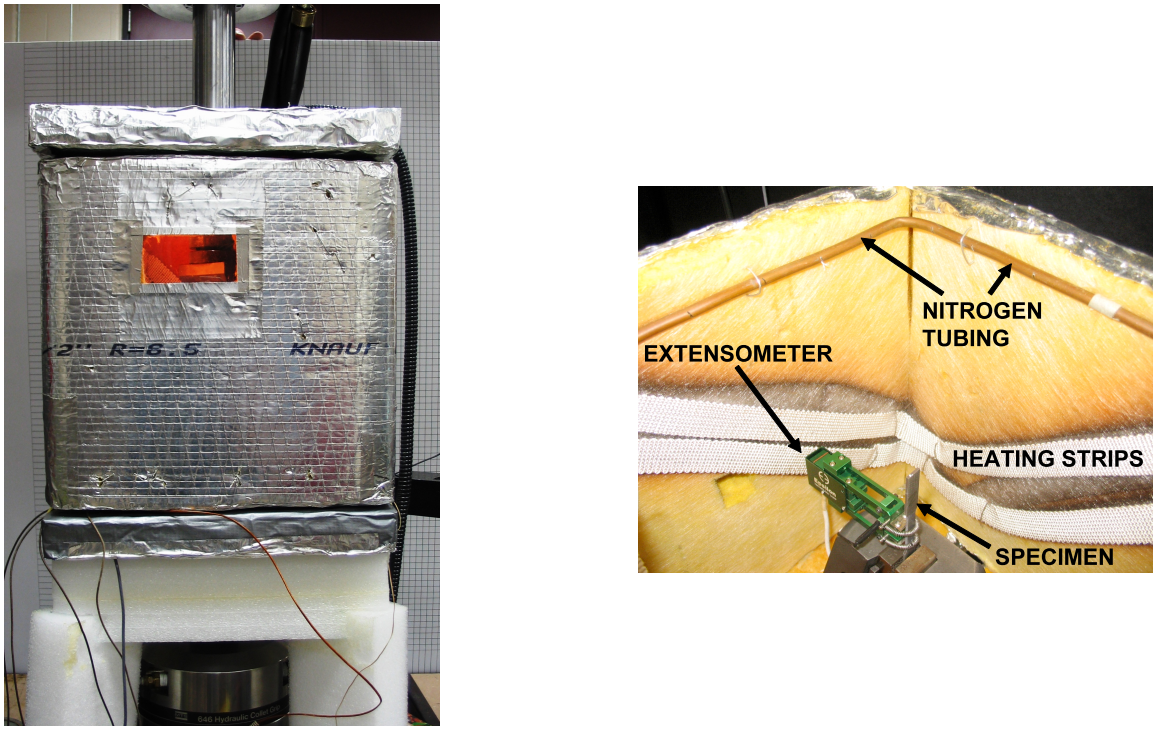

(a) (b)

Fig. 8. Testing setup for the tensile characterization of SMA specimens: a) environmental chamber mounted on MTS frame (exterior view), b) interior view.

and cool through full transformation was approximately 30 minutes. The test setup for characterization is shown in Fig. 8.

2. Thermomechanical characterization

After initially stabilizing (training) the material via thermal cycling through full transformation for 100 cycles [13], the process of characterizing the material began. This stabilization eliminated the cyclic evolution in the actuation response of the material, and is necessary for any material intended for repeatable and reliable utilization (e.g., in aerospace applications). The thermoelastic properties were known from testing the

as-received material and were not expected to have changed significantly with training, so the focus was instead on the actuation properties of the trained material (i.e., critical temperatures for transformation and transformation strain generation).

The strain-temperature results for each of the isobaric thermal cycling tests are shown in Fig. 9a for the lower stress levels and in Fig. 9b for the higher stress levels. For each stress level, the response curve has been shifted downward such that the elastic response of the austenitic phase during initial loading is not shown.

To determine when the forward and reverse transformations began and ended for the stabilized material (i.e., to build a phase diagram), the common method of tangent lines was used. This is illustrated in Fig. 9b for the $\sigma = 300\,\mathrm{MPa}$ curve, where it is shown that the austenitic start temperature for the stabilized material at this stress (A_s^σ) is 43 °C. The temperatures for the beginning and end of the phase transformations (forward and reverse) at all stress test levels are shown in stress-temperature space in Fig. 10. This represents the experimental phase diagram for this material composition (stabilized material). To begin an interpretation of these results, we consider the amount of deformation generated and recovered during these isobaric thermal cycles. Assuming an additive decomposition of the strain and using Hooke's law, we have for the total strain ε

$$\varepsilon = \frac{\sigma_i}{E} + \alpha(T - T_0) + \varepsilon^t, \tag{2.1}$$

where σ_i denotes the constant uniaxial stress applied in the i^{th} test, T the current temperature, and E and α the Young's modulus and coefficient of thermal expansion, respectively. The parameter T_0 is the reference temperature. The uniaxial transformation strain associated with the evolution of the microstructure from the austenitic phase to the martensitic phase is denoted ε^t; given full transformation from austenite into martensite, it takes on the value $H^{cur}(\sigma_i)$, depending on the current applied

stress level (this is known as the maximum transformation strain). Determination of this material-dependent function is one goal of material characterization.

If we consider that the Young's modulus may change with phase, and that all transformation strain is recovered during transformation into austenite, we have for the two phases:

$$\varepsilon_M = \frac{\sigma_i}{E^M} + \alpha(T_{min} - T_0) + H^{cur}(\sigma_i), \tag{2.2}$$

$$\varepsilon_A = \frac{\sigma_i}{E^A} + \alpha(T_{max} - T_0), \tag{2.3}$$

where T_{min} and T_{max} denote the the minimum and maximum test temperatures, respectively, and ε_M is the strain in martensite (at T_{min}), while ε_A is the strain in austenite (at T_{max}). Given the above relations, we find that the 1-D equation for calculating the maximum transformation strain H^{cur} generated under a particular applied stress level σ_i is written as [114]

$$H^{cur}(\sigma_i) = \left| (\varepsilon_M - \varepsilon_A) + \sigma_i \frac{E^M - E^A}{E^M E^A} \right| + \alpha(T_{min} - T_{max}) \tag{2.4}$$

The dependence of maximum transformation strain on applied stress for the current Ni60Ti material is shown in Fig. 11, where the strains generated during transformation of the stabilized (trained) material are compared to equivalent results from preliminary testing of the as-received (untrained) specimen. Note how training reduces the magnitude of recoverable strain.

A review of the experimental results presented in this section allows one to come to quantitative conclusions about the various material properties which can be used to describe the behavior of the stabilized material in the context of past SMA constitutive models found in the literature, especially those of Lagoudas and coworkers [38, 115]. These properties can be divided into three categories as follows:

The first subset of material properties are the thermoelastic properties of the

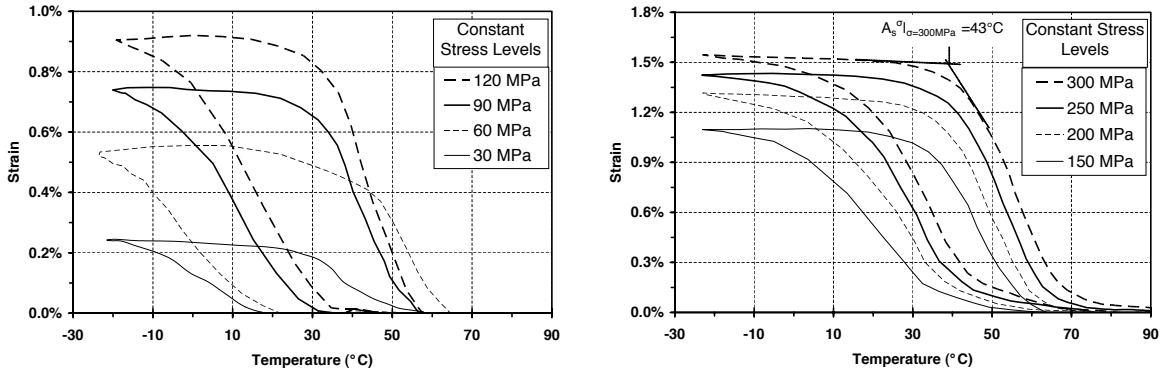

(a) 30, 60, 90, and 120 MPa (b) 150, 200, 250, and 300 MPa

Fig. 9. Experimentally-determined uniaxial strain vs. temperature response of stabilized Ni60Ti under various applied constant uniaxial stresses.

polycrystalline SMA material, where the assumption of material isotropy is used to reduce the number of properties required.

- E^A, E^M – The elastic moduli of austenite and martensite, respectively. The austenitic modulus was determined during initial loading at high temperature before isobaric temperature variations were imposed (e.g., Fig. 9); the martensitic modulus was determined by loading and unloading the material in tension at a low temperature, where the material was known to be martensitic.

- ν – Poisson's ratio, assumed equal for both phases. Taken from literature [38].

- α^A, α^M – The coefficient of thermal expansion of austenite and martensite, respectively. Taken from literature [38].

The next subset of properties describes the configurations of the stress-temperature regions for the existence of pure phases and regions of transformation (i.e., they describe the phase diagram).

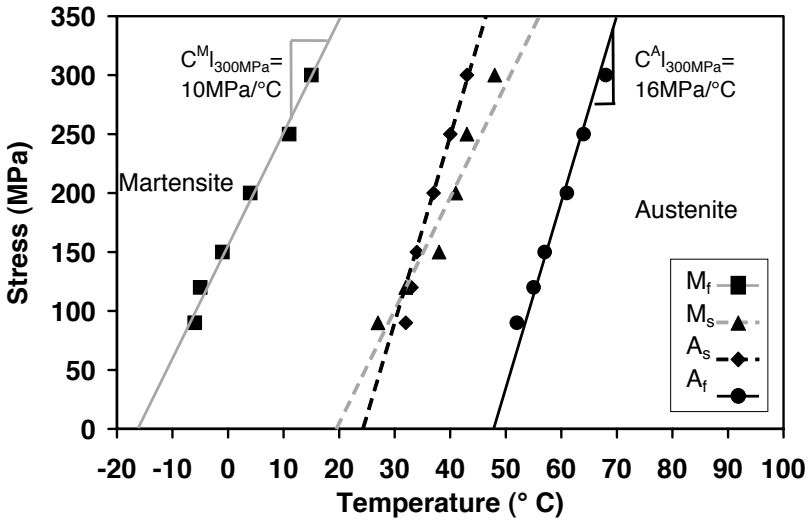

Fig. 10. Experimental transformation regions for stabilized Ni60Ti (determined by tangent intersection method; see Fig. 9b, 300 MPa).

- M_s, M_f, A_s, A_f – The zero-stress transformation temperatures (martensite start, martensite finish, austenite start, and austenite finish) found from the intersections of the transformation surfaces with the stress axis (see Fig. 10).

- $C^A|_\sigma, C^M|_\sigma$ – Stress influence coefficients which describe the slope of the transformation surfaces, as plotted on the phase diagram (Fig. 10).

Finally, the remaining required property captures the generation and recovery of transformation strain as the material undergoes the martensitic transformation.

- $H^{cur}(\sigma_i)$ – The maximum transformation strain as a function of test stress; determined by application of (2.4) using all of the data of Fig. 9 and shown in Fig. 11.

The values for all these properties are given in Table I. As a point of comparison, the equivalent parameter values for equiatomic NiTi material as found in the literature are also provided (approximate values) [1]. Notice that the Ni60Ti material is

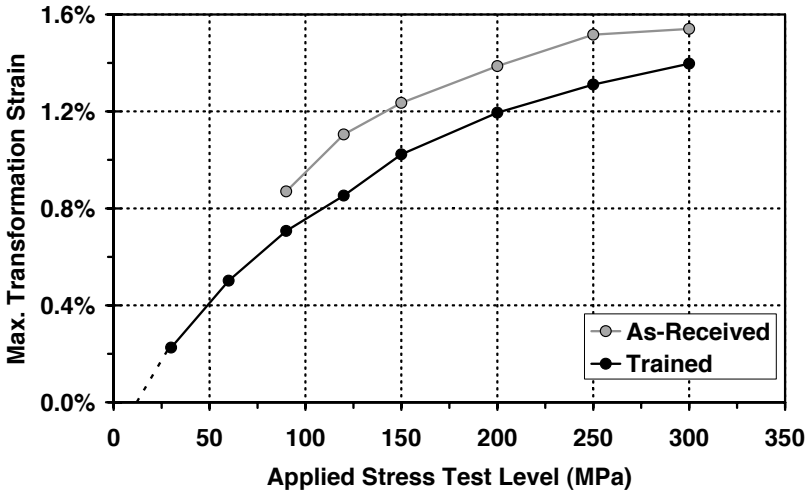

Fig. 11. Transformation strain vs. applied constant stress results for Ni60Ti, as-received and stabilized (trained) conditions.

stiffer in its elastic response, and this may be a result of the creation of stiff Ni-rich precipitates in the material during heat treatment and processing [116]. The transformation temperatures are lower in this nickel-rich material, and this is a known result of the addition of nickel to the equiatomic alloy [4]. The slopes of the transformation surfaces C^A and C^M are somewhat higher for the Ni-rich material, and this may preclude the use of this material for pseudoelastic applications as very high stresses are needed to complete transformation for temperatures above A_f. Finally, the maximum thermally-induced transformation strain which can be obtained from the Ni60Ti material under constant applied stress is less than 2%, lower than the 5–6% observed in equiatomic NiTi SMA [117]. Again, this may be a result of the many precipitates which form in the material and hinder the formation of similarly oriented variants which is the underlying mechanism for the generation of transformation strains.

Table I. Material properties for stabilized Ni60Ti and comparison with nominal properties for equiatomic NiTi (Ni55Ti, taken from literature [1]).

Parameter	**Ni60Ti**	**Ni55Ti***
Thermoelastic Properties (Taken from experiments on as-received material, see [13])		
E^A	90GPA	70GPA
E^M	63GPA	30GPA
$\nu^M = \nu^A$	0.33*	0.33
$\alpha^A = \alpha^M$	10e-6/ ℃*	10e-6/ ℃
Phase Diagram Properties (Interpreted from Fig. 10, tangent method)		
M_s	20 ℃	55 ℃
M_f	−16 ℃	15 ℃
A_s	24 ℃	80 ℃
A_f	48 ℃	89 ℃
$C^A\|_{\sigma=300MPa}$	14.9MPa/ ℃	7–10MPa/ ℃
$C^M\|_{\sigma=300MPa}$	10.6MPa/ ℃	7–10MPa/ ℃
Transformation Strain Properties (Derived from Fig. 11)		
$H^{cur}(\sigma)$	$= 0.0135[1 - e^{(-720\sigma/E^A)}]$	6%

B. Proposed Improvements for Conventional SMA Models

Using the characterization data from Section A, it can now be shown how on popular SMA constitutive model in particular, known as the "unified model," [37, 38] is unable to accurately predict some important material behaviors. We first calibrate this existing model and then use it to simulate the isobaric loading experiments. Most of the properties in Table I can be used directly, and the model predictions based on these parameters are shown below. One model parameter that does not have a direct

correlation with a material property in Table I is H^{cur}, the maximum transformation strain. While experiments show that this value varies with applied load, the original unified model [38] admits only a single material *constant*. Therefore, an averaged value of $H^{cur} = H = 0.95\%$ is used in calculating the following results[1].

The pre-existing model considered here (the unified model) can then be used to simulate the experimental results for thermal cycling under isobaric loading conditions. These simulations are shown here in Fig. 12 for applied stress levels of 90, 150, and 200 MPa. The standard implementation of the unified model [38, 115] is unable to capture two key features of the experimental results. It does not capture the change in the hysteresis height with changing applied stress level; it also does not capture the gradual (or smooth) transition from thermoelastic response to transformation response.

If we consider the 1-D tensile testing discussed in Section A, the *maximum transformation strain* is the inelastic recoverable strain generated in the loading direction over the course of *full* transformation from austenite to martensite (forward transformation) (cf. (2.4)). In the modeling of SMAs, the concept of maximum transformation strain has most commonly been captured by a single constant-valued material property that prescribes a value for this strain independent of loading conditions (independent of loading stress level). This trend can be seen in early models [34, 31, 37, 38], and constant maximum transformation strains continue to be postulated even in recent models [53, 51, 118, 35, 41, 42]. This assumption is sometimes

[1]The work of Bo and Lagoudas [54], which represents an extension of the unified model, should be acknowledged for also considering a variable H^{cur}, and was a major motivation for the current discussion. In that work, this variation of maximum transformation strain was related to internal (back) stresses and other effects not currently considered. For the sake of following the straightforward experimental calibration methods of the previous section and providing researchers with an accurate tool for doing similar calibrations in the future, here we use the empirically motivated form of H^{cur} given in Table I.

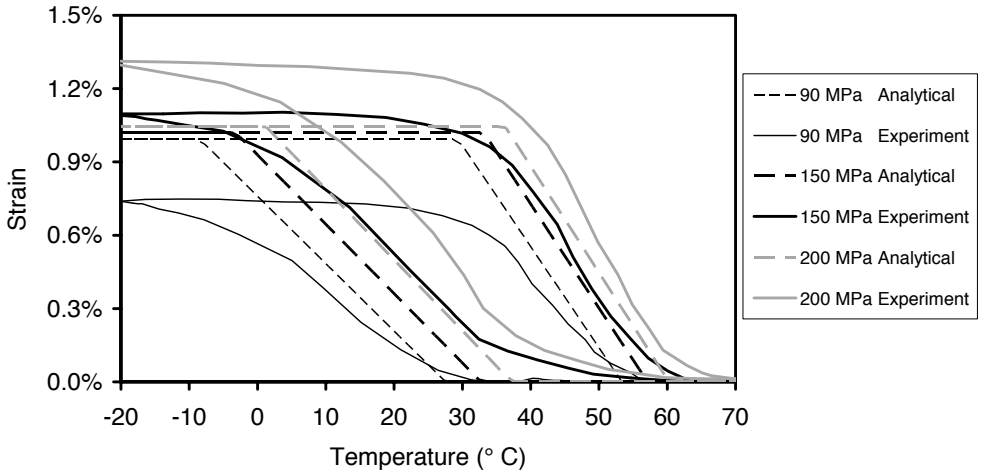

Fig. 12. Experimental results and "unified model" [37, 38] simulations for isobaric thermal cycling of Ni60Ti at three constant stress levels.

applicable because in many SMA compositions, especially near-equiatomic NiTi, training of the material will lead to *two-way shape memory effect* (TWSME) [1, 4]. In such materials, the maximum transformation strain observed during forward transformation can be described by one constant that applies whether the applied stress level is high, low, or null.

Assessment of experimental results throughout the literature, on the other hand, especially that of Bo, Lagoudas, and coworkers [54, 55], indicates that the magnitude of transformation strain generated during forward transformation can be dependent on stress level. Constant stress thermal cycling experiments, important for the development of actuators, highlight this dependence, which occurs especially in polycrystalline materials. These same trends can also be observed in pseudoelastic experiments (see [68], Fig. 17b). At the microstructural level, some materials transform into primarily self-accommodated martensite given zero applied stress, resulting in negligible observed transformation strain. This is especially noticeable as the amount

of nickel (and associated precipitates) increases [119]. A higher magnitude of externally applied stress causes favored variants to be formed at the expense of others during transformation, increasing the observed transformation strain. The extent of this stress influence can vary with the amount and configuration of precipitates in each grain (crystal) [119], and in polycrystalline materials may further be influenced by the presence of grain boundaries (see also the work of Sittner [120]). Only a few models have attempted to account for this behavior [54, 59], and here we address it in an empirical and straightforward manner.

An additional feature of the material response that should be considered is related to the material hardening during transformation. Throughout the history of SMA modeling, several hardening responses have been considered, including those formulated with exponential [121], trigonometric [33], and linear [37] forms. These theoretical forms do not always match the experimental results effectively. For Ni60Ti, it is observed that the transition from the thermoelastic response to the transformation response (and vice versa) is more "smooth" than any of these three models is capable of predicting (see Fig. 12 above). To capture this behavior, the mathematical model clearly must allow for continuous first derivatives in the strain-temperature response across the entire temperature range of actuation. This requirement may not apply to more common equiatomic NiTi compositions, where the transitions to and from transformation can be quite abrupt (see for example [68]). Examining Fig. 12, it can also be observed that the ability to mathematically adjust these derivatives (and thus the smoothness) at each of the hysteresis corners would also be useful. A similar smoothness requirement motivated the implementation of a new hardening form as proposed by Machado et al. [122, 123]. This form was developed in the course of studying the non-linear dynamics of pseudoelastic SMAs, during which it was noted that such continuous derivatives during the transition from elastic to transformation

response stabilized the numerical solution process.

C. Derivation of Improved SMA Constitutive Model

A full 3-D thermomechanical model for the thermoelastic and transformation response of a conventional (rate-independent) shape memory alloy is derived below, where much of what follows is guided by a methodology originally used in the past works of Lagoudas and coworkers [38, 124, 122]. In the current work, new features are added or improved to increase the fidelity of the model in capturing the transformation deformation response of a larger class of SMA material systems. These improvement include the variable maximum transformation strain and smooth hardening. An additional development is the formulation of the transformation hardening energy as an internal variable with its own evolution equation [125]. Some hold that the free energy potential should only be a function of the current values and histories of the internal variables but not of their rates, and the current framework satisfies this requirement on the state function.

1. Formulation of specific Gibbs free energy potential

Assumption 1: The state of the material is described by a Gibbs free energy thermodynamic potential, which is decomposed into an austenitic, martensitic, and mixing contribution, and which is dependent on particular external and internal state variables.

The derivation of the SMA transformation model begins with the choice of a free energy potential and complementary independent state variables (both externally applied and internally evolving). Using the framework of Lagoudas and coworkers [1], we choose the Gibbs energy, denoted G, which is additively decomposed into a contri-

bution G^A from the local material regions in the austenitic phase, a contribution G^M from regions in the martensitic phase, and a contribution due to mixing of austenite and martensite, G^{mix}. Here we postulate that $G = G(\boldsymbol{\sigma}, T, \boldsymbol{\zeta}^t)$, where the external state variables are the macroscopic *stress* $\boldsymbol{\sigma}$ and *temperature* T and where $\boldsymbol{\zeta}^t$ denotes the set of *transformation internal state variables* containing both scalars and tensors. Specifically, we assume $\boldsymbol{\zeta}^t = \{\boldsymbol{\varepsilon}^t, \xi, g^t\}$ where each variable is described as follows: the *transformation strain* $\boldsymbol{\varepsilon}^t$ is the recoverable inelastic strain generated during transformation from austenite to martensite and subsequently recovered during full reverse transformation, the *total martensitic volume fraction* ξ accounts for the generation and recovery of all martensitic variants and is bounded by $0 \leq \xi \leq 1$, and the *transformation hardening energy* g^t is a measure of the nonlinear change in the mixing energy as transformation progresses at constant stress. Given these state variables, the Gibbs energy for the overall SMA material (austenite/martensite composite) is then written:

$$G(\boldsymbol{\sigma}, T, \boldsymbol{\varepsilon}^t, \xi, g^t) := (1-\xi)G^A(\boldsymbol{\sigma}, T) + \xi G^M(\boldsymbol{\sigma}, T) + G^{mix}(\boldsymbol{\sigma}, \boldsymbol{\varepsilon}^t, g^t), \tag{2.5}$$

where, for the assumption of a quadratic dependence on stress,

$$\begin{aligned} G^\gamma(\boldsymbol{\sigma}, T) &= -\frac{1}{2\rho}\boldsymbol{\sigma} : \boldsymbol{\mathcal{S}}^\gamma \boldsymbol{\sigma} - \frac{1}{\rho}\boldsymbol{\sigma} : \boldsymbol{\alpha}(T - T_0) \\ &+ c\left[(T - T_0) - T\ln\left(\frac{T}{T_0}\right)\right] - s_0^\gamma T + u_0^\gamma, \end{aligned} \tag{2.6}$$

for $\gamma = A, M$. The energy of mixing is given as:

$$G^{mix}(\boldsymbol{\sigma}, \boldsymbol{\varepsilon}^t, g^t) = -\frac{1}{\rho}\boldsymbol{\sigma} : \boldsymbol{\varepsilon}^t + \frac{1}{\rho}g^t. \tag{2.7}$$

The material constants $\mathcal{S}$, s_0 and u_0 denote the compliance tensor, specific entropy at the reference state, and specific internal energy at the reference state, respectively,

and are assumed to be different for each phase. On the other hand, $\boldsymbol{\alpha}$, ρ, and c denote the thermal expansion coefficient tensor, density, and specific heat, respectively, and are assumed to be invariant during phase change.[2].

2. Application of the laws of thermodynamics via the Coleman-Noll procedure

To continue the derivation, we apply the laws of thermodynamics to the chosen form of the Gibbs free energy potential. The methodology used is commonly referred to as the Coleman-Noll procedure [126, 127, 128], and is described for shape memory alloys elsewhere [122]. Here the pertinent steps are addressed.

After satisfying the conservation of mass, linear momentum, and angular momentum (see standard continuum mechanics texts), the *first law of thermodynamics* (conservation of energy) can be written at a local material point as

$$\rho \dot{u} = \boldsymbol{\sigma} : \dot{\boldsymbol{\varepsilon}} - \mathrm{div}(\mathbf{q}) + \rho r, \tag{2.8}$$

where the overdot ($\dot{}$) denotes the time rate of change of the dotted quantity. The variable $\boldsymbol{\varepsilon}$ is the total (infinitesimal) strain, $\mathbf{q}$ is the heat flux vector, and r is the rate of internal heat generation.

Likewise, provided that the conservation laws are satisfied, the *second law of thermodynamics* can be locally written in the form of the Clausius-Planck inequality, given as

$$\rho \dot{s} + \frac{1}{T}\mathrm{div}(\mathbf{q}) - \frac{\rho r}{T} \geq 0. \tag{2.9}$$

---

[2]Many past models have assumed that the thermal expansion coefficient and specific heat are functions of the phase, which is true in general. However, motivated by the fact that such dependencies lead to very small effects in the final constitutive equations, phase dependence of these properties is neglected for the sake of a clarified presentation

Multiplying (2.9) through by T and substituting in (2.8) to eliminate $\mathrm{div}(\mathbf{q})$, we find

$$\rho \dot{s} T + \boldsymbol{\sigma} : \dot{\boldsymbol{\varepsilon}} - \rho \dot{u} \geq 0. \tag{2.10}$$

The various energy potentials (e.g., Gibbs, Helmholtz, etc.) at a material point are related by the *Legendre transformations*. Here we consider only the relationship between the internal energy u and Gibbs free energy G, given as

$$G = u - \frac{1}{\rho} \boldsymbol{\sigma} : \boldsymbol{\varepsilon} - sT. \tag{2.11}$$

Substituting the time rate of change of (2.11) into (2.10), we arrive at the following thermodynamic constraint on the rate of the Gibbs free energy:

$$-\rho \dot{G} - \dot{\boldsymbol{\sigma}} : \boldsymbol{\varepsilon} - \rho s \dot{T} \geq 0. \tag{2.12}$$

Applying the chain rule to G and using the assumed internal variable set of (2.5), this gives

$$-\rho \left(\partial_{\boldsymbol{\sigma}} G : \dot{\boldsymbol{\sigma}} + \partial_T G \, \dot{T} + \partial_{\boldsymbol{\varepsilon}^t} G : \dot{\boldsymbol{\varepsilon}}^t + \partial_\xi G \, \dot{\xi} + \partial_{g^t} G \, \dot{g}^t \right) - \dot{\boldsymbol{\sigma}} : \boldsymbol{\varepsilon} - \rho s \dot{T} \geq 0, \tag{2.13}$$

where the notation $\partial_{\boldsymbol{\sigma}} G$ denotes the partial derivative of G with respect to $\boldsymbol{\sigma}$, for example.

The Coleman-Noll procedure continues by strictly enforcing the condition that the constraint (2.13) must be satisfied for all possible thermodynamic paths. These include those paths where all variables are held fixed except for one, which is evolving. If we consider, for example, a thermomechanical path in which only the temperature is changing, (2.13) reduces to

$$-\rho \left(\partial_T G + s \right) \dot{T} \geq 0, \tag{2.14}$$

which must be satisfied whether the temperature is increasing or decreasing, and this

is possible if and only if

$$\partial_T G + s = 0. \tag{2.15}$$

Thus, considering the form of G currently assumed, we have the following constitutive relationship for entropy in terms of the state variables:

$$s = -\partial_T G = \frac{1}{\rho}\boldsymbol{\sigma} : \boldsymbol{\alpha} + c \ln\left(\frac{T}{T_0}\right) + s_0(\xi). \tag{2.16}$$

Applying the same procedure while considering only the evolution of stress gives the following relation for the total infinitesimal strain, which arises as a direct result of assumptions made in (2.5), (2.6), and (2.7):

$$\boldsymbol{\varepsilon} = -\rho\partial_{\boldsymbol{\sigma}} G = \boldsymbol{\mathcal{S}}(\xi) : \boldsymbol{\sigma} + \boldsymbol{\alpha}(T - T_0) + \boldsymbol{\varepsilon}^t. \tag{2.17}$$

Note that rewriting (2.17) in terms of stress and introducing $\boldsymbol{\mathcal{C}} = \boldsymbol{\mathcal{S}}^{-1}$, we arrive at the common form of Hooke's law which will be useful during implementation:

$$\boldsymbol{\sigma} = \boldsymbol{\mathcal{C}}\left[\boldsymbol{\varepsilon} - \boldsymbol{\alpha}(T - T_0) - \boldsymbol{\varepsilon}^t\right] = \boldsymbol{\mathcal{C}}\left[\boldsymbol{\varepsilon} - \boldsymbol{\varepsilon}^{th} - \boldsymbol{\varepsilon}^t\right]. \tag{2.18}$$

Also, due to the decomposition of G into an austenitic and martensitic component, the material constants $\boldsymbol{\mathcal{S}}$ and s_0 involved in the definition of strain and entropy are now defined in terms of the martensitic volume fraction ξ by the rule of mixtures (e.g., $\boldsymbol{\mathcal{S}}(\xi) := \boldsymbol{\mathcal{S}}^A + \xi\widetilde{\boldsymbol{\mathcal{S}}}$, etc).[3]

The remaining dissipative terms resulting from the above application of the second law (Clausius-Planck inequality) consist of the partial derivatives of G with re-

[3]Throughout this work we will adopt the notation that, for any quantity x defined in the pure austenitic phase (x^A) and pure martensitic phase (x^M), the difference is given as $\tilde{x} = x^M - x^A$. The use of the symbol Δ, commonly applied for this purpose, is reserved for discussions of discretized time evolutions (e.g., Chapter III, Section A).

spect to each of the two independent internal variables. This is written as

$$-\rho\left[\partial_{\xi}G\ \dot{\xi}+\partial_{\boldsymbol{\varepsilon}^t}G^{mix}:\dot{\boldsymbol{\varepsilon}}^t+\partial_{g^t}G^{mix}\dot{g}^t\right]\geq 0. \tag{2.19}$$

3. Evolution of internal variables

Assumption 2: The rate of evolution of the transformation internal state variables $\boldsymbol{\zeta}^t$ are proportional to the rate of evolution of the martensitic volume fraction, $\dot{\xi}$, and this rate alone.

Here we postulate evolution equations for the tensorial internal state variable $\boldsymbol{\varepsilon}^t$ and the scalar internal variable g^t in terms of the rate of the scalar quantity ξ. The proposed form for the transformation strain evolution is consistent with the evolution equations (or "flow laws") commonly used in classical rate-independent plasticity with Mises-type (J_2-type) yield surfaces [129, 130] and is given as follows:

$$\dot{\boldsymbol{\varepsilon}}^t=\dot{\xi}\boldsymbol{\Lambda}^t, \tag{2.20}$$

where, inspired by the most general form in [54], we have

$$\boldsymbol{\Lambda}^t=\begin{cases}\boldsymbol{\Lambda}^t_{fwd}=H^{cur}(\bar{\sigma})\dfrac{3}{2}\dfrac{\boldsymbol{\sigma}'}{\bar{\sigma}} & ;\quad \dot{\xi}>0\\ \boldsymbol{\Lambda}^t_{rev}=\dfrac{\boldsymbol{\varepsilon}^{t-r}}{\xi^r} & ;\quad \dot{\xi}<0\end{cases}. \tag{2.21}$$

During forward transformation ($\dot{\xi}>0$), the transformation strain is clearly generated in the direction of the deviatoric stress $\boldsymbol{\sigma}'$ which is normalized by the *Mises equivalent stress* $\overline{\sigma}=\sqrt{(3/2\ \boldsymbol{\sigma}':\boldsymbol{\sigma}')}$ [122]. During full reverse transformation ($\dot{\xi}<0$), the transformation strain generated during the previous forward transformation is recovered. This motivates the form of $\boldsymbol{\Lambda}^t$ during reverse transformation, where $\boldsymbol{\varepsilon}^{t-r}$ denotes the transformation strain at transformation reversal (i.e., the state at which

the most recent *forward* transformation ended) and the scalar ξ^r is the martensitic volume fraction at the transformation reversal, used for renormalization.

A scalar measure of the magnitude of the transformation strain is the *effective transformation strain*, defined as $\overline{\epsilon}^t = \sqrt{(2/3\ \boldsymbol{\varepsilon}^t : \boldsymbol{\varepsilon}^t)}$ (which differs from its classical plasticity counterpart in that it can be fully recovered). In 3-D SMA modeling, the maximum effective transformation strain $H^{cur}(\overline{\sigma})$ (introduced earlier in the context of 1-D response) then represents the value of $\overline{\epsilon}^t$ generated during full transformation from austenite to martensite at a given applied stress level.

Variable maximum transformation strain

In general, SMA materials do not exhibit a constant maximum transformation strain at all stress levels. For example, the Ni60Ti material discussed in Section A does not exhibit measurable transformation strains unless sufficiently high stresses are applied; it does not exhibit TWSME. Instead, increasing magnitudes of forward transformation strain are generated in a given direction with an increasing level of applied stress in that same direction. The importance of accurately accounting for this stress dependence is heightened when the goal application utilizes the bending of SMA beams because stress levels vary spatially throughout the beam leading to associated variations in the amount of transformation strain generated during full transformation. Even small errors in predicted strain locally can lead to substantial errors in the predicted deflection response globally, and this error is further magnified by large rigid body rotations. Therefore, in predicting the response of Ni60Ti and other material compositions not exhibiting TWSME, it is necessary to use a model that accounts for the effect of stress level on the generation of transformation strain in both its mathematical relations and subsequent numerical implementation.

In choosing the form of $H^{cur}(\overline{\sigma})$, several criteria must be considered based on

the features of the experimental data sets found in the literature. Specifically, it is required that:

- the form should capture a range of experimental data sets that generally show the magnitude of current maximum transformation strain rising from a lower value at lower applied stresses and stabilizing at a higher value as the stress level increases (Fig. 13a,c).
- the form should capture *constant* or nearly constant maximum transformation strain for those trained materials which exhibit such behavior (i.e., TWSME) (Fig. 13b).
- the form should not predict unreasonably high maximum transformation strains for any level of applied stress.

After consideration of other forms (various order polynomials, etc.), it was decided that an exponential function of the form (cf. also (2.4) and Table I)

$$H^{cur}(\overline{\sigma}) = \begin{cases} H_{\min} & ; \quad \overline{\sigma} \leq \overline{\sigma}_{crit} \\ H_{\min} + (H_{\max} - H_{\min})(1 - e^{-k(\overline{\sigma} - \overline{\sigma}_{crit})}) & ; \quad \overline{\sigma} > \overline{\sigma}_{crit} \end{cases} \tag{2.22}$$

was most appropriate. Here $H_{\min}$ corresponds to the observable uniaxial TWSME (or the intersection of the H^{cur} curve with the ordinate axis, if such an intersection exists). The parameter $H_{\max}$ describes the ultimate transformation strain given uniaxial loading (i.e., the maximum recoverable transformation strain generated considering all applicable stress levels, or the maximum level of the H^{cur} curve). Additionally, $\overline{\sigma}_{crit}$ denotes the critical Mises equivalent stress below which $H^{cur}(\overline{\sigma}) = H_{\min}$ (or the intersection of the H^{cur} curve with the stress axis, if such an intersection exists). The parameter k controls the rate at which $H^{cur}(\overline{\sigma})$ exponentially evolves from $H_{\min}$ to $H_{\max}$, and can be fit by minimizing the square of the error between the H^{cur} curve and the available data points, for example. Fig. 13 demonstrates the ability of this single function to fit three distinct data sets from three independent experimental sources, one of which is that discussed in Section A. Note that, in comparison with the description of H^{cur} found in [54], this form is easily calibrated from experimental data.

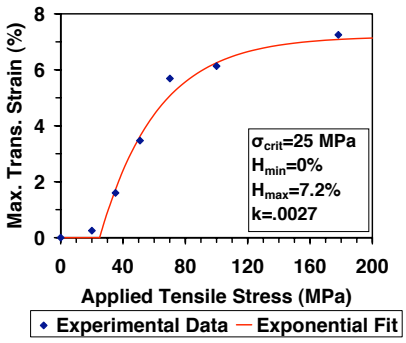

(a) Eqiatomic NiTi, untrained, from work of Bo and Lagoudas ([54], Fig. 2)

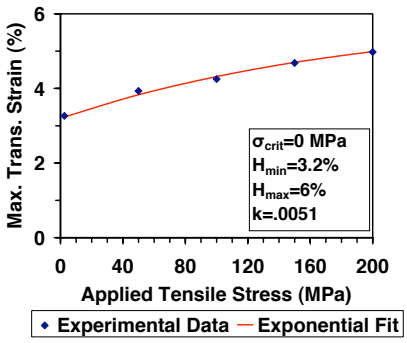

(b) Eqiatomic NiTi, trained, from work of Bo et al. ([55], Fig. 4)

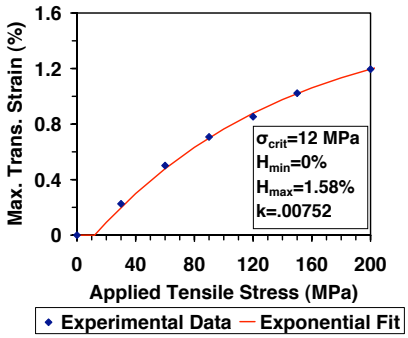

(c) Ni60Ti40 (wt%), trained, from Section A above (Fig. 11)

Fig. 13. Three example experimental data sets showing maximum transformation strain vs. stress and functional fit using the form (2.22).

Finally, the ability to consider variable maximum transformation strains also enhances convergence in the numerical implementation algorithms. Consider for example the special case of proportional loading during forward transformation ($\dot{\xi} > 0$). Such a loading path could be given as follows [131, 132]:

$$\boldsymbol{\sigma}(t) = K(t)\boldsymbol{\sigma}^0, \tag{2.23}$$

where $\boldsymbol{\sigma}^0$ is a constant tensor and $K(t)$ is a monotonically increasing scalar-valued function of the loading parameter t. Further consider that the stress might be zero-valued at some time t_0 such that $K(t) < 0$ when $t < t_0$ and $K(t) > 0$ when $t > t_0$ (this being an extension of the more common form wherein $K(t) \geq 0, \quad t \geq 0$). For example, this form could represent a uniaxial stress state transitioning continuously from compression to tension or a torque tube undergoing a change in torque direction. For such a case, the deviatoric stress and Mises equivalent stress can be given as

$$\boldsymbol{\sigma}'(t) = K(t)\boldsymbol{\sigma}^{0'} \qquad \text{and} \qquad \overline{\sigma}(t) = \begin{cases} -K(t)\overline{\sigma^0} & ; \quad t < t_0 \\ K(t)\overline{\sigma^0} & ; \quad t > t_0 \end{cases} \tag{2.24}$$

respectively. Note that $\overline{\sigma}$ is positive at all times. Using (2.21) in (2.20) while considering the forward transformation and the current assumed stress evolution, we find that

$$\dot{\boldsymbol{\varepsilon}}^t = \frac{3}{2} H^{cur}\left(\overline{\sigma}(t)\right) \frac{\boldsymbol{\sigma}'(t)}{\overline{\sigma}(t)} \dot{\xi} = \frac{3}{2} \frac{\boldsymbol{\sigma}^{0'}}{\overline{\sigma^0}} \dot{\xi} \begin{cases} -H^{cur}\left(\overline{\sigma}(t)\right) & ; \quad t < t_0 \\ H^{cur}\left(\overline{\sigma}(t)\right) & ; \quad t > t_0 \end{cases}, \tag{2.25}$$

where $(\boldsymbol{\sigma}^{0\prime}/\overline{\sigma^0})$ is a constant-valued tensor. Thus, there is a discontinuity in $\dot{\boldsymbol{\varepsilon}}^t$ at $t = t_0$ where the magnitude of this rate jumps by $2H^{cur}(0)$. The process of numerically integrating the constitutive equations using numerical methods such as the return mapping algorithm [129] is hindered at t_0 by such a jump and convergence may be

prevented completely. Therefore, it is advantageous to consider a function form of $H^{cur}(\overline{\sigma})$ such that $H^{cur}(0) = 0$ when analyzing structural components experiencing local changes in the stress direction (i.e., tensile to compressive loading)[4]. A beam represents such a component, and the current VGC modeling obviously requires the consideration of such SMA beam actuation.

Specification of "smooth" hardening function

Like the transformation strain, the transformation hardening energy g^t is also assumed to evolve with ξ. The proposed evolution equation is then given as

$$\dot{g}^t = \dot{\xi} \begin{cases} \frac{1}{2}a_1\left(1 + \xi^{n_1} - (1-\xi)^{n_2}\right) + a_3; & \dot{\xi} > 0 \\ \\ \frac{1}{2}a_2\left(1 + \xi^{n_3} - (1-\xi)^{n_4}\right) - a_3; & \dot{\xi} < 0 \end{cases} = \dot{\xi} \begin{cases} f^t_{fwd}; & \dot{\xi} > 0 \\ \\ f^t_{rev}; & \dot{\xi} < 0 \end{cases} = \dot{\xi} f^t. \quad (2.26)$$

The proportionality between the rate of evolution of the hardening energy and the rate of the martensitic volume fraction is then f^t and is known as the *transformation hardening function*. The form of this function specified here was only recently proposed by Machado and coworkers [56, 122], and provides a smooth (continuous derivative) transition from thermoelastic behavior to transformation, the degree of smoothness being based on the selection of the parameters n_i. However, here the form is modified to consider one additional constant, denoted a_3. It will be shown in the following section that this additional constant is neccesary to include smooth hardening in a thermodynamically consistent manner. Further, Appendix B demonstrates how, in the case of $n_1 = n_2 = n_3 = n_4 = 1$, the smooth model reduces identically to the form of hardening found in the model of Boyd and Lagoudas [37].

---

[4]Note that, even when two-way SME is observed in the material ($H_{min} \neq 0$ experimentally), it still may be advantageous for the purposes of numerical analysis to form the function H^{cur} such that this function passes through the origin and then quickly (though smoothly) rises to H_{min} at some small non-zero stress level.

4. Thermomechanical criteria for transformation

Substituting the proposed evolution equations into the dissipation inequality (2.19), we arrive at

$$\left[\boldsymbol{\sigma} : \boldsymbol{\Lambda}^t - \rho\partial_\xi G - f^t\right]\dot{\xi} = \pi^t\dot{\xi} \geq 0, \tag{2.27}$$

where π^t is known as the *thermodynamic driving force for transformation.*

Assumption 3: The process of phase transformation is strongly dissipative.

The application of thermodynamics to the proposed free energy G (via the Coleman-Noll procedure) provides information on the relationships between temperature and entropy per (2.16) and stress and the transformation strain per (2.17). The proposed evolution equations define how the inelastic transformation strain evolves. The combination of these two (thermodynamics and evolution equations) provides the constraint (2.27), but no explicit criterion for the initiation of transformation has been proposed. To formulate such a criterion, we first assume that, during evolution of the internal variables, a strict dissipation inequality is enforced [46]. This assumption follows naturally from the observation that the SMA material response is hysteretic, and thus some net energy is dissipated during each transformation cycle (i.e., $\pi^t\dot{\xi} = 0 \Leftrightarrow \dot{\xi} = 0$). Applying the strictly dissipative assumption, we have

$$\left[\boldsymbol{\sigma} : \boldsymbol{\Lambda}^t - \rho\partial_\xi G - f^t\right]\dot{\xi} = \pi^t\dot{\xi} > 0 \quad \forall \quad \dot{\xi} \neq 0. \tag{2.28}$$

The term $\rho\partial_\xi G$ is important in capturing the temperature dependence of the critical transformation stress. From (2.5), (2.6), and (2.7) it can be shown that

$$\rho\partial_\xi G = -\frac{1}{2}\boldsymbol{\sigma} : \widetilde{\boldsymbol{\mathcal{S}}}\boldsymbol{\sigma} - \rho\tilde{s}_0 T + \rho\tilde{u}_0. \tag{2.29}$$

We continue by acknowledging that, given (2.28), the thermodynamic driving

force π^t must be positive when ξ is increasing, and negative when ξ is decreasing. We further define a *critical thermodynamic driving force* Y^t to both initiate and sustain transformation, such that this critical value is not exceeded so long as transformation continues. Combining the ideas of positive dissipation and a critical driving force, and also considering the limits on ξ, we can list the criteria for transformation as

$$\begin{aligned} \pi^t &= Y^t; \qquad \dot{\xi} > 0, \\ \pi^t &= -Y^t; \qquad \dot{\xi} < 0, \\ 0 &\leq \xi \leq 1. \end{aligned} \tag{2.30}$$

Considering that (2.28) describes the dissipation of energy during transformation, and further considering the form of (2.30), it can be see that the amount of energy dissipated during a full forward-reverse transformation cycle is given by

$$\int_0^1 \pi^t \, \mathrm{d}\xi \; + \int_1^0 \pi^t \, \mathrm{d}\xi \; = 2Y^t.$$

Past models assuming bounds such as (2.30) have also assumed that the model parameter Y^t takes a constant value, calibrated from material properties related to the phase diagram. However, it will be shown in the following discussion of model calibration that this assumption holds only for SMA materials where the slope of the forward transformation surface (in a uniaxial stress-temperature space) is equal to that of the reverse transformation surface. Such equivalence in slopes is not common in experimental phase diagrams [133, 134, 68], thus the ability to account for different slopes must be considered. Pending further detailed discussion, here we simply postulate that

$$Y^t = Y^t(\boldsymbol{\sigma}). \tag{2.31}$$

The equality of the thermodynamic driving force π^t to a critical value Y^t during dissipation (transformation) allows the definition of a *transformation function* Φ^t and

an associated consistency condition, which defines the thermomechanical criteria for the evolution of the transformation process and is given as

$$\dot{\xi}\Phi^t = 0; \qquad \Phi^t = \begin{cases} \Phi^t_{fwd} = \pi^t - Y^t \leq 0; & \dot{\xi} > 0, \\ \Phi^t_{rev} = -\pi^t - Y^t \leq 0; & \dot{\xi} < 0, \end{cases} . \tag{2.32}$$

The relationship between the form of the transformation function Φ^t and the form of the evolution equation for transformation strain (2.20) motivates a brief discussion of "normality" (or "associativity"). Associativity between the transformation function (2.32)) and the complementary evolution equation (2.20) is taken to mean that the evolution must have the form (using the current inelastic definitions) $\dot{\boldsymbol{\varepsilon}}^t = \dot{\xi}\partial_{\boldsymbol{\sigma}}\Phi^t$, where ξ is obviously scalar-valued. In other words, the direction of inelastic strain evolution at some state should be equivalent to the direction of the normal to the transformation surface at that same state. In classical plasticity, this condition has been shown to be a requirement for satisfying Drucker's stability postulate [132, 131] (as well as the principle of maximum dissipation [129]), and these same principles are here generalized to the discussion of phase transformation. Comparing (2.32) (which includes (2.28), (2.29), and (2.31)) with (2.29), the condition for normality does not appear to be satisfied, especially due to the term $\frac{1}{2}\boldsymbol{\sigma} : \widetilde{\boldsymbol{\mathcal{S}}}\boldsymbol{\sigma}$. However, it has been shown [132] that in the special case that the elastic tensor varies with progression of the inelastic phenomenon (i.e., $\boldsymbol{\mathcal{S}} = \boldsymbol{\mathcal{S}}(\xi)$), the proper form for satisfying the Drucker stability postulate is actually (using current variables) $\dot{\boldsymbol{\varepsilon}}^t = \dot{\xi}\left(\partial_{\boldsymbol{\sigma}}\Phi^t - \partial_{\xi}\boldsymbol{\mathcal{S}} : \boldsymbol{\sigma}\right)$. Pending the form of $Y^t(\boldsymbol{\sigma})$, this appears to agree with the current evolution equation. Therefore, if $Y^t(\boldsymbol{\sigma})$ is given the appropriate form such that $\partial_{\boldsymbol{\sigma}}Y^t(\boldsymbol{\sigma}) = a\boldsymbol{\Lambda}^t$ (where a is a scalar-valued constant), then the current form of Φ^t will satisfy Drucker's stability postulate.

5. Reduction to 1-D form and calibration of parameters

Of the various relations specified above, four are sufficient to analyze the thermomechanical response of an SMA material point. These are as follows: Hooke's law (2.18), the evolution of transformation strain (2.20), the evolution of transformation hardening energy (2.26), and the Kuhn-Tucker type conditions on transformation (2.32). Given general three-dimensional loading, this set of 14 total equations can be solved for the 14 total unknowns ($\boldsymbol{\sigma}$, $\boldsymbol{\varepsilon}^t$, ξ, and g^t).

Here we consider the calibration of the proposed model, where it is fit to a known (experimental) material response and the various model parameters are quantitatively specified. As in classical plasticity, the experimental response of the material under uniaxial loading is sufficient for calibration. To this end, here the model (the set of needed constitutive equations) is reduced to a form sufficient to describe a 1-D stress state (i.e., $\boldsymbol{\sigma} \to \sigma_{11} = \sigma$, $\boldsymbol{\varepsilon} \to \varepsilon_{11} = \varepsilon$, etc.).

The relation between the current stress and strains is written as

$$\sigma = E(\xi)\left[\varepsilon - \alpha(T - T_0) - \varepsilon^t\right], \tag{2.33}$$

where, per (2.17), the current Young's modulus is given as

$$E(\xi) = \left(1/E^A + \xi(1/E^M - 1/E^A)\right)^{-1}. \tag{2.34}$$

The evolution equation for the transformation strain is given as[5]

$$\dot{\varepsilon^t} = \dot{\xi}\Lambda^t; \quad \Lambda^t = \begin{cases} H^{cur}(\sigma)\mathrm{sgn}\,(\sigma); & \dot{\xi} > 0 \\ \varepsilon^{t-r}/\xi^r; & \dot{\xi} < 0 \end{cases}, \tag{2.35}$$

and the evolution of the hardening energy, being scalar in both its arguments and

[5]The function "sgn" is defined such that, for any x, $\mathrm{sgn}\,(x) = \frac{x}{|x|}$.

result, is unchanged from (2.26). We then write out the transformation function during forward transformation. This is given as

$$\begin{aligned}\Phi^t_{fwd}(\sigma,T,\xi) &= |\sigma|\, H^{cur}(\sigma) + \frac{1}{2}\left(\frac{1}{E^M}-\frac{1}{E^A}\right)\sigma^2 + \rho\tilde{s}_0 T - \rho\tilde{u}_0 \\ &- f^t_{fwd}(\xi) - Y^t(\sigma) = 0 \end{aligned} \tag{2.36}$$

while for reverse transformation it is given as

$$\begin{aligned}\Phi^t_{rev}(\sigma,T,\xi) &= -\sigma\frac{\varepsilon^{t-r}}{\xi^r} - \frac{1}{2}\left(\frac{1}{E^M}-\frac{1}{E^A}\right)\sigma^2 - \rho\tilde{s}_0 T + \rho\tilde{u}_0 \\ &+ f^t_{rev}(\xi) - Y^t(\sigma) = 0. \end{aligned} \tag{2.37}$$

Considering these needed constitutive relations, the following model parameters must be calibrated: *i*) the elastic moduli of martensite and austenite (E^M and E^A), *ii*) the functional description of the maximum transformation strain ($H^{cur}(\sigma)$), and *iii*) five additional model parameters ($\rho\tilde{s}_0$, $\rho\tilde{u}_0$, a_1, a_2, a_3) and the form of $Y^t(\sigma)$. Note that the hardening coefficients $n_1 - n_4$ are directly chosen to best fit the four corners of the transformation hysteresis. Per the discussion of Section A, the elastic constants can be calculated directly from isothermal stress-strain curves where loads are applied at temperatures outside of transformation regions. As shown in Fig. 11, H^{cur} is calibrated directly from isobaric material testing or by otherwise considering the change in maximum transformation strain with stress. The remaining five parameters and $Y^t(\sigma)$ are then calibrated by considering the conditions under which the two transformations (forward and reverse) begin and end.

A straightforward method for calibrating these is to consider transformation occurring under stress-free conditions. At zero stress, we have

$$Y^t(0) = Y^t_0. \tag{2.38}$$

Forward transformation ($\dot{\xi} > 0$) at zero stress begins at the martensitic start tem-

perature M_s and ends at M_f. Likewise, reverse transformation ($\dot{\xi} < 0$) at zero stress begins at A_s and ends at A_f. Given these four characteristic temperatures (which are material properties, cf. Table I), we can consider the following four states, providing four independent equations:

1. Beginning of forward transformation: $\Phi^t_{fwd}(0, M_s, 0) = 0$

2. Ending of forward transformation: $\Phi^t_{fwd}(0, M_f, 1) = 0$

3. Beginning of reverse transformation: $\Phi^t_{rev}(0, A_s, 1) = 0$

4. Ending of reverse transformation: $\Phi^t_{rev}(0, A_f, 0) = 0$

A fifth condition is provided by considering the meaning of the free energy potential as an equation of state. When an SMA material point is subjected to a closed thermomechanical loading path that induces a full transformation cycle, that point is returned to a thermomechanical-material state which is identical to the one at which it started. For example, if the point was initially purely austenitic and then undergoes transformation into and then back out of martensite, and if the stress and temperature states are returned to their initial values, the Gibbs free energy potential must also return to its initial value. Examining (2.5), (2.6), and (2.7), it can be seen that this is only possible if there is zero net change in value of g^t. Considering (2.26), this provides a fifth condition given as:[6]

5. $\displaystyle\int_0^1 f^t_{fwd}\,\mathrm{d}\xi + \int_1^0 f^t_{rev}\,\mathrm{d}\xi = 0.$

Applying these five conditions, we arrive at the following relations for the five

[6]Thus if the fifth parameter a_3 were omitted from $f^t(\xi)$, this fifth condition would not be needed, and the thermodynamic requirements it represents would not be accounted for.

model parameters $\rho\tilde{u}_0$, a_1, a_2, a_3, and Y_0^t:

$$\begin{gathered} a_1 = \rho\tilde{s}_0(M_f - M_s), \quad a_2 = \rho\tilde{s}_0(A_s - A_f), \\ a_3 = -\frac{a_1}{4}\left(1 + \frac{1}{n_1+1} - \frac{1}{n_2+1}\right) + \frac{a_2}{4}\left(1 + \frac{1}{n_3+1} - \frac{1}{n_4+1}\right), \\ \rho\tilde{u}_0 = \frac{\rho\tilde{s}_0}{2}(M_s + A_f), \quad Y_0^t = \frac{\rho\tilde{s}_0}{2}(M_s - A_f) - a_3. \end{gathered} \tag{2.39}$$

Calibration of $\rho\tilde{s}_0$ and the total form of $Y^t(\boldsymbol{\sigma})$ is performed by considering the slope of the transformation surface in a uniaxial stress-temperature space as measured at some reference stress level, here denoted σ^*. The Kuhn-Tucker conditions (2.32) imply that the transformation function Φ^t (and thus its rate) are zero-valued during transformation, allowing us to write (in 1-D form)

$$\mathrm{d}\Phi^t = \partial_\sigma \Phi^t \,\mathrm{d}\sigma + \partial_T \Phi^t \,\mathrm{d}T + \partial_\xi \Phi^t \,\mathrm{d}\xi = 0. \tag{2.40}$$

For this calibration, we consider the configuration of the transformation surface at some known constant ξ (usually $\xi = 0$ or $\xi = 1$), thus $\mathrm{d}\xi = 0$. Evaluating the remaining partials and solving for the stress-temperature derivatives, we find

$$\left.\frac{\mathrm{d}\sigma}{\mathrm{d}T}\right|_{\sigma=\sigma^*,\dot{\xi}>0} = \left.\frac{-\rho\tilde{s}_0}{\Lambda^t + \sigma\partial_\sigma\Lambda^t_{fwd} + \sigma\left(\frac{1}{E^M} - \frac{1}{E^A}\right) - \partial_\sigma Y^t}\right|_{\sigma=\sigma^*}, \tag{2.41}$$

for forward transformation and

$$\left.\frac{\mathrm{d}\sigma}{\mathrm{d}T}\right|_{\sigma=\sigma^*,\dot{\xi}<0} = \left.\frac{-\rho\tilde{s}_0}{\Lambda^t + \sigma\partial_\sigma\Lambda^t_{rev} + \sigma\left(\frac{1}{E^M} - \frac{1}{E^A}\right) + \partial_\sigma Y^t}\right|_{\sigma=\sigma^*}. \tag{2.42}$$

for reverse.

In the case of isobaric loading and full transformation, $\boldsymbol{\Lambda}^t_{fwd} = \boldsymbol{\Lambda}^t_{rev}$ (see (2.21)). Thus, if $\partial Y^t = 0$, the slope of the analytical transformation surface for forward transformation is identical to that for reverse. However, this is not in agreement with much of the experimental data found in the literature where, in a uniaxial

stress-temperature space, the slopes of the forward transformation surfaces may vary markedly from those for reverse transformation [133, 134, 68] (cf. also Fig. 10 above).

To provide for different transformation surface slopes, we take advantage of assumption (2.31) and examine its form. In choosing an appropriate $Y^t(\boldsymbol{\sigma})$, we should be mindful of two criteria:

1. The value of Y^t represents the rate of dissipation (cf. (2.28) and (2.30)), and thus its form must not result in $Y^t < 0$ for any meaningful thermomechanical state.

2. The form should reduce to $Y^t = Y_0^t$ at $\sigma = 0$ (cf. (2.38)) to preserve the calibration results of (2.40).

A natural choice for $Y^t(\boldsymbol{\sigma})$ motivated by the form of (2.32) is (in 3-D)

$$Y^t = Y_0^t + D\boldsymbol{\sigma} : \boldsymbol{\Lambda}^t = Y_0^t + D\overline{\sigma}H^{cur}(\overline{\sigma}), \tag{2.43}$$

or, in one dimension

$$Y^t = Y_0^t + D\sigma\Lambda^t. \tag{2.44}$$

Calculating the slopes anew in the same manner used for (2.41) and (2.42), we find

$$\left.\frac{\mathrm{d}\sigma}{\mathrm{d}T}\right|_{\sigma=\sigma^*,\dot{\xi}>0} = \left.\frac{-\rho\tilde{s}_0}{(1-D)\left(\Lambda^t + \sigma\partial_\sigma\Lambda^t\right) + \sigma\left(\frac{1}{E^M} - \frac{1}{E^A}\right)}\right|_{\sigma=\sigma^*}, \tag{2.45}$$

for forward transformation and

$$\left.\frac{\mathrm{d}\sigma}{\mathrm{d}T}\right|_{\sigma=\sigma^*,\dot{\xi}<0} = \left.\frac{-\rho\tilde{s}_0}{(1+D)\left(\Lambda^t + \sigma\partial_\sigma\Lambda^t\right) + \sigma\left(\frac{1}{E^M} - \frac{1}{E^A}\right)}\right|_{\sigma=\sigma^*}. \tag{2.46}$$

for reverse.

To calibrate the two parameters $\rho\tilde{s}_0$ and D, two phase diagram slopes are measured at some reference stress level σ^*. Denoting these slopes (measured at σ^*) as C^M for forward transformation and C^A for reverse, the following two equations are

solved for the two unknown parameters:

$$C^M = \left.\frac{-\rho\tilde{s}_0}{(1-D)\left(\Lambda^t + \sigma\partial_\sigma\Lambda^t\right) + \sigma\left(\frac{1}{E^M} - \frac{1}{E^A}\right)}\right|_{\sigma=\sigma^*}, \tag{2.47}$$

$$C^A = \left.\frac{-\rho\tilde{s}_0}{(1+D)\left(\Lambda^t + \sigma\partial_\sigma\Lambda^t\right) + \sigma\left(\frac{1}{E^M} - \frac{1}{E^A}\right)}\right|_{\sigma=\sigma^*}. \tag{2.48}$$

For calibration from isobaric experiments, this yields

$$\begin{aligned} \rho\tilde{s}_0 &= \left.\frac{-2\left(C^M C^A\right)\left[H^{cur}(\sigma) + \sigma\partial_\sigma H^{cur}(\sigma) + \sigma\left(\frac{1}{E^M} - \frac{1}{E^A}\right)\right]}{C^M + C^A}\right|_{\sigma=\sigma^*}, \\ D &= \left.\frac{\left(C^M - C^A\right)\left[H^{cur}(\sigma) + \sigma\partial_\sigma H^{cur}(\sigma) + \sigma\left(\frac{1}{E^M} - \frac{1}{E^A}\right)\right]}{\left(C^M + C^A\right)\left[H^{cur}(\sigma) + \sigma\partial_\sigma H^{cur}(\sigma)\right]}\right|_{\sigma=\sigma^*}. \end{aligned} \tag{2.49}$$

To summarize, the minimum number of experiments required to calibrate the model are either:

- Two pseudoelastic tests, each at a different temperature. From these, the elastic properties of austenite and (reoriented) martensite can be directly determined, and a phase diagram can be derived (giving M_s, M_f, A_s, A_f, C^A, and C^M). Finally, the maximum transformation strain $H^{cur}(\sigma)$ can be determined by measuring the amount of transformation strain generated versus the average stress level of the forward transformation plateau.

- Elastic monotonic loading of pure austenite and pure martensite combined with two constant load bias thermal transformation tests (isobaric tests), each a different constant stress level σ_i. These two tests also allow derivation of a phase diagram, and $H^{cur}(\sigma_i)$ is derived from (2.4).

D. Experimental Calibration of Model and Simulation of Results

Having described in detail the improved constitutive model for conventional SMA materials, we now revisit the experimental material characterization intended for the calibration of this model and further examine how it replicates the characterization curves. It is important that the form of the model be used to guide the interpretation of experimental data when reducing the isobaric testing data series to quantitative material parameters; this is especially important when constructing the stress-temperature phase diagram.

If the model assumes linear hardening [37], the transformation temperatures at a given stress level are determined by simply constructing lines tangent to the strain-temperature response hysteresis and then determining the temperatures at which these lines intersect. This is illustrated in Fig. 14 for A_s. When the smooth hardening function is used to fit the data, however, the four transformation temperatures which describe the points of transition from thermoelastic behavior to phase transformation behavior must all be shifted. This is also shown in Fig. 14 for the example Ni60Ti material under 200 MPa applied stress. Note that the assumption of smooth hardening matches the experimental data well, and that its use predicts the transition from thermoelastic behavior to reverse transformation behavior occurs at a *lower* temperature than would be predicted by an assumption of linear hardening. A method for directly calculating smooth hardening transformation temperatures from tangent line (linear hardening) temperatures can be found elsewhere [14].

Both a shift in the transformation temperatures and the consideration of variable maximum transformation strain lead to new configurations of the analytical phase diagram. The analytical phase diagram calculated assuming the unified model with linear hardening [38] (equivalent to the so-called "Boyd-Lagoudas" model [38]) is

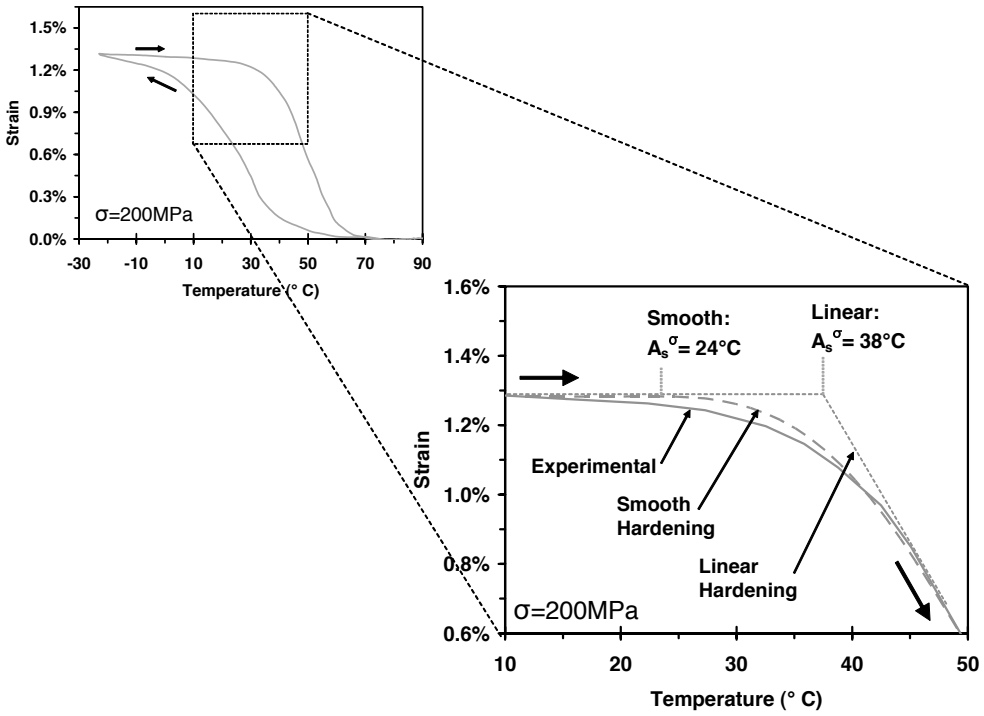

Fig. 14. Comparison of linear and smooth hardening approximations and their effects on interpretation of transformation temperatures.

nearly identical to the experimentally-derived phase diagram shown in Fig. 10. The analytical phase diagram for the linear hardening model is shown in Fig. 15.

Now the effects of variable maximum transformation strain and smooth hardening on the configuration of the phase diagram are considered. If we first consider the linear hardening analytical phase diagram (Fig. 15) and then add only the effects of variable transformation strain, the analytical phase diagram of Fig. 16a results. Note that the slopes of these surfaces are described in (2.45) and (2.46) and that, considering (2.21), infinite slopes at zero stress will result whenever $H^{cur}(0) = 0$. As this is the case for the current material, infinite slopes are observed in the associated phase diagram. Additionally, if smooth hardening is assumed and appropriate values for the n's are determined, a shift in all four of the transformation temperatures is needed

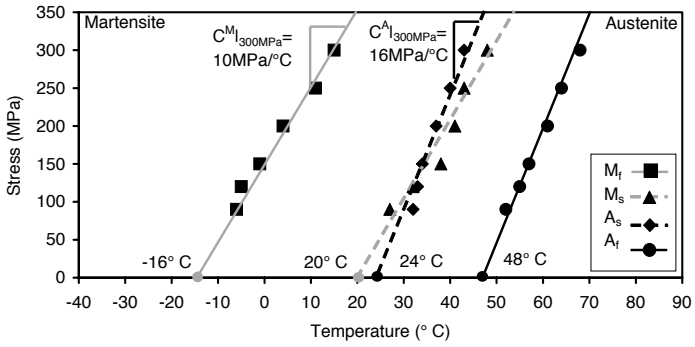

Fig. 15. Analytical phase diagram for Ni60Ti from "unified model" of [38] (linear hardening option).

(per Fig. 14). This yields the final phase diagram used for the model calibration, shown in Fig. 16b.

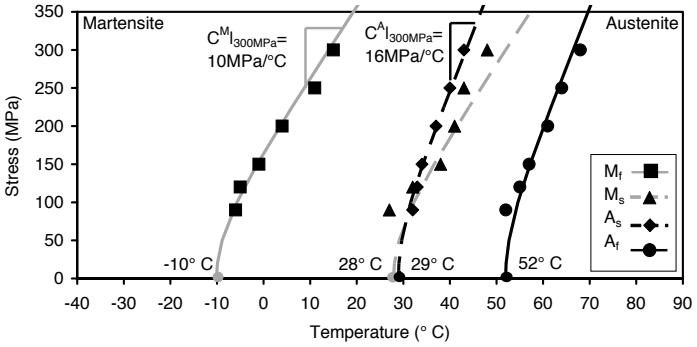

(a) Analytical phase diagram (variable transformation strain, linear hardening)

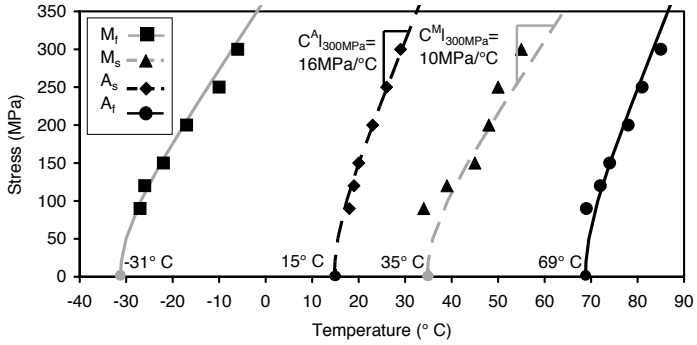

(b) Analytical phase diagram (variable transformation strain, smooth hardening; form used in the remainder of this work)

Fig. 16. Effect of SMA model extensions (variable maximum transformation strain and smooth hardening) on the analytical phase diagram. Note the change in zero-stress transformation temperatures.

Using the experimental results of Section A (especially the material properties described in Table I), using the calibration relations of Section C.5, and reinterpreting the phase diagram as described in the previous discussion, the values for the model parameters needed to simulate the behavior of the Ni60Ti SMA material can be found. These are summarized in Table II.

To show the degree to which the calibrated constitutive model matches the experimental data, the 1-D reduction of the model derived in Section C was numerically implemented in an implicit scheme as described in detail in Appendix C. This incremental scheme is useful for modeling the response of 1-D applications, particularly of tensile actuators opposed to biasing loads, and here it was used to consider the Ni60Ti material subjected to tensile isobaric loading paths at three constant stress levels (90, 150 MPa, and 200 MPa). The results are compared to experimental data as shown in Fig. 17, and agreement is observed. Note how the model improvements (i.e., the variation of transformation hysteresis with applied stress level and the smooth nature of hardening) are necessary to provide such a close match to the experimental data (cf. Fig. 12).

With the simulation of the tensile calibration experiments providing satisfactory validation results, calibration efforts were considered complete. The chosen parameters of Table II were used in all subsequent predictive modeling. No re-calibrations were performed, and the three-dimensional boundary value problems are modeled as discussed in the following chapter.

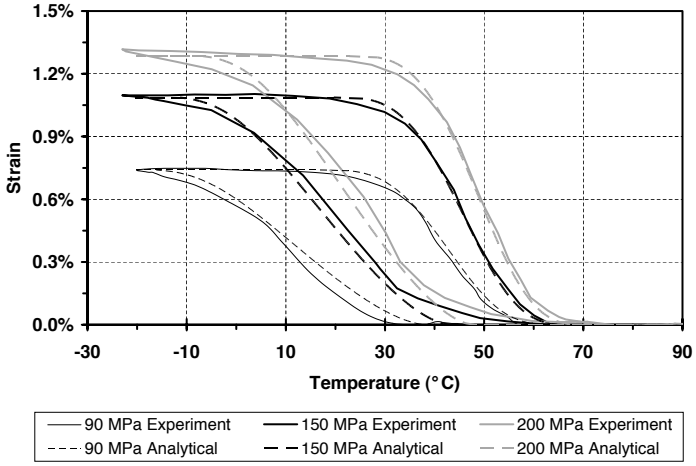

Fig. 17. Simulation of Ni60Ti constant stress thermal cycling experiments using the calibrated constitutive model, including the smooth hardening function.

Table II. Unified model material parameters as defined for stabilized Ni60Ti (transformation temperatures adjusted).

Parameter	**Value**
	Thermoelastic Properties
E^A	90GPA
E^M	63GPA
$\nu^M = \nu^A$	0.33
$\alpha^M = \alpha^M$	10e-6/ °C
	Phase Diagram Properties (Smooth Hardening Method)
M_s	35 °C
M_f	−31 °C
A_s	15 °C
A_f	69 °C
$C^A\|_{\sigma=\sigma^*}$	16 MPa/ °C
$C^M\|_{\sigma=\sigma^*}$	10 MPa/ °C
σ^*	300 MPa
	Transformation Strain Properties
$H^{cur}(\sigma)$	$= 0.0158[1 - e^{-677/E^A(\sigma-\sigma_{crit})}]$
σ_{crit}	12 MPa
	Smooth Hardening Properties
n_1, n_2, n_3, n_4	$0.6, 0.2, 0.2, 0.3$
	Additional Modeling Constants
a_1	$\rho\tilde{s}_0(M_f - M_s)$
a_2	$\rho\tilde{s}_0(A_s - A_f)$
a_3	$-\frac{a_1}{4}\left(1 + \frac{1}{n_1+1} - \frac{1}{n_2+1}\right) + \frac{a_2}{4}\left(1 + \frac{1}{n_3+1} - \frac{1}{n_4+1}\right)$
Y_0^t	$\frac{1}{2}\rho\tilde{s}_0(M_s - A_f) - a_3$
ρu_0	$\frac{1}{2}\tilde{s}_0(M_s + A_f)$
$\rho\tilde{s}_0$ and D	See (2.50)

CHAPTER III

SMA MODEL IMPLEMENTATION AND ANALYSIS OF COMPLEX STRUCTURAL APPLICATIONS

Having introduced the details of the thermally-induced actuation behaviors observed in conventional SMAs in Chapter II, Section A, and further having derived a three-dimensional mathematical model that could account for these behaviors in Chapter II, Section C, this dissertation continues by describing the methods by which this model can be implemented in a numerical environment. Because the end goal is the 3-D analysis of various engineering applications, this chapter discusses the implementation of the model in an FEA framework that accounts for large rotations in SMA bodies. It is arranged as follows: Section A describes the mathematical algorithm in detail, from the overall FEA framework to the local constitutive considerations. Section B then applies this engineering tool to the analysis of complex SMA applications, including a multi-body active structure.

A. Numerical Implementation of the SMA Constitutive Model

Several individual topics are addressed in this first section: *i*) the FEA framework in the context of non-linear materials, *ii*) the possible methods of numerically integrating the local constrained evolution equations, *iii*) the particular form of the algorithm used to mathematically solve for an increment in stress at a material point given an increment in strain and temperature, and *iv*) the algorithmic requirements to objectively account for large rotations. Much of this work follows from the developments found elsewhere in the literature [124, 135], and is heavily inspired by the work of Simo and Hughes [129].

1. Finite element analysis for non-linear materials

To provide the greatest capability for analyzing active structural problems of varying complexity (including multi-step loading, large rotations, contact, etc.), the constitutive model of Chapter II was implemented in the Abaqus Unified Finite Element framework [136] as a *user material subroutine* (UMAT). The method by which such an analysis tool calculates the mechanical response of a structure composed of a custom non-linear material is schematically illustrated in Fig. 18. Here we consider displacement-based (or strain-based) FEA, by far the most popular method of computational mechanics. Given a thermomechanical loading path, the process begins by applying the appropriate thermal and boundary conditions *incrementally* (the bold outlined box in Fig. 18). Based on these boundary conditions, the global solver guesses an initial deformation for all nodes by solving the linear problem (i.e., the stiffness matrix is constructed considering only the elastic behavior of the material) [137].

In each element, at each material point (hence the superscript "mp"), these deformations are used to calculate local total strains, which are then passed into the UMAT. In the UMAT, updated local stresses are computed using the local total strains in addition to any internal variables from the last loading increment. The local tangent stiffness k^{mp} at each material point is also calculated. The stresses are used to integrate the forces on the element, which are assumed to act at its nodes. The forces from all adjacent elements (acting at coincident nodes) are added, where the sum of forces at any given node should equal zero for static equilibrium. The vector of sums is known as the *force residual*; if its magnitude is sufficiently small, the global solution is considered to be correct and the next loading path increment is applied. If the magnitude is too large, Newton's method (also known as the "Newton-Raphson" method) is used to compute a new guess for the global deformations, where

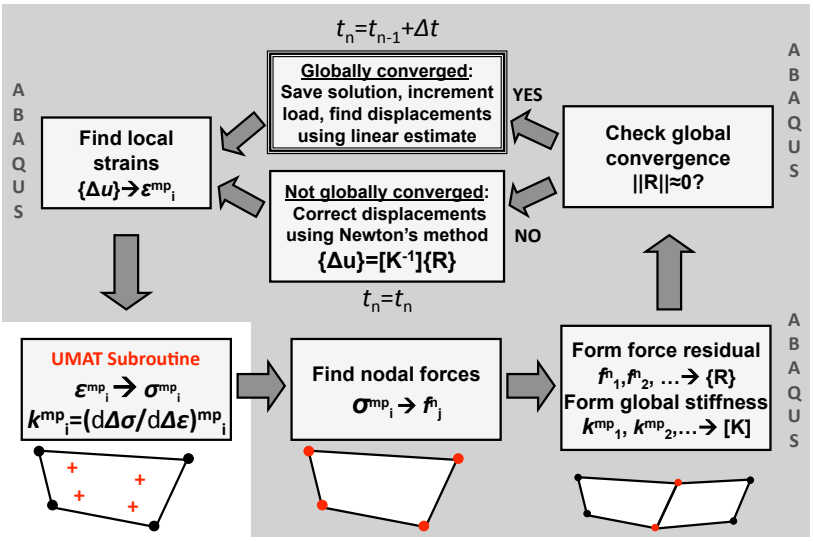

Fig. 18. Schematic illustration of the global FEA solution process considering non–linear history-dependent materials.

the global tangent stiffness matrix (computed from the many local stiffness matrices) relates the deformation increments to the force residual. The process then repeats until convergence, at which point the boundary conditions are updated.

2. Incremental integration of constitutive equations

Here we discuss options by which the material behavior at each integration point in each element of the FEA model could be calculated based on the integration of the rate form of the transformation strain evolution equation (2.20). As described above, any given load applied in the FEA is partitioned into increments, or *loading steps*, and the global FEA solver determines appropriate increments of total strain and temperature for each integration point of each element. Therefore, throughout the remainder of this discussion, values of the total strain and temperature at the current time t_{n+1} are known (i.e., $\boldsymbol{\varepsilon}_{n+1}$ and T_{n+1} are given). Further, using Hooke's

law, the current stress can be calculated from $\boldsymbol{\varepsilon}_{n+1}$, T_{n+1}, and the unknown ${\boldsymbol{\varepsilon}^t}_{n+1}$.

With the local temperature and total strains provided, the fundamental challenge in the numerical implementation of inelastic constitutive models such as the one considered here is the accurate integration of the evolution equation for the inelastic strain (i.e., transformation strain). Discretizing (2.20) in time, we can use the general trapezoidal rule [138] to solve for the inelastic transformation strain in the current loading step under consideration (i.e., at time t_{n+1}), and this is written as[1]

$$ {\boldsymbol{\varepsilon}^t}_{n+1} = {\boldsymbol{\varepsilon}^t}_n + (\xi_{n+1} - \xi_n)\left[(1-\gamma)\boldsymbol{\Lambda}^t_n + \gamma\boldsymbol{\Lambda}^t_{n+1}\right]. \tag{3.1} $$

where γ is an algorithmic parameter that ranges from 0 to 1. Of course, infinitely many options exist for the value of γ, which is often chosen and then held constant during analysis. Values of $\gamma = 1, \frac{1}{2}, 0$ have been discussed in the literature [138]. In the current work, we consider $\gamma = 0$ (known as *forward Euler integration*), and $\gamma = 1$ (known as *backward Euler integration*).

Option 1: Forward Euler Integration

Forward integration is performed by setting $\gamma = 0$ in (3.1), which gives

$$ {\boldsymbol{\varepsilon}^t}_{n+1} = {\boldsymbol{\varepsilon}^t}_n + (\xi_{n+1} - \xi_n)\boldsymbol{\Lambda}^t_n, \tag{3.2} $$

where a purely explicit forward integration depends on the ability to approximate both ξ_{n+1} and $\boldsymbol{\Lambda}^t$ directly from the solution at the previous time step. While the transformation strain direction tensor has a known functional form per (2.21) (giving $\boldsymbol{\Lambda}^t_n = \boldsymbol{\Lambda}^t(\boldsymbol{\sigma}_n)$), a similar form for calculating ξ_n is not immediately evident. We can derive such a relation by using the transformation consistency conditions (2.32).

[1]Here we introduce the notation that, for any quantity x, $\Delta x_{n+1} = x_{n+1} - x_n$.

Enforcing the consistency condition in the current time step, we have

$$\Phi^t_{n+1} = \Phi^t(\boldsymbol{\sigma}_{n+1}, T_{n+1}, \xi_{n+1}) = 0. \tag{3.3}$$

In some particular cases (i.e., $n_1 = n_2 = n_3 = n_4 = 1$ in (2.26)), it is possible to invert (3.3) and find $\xi_{n+1} = \hat{\xi}(\boldsymbol{\sigma}_{n+1}, T_{n+1})$ (for examples, see [38]). Using the forward Euler explicit methodology and recalling that T_{n+1} is provided by the global solver, we then assume that for small increments

$$\xi_{n+1} \approx \hat{\xi}(\boldsymbol{\sigma}_n, T_{n+1}). \tag{3.4}$$

If the function Φ^t is invertible in terms of ξ and $\hat{\xi}(\boldsymbol{\sigma}, T)$ exists, we can then write the explicit forward Euler integration of the transformation strain evolution equation as

$$\boldsymbol{\varepsilon}^t{}_{n+1} = \boldsymbol{\varepsilon}^t{}_n + \left(\hat{\xi}(\boldsymbol{\sigma}_n, T_n) - \xi_n\right) \boldsymbol{\Lambda}^t(\boldsymbol{\sigma}_n), \tag{3.5}$$

This allows for simplified coding and rapid calculation, but, in addition to requiring the existence of $\hat{\xi}(\boldsymbol{\sigma}, T)$, very small time steps are required to achieve accuracy. This reduces the overall efficiency of the scheme. Further, for values of $\gamma < \frac{1}{2}$ (as is considered here with $\gamma = 0$), the integration algorithm can become unstable and thus may not converge to the correct solution [138].

Option 2: Backward Euler integration (direct iteration)

In general, backward Euler integration is performed by using $\gamma = 1$ in the discretized evolution equation (3.1). This makes it implicit in time and gives

$$\boldsymbol{\varepsilon}^t{}_{n+1} = \boldsymbol{\varepsilon}^t{}_n + \Delta\xi_{n+1}\boldsymbol{\Lambda}^t_{n+1} = \boldsymbol{\varepsilon}^t{}_n + \Delta\xi_{n+1}\boldsymbol{\Lambda}^t(\boldsymbol{\sigma}_{n+1}). \tag{3.6}$$

One scheme for solving this implicit relation is to use *direct iteration* or *fixed-point*

iteration (for a general treatment, see the discussions of [139]). Such a scheme again requires that $\hat{\xi}(\boldsymbol{\sigma}, T)$ can be found and then uses it directly such that $\xi_{n+1} = \hat{\xi}(\boldsymbol{\sigma}_{n+1}, T_{n+1})$ exactly. Directly iterating over the resulting discretized evolution equation gives

$$\boldsymbol{\varepsilon}^{t}{}_{n+1}^{(k+1)} = \boldsymbol{\varepsilon}^{t}{}_{n} + \left(\hat{\xi}(\boldsymbol{\sigma}_{n+1}^{(k)}, T_{n+1}) - \xi_n\right) \boldsymbol{\Lambda}^{t}(\boldsymbol{\sigma}_{n+1}^{(k)}), \tag{3.7}$$

where k is the iteration counter and where any quantity x is initialized in the current increment using $x_{n+1}^{(0)} = x_n$. Recall that $\boldsymbol{\sigma}_{n+1}^{(k)}$ is calculated from $\boldsymbol{\varepsilon}^{t}{}_{n+1}^{(k)}$ per Hooke's law (2.18) and that $\boldsymbol{\varepsilon}_{n+1}$ and T_{n+1} are provided by the global solver. To determine the accuracy of the solution (and thus the cessation of iteration), we introduce the *transformation strain residual*

$$\mathbf{R}_{n+1}^{(k)} = \boldsymbol{\varepsilon}^{t}{}_{n+1}^{(k)} - \boldsymbol{\varepsilon}^{t}{}_{n} - \Delta\xi_{n+1}^{(k)} \boldsymbol{\Lambda}^{t}(\boldsymbol{\sigma}_{n+1}^{(k)}), \tag{3.8}$$

iterating until $\|\mathbf{R}_{n+1}^{(k)}\|$ is less than some tolerance. While the direct iteration method is accurate in time and is easily implemented, convergence is only first order (and thus slow), and is not in general guaranteed, especially when hardening non-linearities exist [139]. We therefore seek other methods.

Option 3: Backward Euler integration (return mapping algorithms)

Another approach to the integration of (3.6) (i.e., $\gamma = 1$ in (3.1)) is to rewrite this relation such that the resulting form is implicit with respect to both time steps and iterations. This has the distinct advantage of not requiring some explicit form for ξ (i.e., $\hat{\xi}(\boldsymbol{\sigma}, T)$ is not needed). Methods for the implicit integration are well established for plastic and viscoplastic evolution equations [129, 138], and have also been introduced previously in the context of SMA phase transformations [124]. Here we consider the class of methods known as *return mapping algorithms* (RMAs). We

first consider the unknown ξ as analogous to the conventional "plastic multiplier." Given this and the transformation consistency conditions, a number of integration methodologies can now be applied to the transformation problem. Here we consider two forms in particular.

Closest point projection:

The process of numerically solving the discretized transformation evolution equation (3.6) directly and implicitly is known as the *closest point projection algorithm* [129, 138]. This method solves (3.6) with all unknowns implicit both in time and in iteration. Recall again that the current stress is known in terms of $\boldsymbol{\varepsilon}$, T, and $\boldsymbol{\varepsilon}^t$, per Hooke's law (2.18) and that $\boldsymbol{\varepsilon}$ and T are known. Thus the two unknown variables to be solved for implicitly are $\{\boldsymbol{\varepsilon}^t, \xi\}$, and the discretized (incremental and iterative) transformation evolution equation (3.6) becomes

$$\boldsymbol{\varepsilon}^{t}{}_{n+1}^{(k+1)} = \boldsymbol{\varepsilon}^{t}{}_{n} + (\xi_{n+1}^{(k+1)} - \xi_n)\boldsymbol{\Lambda}^t(\boldsymbol{\sigma}_{n+1}^{(k+1)}). \tag{3.9}$$

To find solutions for the unknown scalar $\xi_{n+1}^{(k+1)}$ and the unknown tensor $\boldsymbol{\varepsilon}^{t}{}_{n+1}^{(k+1)}$, we first introduce an iterative update of these two variables per

$$\boldsymbol{\varepsilon}^{t}{}_{n+1}^{(k+1)} = \boldsymbol{\varepsilon}^{t}{}_{n+1}^{(k)} + \Delta\boldsymbol{\varepsilon}^{t}{}_{n+1}^{(k)}; \quad \xi_{n+1}^{(k+1)} = \xi_{n+1}^{(k)} + \Delta\xi_{n+1}^{(k)}, \tag{3.10}$$

where the unknowns in the next iteration $k+1$ are now $\Delta\boldsymbol{\varepsilon}^{t}{}_{n+1}^{(k)}$ and $\Delta\xi_{n+1}^{(k)}$. Linearizing the tensor-valued transformation strain residual $\mathbf{R}$ and the scalar-valued constraint function Φ^t about their roots gives

$$\begin{aligned} \mathbf{R}_{n+1}^{(k+1)} &= \mathbf{R}_{n+1}^{(k)} + \Delta\mathbf{R}_{n+1}^{(k)} \simeq \mathbf{0}, \\ \Phi^{t}{}_{n+1}^{(k+1)} &= \Phi^{t}{}_{n+1}^{(k)} + \Delta\Phi^{t}{}_{n+1}^{(k)} \simeq 0. \end{aligned} \tag{3.11}$$

where $\Delta\mathbf{R}_{n+1}^{(k)}$ and $\Delta\Phi^{t}{}_{n+1}^{(k)}$ are expanded via the chain rule [129]. The closest point

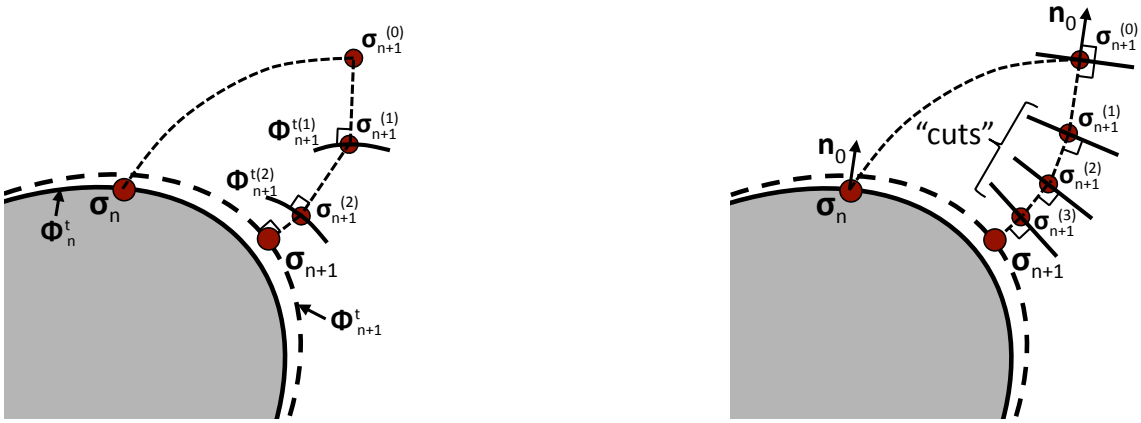

(a) Closest point projection

(b) Convex cutting plane

Fig. 19. Schematic illustrations showing the solution behaviors of the closest point projection and convex cutting plane algorithms in stress space.

projection algorithm then relies on the solution of the system of equations (3.11) for the set of unknowns $\{\Delta\boldsymbol{\varepsilon}^{t(k)}_{n+1}, \Delta\xi^{(k)}_{n+1}\}$, which are then used in (3.10). The resulting algorithm is unconditionally stable and thus will always converge to the correct solution so long as the constraint function is convex (which is the case for the current function Φ^t) [138]. It is commonly used in the the integration of inelastic constitutive equations [136]. As a point of interest, the key features of the algorithm, especially in terms of its behavior in stress space, have been schematically illustrated in Fig. 19a. Given an initial guess stress $\boldsymbol{\sigma}^{(0)}_{n+1}$ determined by an elastic prediction (discussed further in the following subsection), the algorithm proceeds by satisfying the consistency condition $\Phi^t = 0$ in the next iteration by advancing to the "closest point" on the next transformation surface. In other words, normality is enforced on the next (unknown) transformation surface [129].

However, the closest point projection algorithm has a number of disadvantages relevant to the current work [129, 140]. First, the expansion of $\Delta\mathbf{R}$ via the chain rule

requires the evaluation of a number of gradients, some of them being fourth-order tensors (e.g., $\partial_{\boldsymbol{\sigma}} \boldsymbol{\Lambda}^t$), and this "may prove exceedingly laborious." [140] Secondly, while (3.11) represents a 7x7 system of equations,[2]the additional consideration of plasticity and/or viscoplasticity, which is the focus of this dissertation, may increase the size of the system of equations as each new phenomenon (e.g., plasticity) adds six new unknown strain components and a new scalar measure (e.g., the plastic multiplier). Furthermore, due to coupling provided by Hooke's law (in addition to any other constitutive assumptions), this system of equations can become highly non-linear. The form of these coupled algebraic equations becomes quite complex and the derivation of them requires many more complicated and coupled terms. Finally, the implementation of this algorithm, especially the coupled phase transformation-plastic (or viscoplastic) form, requires both a substantial amount of complicated coding as well as a higher number of numerical operations per iteration compared to alternative algorithms (again, including the evaluation of fourth-order gradient tensors). For these reasons, we explore a slightly simplified form of the return mapping algorithm.

Convex cutting plane:

This method simplifies the closest point projection algorithm by neglecting the implicit nature of the *direction* of $\boldsymbol{\varepsilon}^t$ while focusing on the change in its magnitude from iteration to iteration [140]. It is most effective for the consideration of loading paths that are approximately "proportional" such that the direction of stress and resulting direction of transformation strain generation do not vary significantly from one loading step to the next.[3]. As with the closest point projection, this algorithm

[2]Consideration of the incompressibility condition decreases the number of unknown inelastic strains by one, giving a total system size of 6x6 [84, 129].

[3]Note that, in the case of perfect proportional loading, the convex cutting plane and closest point projection algorithms yield identical results

is convergent provided that the transformation function is convex in stress (where convergence occurs at a quadratic rate) [129]. The incremental-iterative form of the discretized evolution equation is then given as

$$\boldsymbol{\varepsilon}^{t}{}_{n+1}^{(k+1)} = \boldsymbol{\varepsilon}^{t}{}_{n} + (\xi_{n+1}^{(k+1)} - \xi_n)\boldsymbol{\Lambda}^t(\boldsymbol{\sigma}_{n+1}^{(k)}). \tag{3.12}$$

Clearly $\boldsymbol{\Lambda}^t$ is calculated from the solution of the last iteration. This is graphically depicted in the schematic illustration of the algorithm provided in Fig. 19b. It is seen that, in each iteration, the linearization of the transformation function forms a local "cut", and that the direction of stress evolution in the next iteration is determined from the normal to the transformation surface in the last (known) iteration (where the direction for the first iteration is taken from the solution at the previous time step). [140] Having discussed the determination of $\boldsymbol{\Lambda}^t$, the determination of a current solution for ξ is discussed in detail in the following section.

3. Implementation using the convex cutting plane algorithm

We now continue by applying the convex cutting plane to the integration of the transformation equations. For each of the analysis examples throughout this dissertation, it was found that the convex cutting plane form of the RMA provided sufficiently fast convergence while requiring simplified coding, as previously mentioned. In addition to providing a complete description of SMA constitutive model numerical implementation that will be expanded in later chapters, the material in this section extends past work by providing the relations needed to account for large rotations.

Given that the solution methodology is globally incremental via the application of loading steps and locally iterative via the correction process, we can rewrite needed relations from Chapter II, Section C using the numerical notation introduced

previously.[4] For example, the stress computed from (2.18) is written here during the current loading increment $n+1$ at the end of each iteration (k) as

$$\boldsymbol{\sigma}_{n+1}^{(k)} = \boldsymbol{\mathcal{C}}_{n+1}^{(k)} : [\boldsymbol{\varepsilon}_{n+1} - \boldsymbol{\varepsilon}^{th}{}_{n+1} - \boldsymbol{\varepsilon}^{t(k)}_{n+1}]. \tag{3.13}$$

Recall that for each loading step, the total strain increment and temperature increment are supplied by the global solver and are thus known. Given these two inputs, the solution of the constitutive relations can be accomplished via a predictor/corrector scheme. The algorithm begins at iteration (0) with a thermoelastic prediction assuming no evolution in the transformation internal variables, or

$$\boldsymbol{\varepsilon}^{t(0)}_{n+1} = \boldsymbol{\varepsilon}^{t}{}_{n}, \quad \xi_{n+1}^{(0)} = \xi_n. \tag{3.14}$$

The transformation function is calculated based on this prediction, and the constraints $\Phi^{t(0)}_{n+1} \leq 0$ is checked for violation. If no violation exists, the elastic solution is accepted as correct and is returned to the global solver. However, if the constraint is violated, correction of the solution via the return mapping algorithm will be applied to satisfy $\Phi^t = 0$ to within some tolerance.

The convex cutting plane form of the return mapping algorithm used here is based on explicit discretization of the evolution equation (2.20), which gives [124].

$$\Delta\boldsymbol{\varepsilon}^{t(k)}_{n+1} = \Delta\xi_{n+1}^{(k)} \boldsymbol{\Lambda}^{t(k)}_{n+1}. \tag{3.15}$$

During iterative correction, we hold the total current strain and temperature constant

[4] To summarize, the notation is as follows: given any quantity x, its value is updated from the previous time step to the current in the backward Euler sense per $x_{n+1} = x_n + \Delta x_{n+1}$. Such an implicit relation is solved iteratively, and the current value is updated from iteration to iteration per $x_{n+1}^{(k+1)} = x_{n+1}^{(k)} + \Delta x_{n+1}^{(k)}$ until x_{n+1} has converged (i.e., $\Delta x_{n+1}^{(k)} \approx 0$).

such that

$$\Delta\boldsymbol{\varepsilon}_{n+1}^{(k)} = \mathbf{0}, \qquad \Delta T_{n+1}^{(k)} = 0. \tag{3.16}$$

Comparison of the discretization of (2.17) (considering (3.15) and (3.16)) with the partial of (2.32) with respect to stress (considering (2.43)), it can be shown that

$$\Delta\boldsymbol{\sigma}_{n+1}^{(k)} = -\Delta\xi_{n+1}^{(k)}\boldsymbol{\mathcal{C}}_{n+1}^{(k)} : \begin{cases} \partial_{\boldsymbol{\sigma}}\Phi^{t}{}_{n+1}^{(k)} + D\boldsymbol{\Lambda}^{t}{}_{n+1}^{(k)}; & \dot{\xi} > 0 \\ -\partial_{\boldsymbol{\sigma}}\Phi^{t}{}_{n+1}^{(k)} - D\boldsymbol{\Lambda}^{t}{}_{n+1}^{(k)}; & \dot{\xi} < 0 \end{cases}. \tag{3.17}$$

Here we introduce the notation of "$\mp$" (or likewise "$\pm$" as needed) where the upper sign corresponds to forward transformation and the lower sign to reverse. This notation will be used throughout the remainder of this dissertation as it allows (3.17) to be written more concisely as

$$\Delta\boldsymbol{\sigma}_{n+1}^{(k)} = \mp\boldsymbol{\mathcal{C}}_{n+1}^{(k)} : \left(\partial_{\boldsymbol{\sigma}}\Phi^{t}{}_{n+1}^{(k)} + D\boldsymbol{\Lambda}^{t}{}_{n+1}^{(k)}\right)\Delta\xi_{n+1}^{(k)}. \tag{3.18}$$

To illustrate its dependence on the solution-dependent variables, the transformation function given in (2.32) is written out as

$$\Phi^{t}(\boldsymbol{\sigma}, T, \xi) = \pm\left(\boldsymbol{\sigma} : \boldsymbol{\Lambda}^{t}(\boldsymbol{\sigma}) - \rho\partial_{\xi}G(\boldsymbol{\sigma}, T) - f^{t}(\xi)\right) - \left(Y_0^t + D\boldsymbol{\sigma} : \boldsymbol{\Lambda}^{t}(\boldsymbol{\sigma})\right) = 0 \tag{3.19}$$

where $\rho\partial_{\xi}G(\boldsymbol{\sigma}, T)$ is given in (2.29). The attempt to enforce the consistency condition for the transformation function $\Phi^{t}(\boldsymbol{\sigma}, \xi)$ in the next iteration requires that

$$\Phi^{t}{}_{n+1}^{(k)} + \Delta\Phi^{t}{}_{n+1}^{(k)} = \Phi^{t}{}_{n+1}^{(k+1)} \simeq 0. \tag{3.20}$$

Application of the chain rule to this relation gives

$$\Phi^{t}{}_{n+1}^{(k)} + \partial_{\boldsymbol{\sigma}}\Phi^{t}{}_{n+1}^{(k)} : \Delta\boldsymbol{\sigma}_{n+1}^{(k)} + \partial_{\xi}\Phi^{t}{}_{n+1}^{(k)}\Delta\xi_{n+1}^{(k)} + \simeq 0 \tag{3.21}$$

Substituting the stress increment (3.18) into (3.20) after application of the chain

rule per (3.21), we find

$$\Phi^{t(k)}_{n+1} \mp \partial_{\boldsymbol{\sigma}} \Phi^{t(k)}_{n+1} : \boldsymbol{\mathcal{C}}^{(k)}_{n+1} \left(\partial_{\boldsymbol{\sigma}} \Phi^{t(k)}_{n+1} + D\boldsymbol{\Lambda}^{t(k)}_{n+1} \right) \Delta\xi^{(k)}_{n+1} + \partial_{\xi} \Phi^{t(k)}_{n+1} \Delta\xi^{(k)}_{n+1} \simeq 0. \quad (3.22)$$

The required partial derivatives of the transformation function can be evaluated using (3.19) and considering (2.29), resulting in the following:

$$\partial_{\boldsymbol{\sigma}} \Phi^t = \pm \left(\boldsymbol{\Lambda}^t + \frac{1}{2} \widetilde{\boldsymbol{\mathcal{S}}} \boldsymbol{\sigma} \right) - D\boldsymbol{\Lambda}^t; \quad \partial_{\xi} \Phi^t = \mp \partial_{\xi} f^t \quad (3.23)$$

Solving (3.22) for the correction in ξ at the given iteration yields

$$\Delta\xi^{(k)}_{n+1} = \frac{-\Phi^{t(k)}_{n+1}}{A^t_2}, \quad (3.24)$$

where

$$A^t_2 = \partial_{\xi} \Phi^{t(k)}_{n+1} \mp \partial_{\boldsymbol{\sigma}} \Phi^{t(k)}_{n+1} : \boldsymbol{\mathcal{C}}^{(k)}_{n+1} \left(\partial_{\boldsymbol{\sigma}} \Phi^{t(k)}_{n+1} + D\boldsymbol{\Lambda}^{t(k)}_{n+1} \right).$$

It is important to recall that transformation ends when $\xi^{(k+1)}_{n+1}$ reaches one of two limits, specifically

$$0 \leq \xi^{(k)}_{n+1} \leq 1, \quad (3.25)$$

and that one of the bounds may eventually be reached during the iterative scheme within a single loading increment. Therefore, the implemented algorithm must account for this common and expected occurrence.

Given these increments in the scalar measures of the two inelastic strains, we can update the inelastic strain $\boldsymbol{\varepsilon}^t$ using (2.20), which yields

$$\boldsymbol{\varepsilon}^{t(k+1)}_{n+1} = \boldsymbol{\varepsilon}^{t(k)}_{n+1} + \Delta\xi^{(k)}_{n+1} \boldsymbol{\Lambda}^{t(k)}_{n+1}. \quad (3.26)$$

The transformation strains and the updated elastic stiffness are used in (3.13) to calculate an updated stress, which is itself used to calculate the updated transformation function. The iterative scheme then continues until $\Phi^{t(k+1)}_{n+1}$ is smaller than some

tolerance.

4. Continuum tangent modulus

In addition to requiring the updated thermomechanical state of the material (updated stress and internal variables), the global solver also requires the tangent modulus (or tangent stiffness tensor) [124] $\boldsymbol{\mathcal{L}}$, which defines the current rate of change of stress with a change in total strain, given by

$$\mathrm{d}\boldsymbol{\sigma} = \boldsymbol{\mathcal{L}}\,\mathrm{d}\boldsymbol{\varepsilon}\,. \tag{3.27}$$

Coupled thermal and mechanical analysis (i.e., thermomechanical analysis including heat transfer) also requires the thermal tangent modulus, though this is not addressed in this work. It is explained in the literature [124, 129] that the convex cutting plane form of the RMA utilizes the *continuum tangent modulus*. The derivation of this tensor proceeds as follows.

To derive $\boldsymbol{\mathcal{L}}$, the constitutive relation in (2.17) is rewritten in differential form and the transformation strain flow rule (2.20) is substituted to get

$$\mathrm{d}\boldsymbol{\sigma} = \boldsymbol{\mathcal{C}} : \{\, \mathrm{d}\boldsymbol{\varepsilon} - \boldsymbol{\alpha}\,\mathrm{d}T - [\widetilde{\boldsymbol{\mathcal{S}}} : \boldsymbol{\sigma} + \boldsymbol{\Lambda}^t]\,\mathrm{d}\xi\,\}. \tag{3.28}$$

Using (2.32) with (2.28) and (2.29), and further by neglecting the $\mathrm{d}T$ term (as the thermal tangent modulus is not currently required) the above equation reduces to the following (cf. (3.18)):

$$\mathrm{d}\boldsymbol{\sigma} = \boldsymbol{\mathcal{C}}\left[\,\mathrm{d}\boldsymbol{\varepsilon} \mp \mathrm{d}\xi\,\left(\partial_{\boldsymbol{\sigma}}\Phi^t + D\boldsymbol{\Lambda}^t\right)\right]. \tag{3.29}$$

The differentiation of the transformation function (consistency condition) at a speci-

fied constant temperature results in

$$\mathrm{d}\Phi^{\,t} = \partial_{\boldsymbol{\sigma}}\Phi^t : \mathrm{d}\boldsymbol{\sigma} + \partial_\xi \Phi^t \,\mathrm{d}\xi = 0. \tag{3.30}$$

An expression for the differential of the martensitic volume fraction $\mathrm{d}\xi$ is obtained by substituting $\mathrm{d}\boldsymbol{\sigma}$ from (3.29) into (3.30), giving

$$\mathrm{d}\xi = \frac{-\partial_{\boldsymbol{\sigma}}\Phi^t : \boldsymbol{\mathcal{C}}\,\mathrm{d}\boldsymbol{\varepsilon}}{\mp\partial_{\boldsymbol{\sigma}}\Phi^t : \boldsymbol{\mathcal{C}}\left(\partial_{\boldsymbol{\sigma}}\Phi^t + D\boldsymbol{\Lambda}^t\right) + \partial_\xi\Phi^t}. \tag{3.31}$$

Now (3.31) can be used to eliminate $\mathrm{d}\xi$ in (3.29), giving

$$\mathrm{d}\boldsymbol{\sigma} = \boldsymbol{\mathcal{C}}\,\mathrm{d}\boldsymbol{\varepsilon} \pm \boldsymbol{\mathcal{C}}\left[\frac{\partial_{\boldsymbol{\sigma}}\Phi^t : \boldsymbol{\mathcal{C}}\,\mathrm{d}\boldsymbol{\varepsilon}}{\mp\partial_{\boldsymbol{\sigma}}\Phi^t : \boldsymbol{\mathcal{C}}\left(\partial_{\boldsymbol{\sigma}}\Phi^t + D\boldsymbol{\Lambda}^t\right) + \partial_\xi\Phi^t}\left(\partial_{\boldsymbol{\sigma}}\Phi^t + D\boldsymbol{\Lambda}^t\right)\right]. \tag{3.32}$$

By applying the definition and identities related to the tensor product[5] this can be rearranged to find the continuum tangent modulus, given by $\boldsymbol{\mathcal{L}}$ per

$$\mathrm{d}\boldsymbol{\sigma} = \left[\boldsymbol{\mathcal{C}} \pm \frac{\mathbf{B}_1^t \otimes \mathbf{B}_2^t}{\mp\partial_{\boldsymbol{\sigma}}\Phi^t : \boldsymbol{\mathcal{C}}\left(\partial_{\boldsymbol{\sigma}}\Phi^t + D\boldsymbol{\Lambda}^t\right) + \partial_\xi\Phi^t}\right]\mathrm{d}\boldsymbol{\varepsilon} = \boldsymbol{\mathcal{L}}\,\mathrm{d}\boldsymbol{\varepsilon}\,, \tag{3.33}$$

where the second-order tensors $\mathbf{B}_1^t$ and $\mathbf{B}_2^t$ are given as

$$\mathbf{B}_1^t = \boldsymbol{\mathcal{C}}\left(\partial_{\boldsymbol{\sigma}}\Phi^t + D\boldsymbol{\Lambda}^t\right); \qquad \mathbf{B}_2^t = \boldsymbol{\mathcal{C}}\partial_{\boldsymbol{\sigma}}\Phi^t. \tag{3.34}$$

5. Consideration of large rotations

The purpose of using SMA components in engineering applications is to provide a force over some usefully large displacement, either via the pseudoelastic or shape memory effect. To convert the moderate transformation strains ($\sim 5-8\%$) to large global

[5]The second term in (3.32) can be represented in general as $\boldsymbol{\mathcal{C}}\left[(\mathbf{b} : \boldsymbol{\mathcal{C}}\mathbf{c})\mathbf{d}\right]$ where $\boldsymbol{\mathcal{C}}$ can numerically be represented by a second-order tensor, lower case variables represent vectors, and $\mathbf{c}$ in particular represents $\mathrm{d}\boldsymbol{\varepsilon}$ which must be factored out. The definition of the tensor products gives $(\mathbf{b} : \mathbf{v})\mathbf{a} = (\mathbf{a} \otimes \mathbf{b})\mathbf{v}$ and thus this second terms becomes $\boldsymbol{\mathcal{C}}\left[(\mathbf{d} \otimes \mathbf{b})\boldsymbol{\mathcal{C}}\mathbf{c}\right]$. Application of two additional identities [141] (i.e., $(\mathbf{b} \otimes \mathbf{c})\boldsymbol{\mathcal{C}} = \mathbf{b} \otimes \boldsymbol{\mathcal{C}}^{\mathsf{T}}\mathbf{c}$ and $\boldsymbol{\mathcal{C}}(\mathbf{b} \otimes \mathbf{c}) = \boldsymbol{\mathcal{C}}\mathbf{b} \otimes \mathbf{c}$) gives $(\boldsymbol{\mathcal{C}}\mathbf{d} \otimes \boldsymbol{\mathcal{C}}\mathbf{b})\mathbf{c}$, allowing $\mathrm{d}\boldsymbol{\varepsilon}$ to be factored out.

displacements, structural components such as beams and torque tubes are often used. However, the infinitesimal strain formulation of many constitutive models (including the model described above) is not objective under the large rigid-body rotations expected when a beam bends or a torque tube rotates by many degrees (see [52], p. 140). Further, linear FEA implementations of infinitesimal strain models result in non-physical solutions if large rotations exist, such as the homogeneous expansion of elements in the plane of rotation (for example, see [48], Section 9.3, as well as Appendix D in the current work)[6].

To satisfy objectivity while continuing to employ infinitesimal strain constitutive models, FEA packages such as Abaqus [136] and ANSYS [143] employ the Hughes-Winget algorithm [50, 129]. This algorithm was proposed as a simple method for numerically integrating constitutive equations in rate form (cf. (2.20)) in an objective manner, even in the case of large rotations (i.e., given the incremental loading framework, they are *incrementally objective*). A similar methodology has been used for SMA modeling in the past [51], and is described in more detail here, specifically applied to the model of Section C.

For problems involving large local rotations, the algorithm proposes that objectivity can be maintained if the stress $\boldsymbol{\sigma}_{n+1}^{(k)}$ in the new loading step is the sum of the properly rotated contribution from the last loading step and the new stress increment

[6]The infinitesimal strain tensor considered throughout this dissertation is mathematically defined in terms of the local displacement vector $\mathbf{u}$ as $\boldsymbol{\varepsilon} = \frac{1}{2}\left(\nabla\mathbf{u} + \nabla\mathbf{u}^T\right)$. Given a displacement field that consists only of a proper rotation $\boldsymbol{\mathcal{Q}}$ about the x-axis (i.e., no stretching), it can be shown [142] that $\varepsilon_{22} = \varepsilon_{33} = 2\cos\theta - 2$, while the material remains undeformed axially (i.e., there is no extension of the material, only rotation). For a rotation of 18 degrees, this corresponds to an (erroneous) strain of $\sim 10\%$.

$\Delta\boldsymbol{\sigma}^{(k)}_{n+1}$. This is written

$$\begin{aligned}\boldsymbol{\sigma}^{(k)}_{n+1} &= \overline{\boldsymbol{\sigma}}^{(k)}_{n+1} + \Delta\boldsymbol{\sigma}^{(k)}_{n+1} \\ &= \boldsymbol{\mathcal{Q}}_{n+1} : \boldsymbol{\sigma}^{(k)}_{n} : \boldsymbol{\mathcal{Q}}^{\mathrm{T}}_{n+1} + \Delta\boldsymbol{\sigma}^{(k)}_{n+1}\end{aligned} \tag{3.35}$$

where the current stress increment $\Delta\boldsymbol{\sigma}^{(k)}_{n+1}$ is calculated using tensors ($\boldsymbol{\varepsilon}$, $\boldsymbol{\varepsilon}^t$, etc) that have been rotated into the current local configuration via $\boldsymbol{\mathcal{Q}}_{n+1}$. The form of the orthogonal rotation tensor $\boldsymbol{\mathcal{Q}}_{n+1}$ is central to the algorithm and is calculated in terms of the skew-symmetric part of the velocity gradient via the midpoint rule. The details of these developments are discussed elsewhere [50, 129, 144].

To improve the algorithm of Section A.3 to further consider large rotations requires that the constitutive relations be expressed in the form of (3.35). We first consider the proposed form where geometric nonlinearities are *not* considered. For iteration (k) in loading step $n+1$, (3.26) implies that the current transformation strain is determined by

$$\boldsymbol{\varepsilon}^{t(k)}_{n+1} = \boldsymbol{\varepsilon}^{t}{}_{n} + \sum_{i=1}^{k} \Delta\boldsymbol{\varepsilon}^{t(i)}_{n+1} = \boldsymbol{\varepsilon}^{t}{}_{n} + \boldsymbol{\Lambda}^{t(i)}_{n+1}\Delta\xi^{(i)}_{n+1}, \tag{3.36}$$

where summation over the repeated index i is assumed. The total strain and thermal strain are updated at the beginning of each increment and all strain evolutions are substituted into (3.13) to yield

$$\boldsymbol{\sigma}^{(k)}_{n+1} = \boldsymbol{\mathcal{C}}^{(k)}_{n+1} : \big[(\boldsymbol{\varepsilon}_n + \Delta\boldsymbol{\varepsilon}_{n+1}) - (\boldsymbol{\varepsilon}^{th}_n + \Delta\boldsymbol{\varepsilon}^{th}{}_{n+1}) - (\boldsymbol{\varepsilon}^{t}{}_{n} + \boldsymbol{\Lambda}^{t(i)}_{n+1}\Delta\xi^{(i)}_{n+1})\big]. \tag{3.37}$$

Gathering terms from the last loading increment separately from those calculated for the next, we have for *small* rotations

$$\begin{aligned}\boldsymbol{\sigma}^{(k)}_{n+1} &= \boldsymbol{\mathcal{C}}^{(k)}_{n+1} : (\boldsymbol{\varepsilon}_n - \boldsymbol{\varepsilon}^{th}_n - \boldsymbol{\varepsilon}^{t}{}_{n}) + \\ &+ \boldsymbol{\mathcal{C}}^{(k)}_{n+1} : (\Delta\boldsymbol{\varepsilon}_{n+1} - \Delta\boldsymbol{\varepsilon}^{th}{}_{n+1} - \boldsymbol{\Lambda}^{t(i)}_{n+1}\Delta\xi^{(i)}_{n+1}).\end{aligned} \tag{3.38}$$

The consideration of *finite* rotations requires that tensors passed into the return mapping algorithm from the last converged loading increment n be rotated into the current local configuration via $\boldsymbol{\mathcal{Q}}_{n+1}$. Recall that the current total strain (and thus the local rotation) remain constant over all iterations (k) within loading step $n+1$. Given this, in the case of large rotation analysis the current local stress is written as

$$\begin{aligned} \boldsymbol{\sigma}_{n+1}^{(k)} &= \boldsymbol{\mathcal{Q}}_{n+1} : \left[\boldsymbol{\mathcal{C}}_{n+1}^{(k)} : (\boldsymbol{\varepsilon}_n - \boldsymbol{\varepsilon}_n^{th} - \boldsymbol{\varepsilon}^t{}_n) \right] : \boldsymbol{\mathcal{Q}}_{n+1}^{\mathrm{T}} + \\ &+ \boldsymbol{\mathcal{C}}_{n+1}^{(k)} : (\Delta\boldsymbol{\varepsilon}_{n+1} - \Delta\boldsymbol{\varepsilon}^{th}{}_{n+1} - \boldsymbol{\Lambda}^{t(i)}{}_{n+1} \Delta\xi_{n+1}^{(i)}). \end{aligned} \tag{3.39}$$

If we consider the special case of isotropic symmetry in the material elastic properties (not a necessity, but a common approach in SMA modeling), then $\boldsymbol{\mathcal{C}}$ is invariant under the rotation $\boldsymbol{\mathcal{Q}}$. Assuming this for the current model and using the notation of Hughes and Winget [50], we find

$$\begin{aligned} \boldsymbol{\sigma}_{n+1}^{(k)} &= \boldsymbol{\mathcal{C}}_{n+1}^{(k)} : \left[(\overline{\boldsymbol{\varepsilon}}_{n+1} - \overline{\boldsymbol{\varepsilon}}_{n+1}^{th} - \overline{\boldsymbol{\varepsilon}}^t{}_{n+1}) \right] + \\ &+ \boldsymbol{\mathcal{C}}_{n+1}^{(k)} : (\Delta\boldsymbol{\varepsilon}_{n+1} - \Delta\boldsymbol{\varepsilon}^{th}{}_{n+1} - \boldsymbol{\Lambda}^{t(i)}{}_{n+1} \Delta\xi_{n+1}^{(i)}). \end{aligned} \tag{3.40}$$

This is analogous to the stress form (3.35) addressed by the Hughes-Winget algorithm and thus is consistent with the solution methodology of the Abaqus FEA package, for example. Considering (2.20), (2.21), and (3.40), it is clear that the global variable $\boldsymbol{\sigma}_n$ and the local stored constant $\boldsymbol{\varepsilon}_n^{t-r}$ must also be properly rotated in order to calculate $\boldsymbol{\Lambda}^t{}_{n+1}$ correctly. Of course, the rotated tensors are also used to compute the transformation function (2.32). The global FEA solver may compute the rotated global variables $\overline{\boldsymbol{\varepsilon}}_n$ and $\overline{\boldsymbol{\sigma}}_n$ prior to each call to the user material subroutine (Abaqus, for example, performs such a pre-rotation when the `NLGEOM` option is activated), but it is the role of the subroutine to rotate the tensorial internal variables. These rotations become a new first step of the return mapping algorithm.

Appendix D provides two example numerical analyses of SMA components undergoing large rotations. The first is a uniaxial rod which is simultaneously rotated and pseudoelastically loaded in tension, while the second is an SMA torque tube actuator that rotates in excess of 45° as it undergoes thermally induced transformation while subjected to a linear biasing force (i.e., torsional spring). The analysis results show that the methods described in this section are necessary for the prevention of spurious element deformations, convergence difficulties, and erroneous results.

6. Summary of Implementation

Table III provides a summary of the full RMA (convex cutting plane) needed to integrate the constitutive relations in an FEA framework while considering large rotations.

B. Experimentally Calibrated Analysis of SMA Applications

To demonstrate the capability of the model to predict 3-D structural response, a series of analyses were performed. The first considered 3-D beams (or flexures) composed of the same material as was simulated in Chapter II, Section D and compared their actuation behavior to that predicted by the implemented model (as calibrated per Table II). The second considered the multi-component response of the Boeing VGC where these same flexures were fastened to a composite substrate and actuated in opposition to such an elastic biasing load.

Because the motivation for much of this work was the development and analysis of the Boeing VGC, it is important to describe the configuration and operation of this engineering application [13]. A single chevron consists of multiple components, the first of which is an elastic composite laminate substrate which has a complex curved

Table III. Return Mapping Algorithm (Convex Cutting Plane form) for modeling of phase transformation phenomena in SMAs.

1. Initialize

a. Rotate all tensors from last increment n by $\boldsymbol{\mathcal{Q}}_{n+1}$

b. Let $k = 0$, $\xi_{n+1}^{(0)} = \xi_n$, $\boldsymbol{\varepsilon}^t{}_{n+1}^{(0)} = \boldsymbol{\varepsilon}^t{}_n$,
$\mathbf{S}_{n+1}^{(0)} = \mathbf{S}_n$, $\boldsymbol{\alpha}_{n+1}^{(0)} = \boldsymbol{\alpha}_n$, $\xi_{irr} = \xi_{irr}(\bar{\epsilon}^p{}_n)$

2. Elastic Prediction

a. $\boldsymbol{\sigma}_{n+1}^{(0)} = \boldsymbol{\mathcal{C}}_{n+1}^{(0)} \left[\boldsymbol{\varepsilon}_{n+1} - \boldsymbol{\alpha}(T_{n+1} - T_0) - \boldsymbol{\varepsilon}^t{}_{n+1}^{(0)}\right]$

c. Find $\Phi^t{}_{n+1}^{(0)}$.

d. IF $\Phi^t{}_{n+1}^{(0)} \leq 0$ THEN EXIT (response elastic).

3. Transformation Correction

a. IF $\Phi^t{}_{n+1}^{(0)} > 0$ THEN CONTINUE ELSE EXIT.

b. Find $\Delta\xi_{n+1}^{(k)}$ via (3.24).

c. $\xi_{n+1}^{(k+1)} = \xi_{n+1}^{(k)} + \Delta\xi_{n+1}^{(k)}$, and $\boldsymbol{\varepsilon}^t{}_{n+1}^{(k+1)} = \boldsymbol{\varepsilon}^t{}_{n+1}^{(k)} + \Delta\xi_{n+1}^{(k)} \boldsymbol{\Lambda}^t{}_{n+1}^{(k)}$

d. IF $\xi_{n+1}^{(k+1)}$ within bounds per (3.25) THEN CONTINUE ELSE set $\xi_{n+1}^{(k+1)}$ to violated bound and recalculate $\Delta\xi_{n+1}^{(k)}$.

e. $\boldsymbol{\sigma}_{n+1}^{(k+1)} = \boldsymbol{\mathcal{C}}_{n+1}^{(k+1)} \left[\boldsymbol{\varepsilon}_{n+1} - \boldsymbol{\alpha}(T_{n+1} - T_0) - \boldsymbol{\varepsilon}^t{}_{n+1}^{(k+1)}\right]$

f. IF $\Phi^t{}_{n+1}^{(k+1)} > TOL^t$ per (2.32) THEN CONTINUE ELSE EXIT

g. Increment k and GOTO 3b

shape in the stress-free (reference) conguration. Three Ni60Ti SMA tapered flexures, precurved in the stress-free state, are mounted onto this substrate and then covered by a thin aerodynamic composite panel (not considered here); the combination of a substrate, three flexures, and the aerodynamic panel comprises one chevron. A number of chevrons can then be installed along the aft edge of a jet engine fan cowl, depending on the size of the engine. The total chevron assembly is summarized in Fig. 20 where installation on a GE90-115B engine is considered. The purpose of the SMA flexure as used in the chevron is to provide bending forces to the elastic laminate substrate via the shape memory effect. The pre-curved flexure is fastened at its center

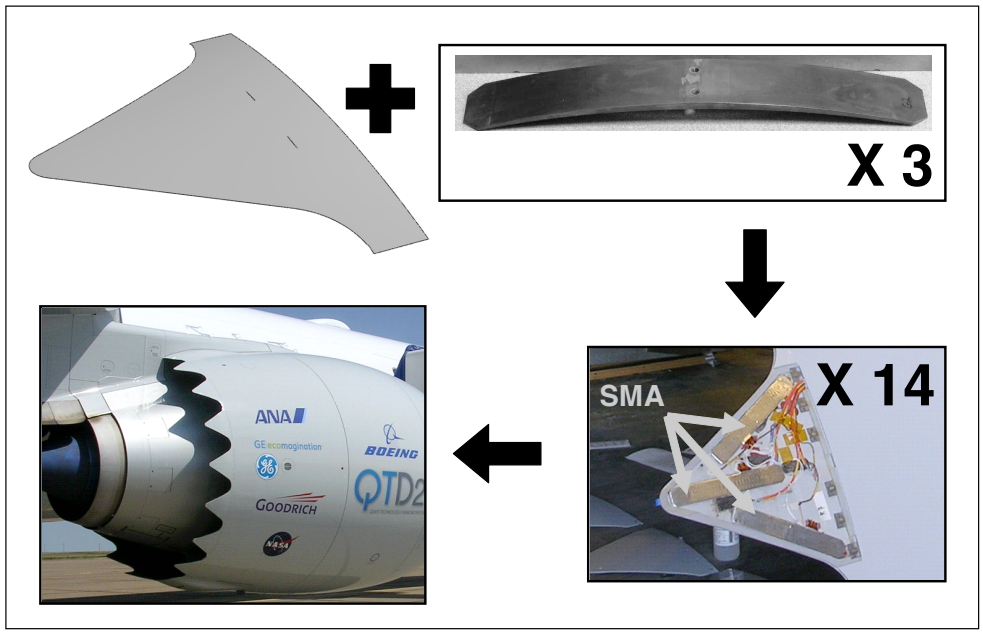

Fig. 20. Configuration of the multi-component Boeing (VGC).

to the substrate, while the two flexure ends are supported by this substrate. The fastening draws the center of the flexure down and, when the flexure is in martensite, removes the curvature of the set shape. When the flexure is sufficiently heated so as to transform into austenite, the pre-curved shape is recovered and this induces bending on the composite substrate, deflecting its aft tip down. This results in a mixture of jet engine fan flow with core flow and a reduction in jet engine noise.

1. Actuation response of Ni60Ti flexures

Experimental testing and numerical analysis of the force and deflection responses of the tapered, precurved Ni60Ti flexure was performed to demonstrate the predictive capabilities of the implementation. The purpose of the SMA flexure as used in the VGC is to provide bending forces to the elastic laminate substrate via the shape memory effect. Therefore, the most important behavior of the active SMA flexure

involves the forces and deflections of the flexure center relative to its ends, and the characterization of the flexure performed at Texas A&M was focused on this behavior. Two particular responses were assessed: (*i*) the flexure response under constant applied load, and (*ii*) the response under linear variable (spring) load.

The tapered and precurved Ni60Ti flexures were 1.5 in (38 mm) wide and 10.0 in (254 mm) long. The taper of the flexures is such that the thickness varies nearly quadratically from 0.175 in (4.45 mm) at the root (i.e., the midpoint) to 0.065 in (1.651 mm) at each of the tips. The experimental setup for the Ni60Ti flexure testing was similar to the setup for the testing of the Ni60Ti tensile specimens, and is illustrated in part in Fig. 21. Force was applied downward at the center of the flexure by the MTS frame, while the tips of the precurved flexure were supported by a "rigid" brass bar. The same environmental chamber described in Chapter II, Section A was used once more, although an internal fan was added to provide forced convection and increase thermal homogeneity along the length of the flexure. The temperature of the SMA flexure was measured by thermocouples installed at three locations (one at each end and an additional thermocouple at the center of the flexure (the temperature reported in this discussion being the average of the three).

The constant load bias testing was performed first. Using the environmental chamber, the average temperature of the flexure was brought to an initial level of 75 °C, a temperature clearly above A_f. A 20 lb (90 N) load was applied to the center of the flexure and held constant. The average temperature was cycled down to -30 °C and then back to 75 °C. When variable force testing was performed, a well-lubricated array of eight compressive springs arranged in parallel was installed inline between the bending tip and the MTS frame. The array provided a linear and repeatable force-deflection response with a spring rate of $k = 63.4$ N/mm. This force-deflection relationship approximated the elastic response of the VGC laminate substrate (per

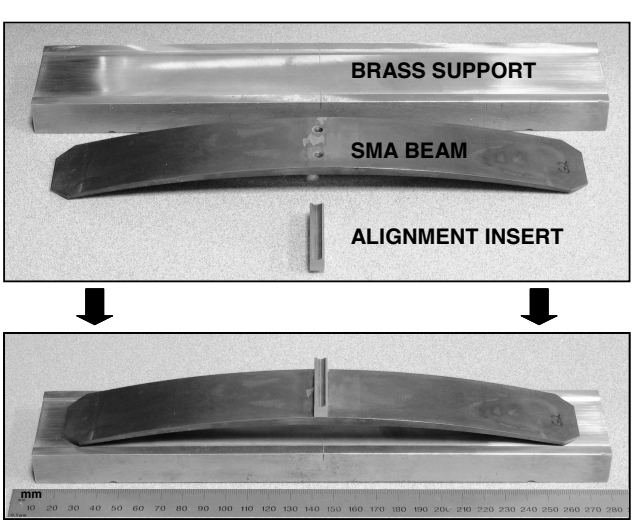

(a) Ni60Ti flexure, brass support bar, and alignment insert

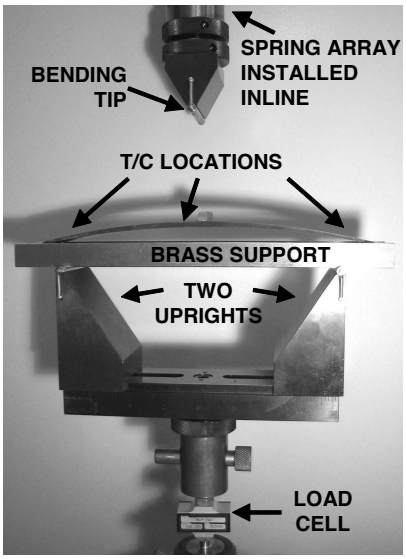

(b) Installation of flexure testing setup on MTS frame

Fig. 21. Experimental setup for the testing of the Ni60Ti active flexure.

elastic testing performed at Boeing). For the variable bias load testing, the flexure was again brought to an initial temperature of 75 °C. The bending tip (with inline spring array installed) applied a force of 325 N to the austenitic flexure. The crossheads of the MTS frame were then locked (fixed) such that all subsequent changes in force applied to the flexure center would be solely proportional to the motion at the center via the linear spring rate of 63.4 N/mm. The flexure was then cooled to below -30 °C and heated back to 75 °C.

The chief objective in testing the response of the SMA flexure was to then show that the implemented model could predict the experimental results given only the 1-D calibration data of Table I. The boundary/initial value problem analyzed was a direct representation of the experimental study. The mechanical load was applied by distributing several nodal forces along a line at the center of the flexure while its

tips were constrained in the vertical direction. To model SMA actuation, quasistatic thermal cycles were applied via the imposition of defined temperature changes applied to every node in the mesh. This analysis setup can be seen in Fig. 22a. Two loading cases were considered: the constant 90 N load and the linearly varying load with a spring rate of 63 N/mm (identical to the experimental load path).

The experimental and analytical deflection-temperature results are shown in Fig. 22b. Note that the results from both load cases show general agreement, but that the modeling predictions for the spring biasing force are more accurate. This can be explained as follows: while a constant load of 90 N results in a maximum surface stress of only 40 MPa, the spring biasing force results in up to 150 MPa stress as the applied force reaches over 300 N. Analysis of the latter case then utilizes data from a greater number of calibration tests, increasing its accuracy overall. Such variable loading is also a better simulation of loading conditions experienced by the flexure when incorporated into the actual chevron system; thus, accurate VGC predictions should follow.

2. Actuation of VGC incorporating Ni60Ti flexures

When analyzing the full VGC structure, the composite laminate substrate had to be modeled in addition to the active flexures previously described. The laminate itself is formed from 15 layers of 90° weave resin-impregnated carbon fiber composite, each layer having a thickness of 0.21 mm. Two stiffening strips ran from the chevron root to its tip and consisted of thickened laminate regions. The substrate was modeled using shell elements and the ABAQUS `SHELLSECTION, COMPOSITE` command, and elastic anisotropic material properties were assigned to each of the 15 layers. The anisotropic constants for a given layer were provided by Boeing. The fully 3-D solid model of the substrate is meshed with 6-node triangular shell elements (`STRI65`) and

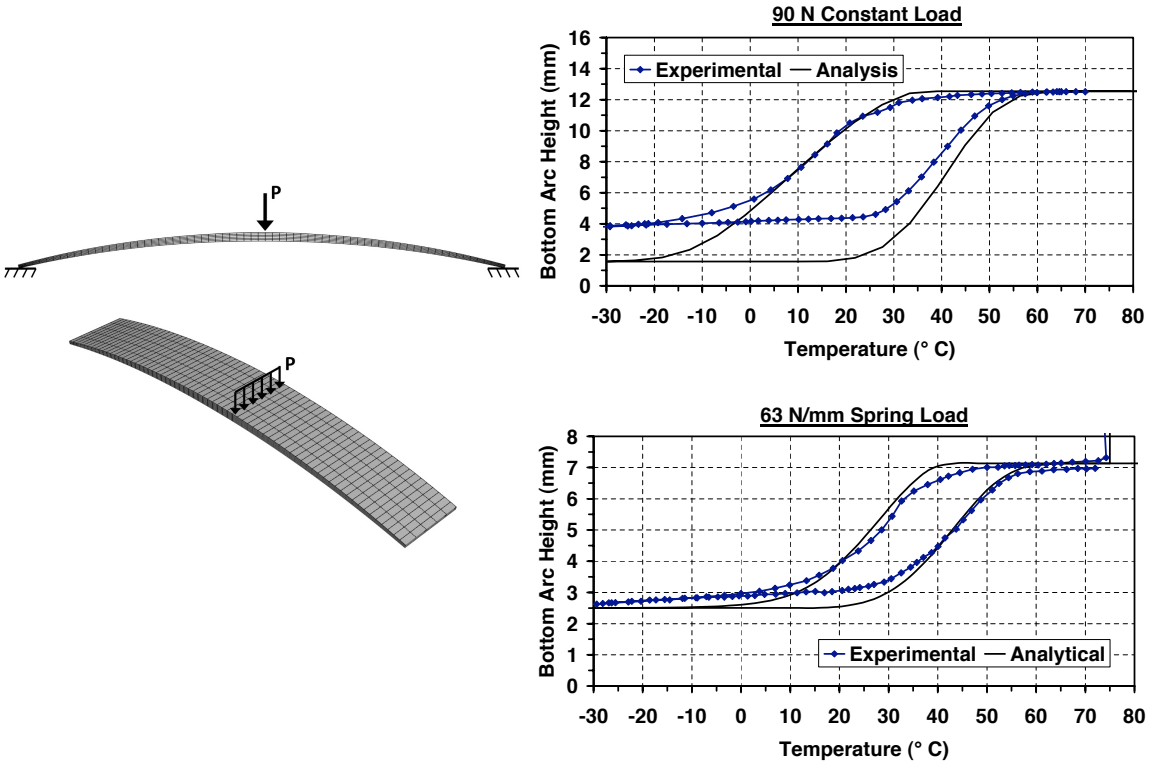

(a) Model setup (b) Experimental and analytical results

Fig. 22. Experimental validation of thermomechanical SMA flexure modeling using material properties from Chapter II.

is 3.16 mm thick.

The proper model assembly of these four structural subcomponents (one chevron substrate and three flexures) involves several considerations. These include the manner by which the flexures are forced flush with the substrate and held there ("clamping"), the enforcement of non-penetration at the flexure/substrate interface, and the methods used to prevent unreasonable flexure rotations about the fastener axis. These considerations are schematically illustrated in Fig. 23. Relative downward motion of the flexure centers toward the substrate was enforced using Abaqus `SLOT` connector elements which prescribe collinear motion of nodes along a single axis. In this case,

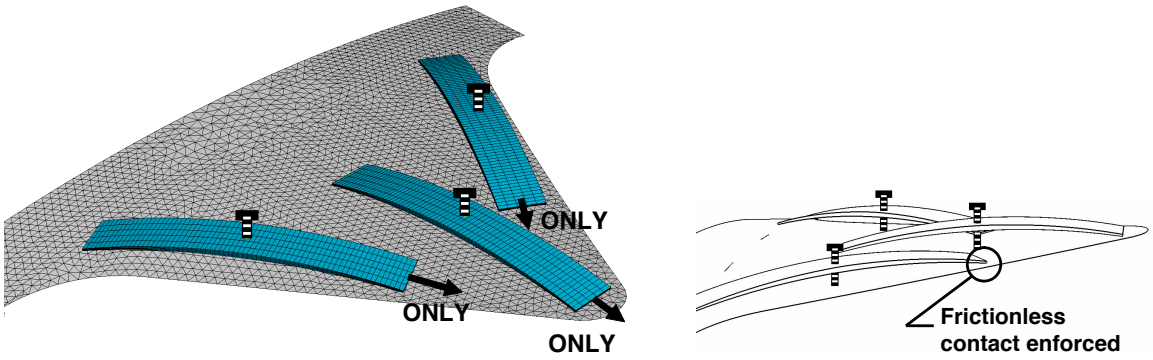

(a) Model setup

(b) Experimental and analytical results

Fig. 23. Assembled 3-D FEA model of the VGC system from: a) isometric and b) side viewpoints. Clamping connector elements are shown schematically.

the clamping axis was aligned with that of the bolts as installed on the flight tested chevron [25]. Penetration of the SMA flexures through the chevron substrate was prevented by defining contact regions on the ends of each flexure, with matching regions being defined over a small local subset of the adjacent chevron surface. Using Abaqus internal contact algorithms, this ensured that the flexure tips could only slide tangentially to the chevron while the normal contact forces at these tips caused bending of the chevron. Note that frictionless sliding contact was assumed in this analysis, which is compatible with the fabrication of the chevron prototypes incorporating lubrication at the interface. Finally, unreasonable flexure rotations about the bolt axis were prevented by the use of `SLIDE-PLANE` connector elements, which enforced that the flexure tips could only translate in a plane containing the reference flexure longitudinal axis and the bolt axis. The multi-component 3-D FEA model is shown in Fig. 23, with the connector elements schematically illustrated. Note that the forward edge of the VGC substrate (left side in Fig. 23) was held fixed by kinematic constraints.

A rigorous validation of the model as implemented in this FEA framework was performed by considering the total VGC actuation response driven by thermal inputs. Four thermomechanical loading steps were applied to this multi-component chevron system. These included one step to test/model the system assembly (Step 1) and an additional three steps to test/model a full cycle of system actuation (Steps 2–4). The loading steps applied to both the experimental prototype and FEA model were as follows:

1. Clamp the flexures in the martensitic state onto the substrate such that the lower surface of the flexures contact the upper surface of the substrate.

2. Heat the flexures through full transformation into austenite (80°C).

3. Cool the flexures to room temperature (20°C), during which transformation into martensite is initiated but *not* completed.

4. Heat the flexures through full transformation into austenite once again.

The result of interest was the change in assembled chevron *topography* as the temperature of the SMA flexures changed. In the experimental setup, *photogrammetry* was used to determine the surface topography of the chevron under different loading conditions. In this process, multiple cameras are used to stereographically determine the 3-D location of various reflective "dots" or "targets" applied to the substrate surface [25, 145, 146]. The topological contours for the analytical case are found by summing the reference locations for each node in the FEA mesh with the calculated displacements at that node.

The surface topographies at the end of Step 2 (80 °C), during Step 3 (40 °C, an intermediate temperature), and at the end of Step 3 (20 °C) are shown in the contour plots provided in Fig. 24. Both experimental and numerical results are shown, and the

numerical predictions are notably accurate. Fig. 25 illustrates the measured positions of various points along the VGC *centerline* at 80 °C and 20 °C using both photogrammetry and numerical analysis data. It was calculated that the least-squares error in the topology, as measured along the centerline, was $\sim 6\%$ at 80 °C. The evolution of the VGC tip location is shown in Fig. 26. While the accuracy of the predictions is impressive considering the complexity of the problem, it should not be altogether surprising when one further considers the success with which the model captured the simple constitutive response (Fig. 17) and the accuracy of the Abaqus FEA implementation in capturing the response of the SMA flexure under load (predictive validation, Fig. 22).

Finally, to illustrate the evolution of the VGC configuration over the loading path, Fig. 27 is provided. Here, the reference, clamped, heated, and cooled configurations are shown from a point of view that highlights that VGC deflection. In the upper portion of each picture, all four components of the assembled VGC model (substrate and three flexures) are shown. Also shown is the reference (load free) configuration of the laminate, illustrated by the translucent layer. The contours represent the Mises equivalent stress ($\overline{\sigma}$) throughout the flexure thickness and over the upper surface of the substrate (i.e., in the upper-most lamina). In the bottom portion of each image, the response of the center flexure is illustrated in more detail, and the stress distribution throughout its thickness is made more clear.

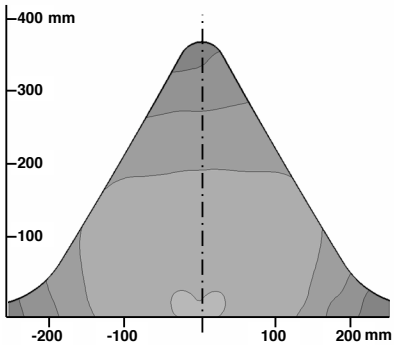

(a) Heated, 80 °C (exp.)

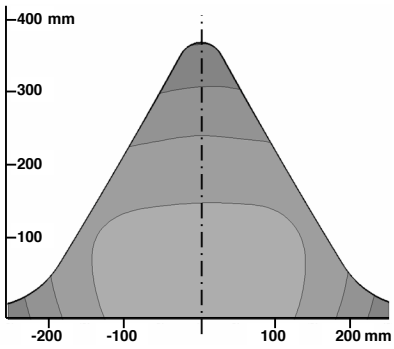

(b) Heated, 80 °C (analysis)

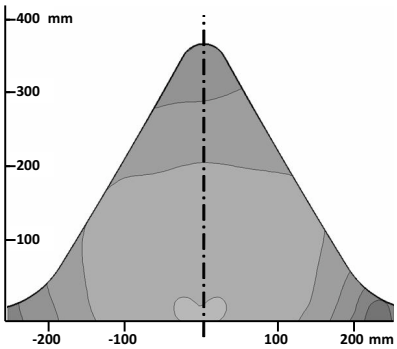

(c) Cooled, 40 °C (exp.)

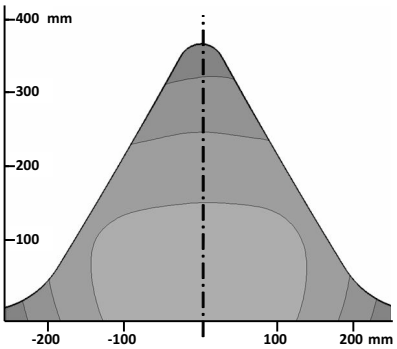

(d) Cooled, 40 °C (analysis)

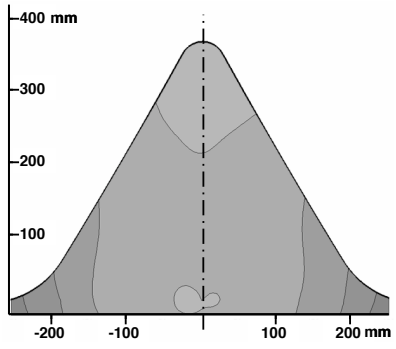

(e) Cooled, 20 °C (exp.)

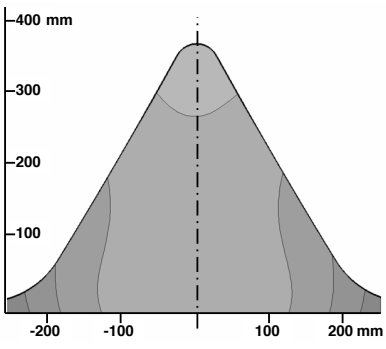

(f) Cooled, 20 °C (analysis)

Fig. 24. Experimental data and analytical predictions for the surface topology during thermal actuation of the multicomponent VGC (contour lines represent 5 mm increments in elevation).

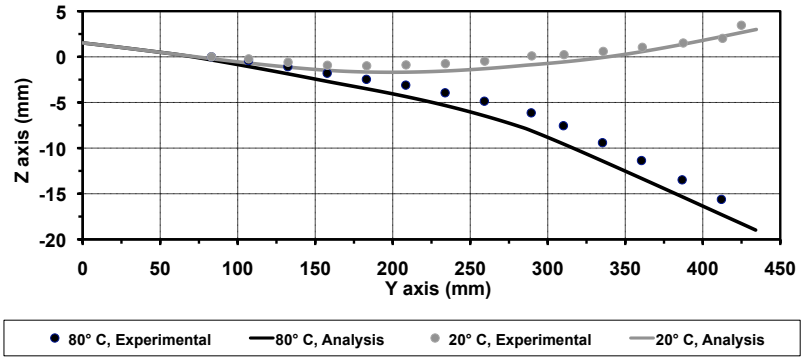

Fig. 25. Spatial location of points along the centerline of the VGC after heating to 80 ℃ and then cooling to 20 ℃ (experimental and analytical results).

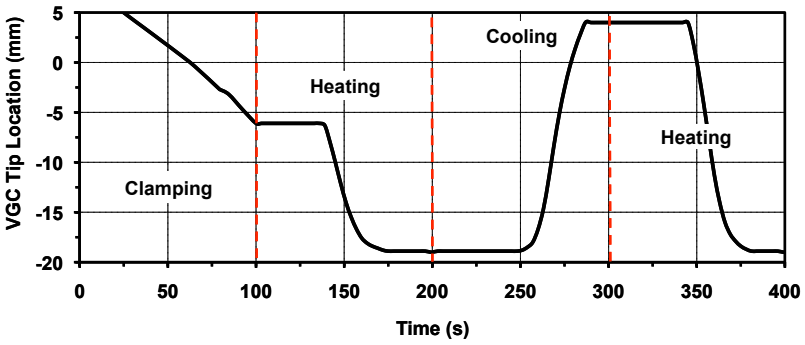

Fig. 26. Evolution of the location of the VGC tip throughout the analysis.

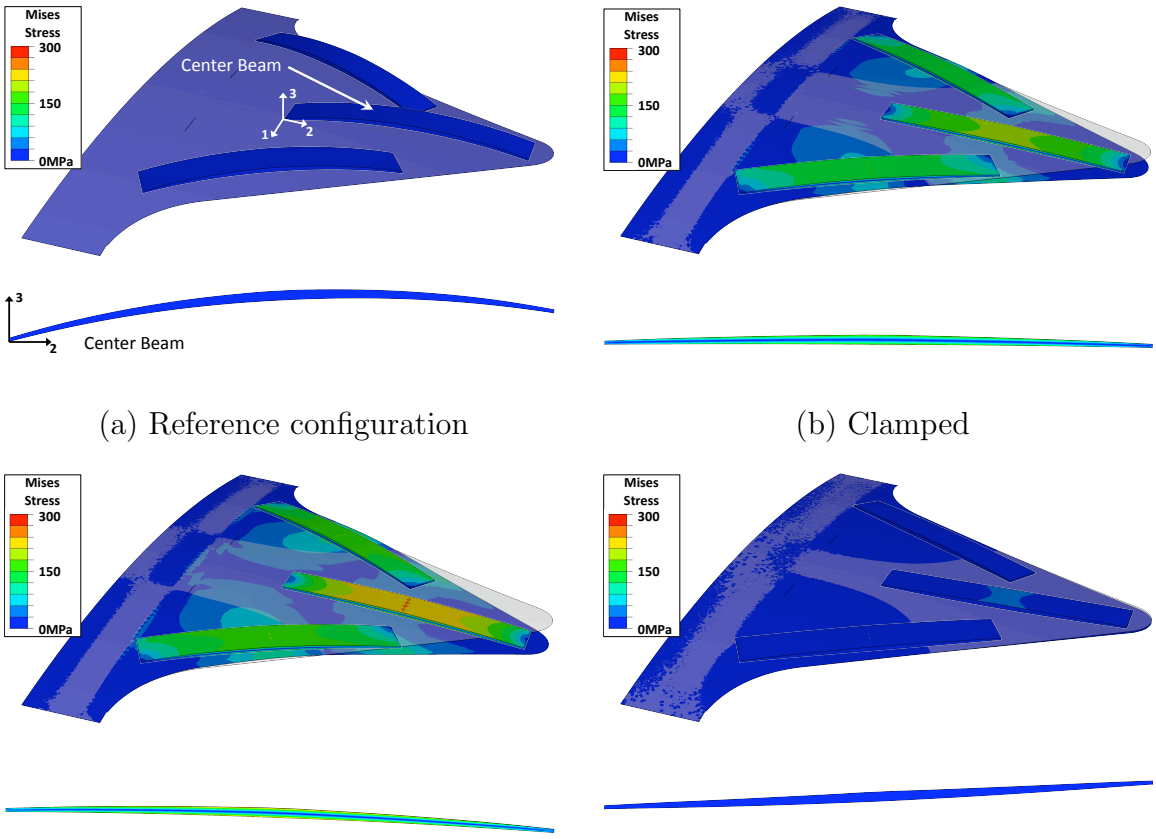

(a) Reference configuration

(b) Clamped

(c) Heated to 80 °C

(d) Cooled to 20 °C

Fig. 27. FEA predictions for the deformation and Mises equivalent stress distribution throughout the assembled VGC structure and through the thickness of the center SMA flexure.

CHAPTER IV

RATE-INDEPENDENT PLASTIC DEFORMATIONS IN SMAS

This chapter[1] extends both the constitutive model and numerical implementation methods described in the previous two chapters by additionally considering the generation and evolution of rate-independent plastic strains in SMAs and their resulting impact on transformation behavior. As discussed in Chapter I, this work is motivated by experimental evidence indicating that martensitic phase transformation and plastic yielding can occur simultaneously [67, 68]; additional experimental results are provided early in the chapter. Further motivation for the development of these new modeling techniques stems from engineering problems such as the fastening [24] and indentation [76] of SMAs and new tribological considerations [74, 75]. Each of these has as a consequence the possible localized yielding of SMA materials.

This chapter is organized as follows: Section A describes how experimental findings motivate the developments that follow, while Section B describes the derivation of the SMA transformation-plastic yield constitutive model using continuum thermodynamics and various assumptions on the interactions of transformation and plastic yield processes; Section C discusses the numerical implementation of the model in an FEA framework that further accounts for large rotations in SMA bodies; Section D includes model calibration and simulation of experiments, and provides example analyses that demonstrate the unique capabilities and accuracy of the proposed model and implementation.

---

[1]Portions reprinted from *Smart Materials and Structures*, Vol. 18, DOI 10.1088/0964-1726/18/10/104017, Hartl, D. and Lagoudas, D., Copyright 2009, with permission from Institute of Physics

A. Experimental Motivation for the Coupled Model

Prior to developing a new model, an experimental study was performed to ascertain the qualitative characteristics of plastic yield in SMAs and to provide quantitative data for eventual model calibration. In this study, nominally isothermal mechanical loads were applied to SMA tensile specimens initially in the austenitic state[2]. Loading below the austenitic start temperature A_s ($T < 100\,^{\circ}\mathrm{C}$) led to the initiation and completion of stress-induced phase transformation followed by yielding of the material. Higher temperatures ($100\,^{\circ}\mathrm{C} \leq T \leq 177\,^{\circ}\mathrm{C}$) increased the stability of austenite such that mechanical loading led to plastic slip followed by stress-induced transformation. Loading continued such that most or all of forward transformation was completed. During mechanical unloading, little reverse transformation was observed. The unloading step was followed by a slow heating to assess the effects of plastic strain on the thermal recovery behavior (shape memory effect). The reduction in recoverable strain and the shift in temperature required to initiate and complete transformation were noted. The entire series of loading/unloading/thermal recovery results is summarized in Figure 28.[3]

In the case that plastic yield resulted during loading in the first cycle, its influence on transformation can be observed both during the heating step and additionally by considering a second loading cycle. An example of this is shown for $T = 120\,^{\circ}\mathrm{C}$ in Figure 29, where the stresses in the first cycle exceed the critical stress for plastic

---

[2]The material chosen for experimental characterization was equiatomic NiTi (cold rolled to 30% reduction in thickness, heat treated for 1 hour at $400\,^{\circ}\mathrm{C}$, quenched, with specimens cut along rolling direction).

[3]With respect to the discussion of Chapter I, Section B, and Fig. 5, the temperatures M_d^c, M_d^p, and M_d for this current set of experimental results are approximately as follows: $M_d^c \approx 95\,^{\circ}\mathrm{C}$, $M_d^p \approx 130\,^{\circ}\mathrm{C}$, and $M_d \approx 170\,^{\circ}\mathrm{C}$.

slip.[4] The first effect of plasticity is to reduce the amount of transformation strain recovered during subsequent heating. Another effect is to decrease the critical transformation stress when the specimen is loaded a second time. Clearly the mechanisms of phase transformation are influenced by the presence of local plastic deformations. Additional tests showed that the monotonic yielding behavior varied with material phase. Thus, the transformation response and plastic response are strongly coupled.

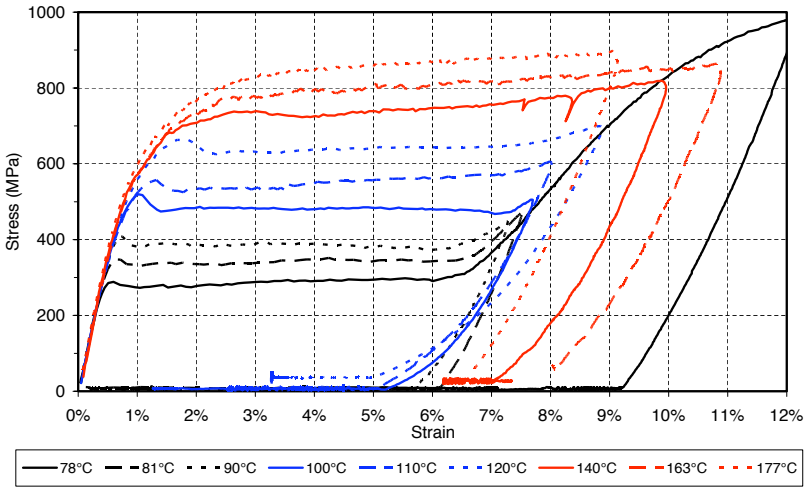

Fig. 28. Results from a series of uniaxial tensile tests on equiatomic NiTi at various nominally constant test temperatures, including subsequent thermal strain recovery.

[4]The "overstress" phenomenon observed at the initiation of stress-induced transformation into martensite has been discussed in detail by Shaw and coworkers [147, 118]. This is observed here in the 90 °C, 100 °C, 110 °C, and 120 °C tests. Referred to as a "nucleation stress" (as opposed to the nominal plateau stress level referred to as the "propagation stress"), it is thought to represent the stress required to nucleate transformation when stress and temperature fields are homogeneous. Once the transformation has nucleated, stress, strain, and temperature gradients at the boundaries of the local transformation zones reduce the stress required to propagate the transformation.

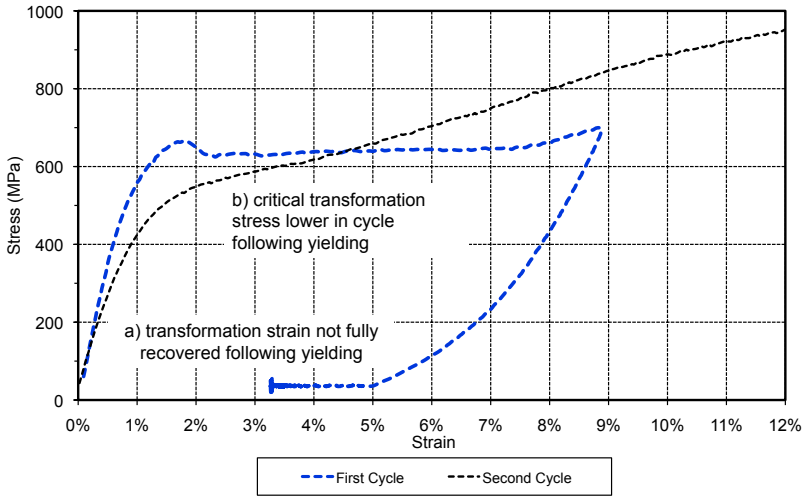

Fig. 29. Results of uniaxial tensile testing of equiatomic NiTi at 120 °C showing influences of plastic strain generation on transformation behavior.

The current work proposes to account for this coupling in three ways. First, the plastic hardening parameters that describe yielding of the austenitic material are assumed to differ from those describing martensitic material, thus a change in phase affects a change in plastic yielding behavior. Secondly, a plastic *back stress* is introduced that results from plastic dislocations but also influences the transformation criteria, thus capturing the shift in critical transformation stress. Finally, an increase in accumulated plastic deformation is assumed to result in *retained martensite*, or martensite which cannot be converted back into austenite. This prevention of full transformation naturally results in the reduction of recovered transformation strain. These three coupling mechanisms have been captured in the model described herein.

B. Derivation of Coupled Constitutive Model

In this chapter, the initiations and evolutions of two distinct dissipative processes are considered. These processes, martensitic transformation and plastic slip, are the results of two different underlying physical mechanisms and they cause distinct thermomechanical material responses. The processes are coupled in their effects, especially the manner in which residual plastic deformation alters the transformation characteristics (the critical transformation temperatures and recoverable strain) in subsequent transformation cycles [82]. In addition to being discussed in the literature, this behavior was also observed during in-house experimental studies previously discussed.

A full 3-D thermomechanical model for these behaviors is summarized below. The relations describing the transformation behavior are derived in detail in Chapter II, and only altered or altogether new relations pertaining to plastic strain evolution are presented here. As with the model of Chapter II (transformation only),

the energies associated with material hardening, both for transformation and plastic yield, are formulated as internal variables with their own evolution equations. This again ensures that the free energy potential is a function only of the histories of the internal variables but not of their rates.

1. Formulation of specific Gibbs free energy potential

The derivation begins by assuming the same free energy potential as was used in Chapter II, though with a new form.

Assumption 1: The state of the material is described by a Gibbs free energy thermodynamic potential, which is decomposed into an austenitic, martensitic, and mixing contribution, and which is dependent on particular external and internal state variables.

Here we postulate that $G = G(\boldsymbol{\sigma}, T, \boldsymbol{\zeta}^t, \boldsymbol{\zeta}^p, \boldsymbol{\beta})$, where again the external state variables are the macroscopic stress $\boldsymbol{\sigma}$ and temperature T. In this new model, $\boldsymbol{\zeta}^t$ retains its meaning, while $\boldsymbol{\zeta}^p$ denotes the *plastic internal state variables*; each set $\boldsymbol{\zeta}^t$ and $\boldsymbol{\zeta}^p$ contains both scalars and tensors. For transformation, we again assume $\boldsymbol{\zeta}^t = \{\boldsymbol{\varepsilon}^t, \xi, g^t\}$ where each element in the set is as used in Chapter II, Section C.

For the newly considered process of plastic yield, we assume $\boldsymbol{\zeta}^p = \{\boldsymbol{\varepsilon}^p, g_A^p, g_M^p\}$ where each element in the set is described as follows: the *plastic strain* $\boldsymbol{\varepsilon}^p$ is the irrecoverable inelastic strain due to the generation and propagation of dislocations existing in either the martensitic or austenitic regions of the material, and the *plastic hardening energies* g_A^p and g_M^p measure the increase in the free energy due to isotropic hardening as plastic yield progresses in austenitic and martensitic regions, respectively. Such isotropic hardening is associated with dislocation entanglement (or the homogeneous dislocation "forest") [84]. The last internal variable included in

the formulation of G is the plastic *back stress* $\boldsymbol{\beta}$, which is key to the transformation-plastic yield coupling. This internal stress field accounts for forces generated due to pile-up of dislocations in a particular direction [84] and resulting incompatibility between yielded regions within the material [83]. Given these state variables, the Gibbs energy for the overall SMA material (austenite/martensite composite) considering plastic yielding is then written[5]:

$$\begin{aligned} G(\boldsymbol{\sigma}, T, \boldsymbol{\varepsilon}^t, \xi, g^t, \boldsymbol{\varepsilon}^p, g^p_A, g^p_M, \boldsymbol{\beta}) &= (1-\xi) G^A(\boldsymbol{\sigma}, T, \boldsymbol{\varepsilon}^p, g^p_A, \boldsymbol{\beta}) \\ &+ \quad \xi \quad G^M(\boldsymbol{\sigma}, T, \boldsymbol{\varepsilon}^p, g^p_M, \boldsymbol{\beta}) \\ &+ \qquad G^{mix}(\boldsymbol{\sigma}, \boldsymbol{\varepsilon}^t, g^t), \end{aligned} \tag{4.1}$$

where

$$\begin{aligned} G^\gamma(\boldsymbol{\sigma}, T, \boldsymbol{\varepsilon}^p, {g^p}_\gamma, \boldsymbol{\beta}) = -\tfrac{1}{2\rho}\boldsymbol{\sigma} : \boldsymbol{\mathcal{S}}^\gamma \boldsymbol{\sigma} - \tfrac{1}{\rho}(\boldsymbol{\sigma} - \boldsymbol{\beta}) : \boldsymbol{\varepsilon}^p + \tfrac{1}{\rho} {g^p}_\gamma - \tfrac{1}{2\rho K^\gamma_\beta}\boldsymbol{\beta} : \boldsymbol{\beta} \\ -\tfrac{1}{\rho}\boldsymbol{\sigma} : \boldsymbol{\alpha}(T - T_0) + c\left[(T - T_0) - T\ln\left(\tfrac{T}{T_0}\right)\right] - s^\gamma_0 T + u^\gamma_0 \end{aligned} \tag{4.2}$$

for $\gamma = A, M$. Each G^γ represents the Gibbs energy of a conventional elastoplastic material exhibiting kinematic hardening (e.g., elastoplastic austenite). The transformation is accounted for by the form of (4.1) and the energy of mixing accounting for the recoverable strain of transformation is given in (2.7). The energetic consequences of incompatibility between plastically deformed regions and transformation

[5]The following derivation relies on two assumptions that are subject to debate: *i*) that the total strain should be additively decomposed into parts, where each inelastic mechanism is represented by a different inelastic strain, and *ii*) that the free energy potential should admit as internal variables even those quantities that track irrecoverable processes and thus do not contribute to work upon unloading. Appendix E provides an alternative derivation methodology that includes neither of these assumptions and proposed an additive decomposition of the *rates* of irrecoverable strain measures.

regions is accounted for in the evolution of g^t. Most of the material constants (and the assumptions related to them) are unchanged from the model of Chapter II with the exception of K_β, which denotes the kinematic hardening modulus, assumed to be different for each phase.

2. Application of the laws of thermodynamics

Application of the first and second laws of thermodynamics via the Coleman-Noll procedure (see Chapter II, Section C.2) then gives the following for the total infinitesimal strain (the relation for entropy being identical to (2.16)):

$$\boldsymbol{\varepsilon} = -\rho\partial_{\boldsymbol{\sigma}} G = \boldsymbol{\mathcal{S}}(\xi) : \boldsymbol{\sigma} + \boldsymbol{\alpha}(T - T_0) + \boldsymbol{\varepsilon}^t + \boldsymbol{\varepsilon}^p. \tag{4.3}$$

Again rewriting this in terms of stress, we have for Hooke's law:

$$\boldsymbol{\sigma} = \boldsymbol{\mathcal{C}}\left[\boldsymbol{\varepsilon} - \boldsymbol{\alpha}(T - T_0) - \boldsymbol{\varepsilon}^t - \boldsymbol{\varepsilon}^p\right] = \boldsymbol{\mathcal{C}}\left[\boldsymbol{\varepsilon} - \boldsymbol{\varepsilon}^{th} - \boldsymbol{\varepsilon}^t - \boldsymbol{\varepsilon}^p\right]. \tag{4.4}$$

Note that material parameters $\boldsymbol{\mathcal{S}}$ and s_0 are again defined by the rule of mixtures with respect to the austenitic and martensitic phases (see Chapter II). The remaining dissipative terms resulting from application of the second law (Clausius-Planck inequality) consist of the partial derivatives of G with respect to each independent internal variable. Separated into transformation and plastic yield contributions, this is written

$$\begin{aligned} -\rho\left[\partial_\xi G\ \dot{\xi} + \partial_{\boldsymbol{\varepsilon}^t} G^{mix} : \dot{\boldsymbol{\varepsilon}}^t + \partial_{g^t} G^{mix}\dot{g}^t\right] \quad &+ \\ -\rho\Big[\left((1-\xi)\partial_{\boldsymbol{\varepsilon}^p} G^A + \xi\partial_{\boldsymbol{\varepsilon}^p} G^M\right) : \dot{\boldsymbol{\varepsilon}}^p \quad &+ \\ (1-\xi)\partial_{g^p_A} G^A\ \dot{g}^p_A + \xi\partial_{g^p_M} G^M\ \dot{g}^p_M\Big] - \rho\partial_{\boldsymbol{\beta}} G : \dot{\boldsymbol{\beta}} \quad &\geq 0. \end{aligned} \tag{4.5}$$

The derivation of the rate-independent constitutive model then continues based

on four additional major assumptions.

3. Evolution of internal variables

Assumption 2: The rates of the transformation internal state variables $\boldsymbol{\zeta}^t$ are proportional to the rate of the martensitic volume fraction, $\dot{\xi}$, and this rate alone. Likewise, the rates of the plastic internal state variables $\boldsymbol{\zeta}^p$ are proportional to the rate of the effective plastic strain, $\dot{\bar{\epsilon}}^p$, and this rate alone.

Here we postulate evolution equations for the three tensorial internal state variables $\boldsymbol{\varepsilon}^t$, $\boldsymbol{\varepsilon}^p$, and $\boldsymbol{\beta}$ and the three scalar internal variables g^t, g^p_A, and g^p_M in terms of the rates of the two scalar quantities ξ and $\bar{\epsilon}^p$, where $\bar{\epsilon}^p$ is a measure of the history of plastic strain evolution given as $\bar{\epsilon}^p = \int_{-\infty}^{t} \|\dot{\boldsymbol{\varepsilon}}^p\| d\tau$. Because the two processes can occur independently [62, 64], the postulated rate form of the evolution equations provides for the independence of these two sets of internal variables ($\boldsymbol{\zeta}^t$ and $\boldsymbol{\zeta}^p$). The flow law for the transformation strain is given in (2.20), while that proposed for the plastic strain is also consistent with the evolution equations (or "flow laws") commonly used in classical rate-independent plasticity with Mises-type (J_2-type) yield surfaces [129, 130] and is given as follows:

$$\dot{\boldsymbol{\varepsilon}}^p = \dot{\bar{\epsilon}}^p \boldsymbol{\Lambda}^p. \tag{4.6}$$

In the simultaneous phase transformation, two *effective stresses* are introduced (described shortly). Given this new net measure of stress, the transformation and plastic yield direction tensors are written as

$$\boldsymbol{\Lambda}^t = \begin{cases} H^{cur}(\bar{\sigma}_t^{eff}) \dfrac{3}{2} \dfrac{\boldsymbol{\sigma}_t^{eff\prime}}{\bar{\sigma}_t^{eff}} & ; \quad \dot{\xi} > 0 \\ \dfrac{\boldsymbol{\varepsilon}^{t-r}}{\xi^r} & ; \quad \dot{\xi} < 0 \end{cases} ; \qquad \boldsymbol{\Lambda}^p = \frac{3}{2} \frac{\boldsymbol{\sigma}_p^{eff\prime}}{\bar{\sigma}_p^{eff}}. \tag{4.7}$$

During forward transformation ($\dot{\xi} > 0$), both inelastic strains are assumed to evolve in the direction of the deviatoric part of the two *effective stresses*, $\boldsymbol{\sigma}_t^{eff}$ for the transformation strain and $\boldsymbol{\sigma}_p^{eff}$ for the plastic strain. The scalar term $\bar{\sigma}^{eff}$ denotes the *Mises equivalent* of the effective stress given. Specifically, the following definitions are used:

$$\begin{aligned} \boldsymbol{\sigma}_t^{eff} &= (\boldsymbol{\sigma} + \boldsymbol{\beta}) \quad ; \qquad & \boldsymbol{\sigma}_p^{eff} &= (\boldsymbol{\sigma} - \boldsymbol{\beta}); \\ \boldsymbol{\sigma}_t^{eff\prime} &= dev(\boldsymbol{\sigma}_t^{eff}) \quad ; \qquad & \boldsymbol{\sigma}_p^{eff\prime} &= dev(\boldsymbol{\sigma}_p^{eff}); \\ \bar{\sigma}_t^{eff} &= \sqrt{3/2\ \boldsymbol{\sigma}_t^{eff\prime} : \boldsymbol{\sigma}_t^{eff\prime}} \quad ; \qquad & \bar{\sigma}_p^{eff} &= \sqrt{3/2\ \boldsymbol{\sigma}_p^{eff\prime} : \boldsymbol{\sigma}_p^{eff\prime}}, \end{aligned} \tag{4.8}$$

where $\boldsymbol{\sigma}_p^{eff}$ is given a form consistent with classical plasticity while the form of $\boldsymbol{\sigma}_t^{eff}$, having an opposite sign, captures the phenomenological effects that plastic internal stresses have on subsequent transformation behavior (see Figure 29 and related discussion). The functional form of $H^{cur}(\bar{\sigma}_t^{eff})$ is given in (2.22). The reverse transformation form of $\boldsymbol{\Lambda}^t$ is unchanged from the transformation-only model of Chapter II.

The evolutions of the plastic hardening energies are given as follows:

$$\dot{g}_\gamma^p = \dot{\bar{\epsilon}}^p \left[(Y_m^\gamma - Y_0^\gamma)\left(1 - e^{-C_H \bar{\epsilon}^p}\right) - K_\beta^\gamma \bar{\epsilon}^p \right] = \dot{\bar{\epsilon}}^p f^p{}_\gamma, \tag{4.9}$$

where $\gamma = A, M$. Thus, at all times during plastic loading, the rate of increase in the plastic hardening energy is proportional to the rate of the effective plastic strain by the factor f_γ^p, which is phase-dependent. The plastic yield hardening is assumed to have an asymptotic exponential form as suggested in the literature [129]. The first term in (4.9) provides isotropic hardening of an exponential type where the asymptotic evolution of the monotonic loading response from an initial yield stress of Y_0 toward a plastic yield plateau at stress level Y_m is consistent with uniaxial experimental

observations. The second term preserves asymptotic yielding in the uniaxial sense (see Figure 28). The variation of the proposed material plastic properties (Y_m, Y_0, and K_β) with phase fraction introduces transformation-yield coupling into the model beyond the effects of $\boldsymbol{\beta}$ in (4.10) below.

The transformation hardening energy is influenced both by the progression of martensitic transformation as well as the presence of plastic back stress, and the form of its evolution is modified slightly from that given in (2.26), becoming

$$\dot{g}^t = \dot{\xi}\left[-\boldsymbol{\beta} : \boldsymbol{\Lambda}^t + f^t(\xi)\right]. \tag{4.10}$$

Thus, during transformation, the rate of increase in the transformation hardening energy is proportional to the rate of ξ by a factor which consists of a transformation-only part $f^t(\xi)$ and a coupled transformation-plastic yield part $(-\boldsymbol{\beta} : \boldsymbol{\Lambda}^t)$.

Assumption 3: The back stress $\boldsymbol{\beta}$ evolves during both phase transformation and plastic yield such that its rate is proportional to both the rate of the martensitic volume fraction, $\dot{\xi}$, and the rate of the plastic strain, $\dot{\boldsymbol{\varepsilon}}^p$.

For conventional plastic models with linear kinematic hardening, the rate of $\boldsymbol{\beta}$ is taken to be proportional to the rate of $\boldsymbol{\varepsilon}^p$ via the kinematic hardening modulus K_β, a constant in most materials [83]. Here the concept is simply extended for the two-phase material where the kinematic hardening modulus may vary during transformation, becoming a function of ξ. The conventional evolution equation for $\boldsymbol{\beta}$ is then generalized as follows:

$$\dot{\boldsymbol{\beta}} = \frac{d}{dt}\Big(K_\beta(\xi)\boldsymbol{\varepsilon}^p\Big). \tag{4.11}$$

This relation can be easily integrated such that $\boldsymbol{\beta}$ is explicitly a function of $\boldsymbol{\varepsilon}^p$ and ξ,

given as

$$\boldsymbol{\beta} = K_\beta(\xi)\boldsymbol{\varepsilon}^p + \boldsymbol{\beta}_0, \tag{4.12}$$

where $\boldsymbol{\beta}_0$ denotes an initial backstress in the reference configuration. This relation will serve as the definition of $\boldsymbol{\beta}$ throughout the remainder of this work; $\boldsymbol{\beta}$ is no longer treated as an independent variable.

Substituting the proposed evolution equations into the dissipative inequality (4.5) and utilizing the "$\sim$" notation such that $\tilde{f}^p = (f^p_M - f^p_A)$, we arrive at

$$\begin{aligned}\left[(\boldsymbol{\sigma}+\boldsymbol{\beta}) : \boldsymbol{\Lambda}^t - \rho\partial_\xi G - f^t\right]\dot{\xi} + \\ \left[(\boldsymbol{\sigma}-\boldsymbol{\beta}) : \boldsymbol{\Lambda}^p - ({f^p}_A + \xi\tilde{f}^p)\right]\dot{\bar{\epsilon}}^p \geq 0.\end{aligned} \tag{4.13}$$

4. Criteria for transformation and plastic yield

Assumption 4: The two processes of phase transformation and plastic yield are independently strongly dissipative. The Clausius-Duhem inequality is decomposed into two contributions, each being strictly positive during evolution of the associated internal variable.

$$\left[(\boldsymbol{\sigma}+\boldsymbol{\beta}) : \boldsymbol{\Lambda}^t - \rho\partial_\xi G - f^t\right]\dot{\xi} = \pi^t\dot{\xi} > 0 \quad \forall \quad \dot{\xi} \neq 0; \tag{4.14}$$

$$\left[(\boldsymbol{\sigma}-\boldsymbol{\beta}) : \boldsymbol{\Lambda}^p - (f^p_A + \xi\tilde{f}^p)\right]\dot{\epsilon}^p = \pi^p\dot{\bar{\epsilon}}^p > 0 \quad \forall \quad \dot{\bar{\epsilon}}^p > 0. \tag{4.15}$$

As discussed in Chapter II, Section C.4, the application of the laws of thermodynamics to the proposed free energy provides no further information beyond the equalities (2.16), (4.3), and the constraint (4.13). To continue, we again assume that a strict inequality is enforced [46]. Further, it has been postulated that some materials satisfy

an even stronger form of (4.13) such that each bracketed term must independently be non-negative [148][6].This is a sufficient condition to ensure that the total inequality will also be satisfied. The condition of independent non-negativity can be shown to be *necessary* given a loading path for which one of the two simultaneous processes abruptly ends (e.g., a path during which transformation completes). The proof of this is provided in Appendix F.

The term $\rho\partial_\xi G$ is an important term capturing many effects including the temperature dependence of the critical transformation stress. From (2.7), (4.1), and (4.2) it can be shown that

$$\rho\partial_\xi G = -\frac{1}{2}\boldsymbol{\sigma} : \widetilde{\boldsymbol{\mathcal{S}}}\boldsymbol{\sigma} - \rho\tilde{s}_0 T + \rho\tilde{u}_0 + \tilde{g^p} + \frac{1}{2}\tilde{\boldsymbol{\beta}} : \boldsymbol{\varepsilon}^p, \tag{4.16}$$

where $\tilde{g^p}$ can be evaluated in closed form from

$$\tilde{g^p} = \int_0^{\bar{\epsilon}^p} \tilde{f}^p(\epsilon)d\epsilon. \tag{4.17}$$

The two processes are assumed to begin only once the thermodynamic forces π^t and π^p reach critical levels $Y^t = Y_0^t + D\bar{\sigma}_t^{eff}$ (cf. (2.43)) and $Y^p = Y_0(\xi)$, respectively. Clearly, π^t must satisfy (4.14), while π^p satisfies (4.15). It is further assumed that these critical forces cannot be exceeded. This gives

$$-Y^t \leq \pi^t \leq Y^t, \qquad \pi^p \leq Y^p(\xi). \tag{4.18}$$

The equality of the thermodynamic forces to their respective critical levels during dissipation allows the definition of the transformation function Φ^t (previously

[6]It is worth noting that a similar assumption of independent dissipation was made in the original derivation of the Boyd-Lagoudas SMA model [37], though in a different context. In that work, both phase transformation and reorientation processes were considered (Section IV.2), and the dissipative terms from each of these were assumed to be independently non-negative.

given in (2.32)), and a new *plastic yield function* Φ^p. Combined with (4.18) and the constraint that the evolution of effective plastic strain be always positive (to ensure positive dissipation), these form the Kuhn-Tucker conditions on the evolution of the transformation process (see (2.32)) and the plastic process, given as

$$\dot{\overline{\epsilon}}^p \Phi^t = 0; \quad \dot{\overline{\epsilon}}^p \geq 0; \quad \Phi^p = \pi^p - Y^p \leq 0. \tag{4.19}$$

5. Effects of plasticity on the recovery of martensite

Assumption 5: The bounds on the martensitic volume fraction ξ are influenced by the increase in plastic deformation as measured by $\overline{\epsilon}^p$.

If we consider the bounds on ξ , then the lower bound is equivalent to the fraction of *retained martensite* or fraction of martensite which *cannot* be converted back into austenite (taken to be 0 when all martensite is recoverable), while the upper bound is equivalent to the maximum fraction of martensite which can be generated from austenite (usually taken to be 1). Here the increase in retained martensite due to increasing plastic yield [62, 67, 68, 81] is addressed. The *irrecoverable martensitic volume fraction*, denoted ξ_{irr}, represents this retained martensite and is postulated to be a function of the effective plastic strain such that increasing $\overline{\epsilon}^p$ up to and beyond some critical level $\overline{\epsilon}^p{}_{crit}$ drives ξ_{irr} from its initial value of 0 (all martensite is recoverable) to a final value of 1 (no martensite is recoverable). For simplicity, a linear relationship between ξ_{irr} and $\overline{\epsilon}^p$ is assumed, which is given as [62]

$$\xi_{irr} = \begin{cases} \dfrac{\overline{\epsilon}^p}{\overline{\epsilon}^p{}_{crit}} & ; \overline{\epsilon}^p < \overline{\epsilon}^p{}_{crit} \\ 1 & ; \overline{\epsilon}^p \geq \overline{\epsilon}^p{}_{crit} \end{cases} . \tag{4.20}$$

During reverse transformation, some martensite may be irrecoverable such that ξ is bounded from below, while during forward transformation, the material can be converted fully to martensite and the lower bound is inactive. These constraints are written

$$\xi_{irr} \leq \xi; \quad \dot{\xi} < 0, \tag{4.21}$$

$$\xi \leq 1; \quad \dot{\xi} > 0. \tag{4.22}$$

Note that the condition $\xi < \xi_{irr}$ is a meaningful possibility and must be accounted for (e.g., during the plastic yielding of pure austenite, during which $\xi = 0$ and $\xi_{irr}(\overline{\epsilon}^p) > 0$).

6. Reduction to 1-D form and calibration of parameters

Of the various relations specified for the coupled SMA transformation-plastic yield model, eight are sufficient to analyze the thermomechanical response of an SMA material point. These are as follows: Hooke's law (4.4), the evolution of transformation strain (2.20), the evolution of plastic strain (4.6), the evolution of transformation hardening energy (4.10), the evolution of plastic hardening energy (4.9), the definition of the plastic back stress (4.12), and the Kuhn-Tucker type conditions on transformation (2.32) and plastic yield (4.19). Given general three-dimensional loading, these combined yield 28 total equations for the 28 total unknowns ($\boldsymbol{\sigma}$, $\boldsymbol{\varepsilon}^t$, ξ, g^t,$\boldsymbol{\varepsilon}^p$, $\overline{\epsilon}^p$, g^p, and $\boldsymbol{\beta}$).

Here, as in Chapter II, Section C.5, we consider the calibration of the proposed model, where the model is fit to a known (experimental) material response and the various model parameters quantitatively specified. However, the consideration of plastic phenomena and the strong coupling between transformation and plastic yielding complicates the calibration, and proper methods are discussed below. To begin,

the new model is reduced to its 1-D form. Specifically, this gives:[7]

$$\boldsymbol{\sigma} \rightarrow \sigma_{11} = \sigma, \quad \boldsymbol{\sigma}_t^{eff} \rightarrow {\sigma_t^{eff}}_{11} = \sigma_t^{eff}, \quad \boldsymbol{\sigma}_p^{eff} \rightarrow {\sigma_p^{eff}}_{11} = \sigma_p^{eff},$$

$$\boldsymbol{\varepsilon} \rightarrow \varepsilon_{11} = \varepsilon, \quad \boldsymbol{\varepsilon}^t \rightarrow \varepsilon_{11}^t = \varepsilon^t, \quad \boldsymbol{\varepsilon}^p \rightarrow \varepsilon_{11}^p = \varepsilon^p, \quad \boldsymbol{\beta} \rightarrow \beta_{11} = \beta.$$

The relation between the current stress and strains is written in 1-D as

$$\sigma = E(\xi)\left[\varepsilon - \alpha(T - T_0) - \varepsilon^t - \varepsilon^p\right], \tag{4.23}$$

where the current Young's modulus is given in (2.34). The evolution equation for the transformation strain is given by

$$\dot{\varepsilon^t} = \dot{\xi}\Lambda^t; \quad \Lambda^t = \begin{cases} H^{cur}(\sigma_t^{eff})\mathrm{sgn}\,(\sigma_t^{eff}); & \dot{\xi} > 0 \\ \varepsilon^{t-r}/\xi^r; & \dot{\xi} < 0 \end{cases}, \tag{4.24}$$

while for plastic yield, it is given as

$$\dot{\varepsilon^p} = \dot{\bar{\epsilon}}^p \mathrm{sgn}\,(\sigma_p^{eff}). \tag{4.25}$$

The evolution of the transformation hardening energy is written in 1-D as

$$\dot{g}^t = \dot{\xi}\left[-\beta\Lambda^t + f^t(\xi)\right], \tag{4.26}$$

while the evolution for the plastic hardening energy is unchanged from (4.9). The 1-D plastic back stress is given by

$$\beta = K_\beta(\xi)\varepsilon^p + \beta_0. \tag{4.27}$$

Finally, to write out the transformation function, we use the form of $Y^t(\sigma_t^{eff})$, which

[7] In the special case of non-cyclic tensile loading, $\varepsilon^p = \bar{\epsilon}^p$. Similarly, in the case of non-cyclic compressive loading, $\varepsilon^p = -\bar{\epsilon}^p$.

is given in 1-D for the coupled transformation-plastic model as

$$Y^t(\sigma_t^{eff}) = Y_0^t + D\sigma_t^{eff}\Lambda^t. \tag{4.28}$$

We then write out the transformation function during forward transformation as

$$\begin{aligned}\Phi_{fwd}^t(\sigma, T, \xi, \bar{\epsilon}^p, \varepsilon^p) &= \left|\sigma_t^{eff}\right| H^{cur}(\sigma_t^{eff}) + \frac{1}{2}\left(\frac{1}{E^M} - \frac{1}{E^A}\right)\sigma^2 + \rho\tilde{s}_0 T - \rho\tilde{u}_0 \\ &- f_{fwd}^t(\xi) - \tilde{g}^p - \frac{1}{2}\tilde{\beta}\varepsilon^p - Y^t(\sigma_t^{eff}) = 0,\end{aligned} \tag{4.29}$$

while for reverse transformation it is given as

$$\begin{aligned}\Phi_{rev}^t(\sigma, T, \xi, \bar{\epsilon}^p, \varepsilon^p) &= -\sigma_t^{eff}\frac{\varepsilon^{t-r}}{\xi^r} - \frac{1}{2}\left(\frac{1}{E^M} - \frac{1}{E^A}\right)\sigma^2 - \rho\tilde{s}_0 T + \rho\tilde{u}_0 \\ &+ f_{rev}^t(\xi) + \tilde{g}^p + \frac{1}{2}\tilde{\beta}\varepsilon^p - Y^t(\sigma_t^{eff}) = 0.\end{aligned} \tag{4.30}$$

Likewise, the plastic yield function is written as

$$\Phi_{rev}^p(\sigma, \xi, \bar{\epsilon}^p, \varepsilon^p) = \left|\sigma_p^{eff}\right| - \left(f_A^p + \xi\tilde{f}^p\right) - Y_0(\xi) = 0. \tag{4.31}$$

The calibration of the following model parameters has already been addressed in Chapter II, Section C.5:

- the elastic moduli of martensite and austenite (E^M and E^A),
- the functional description of the maximum transformation strain ($H^{cur}(\sigma_t^{eff})$), and
- five additional model parameters ($\rho\tilde{s}_0$, $\rho\tilde{u}_0$, a_1, a_2, a_3) and the parameters Y_0^t and D in $Y^t(\sigma_t^{eff})$.

If these properties are calibrated from experiments in which no plastic strain has been generated, then the calibration methods are unchanged from Chapter II. However, if plastic strains exist in an SMA material prior to testing or are generated during

testing, the calibration of $\rho\tilde{s}_0$, $\rho\tilde{u}_0$, Y_0^t, and D must be reassessed. The maximum transformation strain $H^{cur}(\sigma_t^{eff})$ is easily calibrated using the methods of Chapter II, where the values of both σ and β must now be considered (per the definition of σ_t^{eff}).

To calibrate $\rho\tilde{u}_0$ and Y_0^t, we again consider the conditions under which the two transformations begin and end in a material that may or may not have previously undergone plastic deformations. We examine thermally-induced transformations occurring under zero *applied* stress conditions ($\sigma = 0$), but the possible existence of non-zero back stresses β complicates the calibration relative to Chapter II (i.e., $\sigma_t^{eff} \neq 0$). However, it is assumed that no further evolution in the plastic strain (and thus the back stress) occurs when the applied stress is null. The zero applied stress condition gives (cf. (2.38))

$$Y^t(0) = Y_0^t + D\,|\beta|\,. \tag{4.32}$$

We then consider the same five conditions described in Chapter II, Section C.5, and we find that the calibrations of a_1, a_2, and a_3 are unchanged. In addition, we find

$$\rho\tilde{u}_0 = \frac{\rho\tilde{s}_0}{2}(M_s + A_f) - \tilde{g}^p - \frac{1}{2}\tilde{\beta}\varepsilon^p, \quad Y_0^t = \frac{\rho\tilde{s}_0}{2}(M_s - A_f) - a_3 - D\,|\beta|\,.$$

Again, this calibration of $\rho\tilde{u}_0$ and Y_0^t depends on the condition that the plastic strain not evolve during a thermal cycle at zero applied stress.

Calibration of the remaining parameters ($\rho\tilde{s}_0$ and D) is again performed by considering the slope of the transformation surface in a uniaxial stress-temperature space as measured at reference stress level σ^*. The Kuhn-Tucker conditions (2.32) imply that both the transformation function Φ^t and its rate are zero-valued during transformation. However, for the new coupled model, Φ^t is also a function of the current plastic strain and its history. To use the remainder of the calibration methods

from Chapter II, Section C.5, (i.e., (2.40) and following), we must restrict ourselves to again considering only loading paths that do not cause an increase in plastic strain (i.e., $\mathrm{d}\bar{\varepsilon}^p = 0$). This is not a trivial restriction when constructing a phase diagram, which often extends into stress levels sufficient to cause yielding. Failure to follow this restriction, however, violates (2.40) and the developments that follow it. Therefore, when calibrating the coupled transformation-plastic yield model, one can only use phase diagrams generated from loading paths where plastic strain did not evolve. These include isobaric paths at stress levels below the yield limit and pseudoelastic paths where the maximum stress does not exceed the yield limit. Only in the case that this restriction is heeded, the calibration equations for $\rho\tilde{s}_0$ and D are unchanged.

In addition to the material properties related to the phase transformation, the plastic yielding properties must also be calibrated. Each can be derived from experimental data as follows:

- Y_0^A (initial yield stress, austenite): the stress at which pure austenite first deviates from linear elastic response due to *plastic yielding* (i.e., at temperatures where stress induced martensitic transformation is repressed; at $T > M_d$).

- Y_m^A (maximum yield stress, austenite): the maximum stress attainable in pure austenite given monotonic loading; the plateau stress. Must be due to *plastic yielding* (i.e., at $T > M_d$).

- Y_0^M (initial yield stress, martensite): the stress at which pure martensite first deviates from linear elastic response due to *plastic yielding* (i.e., material should first be fully reoriented in the loading direction such that observed "yielding" is not confused with shape memory behaviors).

- Y_m^M (maximum yield stress, martensite): the maximum stress attainable in

pure, *fully reoriented* martensite given monotonic loading; the plateau stress.

- C_H (plastic hardening coefficient): describes the rate (in terms of the effective plastic strain) that the monotonic stress response progresses from the initial yield stress to the maximum yield stress (single valued used for both austenite and martensite).

- $\boldsymbol{\beta}_0$ (plastic back stress in reference configuration): usually taken to be a zero matrix. Can be useful in modeling tension-compression asymmetry in the phase transformation response due to texturing (and therefore due to inherent plastic deformations). Careful assessment of the kinematic "shift" in the transformation surface is required for calibration of this constant tensor.

- $\overline{\epsilon}^p_{crit}$ (critical plastic strain for reverse transformation): the effective plastic strain level at which reverse transformation no longer occurs (usually linearly extrapolated from a comparison of lost transformation recovery vs. accumulated plastic strain, where lost recovery is often related to retained martensitic volume fraction via H^{cur}).

- K^A_β (kinematic hardening modulus of austenite) and K^M_β (kinematic hardening modulus of martensite): given the kinds of loading discussed in this dissertation (i.e., tension), these parameters were calibrated by considering the effect of plastic yield on the transformation criteria in subsequent cycles. Specifically, by considering how a given amount of plastic strain: *i*) increases the temperature needed to thermally induce reverse transformation (i.e., at constant zero applied stress), and *ii*) decreases the stress needed to induce forward transformation (i.e., at constant temperature), and then using (4.30) and (4.29), respectively, these parameters (and thus $\tilde{K}_\beta$) can be found.

7. Consideration of transformation and plastic yield surfaces

The major contribution of the new model is the ability to account for transformation and plasticity simultaneously and to further capture the effects that each inelastic process has on the other. The coupled evolution (size change and translation) of the transformation and plastic yield surfaces formed by the transformation and yield functions in a stress-temperature space allows these effects to be captured. To demonstrate this kinematic and isotropic coupling, the configuration of the transformation and yield surfaces assuming a plane-stress state are shown in Fig. 30. Here the horizontal stress axes are denoted σ_{11} and σ_{22} with temperature on the vertical axis. The start ($\xi = 0$) and finish ($\xi = 1$) bounds of the forward transformation surface are shown in blue and red, respectively, while the plastic surface is shown in gray. The conventional SMA phase diagram shown in Figure 30a is a 1-D reduction of the plane-stress case, where the axes have been rotated such that temperature is horizontal and stress (σ_{11}) is vertical. In agreement with the 1-D phase diagram, the transformation surfaces in the σ_{11}-σ_{22}-T space are tapered while the plastic yield surface is assumed to have no explicit dependence on temperature.

An example uniaxial loading path is considered at constant temperature ($T = A_s + 45\,^{\circ}\mathrm{C} = 145\,^{\circ}\mathrm{C}$), where A_s denotes the temperature at which transformation from martensite to austenite initiates at zero stress. This high temperature maintains the stability of austenite at stress levels exceeding the critical stress for plastic yield. Further loading beyond the initial plastic yield limit simultaneously transforms and plastically yields the material.

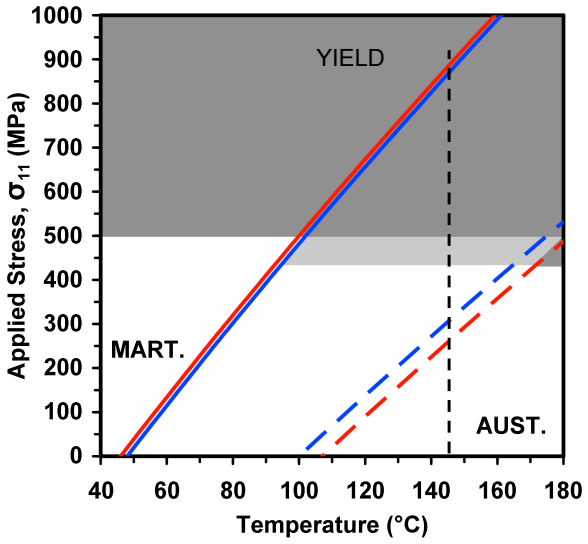

(a) Loading path plotted on a uniaxial stress-temperature phase diagram

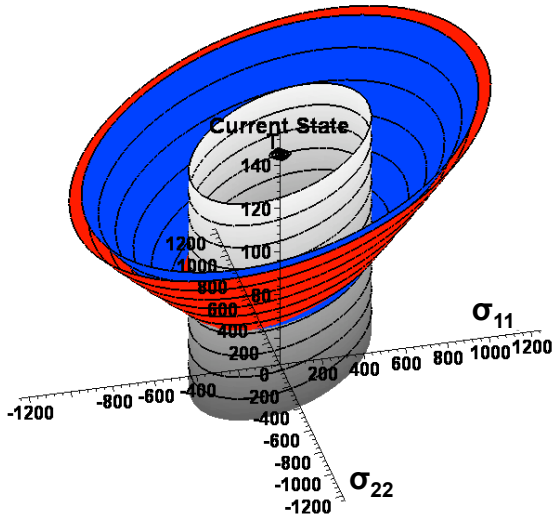

(b) $\sigma_{11} = 0\,\text{MPa}$, $\bar{\epsilon}^p = 0.0\%$, $\xi = 0\%$ (Initial condition)

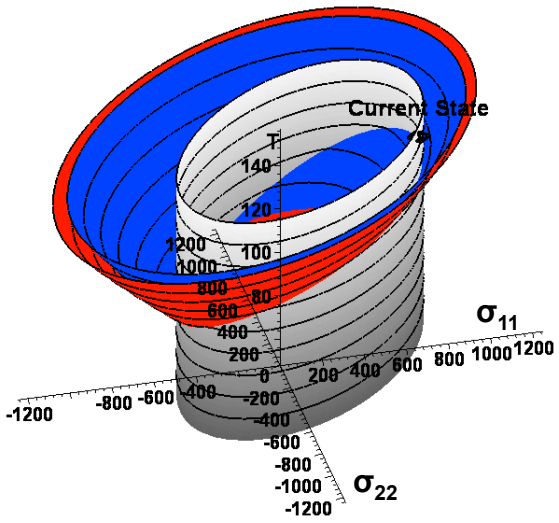

(c) $\sigma_{11} = 658\,\text{MPa}$, $\bar{\epsilon}^p = 0.6\%$, $\xi = 0\%$

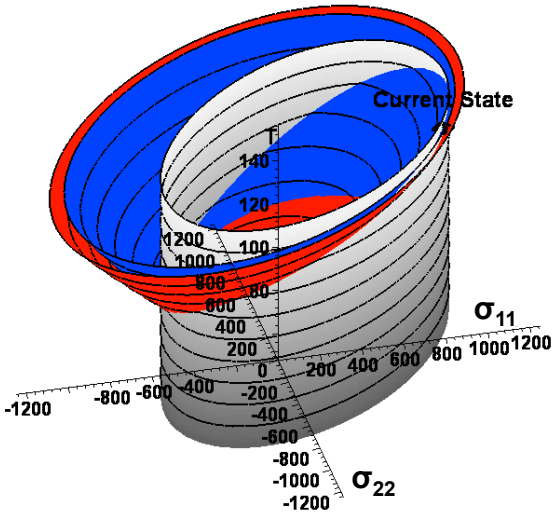

(d) $\sigma_{11} = 787\,\text{MPa}$, $\bar{\epsilon}^p = 0.9\%$, $\xi = 53\%$

Fig. 30. Configuration of the forward transformation and plastic yield surfaces in plane stress-temperature space during uniaxial tensile loading at $T = 145\,^{\circ}\text{C}$.

C. Numerical Implementation of the Coupled Model

Now we discuss the numerical implementation of the constitutive model derived in Section B. The algorithm follows from the derivations discussed previously in Chapter III, Section A, but the requirement of simultaneous evolution in the inelastic variables necessitates the consideration of additional details motivated in part by work on multisurface plasticity [129, 149]. These are described in detail, and a summary of the numerical implementation algorithm is provided.

1. Incremental solution scheme and the return mapping algorithm

As described in Chapter III, Section A, the solution of the constitutive relations can be accomplished via a predictor/corrector scheme where, for each loading step, purely thermoelastic relations are first used to calculate a possible solution based on the assumption that the inelastic strains are not evolving (a prediction). In this new transformation-plastic yield model, there are two inelastic strains and two associated inelastic phenomena that must be considered. If the constraints on the transformation function or plastic function are not violated ($\Phi^t \leq 0$ and $\Phi^p \leq 0$), the prediction is considered to be the true solution. Otherwise, the correction begins as applicable inelastic relations are iteratively applied to restore the Kuhn-Tucker conditions (i.e., to satisfy $\Phi^t = 0$ or $\Phi^p = 0$ or both to within some tolerance). Again, the convex cutting plane was chosen (see Chapter III, Section A.2 for a discussion of algorithmic options). The material in this section extends past work by providing the relations needed to account for the simultaneous evolution of transformation and plastic strains.

Following in the steps of Chapter III, Section A.3, the stress is computed for the current iteration of the current load increment from (4.4), giving

$$\boldsymbol{\sigma}_{n+1}^{(k+1)} = \boldsymbol{C}_{n+1}^{(k+1)} : [\boldsymbol{\varepsilon}_{n+1} - \boldsymbol{\varepsilon}^{th}{}_{n+1} - \boldsymbol{\varepsilon}^{t}{}_{n+1}^{(k+1)} - \boldsymbol{\varepsilon}^{p}{}_{n+1}^{(k+1)}]. \tag{4.33}$$

The algorithm begins at iteration (0) with a thermoelastic prediction assuming no evolution in the inelastic strains, or

$$\boldsymbol{\varepsilon}^{t}{}^{(0)}_{n+1} = \boldsymbol{\varepsilon}^{t}{}_{n}, \qquad \boldsymbol{\varepsilon}^{p}{}^{(0)}_{n+1} = \boldsymbol{\varepsilon}^{p}{}_{n}. \tag{4.34}$$

The transformation and plastic functions are calculated based on this prediction, and the constraints $\Phi^{t}{}^{(0)}_{n+1} \leq 0$ and $\Phi^{p}{}^{(0)}_{n+1} \leq 0$ are checked for violation. If no violation exists, the elastic solution is accepted as correct and is returned to the global solver. However, if one or both of the constraints is violated, correction of the solution via the return mapping algorithm will be applied. The explicit (iterative) discretization of the evolution equations (2.20), (4.6) and (4.9) gives[8]

$$\Delta\boldsymbol{\varepsilon}^{t}{}^{(k)}_{n+1} = \Delta\xi^{(k)}_{n+1}\boldsymbol{\Lambda}^{t}{}^{(k)}_{n+1}, \tag{4.35}$$

$$\Delta\boldsymbol{\varepsilon}^{p}{}^{(k)}_{n+1} = \Delta\bar{\epsilon}^{p}{}^{(k)}_{n+1}\boldsymbol{\Lambda}^{p}{}^{(k)}_{n+1}, \tag{4.36}$$

$$\Delta\tilde{g^{p}}{}^{(k)}_{n+1} = \Delta\bar{\epsilon}^{p}{}^{(k)}_{n+1}\tilde{f}^{p}{}^{(k)}_{n+1}. \tag{4.37}$$

During iterative correction, the total current strain and temperature are held constant such that

$$\Delta\boldsymbol{\varepsilon}^{(k)}_{n+1} = \mathbf{0}, \qquad \Delta T^{(k)}_{n+1} = 0.$$

Given these null increments, it can be shown [124], using (4.14), (2.32), (4.33), (4.35), and (4.36), that the increment in stress during correction is

$$\Delta\boldsymbol{\sigma}^{(k)}_{n+1} = \boldsymbol{\mathcal{C}}^{(k)}_{n+1}\left[\mp\left(\partial_{\boldsymbol{\sigma}}\Phi^{t}{}^{(k)}_{n+1} + D\boldsymbol{\Lambda}^{t}{}^{(k)}_{n+1}\right)\Delta\xi^{(k)}_{n+1} - \boldsymbol{\Lambda}^{p}{}^{(k)}_{n+1}\Delta\bar{\epsilon}^{p}{}^{(k)}_{n+1}\right]. \tag{4.38}$$

where the "$\mp$" corresponds to forward/reverse transformation, respectively.

---

[8]Note that here and in the developments that follow, both g^p_A and g^p_M could have been used separately. Because only the difference of these energies is needed in the formulations, $\tilde{g^p} = g^p_M - g^p_A$ is used for compactness.

To clearly illustrate their dependence on the solution-dependent variables, the transformation and yield functions given in (2.32) (while considering (4.16) and (4.14)) and (4.19) are written out as

$$\begin{aligned}\Phi^t(\boldsymbol{\sigma}, T, \xi, \boldsymbol{\varepsilon}^p, \tilde{g}^p) &= \pm\Big[(\boldsymbol{\sigma} + K_\beta(\xi)\boldsymbol{\varepsilon}^p) : \boldsymbol{\Lambda}^t(\boldsymbol{\sigma}, \xi, \boldsymbol{\varepsilon}^p) + \frac{1}{2}\boldsymbol{\sigma} : \widetilde{\boldsymbol{\mathcal{S}}}\boldsymbol{\sigma} + \rho\tilde{s}_0 T \\ &- \rho\tilde{u}_0 - \tilde{g}^p - \frac{1}{2}\tilde{K}_\beta\boldsymbol{\varepsilon}^p : \boldsymbol{\varepsilon}^p - f^t(\xi)\Big] \\ &- Y_0^t - D\,(\boldsymbol{\sigma} + K_\beta(\xi)\boldsymbol{\varepsilon}^p) : \boldsymbol{\Lambda}^t(\boldsymbol{\sigma}, \xi, \boldsymbol{\varepsilon}^p) = 0, \end{aligned} \tag{4.39}$$

$$\begin{aligned}\Phi^p(\boldsymbol{\sigma}, \xi, \overline{\epsilon}^p, \boldsymbol{\varepsilon}^p) &= \Big[(\boldsymbol{\sigma} - K_\beta(\xi)\boldsymbol{\varepsilon}^p) : \boldsymbol{\Lambda}^p(\boldsymbol{\sigma}, \xi, \boldsymbol{\varepsilon}^p) - f_A^p(\overline{\epsilon}^p) - \xi\tilde{f}^p(\overline{\epsilon}^p))\Big] \\ &- Y_0(\xi) = 0. \end{aligned} \tag{4.40}$$

The attempt to enforce the consistency condition for the transformation function $\Phi^t(\boldsymbol{\sigma}, T, \xi, \boldsymbol{\varepsilon}^p, \tilde{f}^p)$ and the plastic yield function $\Phi^p(\boldsymbol{\sigma}, \xi, \overline{\epsilon}^p, \boldsymbol{\varepsilon}^p)$ in the next iteration requires that

$$\Phi^{t^{(k)}}_{n+1} + \Delta\Phi^{t^{(k)}}_{n+1} = \Phi^{t^{(k+1)}}_{n+1} \simeq 0, \qquad \Phi^{p^{(k)}}_{n+1} + \Delta\Phi^{p^{(k)}}_{n+1} = \Phi^{p^{(k+1)}}_{n+1} \simeq 0. \tag{4.41}$$

Application of the chain rule to these two relations (where $\Delta T = 0$ during the corrector step) implies

$$\begin{aligned}&\Phi^{t^{(k)}}_{n+1} + \partial_{\boldsymbol{\sigma}}\Phi^{t^{(k)}}_{n+1} : \Delta\boldsymbol{\sigma}^{(k)}_{n+1} + \partial_\xi\Phi^{t^{(k)}}_{n+1}\Delta\xi^{(k)}_{n+1} + \\ &\partial_{\boldsymbol{\varepsilon}^p}\Phi^{t^{(k)}}_{n+1} : \Delta\boldsymbol{\varepsilon}^{p^{(k)}}_{n+1} + \partial_{\tilde{g}^p}\Phi^{t^{(k)}}_{n+1}\Delta\tilde{g}^{p^{(k)}}_{n+1} \simeq 0, \end{aligned} \tag{4.42}$$

$$\begin{aligned}&\Phi^{p^{(k)}}_{n+1} + \partial_{\boldsymbol{\sigma}}\Phi^{p^{(k)}}_{n+1} : \Delta\boldsymbol{\sigma}^{(k)}_{n+1} + \partial_\xi\Phi^{p^{(k)}}_{n+1}\Delta\xi^{(k)}_{n+1} + \\ &\partial_{\overline{\epsilon}^p}\Phi^{p^{(k)}}_{n+1}\Delta\overline{\epsilon}^{p^{(k)}}_{n+1} + \partial_{\boldsymbol{\varepsilon}^p}\Phi^{p^{(k)}}_{n+1} : \Delta\boldsymbol{\varepsilon}^{p^{(k)}}_{n+1} \simeq 0. \end{aligned} \tag{4.43}$$

Substituting the discretized evolution equations (4.35), (4.36), and (4.37) and

the stress increment (4.38) into (4.42), we find

$$\Phi^{t(k)}_{n+1} - \partial_{\boldsymbol{\sigma}}\Phi^{t(k)}_{n+1} : \boldsymbol{\mathcal{C}}^{(k)}_{n+1}\left[\pm\left(\partial_{\boldsymbol{\sigma}}\Phi^{t(k)}_{n+1} + D\boldsymbol{\Lambda}^{t(k)}_{n+1}\right)\Delta\xi^{(k)}_{n+1} + \boldsymbol{\Lambda}^{p(k)}_{n+1}\Delta\overline{\epsilon}^{p(k)}_{n+1}\right] + \partial_{\xi}\Phi^{t(k)}_{n+1}\Delta\xi^{(k)}_{n+1} + \left[\partial_{\boldsymbol{\varepsilon}^p}\Phi^{t(k)}_{n+1} : \boldsymbol{\Lambda}^{p(k)}_{n+1} + \partial_{\tilde{g}^p}\Phi^{t(k)}_{n+1}\tilde{f}^{p(k)}_{n+1}\right]\Delta\overline{\epsilon}^{p(k)}_{n+1} \simeq 0. \quad (4.44)$$

Likewise, substituting the discretized evolution equations (4.35) and (4.36) and the stress increment (4.38) into (4.43), we find

$$\Phi^{p(k)}_{n+1} - \partial_{\boldsymbol{\sigma}}\Phi^{p(k)}_{n+1} : \boldsymbol{\mathcal{C}}^{(k)}_{n+1}\left[\pm\left(\partial_{\boldsymbol{\sigma}}\Phi^{t(k)}_{n+1} + D\boldsymbol{\Lambda}^{t(k)}_{n+1}\right)\Delta\xi^{(k)}_{n+1} + \boldsymbol{\Lambda}^{p(k)}_{n+1}\Delta\overline{\epsilon}^{p(k)}_{n+1}\right] + \partial_{\xi}\Phi^{p(k)}_{n+1}\Delta\xi^{(k)}_{n+1} + \left[\partial_{\overline{\epsilon}^p}\Phi^{p(k)}_{n+1} + \partial_{\boldsymbol{\varepsilon}^p}\Phi^{p(k)}_{n+1} : \boldsymbol{\Lambda}^{p(k)}_{n+1}\right]\Delta\overline{\epsilon}^{p(k)}_{n+1} \simeq 0. \quad (4.45)$$

The required partial derivatives of the transformation function can be evaluated using (4.39) while considering the definitions provided in Section B, resulting in the following for Φ^t:

$$\partial_{\boldsymbol{\sigma}}\Phi^t = \pm\left(\boldsymbol{\Lambda}^t + \frac{1}{2}\widetilde{\boldsymbol{\mathcal{S}}}\boldsymbol{\sigma}\right) - D\boldsymbol{\Lambda}^t; \quad \partial_{\xi}\Phi^t = (\pm 1 - D)\tilde{K}_{\beta}\boldsymbol{\Lambda}^t : \boldsymbol{\varepsilon}^p \mp \partial_{\xi}f^t(\xi);$$

$$\partial_{\boldsymbol{\varepsilon}^p}\Phi^t = (\pm 1 - D)K_{\beta}(\xi)\boldsymbol{\Lambda}^t \mp \tilde{K}_{\beta}\boldsymbol{\varepsilon}^p; \quad \partial_{\tilde{g}^p}\Phi^t = \mp 1.$$

Likewise, for Φ^p we use (4.40) and the definitions of Section B to obtain the following:

$$\partial_{\boldsymbol{\sigma}}\Phi^p = \boldsymbol{\Lambda}^p; \quad \partial_{\xi}\Phi^p = -\tilde{K}_{\beta}\boldsymbol{\Lambda}^p : \boldsymbol{\varepsilon}^p - \tilde{f}^p(\overline{\epsilon}^p) - \tilde{Y}_0;$$

$$\partial_{\overline{\epsilon}^p}\Phi^p = -\partial_{\overline{\epsilon}^p}\left(f^p_A(\overline{\epsilon}^p) + \xi\tilde{f}^p(\overline{\epsilon}^p)\right); \quad \partial_{\boldsymbol{\varepsilon}^p}\Phi^p = -K_{\beta}(\xi)\boldsymbol{\Lambda}^p.$$

Solving (4.44) for the correction in ξ at the given iteration yields

$$\Delta\xi^{(k)}_{n+1} = \frac{-\Phi^{t(k)}_{n+1} + A^t_1\Delta\overline{\epsilon}^{p(k)}_{n+1}}{A^t_2}, \quad (4.46)$$

where

$$A_1^t = \partial_{\boldsymbol{\sigma}} \Phi^{t(k)}_{\ n+1} : \boldsymbol{\mathcal{C}}^{(k)}_{n+1} \boldsymbol{\Lambda}^{p(k)}_{\ n+1} - \partial_{\boldsymbol{\varepsilon}^p} \Phi^{t(k)}_{\ n+1} : \boldsymbol{\Lambda}^{p(k)}_{\ n+1} - \partial_{\tilde{g}^p} \Phi^{t(k)}_{\ n+1} \tilde{f}^{p(k)}_{\ n+1};$$
$$A_2^t = \partial_{\xi} \Phi^{t(k)}_{\ n+1} \mp \partial_{\boldsymbol{\sigma}} \Phi^{t(k)}_{\ n+1} : \boldsymbol{\mathcal{C}}^{(k)}_{n+1} \left(\partial_{\boldsymbol{\sigma}} \Phi^{t(k)}_{\ n+1} + D\boldsymbol{\Lambda}^{t(k)}_{\ n+1} \right). \tag{4.47}$$

Note that if the constraint on Φ^p has not been violated (transformation only case), this relation (4.46) with $\Delta\overline{\epsilon}^{p(k)}_{\ n+1} = 0$ is used to apply the RMA to the evolution of $\{\xi, \boldsymbol{\varepsilon}^t\}$ while $\{\overline{\epsilon}^p, \boldsymbol{\varepsilon}^p\}$ remain constant. Likewise rearranging (4.45) to find the plastic increment gives

$$\Delta\overline{\epsilon}^{p(k)}_{\ n+1} = \frac{-\Phi^{p(k)}_{\ n+1} + A_1^p \Delta\xi^{(k)}_{n+1}}{A_2^p}. \tag{4.48}$$

where

$$A_1^p = \pm\partial_{\boldsymbol{\sigma}} \Phi^{p(k)}_{\ n+1} : \boldsymbol{\mathcal{C}}^{(k)}_{n+1} \left(\partial_{\boldsymbol{\sigma}} \Phi^{t(k)}_{\ n+1} + D\boldsymbol{\Lambda}^{t(k)}_{\ n+1} \right) - \partial_{\xi} \Phi^{p(k)}_{\ n+1};$$
$$A_2^p = \partial_{\overline{\epsilon}^p} \Phi^{p(k)}_{\ n+1} - \partial_{\boldsymbol{\sigma}} \Phi^{p(k)}_{\ n+1} : \boldsymbol{\mathcal{C}}^{(k)}_{n+1} \boldsymbol{\Lambda}^{p(k)}_{\ n+1} + \partial_{\boldsymbol{\varepsilon}^p} \Phi^{p(k)}_{\ n+1} : \boldsymbol{\Lambda}^{p(k)}_{\ n+1}. \tag{4.49}$$

This relation (4.48) with $\Delta\xi^{(k)}_{n+1} = 0$ is used directly when only plastic yield is occurring.

Solving the two equations (4.46) and (4.48) for the two unknowns $\Delta\xi^{(k)}_{n+1}$ and $\Delta\overline{\epsilon}^{p(k)}_{\ n+1}$, we arrive at the final form for calculating the simultaneous inelastic corrections for the transformation and plastic yielding processes. This correction is given for transformation as

$$\Delta\xi^{(k)}_{n+1} = \frac{-\Phi^{t(k)}_{\ n+1} A_2^p - \Phi^{p(k)}_{\ n+1} A_1^t}{A_2^t A_2^p - A_1^t A_1^p}, \tag{4.50}$$

while for plastic yielding, the simultaneous correction is given as

$$\Delta\overline{\epsilon}^{p(k)}_{\ n+1} = \frac{-\Phi^{p(k)}_{\ n+1} A_2^t - \Phi^{t(k)}_{\ n+1} A_1^p}{A_2^t A_2^p - A_1^t A_1^p}. \tag{4.51}$$

It is important to recall that transformation ends when $\xi^{(k+1)}_{n+1}$ reaches one of two

limits during the iterative scheme within a single loading increment. Specifically

$$\begin{array}{lll} \xi_{irr} \leq \xi_{n+1}^{(k)} & ; & \dot{\xi} < 0 \\ \xi_{n+1}^{(k)} \leq 1 & ; & \dot{\xi} > 0 \end{array} . \tag{4.52}$$

Therefore, the implemented algorithm must allow a switch from (4.51) to (4.48) when $\xi_{n+1}^{(k)}$ reaches a bound, implying $\Delta\xi_{n+1}^{(k)} = 0$.

Given these increments in the scalar measures of the two inelastic strains, we can update the inelastic strains $\boldsymbol{\varepsilon}^t$ and $\boldsymbol{\varepsilon}^p$ using (2.20) and (4.6), which yields.

$$\boldsymbol{\varepsilon}^{t}{}_{n+1}^{(k+1)} = \boldsymbol{\varepsilon}^{t}{}_{n+1}^{(k)} + \Delta\xi_{n+1}^{(k)} \boldsymbol{\Lambda}^{t}{}_{n+1}^{(k)}, \qquad \boldsymbol{\varepsilon}^{p}{}_{n+1}^{(k+1)} = \boldsymbol{\varepsilon}^{p}{}_{n+1}^{(k)} + \Delta\overline{\epsilon}^{p}{}_{n+1}^{(k)} \boldsymbol{\Lambda}^{p}{}_{n+1}^{(k)}. \tag{4.53}$$

These two inelastic strains and the updated elastic stiffness are used in (4.33) to calculate an updated stress, which is itself used to calculate the updated transformation and yield functions. The iterative scheme then continues until $\Phi^{t}{}_{n+1}^{(k+1)}$ and $\Phi^{p}{}_{n+1}^{(k+1)}$ are smaller than some tolerance.

2. Continuum tangent modulus

As discussed in Chapter III, Section A.4, an FEA implementation of non-linear constitutive equations requires the evaluation of the tangent modulus which defines the current rate of change of stress with a change in total strain, and that the convex cutting plane algorithm requires the continuum tangent modulus. The derivation of the simultaneous continuum tangent modulus proceeds as described in Chapter III, Section 4 with the additional requirement that $\mathrm{d}\xi$ and $\mathrm{d}\overline{\epsilon}^p$ both be found simultaneously. This is accomplished in a manner analogous to the derivation of (4.50) and (4.51) above, where two equations must be solved for two unknowns $\mathrm{d}\xi$ and $\mathrm{d}\overline{\epsilon}^p$.

To begin, the constitutive relation (4.3) is rewritten in differential form and the evolution equations (2.20) and (4.6) are substituted. Rewriting in terms of stress,

this gives (cf. (4.38))

$$\mathrm{d}\boldsymbol{\sigma} = \boldsymbol{\mathcal{C}} : \left[\mathrm{d}\boldsymbol{\varepsilon} - \boldsymbol{\alpha}\, \mathrm{d}T \mp \mathrm{d}\xi \left(\partial_{\boldsymbol{\sigma}} \Phi^t + D\boldsymbol{\Lambda}^t \right) - \mathrm{d}\bar{\epsilon}^p\, \boldsymbol{\Lambda}^p \right]. \tag{4.54}$$

Both the transformation function (2.32) and the plastic yield function (4.19) must be satisfied for all acceptable solutions, and taking the differential of these relations at a specified constant temperature ($\mathrm{d}T = 0$) results in two relations ("consistency conditions")

$$\begin{aligned} \mathrm{d}\Phi^t &= \partial_{\boldsymbol{\sigma}} \Phi^t : \mathrm{d}\boldsymbol{\sigma} + \partial_\xi \Phi^t \, \mathrm{d}\xi = 0, \\ \mathrm{d}\Phi^p &= \partial_{\boldsymbol{\sigma}} \Phi^p : \mathrm{d}\boldsymbol{\sigma} + \partial_{\bar{\epsilon}^p} \Phi^p \, \mathrm{d}\bar{\epsilon}^p = 0. \end{aligned} \tag{4.55}$$

Expressions for the differential of the rate of effective plastic strain $\mathrm{d}\bar{\epsilon}^p$ and the martensitic volume fraction $\mathrm{d}\xi$ are obtained by substituting $\mathrm{d}\boldsymbol{\sigma}$ from (4.54) into (4.55). Noting the form of Φ^t and Φ^p and the definitions of A_1^t and A_2^t as given in (4.47) and of A_1^p and A_2^p as given in (4.49), this gives

$$\mathrm{d}\bar{\epsilon}^p = \frac{-\partial_{\boldsymbol{\sigma}} \Phi^p : \boldsymbol{\mathcal{C}}\, \mathrm{d}\boldsymbol{\varepsilon} + A_1^p \, \mathrm{d}\xi}{A_2^p}, \tag{4.56}$$

$$\mathrm{d}\xi = \frac{-\partial_{\boldsymbol{\sigma}} \Phi^t : \boldsymbol{\mathcal{C}}\, \mathrm{d}\boldsymbol{\varepsilon} + A_1^t \, \mathrm{d}\bar{\epsilon}^p}{A_2^t}. \tag{4.57}$$

Solving the two equations (4.56) and (4.57) for the two unknowns $\mathrm{d}\xi$ and $\mathrm{d}\bar{\epsilon}^p$, we find for transformation

$$\mathrm{d}\xi = \frac{-A_2^p \partial_{\boldsymbol{\sigma}} \Phi^t : \boldsymbol{\mathcal{C}}\, \mathrm{d}\boldsymbol{\varepsilon} - A_1^t \partial_{\boldsymbol{\sigma}} \Phi^p : \boldsymbol{\mathcal{C}}\, \mathrm{d}\boldsymbol{\varepsilon}}{A_2^t A_2^p - A_1^t A_1^p}, \tag{4.58}$$

while for plastic yielding, the differential is given as

$$\mathrm{d}\bar{\epsilon}^p = \frac{-A_2^t \partial_{\boldsymbol{\sigma}} \Phi^p : \boldsymbol{\mathcal{C}}\, \mathrm{d}\boldsymbol{\varepsilon} - A_1^p \partial_{\boldsymbol{\sigma}} \Phi^t : \boldsymbol{\mathcal{C}}\, \mathrm{d}\boldsymbol{\varepsilon}}{A_2^t A_2^p - A_1^t A_1^p}, \tag{4.59}$$

Now (4.58) and (4.59) can be used to eliminate $\mathrm{d}\xi$ and $\mathrm{d}\bar{\epsilon}^p$, respectively, in (4.54),

giving

$$\begin{aligned} \mathrm{d}\boldsymbol{\sigma} = \boldsymbol{\mathcal{C}}\,\mathrm{d}\boldsymbol{\varepsilon} \quad &\pm \quad \boldsymbol{\mathcal{C}}\left[\frac{A_2^p \partial_{\boldsymbol{\sigma}}\Phi^t : \boldsymbol{\mathcal{C}}\,\mathrm{d}\boldsymbol{\varepsilon} \; + A_1^t \partial_{\boldsymbol{\sigma}}\Phi^p : \boldsymbol{\mathcal{C}}\,\mathrm{d}\boldsymbol{\varepsilon}}{A_2^t A_2^p - A_1^t A_1^p} \; \left(\partial_{\boldsymbol{\sigma}}\Phi^t + D\boldsymbol{\Lambda}^t\right)\right] \\ &+ \quad \boldsymbol{\mathcal{C}}\left[\frac{A_2^t \partial_{\boldsymbol{\sigma}}\Phi^p : \boldsymbol{\mathcal{C}}\,\mathrm{d}\boldsymbol{\varepsilon} \; + A_1^p \partial_{\boldsymbol{\sigma}}\Phi^t : \boldsymbol{\mathcal{C}}\,\mathrm{d}\boldsymbol{\varepsilon}}{A_2^t A_2^p - A_1^t A_1^p} \; \boldsymbol{\Lambda}^p\right]. \end{aligned} \tag{4.60}$$

By applying the definition and identities related to the tensor product (see footnote in Chapter III, Section A.4), this can be rearranged to find the continuum tangent modulus, given by $\boldsymbol{\mathcal{L}}$ per

$$\begin{aligned} \mathrm{d}\boldsymbol{\sigma} \;&=\; \left\{\boldsymbol{\mathcal{C}} + \frac{A_2^t \mathbf{B}_1^p \otimes \mathbf{B}_2^p + A_1^p \mathbf{B}_1^p \otimes \mathbf{B}_2^t \pm \left[A_2^p \mathbf{B}_1^t \otimes \mathbf{B}_2^t + A_1^t \mathbf{B}_1^t \otimes \mathbf{B}_2^p\right]}{A_2^t A_2^p - A_1^t A_1^p}\right\} \mathrm{d}\boldsymbol{\varepsilon} \\ &=\; \boldsymbol{\mathcal{L}}\,\mathrm{d}\boldsymbol{\varepsilon}\,, \end{aligned} \tag{4.61}$$

where the second-order tensors $\mathbf{B}_1^t$, $\mathbf{B}_2^t$, $\mathbf{B}_1^p$, and $\mathbf{B}_2^p$ are defined as

$$\mathbf{B}_1^t = \boldsymbol{\mathcal{C}}\left(\partial_{\boldsymbol{\sigma}}\Phi^t + D\boldsymbol{\Lambda}^t\right); \quad \mathbf{B}_2^t = \boldsymbol{\mathcal{C}}\partial_{\boldsymbol{\sigma}}\Phi^t; \quad \mathbf{B}_1^p = \boldsymbol{\mathcal{C}}\boldsymbol{\Lambda}^p; \quad \mathbf{B}_2^p = \boldsymbol{\mathcal{C}}\partial_{\boldsymbol{\sigma}}\Phi^p. \tag{4.62}$$

In the case of phase transformation only (i.e., $\mathrm{d}\bar{\epsilon}^p = 0$), the continuum tangent modulus $\boldsymbol{\mathcal{L}}$ is given by (cf. Chapter III, Section A.4):

$$\boldsymbol{\mathcal{L}} = \boldsymbol{\mathcal{C}} + \frac{\mathbf{B}_1^t \otimes \mathbf{B}_2^t}{A_2^t}. \tag{4.63}$$

Likewise, in the case of plastic yielding only (i.e., $\Phi^t \leq 0$), the tangent modulus is given by

$$\boldsymbol{\mathcal{L}} = \boldsymbol{\mathcal{C}} + \frac{\mathbf{B}_1^p \otimes \mathbf{B}_2^p}{A_2^p}. \tag{4.64}$$

3. Algorithmic considerations of plastic yield in SMAs

The implementation of a SMA transformation-plastic yield model presents challenges beyond the calculation of the simultaneous and coupled evolution in the two inelastic strains $\boldsymbol{\varepsilon}^t$ and $\boldsymbol{\varepsilon}^p$. The algorithm must also consider the meaningfulness of the calcu-

lated increments. In particular, the sign of the scalar internal variable increments, the bounds on the martensitic volume fraction, and simultaneous vs. non-simultaneous evolution of the variables must all be considered.

The first consideration is common to all rate-independent plasticity models which consider multiple "yield" surfaces governing the evolution of multiple "plastic" internal variables (see [149] and especially [129], Sect. 5.2, remarks 5.21). the model of the current work is a member of this class, especially in the context of pseudoelastic loading. For such models implemented using an elastic predictor-corrector scheme, it is possible that, at some states and given some total strain increments, the converged solution from the corrector step will include a non-physical increment in one of the two inelastic strains (e.g., $\Delta\overline{\epsilon}^{p}{}_{n+1} < 0$ or $\Delta\xi_{n+1} < 0$ for forward transformation).

As an illustration, consider a material point at pseudoelastic loading step n with stress state $\boldsymbol{\sigma}_n$ that is undergoing transformation but is not yielding ($\Phi^{t}{}_{n} = 0, \quad \Phi^{p}{}_{n} < 0$). A schematic graphical representation is provided in Fig. 31. At loading step $n+1$, assume that the true stress solution $\boldsymbol{\sigma}_{n+1}$ is such that the point continues to transform without yielding (Fig. 31a: $\Phi^{t}{}_{n} = 0, \quad \Phi^{p}{}_{n} < 0, \quad \Delta\xi_{n+1} > 0, \quad \Delta\overline{\epsilon}^{p}{}_{n+1} = 0$). The plastic increment is zero-vaued. However, as a solution methodology, the return mapping algorithm requires an initial elastic prediction $\boldsymbol{\sigma}_{n+1}$ for step $n+1$ that may violate both surfaces (Fig. 31b: $\Phi^{t(0)}_{n+1} > 0, \quad \Phi^{p(0)}_{n+1} > 0$). This is possible if the stress state of the material point at step n is sufficiently close to the plastic yield surface. Given the predicted violation of *both* surfaces, the iterative use of the correction equations of Section C.1, particularly (4.50), (4.51), and (4.53), will result in the calculation of nonzero increments in both ξ and $\overline{\epsilon}^{p}$ (and thus $\boldsymbol{\epsilon}^{t}$ and $\boldsymbol{\epsilon}^{p}$). Convergence will occur as both surfaces and the stress state evolve to satisfy the consistency condition, and in this example, the plastic surface *contracts* unreasonably. In this way, the elastic predictor-corrector scheme computes a physically unreasonable

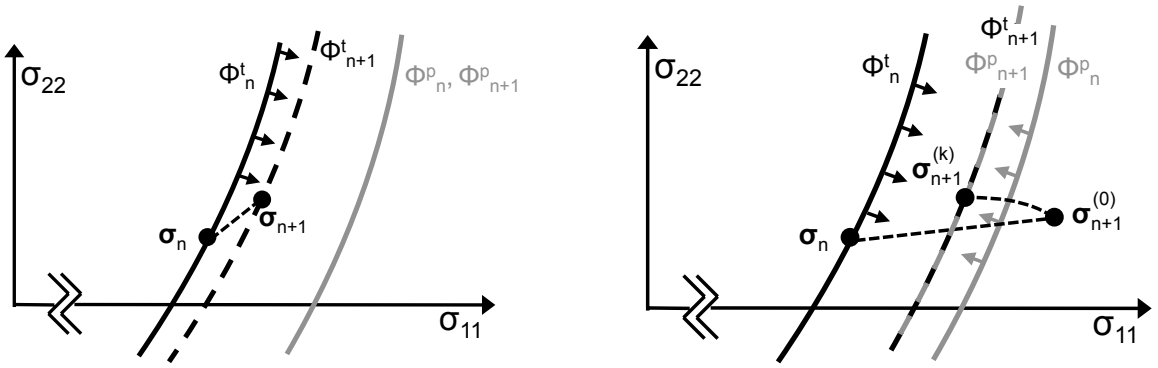

(a) True solution (Transformation progresses, plastic yield does not)

(b) Incorrect RMA solution (Plastic yield function progresses in unreasonable direction)

Fig. 31. Schematic illustration showing the possible erroneous application of the simultaneous transformation-plastic RMA leading to non-physical evolution in the internal variables.

evolution in internal variables and thus an incorrect solution.

It is a convenient (though ultimately necessary) feature of the algorithm that the incorrectly calculated increments will always have a physically unreasonable sign (e.g., $\Delta\overline{\epsilon}^{p}{}_{n+1} < 0$ or $\Delta\xi_{n+1} < 0$ during forward loading). The signs of these increments must be used as checks to determine if the solution, though converged, is incorrect. If $\Delta\overline{\epsilon}^{p} < 0$, the correct solution is determined by starting the algorithm over from the beginning but applying only (4.46) with $\Delta\overline{\epsilon}^{p(k)}_{n+1} = 0$. Likewise, if the sign of $\Delta\xi$ is incorrect based on the transformation direction at the beginning of the loading step, the plastic strain alone is evolved using (4.48) with $\Delta\xi^{(k)}_{n+1} = 0$.

The second algorithmic consideration involves the lower bounds on ξ as discussed in Sect. B. In conventional SMA modeling, $0 \leq \xi \leq 1$ at all times, while for the current model it is postulated that the dislocations associated with plastic deformation can impede the recovery of martensite, and therefore that the irrecoverable marten-

sitic volume fraction ξ_{irr} is functionally dependent on the amount of plastic strain in the material (i.e., $\xi_{irr}(\overline{\epsilon}^p)$). This implies that during reverse transformation ($\dot{\xi} < 0$), the corrector portion of the RMA is active only until $\xi \leq \xi_{irr}$, at which point transformation ends, $\xi = \xi_{irr}$ is enforced, and only the elastoplastic solution is calculated. However, during forward transformation this new lower bound cannot be active. This is made obvious by considering the example of pseudoelastic-type loading applied to a material at a constant temperature sufficiently high such that plastic yield initiates prior to stress-induced transformation. As the amount of plastic strain increases, the predicted irrecoverable martensitic volume fraction also increases per $\xi_{irr}(\overline{\epsilon}^p)$. However, prior to the initiation of transformation, $\xi = 0$. Clearly the lower bound of ξ does not evolve.

A third consideration is related to the solution algorithm when the martensitic volume fraction reaches its limit (i.e., increases to 1 or decreases to ξ_{irr}). This issue is straightforward and was previously discussed. In brief, it will commonly happen that after some iteration during the corrector algorithm, ξ will reach one of the two bounds (upper or lower), depending on the direction of transformation. If only transformation is occurring, the corrector algorithm is simply halted, ξ is set to the appropriate bound, and the solution is returned to the global solver. If, however, simultaneous processes are being considered ($\dot{\xi} \neq 0$, $\dot{\overline{\epsilon}}^p \neq 0$), and if the plastic yield function has not converged to ≈ 0, then two things must happen. First, the martensitic volume fraction must be set to the appropriate bound as before. Additionally, the plastic correction iterations must continue, though a switch *must* be made from the corrective relation (4.51) to the correction given in (4.48), with $\Delta\xi = 0$. Failure to make this alteration while constraining ξ to the value of the appropriate bound will lead to convergence difficulties.

4. Summary of implementation

Table IV provides a summary of the full RMA (convex cutting plane) needed to integrate the constitutive relations for the transformation-plastic yield model in an FEA framework while considering large rotations. Further, the algorithm is graphically summarized in Fig. 32.

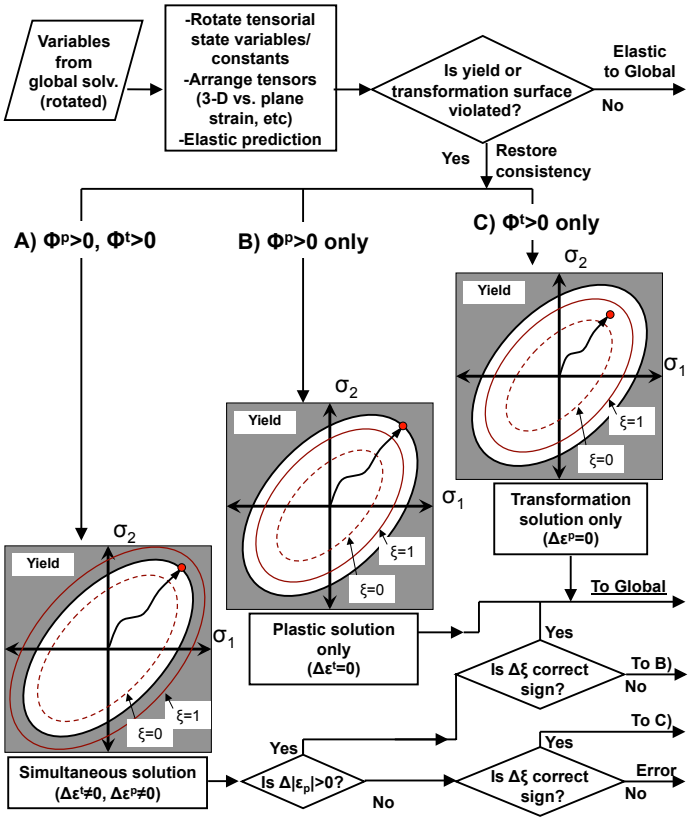

Fig. 32. Schematic representation of the return mapping algorithm for transformation-plastic yield SMA constitutive model (assuming constant temperature loading paths).

Table IV. Return Mapping Algorithm for modeling of transformation and plastic yield phenomena in SMAs.

1. Initialize

a. Rotate all tensors from last increment n by $\boldsymbol{\mathcal{Q}}_{n+1}$

b. Let $k = 0$, $\mathbf{x}_{n+1}^{(0)} = \mathbf{x}_n$ where $\mathbf{x} = \{\xi, \boldsymbol{\varepsilon}^t, \bar{\epsilon}^p, \boldsymbol{\varepsilon}^p, \boldsymbol{\mathcal{C}}, \boldsymbol{\alpha}\}$

2. Elastic Prediction

a. $\boldsymbol{\sigma}_{n+1}^{(0)} = \boldsymbol{\mathcal{C}}_{n+1}^{(0)} \left[\boldsymbol{\varepsilon}_{n+1} - \boldsymbol{\alpha}(T_{n+1} - T_0) - \boldsymbol{\varepsilon}^{t}{}_{n+1}^{(0)} - \boldsymbol{\varepsilon}^{p}{}_{n+1}^{(0)}\right]$

b. Find $\Phi^{t}{}_{n+1}^{(0)}$ and $\Phi^{p}{}_{n+1}^{(0)}$.

c. IF $\Phi^{t}{}_{n+1}^{(0)} \leq 0$ AND $\Phi^{p}{}_{n+1}^{(0)} \leq 0$ THEN EXIT (response elastic).

3. Transformation Correction (no plastic yield)

a. IF $\Phi^{t}{}_{n+1}^{(0)} > 0$ AND $\Phi^{p}{}_{n+1}^{(0)} \leq 0$ THEN CONTINUE ELSE GOTO 4.

b. Find $\Delta\xi_{n+1}^{(k)}$ via (4.46) with $\Delta\bar{\epsilon}^{p}{}_{n+1}^{(k)} = 0$.

c. $\xi_{n+1}^{(k+1)} = \xi_{n+1}^{(k)} + \Delta\xi_{n+1}^{(k)}$, and $\boldsymbol{\varepsilon}^{t}{}_{n+1}^{(k+1)} = \boldsymbol{\varepsilon}^{t}{}_{n+1}^{(k)} + \Delta\xi_{n+1}^{(k)} \boldsymbol{\Lambda}^{t}{}_{n+1}^{(k)}$

d. IF $\xi_{n+1}^{(k+1)}$ within bounds per (4.52) THEN CONTINUE ELSE set $\xi_{n+1}^{(k+1)}$ to violated bound and set $\Delta\xi_{n+1}^{(k)} = 0$.

e. $\boldsymbol{\sigma}_{n+1}^{(k+1)} = \boldsymbol{\mathcal{C}}_{n+1}^{(k+1)} \left[\boldsymbol{\varepsilon}_{n+1} - \boldsymbol{\alpha}(T_{n+1} - T_0) - \boldsymbol{\varepsilon}^{t}{}_{n+1}^{(k+1)} - \boldsymbol{\varepsilon}^{p}{}_{n}\right]$

f. IF $\Phi^{t}{}_{n+1}^{(k+1)} > TOL^t$ per (2.32) THEN CONTINUE ELSE EXIT

g. Increment k and GOTO 3b

4. Plastic Correction (no transformation)

a. IF $\Phi^{p}{}_{n+1}^{(0)} > 0$ AND $\Phi^{t}{}_{n+1}^{(0)} \leq 0$ THEN CONTINUE ELSE GOTO 5.

b.–g.: Analogous to *Transformation Correction* above

5. Simultaneous Transformation-Plastic Correction

a. IF $\Phi^{p}{}_{n+1}^{(0)} > 0$ AND $\Phi^{t}{}_{n+1}^{(0)} > 0$ THEN CONTINUE ELSE EXIT.

b. Find $\Delta\xi_{n+1}^{(k)}$ and $\Delta\bar{\epsilon}^{p}{}_{n+1}^{(k)}$ via (4.50) and (4.51).

c. $\xi_{n+1}^{(k+1)} = \xi_{n+1}^{(k)} + \Delta\xi_{n+1}^{(k)}$, $\boldsymbol{\varepsilon}^{t}{}_{n+1}^{(k+1)} = \boldsymbol{\varepsilon}^{t}{}_{n+1}^{(k)} + \Delta\xi_{n+1}^{(k)} \boldsymbol{\Lambda}^{t}{}_{n+1}^{(k)}$, $\bar{\epsilon}^{p}{}_{n+1}^{(k+1)} = \bar{\epsilon}^{p}{}_{n+1}^{(k)} + \Delta\bar{\epsilon}^{p}{}_{n+1}^{(k)}$, and $\boldsymbol{\varepsilon}^{p}{}_{n+1}^{(k+1)} = \boldsymbol{\varepsilon}^{p}{}_{n+1}^{(k)} + \Delta\bar{\epsilon}^{p}{}_{n+1}^{(k)} \boldsymbol{\Lambda}^{p}{}_{n+1}^{(k)}$

d. IF $\xi_{n+1}^{(k+1)}$ within bounds per (4.52) THEN CONTINUE ELSE set $\xi_{n+1}^{(k+1)}$ to violated bound and set $\Delta\xi_{n+1}^{(k)} = 0$.

e. $\boldsymbol{\sigma}_{n+1}^{(k+1)} = \boldsymbol{\mathcal{C}}_{n+1}^{(k+1)} \left[\boldsymbol{\varepsilon}_{n+1} - \boldsymbol{\alpha}_{n+1}(T_{n+1} - T_0) - \boldsymbol{\varepsilon}^{t}{}_{n+1}^{(k+1)} - \boldsymbol{\varepsilon}^{p}{}_{n+1}^{(k+1)}\right]$

f. IF $\Phi^{t}{}_{n+1}^{(k)} > TOL^t$ OR $\Phi^{p}{}_{n+1}^{(k)} > TOL^p$ THEN GOTO 5i

g. IF $\Delta\xi_{n+1} = \xi_{n+1}^{(k+1)} - \xi_n$ has wrong sign, set $k = 0$ and GOTO 4b ELSE IF $\Delta\bar{\epsilon}^{p}{}_{n+1} = \bar{\epsilon}^{p}{}_{n+1}^{(k+1)} - \bar{\epsilon}^{p}{}_{n} \leq 0$, set $k = 0$ and GOTO 3b ELSE EXIT

i. Find $\Phi^{t}{}_{n+1}^{(k+1)}$, $\Phi^{p}{}_{n+1}^{(k+1)}$ per (2.32), (4.19), increment k, and GOTO 5b

D. Model Calibration and Three-Dimensional Structural Analysis

Having derived a new constitutive model for SMAs undergoing plastic transformation, and further having implemented this model using a scheme that permits consideration of simultaneous martensitic transformation and yielding, we now address the calibration and utilization of this new engineering tool. The model derived above was originally motivated by a qualitative understanding of experimental results for plasticity in SMAs found throughout the literature [67, 68, 81, 69]. Further characterization of SMA material response considering plastic yielding behavior was performed at Texas A&M University to more clearly motivate the new model and to calibrate it in its final form, and some of these results were presented in Fig. 28 and Fig. 29. The elastic behavior, the conventional shape memory behavior, the yielding of pure phases, and the effects of transformation on plasticity and vice versa were all assessed. Simulation of the experiments is provided in this section to show that the model matches the data closely. The discussion of three-dimensional analysis begins with an experimentally validated predictive analysis whereby the tensile specimen used to calibrate the model in Section D.1 is subjected to bending loads. Next, the examination of inelastic behaviors at a crack tip that exists in an NiTi SMA material are considered. This is followed by the modeling of indentation characterization as it applies to SMA thin films, where a sharp indenter induces transformation and localized plastic yielding. Finally, a complicated engineering problem that considers the bending and local buckling of a flexure with a circular arc cross-section [15] is analyzed. For each of these studies, the Abaqus software suite is used as the global solver for the structural FEA boundary value problems [136].

1. Model calibration and simulation of experiments

The uniaxial tensile experimental results (Figure 28) were used to calibrate the 3-D constitutive model as implemented in the FEA framework. The *elastic properties* were determined by assessing the austenite elastic modulus during loading and the martensitic modulus during unloading. A standard Poisson's ratio was assumed. The *transformation properties* included the amount of transformation strain generated and fully recovered during non-yielding isothermal experiments at lower temperatures ($H^{cur} = H$, a constant) and the critical stress for transformation at various temperatures (i.e., via the phase diagram parameterized by four zero-stress transformation temperatures M_s, M_f, A_s, and A_f, and two slopes, C^M and C^A) [114]. Finally, the *plastic properties* were calibrated per the discussion of Section B.6.

By considering the results of the nine experiments shown in Figure 28 ($78\,^{\circ}\mathrm{C} \leq T \leq 177\,^{\circ}\mathrm{C}$), appropriate material properties were found and the model was calibrated. The properties are provided in Table V and the calibration of model parameters related to transformation in terms of these properties is described in Chapter II, Section C. Four of the calibration experiments (four different constant testing temperatures) were then chosen for simulation. The numerically implemented constitutive model in the 3-D FEA framework was then used to model the uniaxial tension boundary value problem. The applied thermomechanical loading paths (temperatures and applied stresses) were intended to match the experimental conditions as closely as possible. The simulation results are compared to the experimental results for $T = 80\,^{\circ}\mathrm{C}$, $110\,^{\circ}\mathrm{C}$, $145\,^{\circ}\mathrm{C}$, and $163\,^{\circ}\mathrm{C}$ in Figure 33. Note the very close agreement overall. One area of disagreement that may motivate future work is the presence of an unloading plateau in some of the analysis results, which is not observed experimentally. However, the final amount of irrecoverable strain is accurately predicted.

Table V. Material properties needed for the transformation-plastic yield model as derived from tensile experiments on equiatomic NiTi.

Parameter	**Value**	**Parameter**	**Value**
	(Thermoelastic Properties)		
E^A	69 GPA	$\nu^M = \nu^A$	0.33*
E^M	38 GPA	$\alpha^M = \alpha^M$	$10e-6/\,^\circ$C*
	(Phase Diagram Properties)		
M_s	48 °C	A_f	107 °C
M_f	46 °C	$C^A\|_{\sigma=0MPa}$	7.0 MPa/ °C
A_s	100 °C	$C^M\|_{\sigma=0MPa}$	8.7 MPa/ °C
	(Transformation Strain Properties)		
$H^{cur}(\sigma) = H$	0.06		
	(Smooth Hardening Properties)		
n_1, n_2	1.0, 1.0	n_3, n_4	0.2, 0.2
	(Plastic Modeling Constants)		
${Y_0}^A$	420 MPa	C_H	80
${Y_0}^M$	500 MPa	${K_\beta}^A$	11.3 GPa
${Y_m}^A$	1000 MPa	${K_\beta}^M$	8.3 GPa
${Y_m}^M$	1050 MPa	$\bar{\epsilon}^p{}_{crit}$	0.022
$\boldsymbol{\beta}_0$	**0** MPa		

*Nominal values taken from literature

As an additional example, it is interesting to observe the model predictions for the independent evolutions of transformation and plastic internal variables in this material given loading paths that induce only transformation or only plastic yielding. Isothermal loading to the maximum stress considered at 80 °C induces only

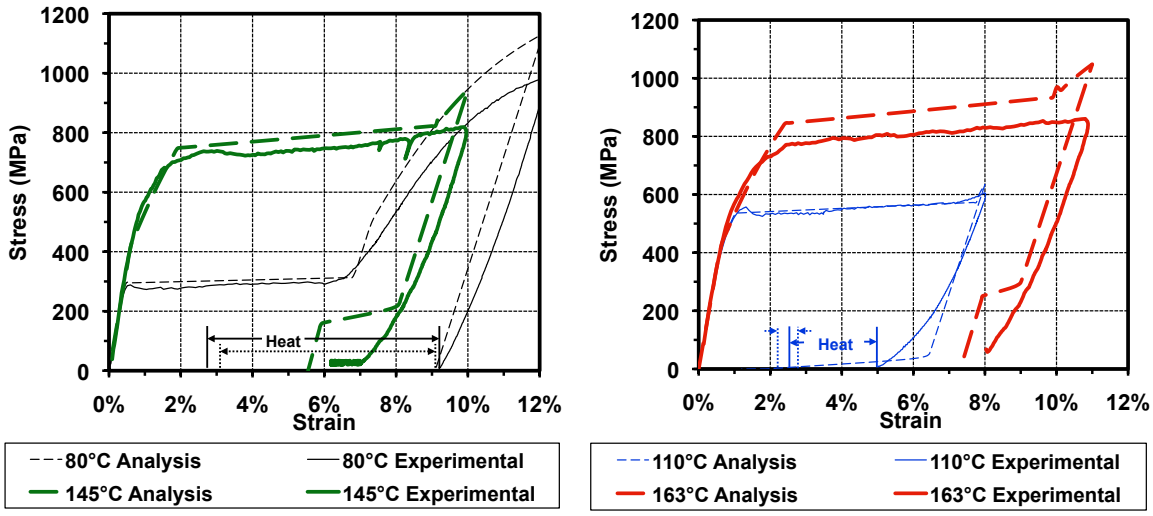

(a) (b)

Fig. 33. Selection of uniaxial tensile results for equiatomic NiTi at four nominally constant test temperatures and comparison with simulation.

forward transformation, and subsequent unloading and heating to above A_f completes reverse transformation. Isothermal loading and unloading at 160 °C induced only plastic yielding. The predictions for these two paths are given in Figure 34. For the 80 °C case, note that no plastic strain (and thus no back stress) is generated as the plastic yield criterion has not been violated, and further that the hardening energy and martensitic volume fraction return to their initial values after completion of transformation and return to the initial material configuration. For the 160 °C case, plastic strain, back stress, and plastic hardening energy all begin to evolve as the plastic criterion is met ($\sigma = 420$ MPa), but the high temperature prevents the onset of stress-induced phase transformation.

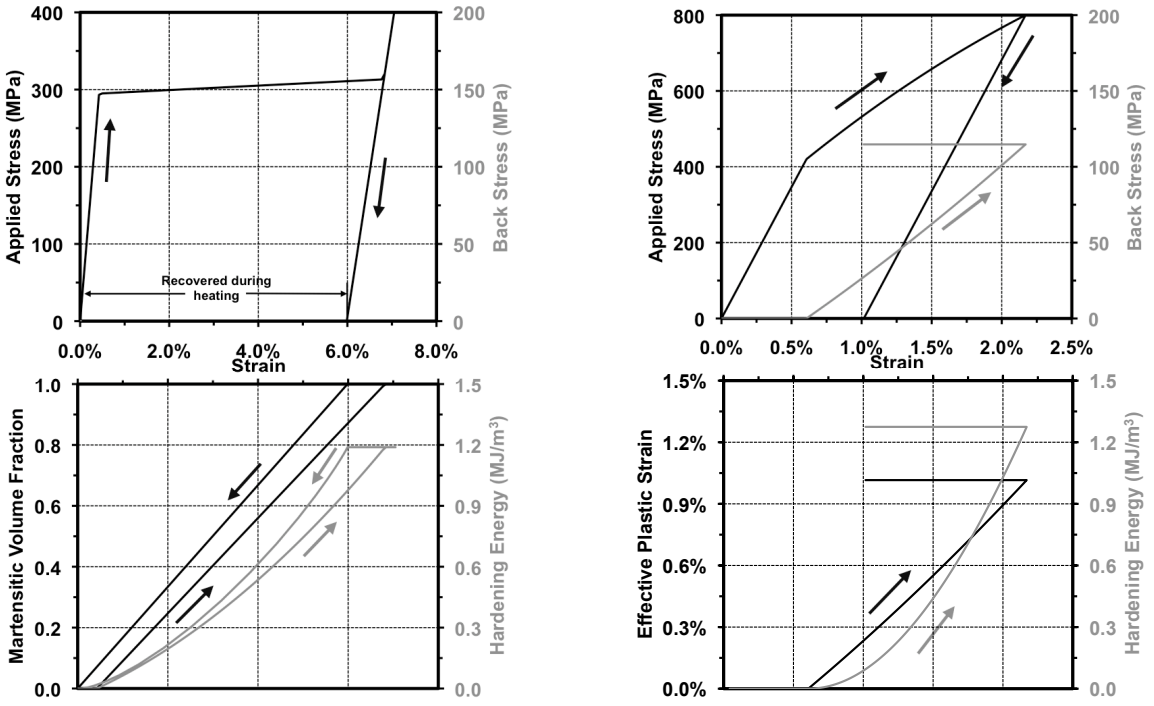

(a) $T = 80\,^{\circ}\mathrm{C}$, $\sigma_{max} = 400\,\mathrm{MPa}$ (b) $T = 160\,^{\circ}\mathrm{C}$, $\sigma_{max} = 800\,\mathrm{MPa}$

Fig. 34. Evolution of internal variables considering transformation-only and plastic yield-only loading of NiTi via the model of Chapter IV, Section B

2. Three-point bending of tensile specimen at elevated temperature

To begin the 3-D analysis examples, the case of an SMA body undergoing thermo-mechanical loading sufficient to induce simultaneous transformation and yielding is reviewed. The loading consists of subjecting a tensile "dogbone" specimen to three-point bending loads at a high temperature ($A_f < T < M_d$). The specimen configuration and material are identical to those considered in Section A and Section D.1, and the model calibration is *unchanged* from that given in Table V. The temperature during the application of bending loads is $T = 133\,^{\circ}\mathrm{C}$, which represents a temperature for which tensile experimental data was not generated.

The FEA model assumes half symmetry (specimen length bifurcated) and uses 576 second-order reduced integration quadrilateral elements in the half gauge section (plus additional elements in the gripping tab), with six elements through the thickness. The analysis considers the complex boundary conditions applied by subjecting such a small specimen to three-point loading using a conventional three-point bending apparatus. Specifically, the two rounded supports and the rounded bending tip are modeled as rigid surfaces and friction between these surfaces and the SMA specimen (1 mm thick) is also considered (friction coefficient of 0.3). The results for the distributed effective plastic strain at the end of loading as well as a comparison in predicted center force-deflection response with experimental results are shown in Figure 35. The predicted response of this structure undergoing simultaneous martensitic transformation and plastic yielding (in addition to large local rotations) is clearly of high accuracy. During loading, the nonlinear plastic yielding and phase transformation can be observed. Upon unloading, a drop in the force is noted due to the effects of friction, followed by reverse transformation leading to recovery of much of the deformation. A small reverse transformation plateau is once again observed (cf. Figure 33).

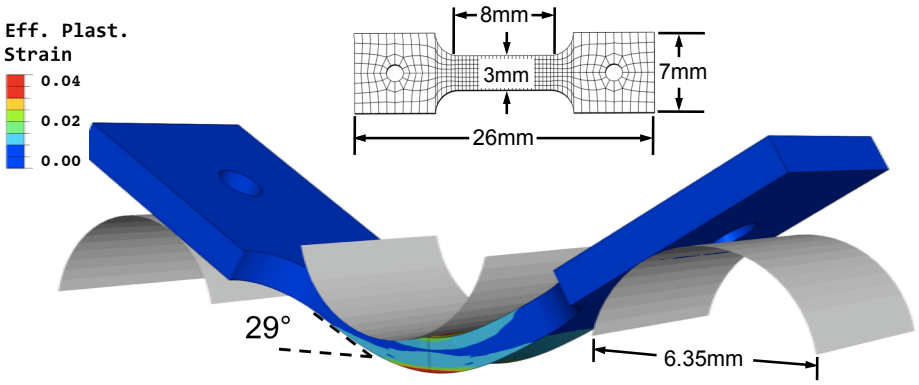

(a) Configuration of the boundary value problem (deformation at full load)

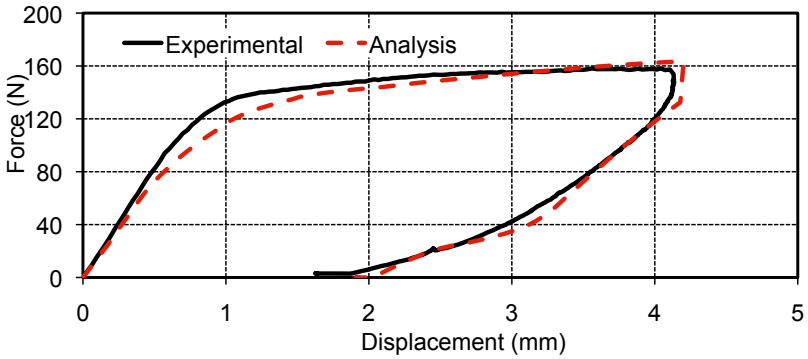

(b) Force-displacement response of specimen under bending (experimental result and analytical prediction)

Fig. 35. Predictive analysis results for the tensile specimen of Chapter IV, Section A and Section D.1 (using the material data of Table V) subjected to bending loads at $T = 133\,^{\circ}\mathrm{C}$.

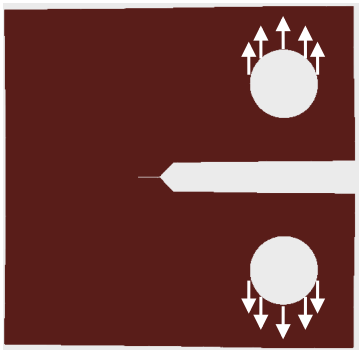

(a) Overall configuration.

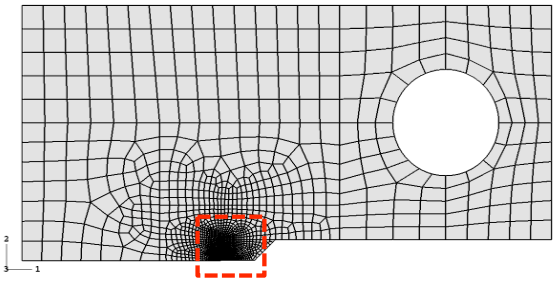

(b) Computational domain and FEA mesh.

Fig. 36. Configuration of the *compact tension* (CT) specimen and associated computational domain.

3. Plastic yielding at a crack tip

Next the consequences of plastic deformation in an SMA material are considered by examining the solution fields near the tip of a pre-crack as it exists in a *compact tension* (CT) specimen under mode I loading [150]. The SMA response at crack tips has been considered elsewhere, both experimentally [81] and numerically [62, 151]. The configuration of the specimen considered in this preliminary study is shown in Fig. 36a where most dimensions have been taken from the literature [151], and a 1.3 mm pre-crack is assumed. The specimen is modeled by taking advantage of the evident symmetry and further by assuming plane strain [150]. The 2-D computational domain, including the mesh refinement at the tip of the pre-crack, is shown in Fig. 36b. Convergence of the mesh has not been addressed in the current preliminary analysis. The material assumed for this analysis is the same that is described in Table V. The FEA analysis considers displacement-controlled loading of the specimen at three different constant temperatures, where the material is assumed to be initially austenitic. This is followed by heating to a given temperature (135 °C) and unloading. The imposed displacement consists of a 0.1 mm upward motion relative to the plane

of symmetry applied at the location of the loading pin (the round hole in the specimen). This motion corresponds to less than 1/10 of the pre-crack length (1.3 mm). The lowest loading temperature of 75 °C is between the zero-stress martensitic start (M_s) and austenitic start (A_s) temperatures, and loading at this temperature results in the initiation and completion of phase transformation prior to the initiation of plastic yielding. A higher loading temperature of 100 °C is sufficient to drive the critical stress to complete transformation up beyond the plastic yield limit, leading to nearly simultaneous transformation and plastic yield. Finally, the highest loading temperature of 135 °C increases the transformation stresses to such a high level that most of the local deformation at the crack tip is accommodated by plastic yielding, though some transformation occurs toward the end of loading.

The results of these three analyses can be seen in Fig. 37, Fig. 38, and Fig. 39, where the view presented is indicated in 36b. As previously described, an increase in loading temperature increases the transformation stress levels, thus transformation is delayed relative to the onset of plastic yielding. This is seen in Fig. 37, which distinguishes regions of elastic response (blue) from regions of transformation (green) and plastic yield (yellow). Note that in the current material, the plastic hardening greatly exceeds the transformation hardening, and further that the yield limit for martensite exceeds that of austenite, as seen in the list of material properties. This particular combination of behaviors implies that at high stresses at 135 °C, it is more favorable to transform only than to transform and yield simultaneously. This is not the case in general, and the model accounts for both situations.

Continuing to examine the results, we see that increasing loading temperature leads to an overall increase in the final stress as observed in Fig. 38. Investigation of the unloading behavior provides further useful information. Recall that after loading, all specimens were heated to 135 °C and then unloaded. The results of Fig. 39 indicate

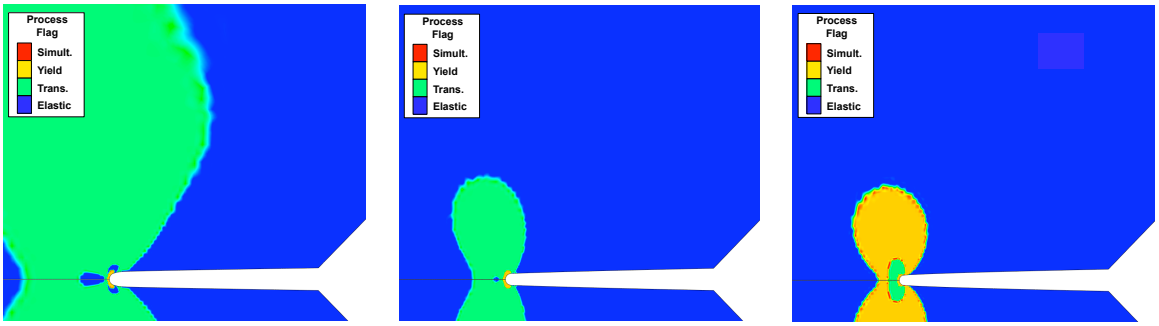

(a) Loading temperature: 75 °C (b) Loading temperature: 100 °C (c) Loading temperature: 135 °C

Fig. 37. Analysis predictions for the transformation and plastic yielding fields at the tip of a crack under mode I loading.

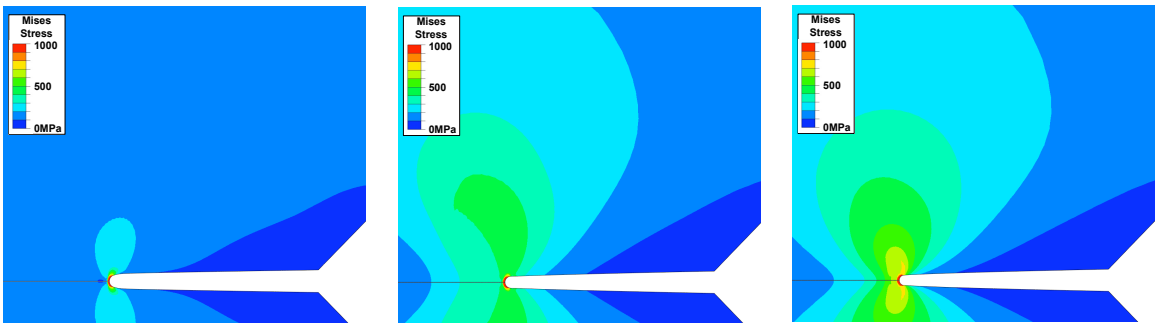

(a) Loading temperature: 75 °C (b) Loading temperature: 100 °C (c) Loading temperature: 135 °C

Fig. 38. Analysis predictions for the Mises equivalent stress ($\overline{\sigma}$) fields at the tip of a crack under mode I loading.

that a residual stress field is formed around the crack tip upon unloading (where the stress nearest the tip is found to be compressive). Further, it appears that a substantially larger field is formed when the specimen had been loaded well above the austenitic finish temperature ($A_f = 110\,°\text{C}$) as compared to loading below A_s. This result could be used for the future development of work hardening procedures applied to material in regions of stress concentrations.

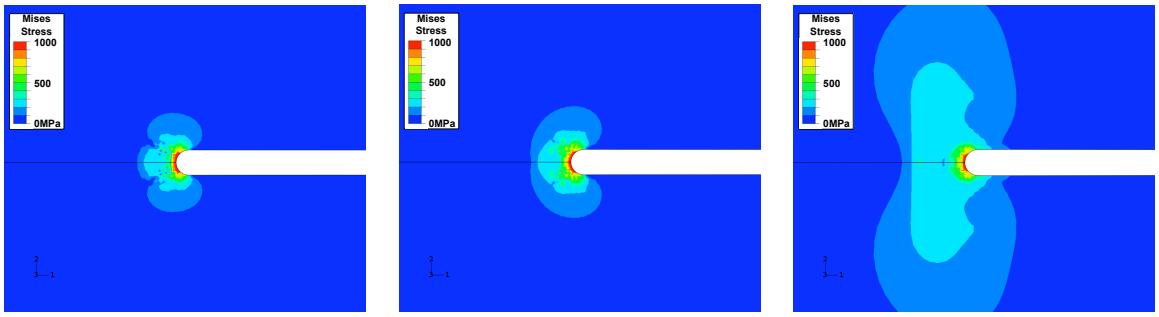

(a) Loading temperature: 75 °C (b) Loading temperature: 100 °C (c) Loading temperature: 135 °C

Fig. 39. Analysis predictions for the Mises equivalent stress ($\overline{\sigma}$) fields at the tip of a crack after *unloading* at 135 °C.

4. Indentation of an SMA thin film

This next 3-D analysis highlights a less obvious use for the SMA-plastic modeling tool: the interpretation of characterization results. Specifically, we consider the characterization of an SMA thin film, where indentation (or micro- or nano-indentation) is used to ascertain the elastic, plastic, and transformation properties of the material. Because complicated, non-homogeneous solution fields result from the local deformations induced by the indenter, the determination of constitutive properties directly from the experimental force-displacement curve is difficult. However, the elastic modulus is one example of a parameter that can be taken directly from this curve; it is taken from the slope during unloading. We seek to determine the remainder of the material properties by calibrating the model in such a way that it can predict the loading and overall recovery responses.[9]

This boundary value problem considers the Berkovich indentation [152] of a 1.5 μm thick layer of conventional NiTi SMA which is deposited on a 1.5 μm thick

[9]This attempt to simulate known behavior using unknown (guess) parameters is counter to the more common effort to predict unknown behavior using known material properties (as was discussed in Section D.2).

layer of silicon nitride (itself deposited on a silicon wafer with a thickness of 37 μm). The problem is modeled using axisymmetry; the three-sided Berkovich tip is approximated as conical using an accepted cone angle [152]. The three-layered body is discretized into $\approx 20,000$ linear axisymmetric elements with reduced integration (where hourglass modes are repressed through the use of the Abaqus `*SECTION CONTROLS, HOURGLASS=ENHANCED` option). The mesh was most refined nearest the indenter using strong biasing. The indenter is modeled as a rigid surface, and interaction between the indenter and material surface was modeled using Abaqus contact algorithms, where the coefficient of friction was taken to be 0.25. The material properties for the analysis are given in Table VI.[10] A subset of the mesh, the material configuration, and the indenter are all shown in Fig. 40a. The silicon layer extends many times further than the thickness of the other two layers, and the model extends several more times to the right, but this zoomed-in view allows the refined mesh to be illustrated. The dashed red box indicates the view used in subsequent figures showing experimental results.

[10]One should note that in the current case, only the force-displacement results are of interest. The temperature response, described by the transformation temperatures and stress influence coefficients (e.g., C^A), is not important and thus these properties were chosen arbitrarily based on conventional NiTi data.

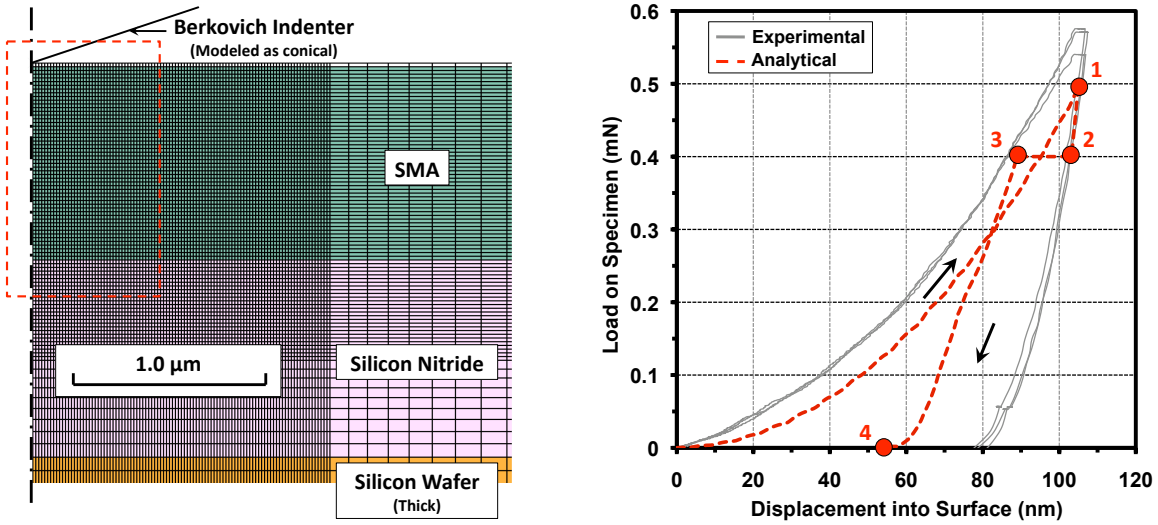

(a) Reference mesh and material layers

(b) Thermomechanical loading path (experimental and analytical)

Fig. 40. Reference mesh, material layup, and applied thermomechanical loading path for the analysis of indentation of an SMA thin film (experimental data provided by Columbia University [153]).

Table VI. Material properties for indentation analysis of equiatomic NiTi thin film.

Parameter	**Value**	**Parameter**	**Value**
	(Thermoelastic Properties)		
E^A	85 GPA	$\nu^M = \nu^A$	0.33*
E^M	85 GPA	$\alpha^M = \alpha^M$	$10e-6/\,^\circ$C*
	(Phase Diagram Properties)**		
M_s	$-58\,^\circ$C	A_f	$1\,^\circ$C
M_f	$-63\,^\circ$C	$C^A\|_{\sigma=200MPa}$	6.7 MPa/ °C
A_s	$-5\,^\circ$C	$C^M\|_{\sigma=200MPa}$	6.7 MPa/ °C
	(Transformation Strain Properties)		
$H^{cur}(\sigma) = H$	0.05		
	(Smooth Hardening Properties)**		
n_1, n_2	0.5, 0.5	n_3, n_4	0.5, 0.5
	(Plastic Modeling Constants)		
${Y_0}^A$	1000 MPa	C_H	20
${Y_0}^M$	1000 MPa	${K_\beta}^A$	0 GPa
${Y_m}^A$	1500 MPa	${K_\beta}^M$	0 GPa
${Y_m}^M$	1500 MPa	${\overline{\epsilon}^p}_{crit}$	0.0
$\boldsymbol{\beta}_0$	**0** MPa		

*Nominal, from literature **Arbitrarily set for the current analysis

Regarding the thermomechanical path applied during the analysis, it is important to review the standard experimental procedure and compare it to that considered here. Conventionally, SMA thin film in the self-accomodated (twinned) martensite configuration is subjected to local indenter loads and reoriented (detwinned), while some plastic deformation is also induced. Subsequent unloading leaves a residual indentation due to both reorientation and plastic slip. In a separate process, the film is heated to induce reverse transformation, and the depth of the indent after this process

is measured to ascertain SME recovery. However, the modeling tools described in this chapter (and, indeed, in this dissertation) are in general unable to consider this loading path for two reasons. The first is that these models do not consider the reorientation of martensite but only its generation from the parent austenite. This problem is easily circumvented as the process of martensitic reorientation can be approximated by the process of stress-inducing oriented martensite from austenite (where austenite and self-accomodated martensite have the same macroscopic configuration). The second reason is associated with a greater challenge: the current models are not intended to capture the response of an SMA material point where martensite has been oriented in a given direction (due to biasing forces in that direction), but then recovered while under a biasing load in the opposite direction. To clarify, consider a point in the thin film that is compressed by the action of the indenter, and compression-favored martensite is formed there. During unloading, the influence of surrounding material that has been plastically deformed leads to local stress regions that are *tensile*. Given subsequent heating, it is not clear when or how the local transformation strains (generated in the compressive direction) will be recovered given that the local stress field is now tensile. Attempts to numerically analyze such a problem can (and did) lead to convergence issues. In fact, throughout the literature, this problem has not been addressed, neither in the constitutive models nor in their implementations.

For these reason, we consider the following modified thermomechanical path that maintains compressive stresses throughout the reverse transformation process. Note that the initial material state is austenitic.

1. Move the rigid indenter 100 nm down into the SMA material,
2. Partially unload, maintaining a 0.4 mN downward force,
3. Uniformly heat the SMA to $A_f + 80\,^{\circ}\mathrm{C}$,

4. Fully unload the specimen at $A_f + 80\,^{\circ}\mathrm{C}$.

The force-displacement results given this loading path are shown in Fig. 40b, where they are compared to several experimental results obtained at Columbia University [153]. Note that the loading behavior is captured relatively accurately, and further parameter adjustment could increase this accuracy. Note also that the initial unloading slope is very accurate. Shape memory recovery is observed during heating (Step 3), though in the current case, no experimental deformation recovery data was provided for comparison. The evolution of the solution fields for Mises equivalent stress ($\overline{\sigma}$) and martensitic volume fraction (ξ) can be seen in Fig. 41. Note the increase in stress nearest the indenter when the material is heated (i.e., compare Fig. 41b and Fig. 41c). This is due to the plastic yielding region local to the indenter tip, where the high stresses are created as this yielded region prevents transformation of the underlying material back into austenite, even as the temperature climbs far above A_f. When all the load is removed, local stresses continue to prevent full reverse transformation of all regions despite the elevated temperature (Fig. 41d).

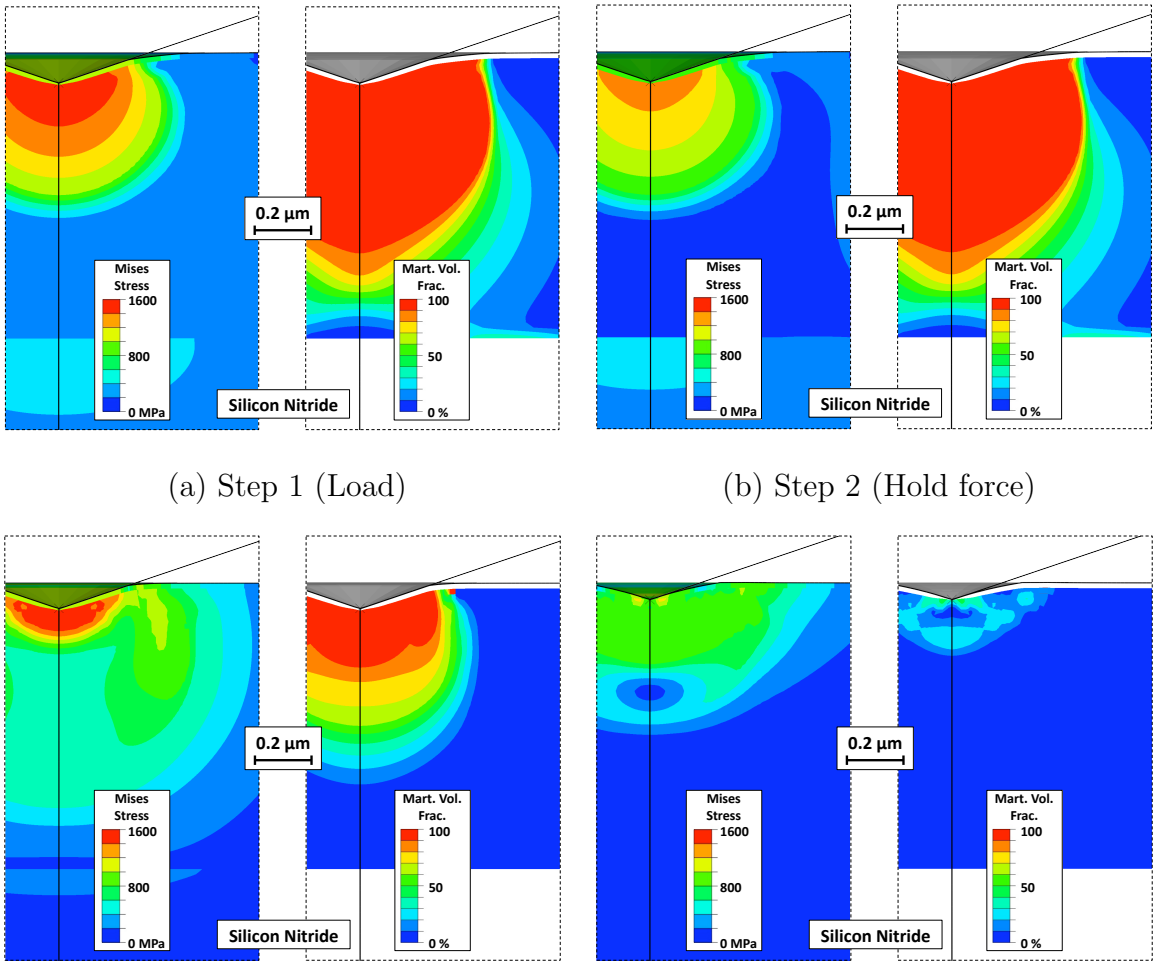

(a) Step 1 (Load)

(b) Step 2 (Hold force)

(c) Step 3 (Heat)

(d) Step 4 (Unload)

Fig. 41. Mises equivalent stress and martensitic volume fraction distribution results of SMA indentation analysis.

5. SMA flexure experiencing local buckling

To conclude the chapter, we consider a complex problem involving large rotations, plasticity, and local unstable buckling behavior. The analysis case is inspired by the *lightweight flexible solar array* (LFSA) project that utilized SMA flexures with circular arc cross-sections as active hinges for the deployment of solar panels [15]. This same design has also been studied for use with shape memory polymers [154]. Such active hinge components provide a high initial stiffness while also providing large bending motions due to the local buckling. Analyses of SMA components experiencing local buckling are not found in the literature and require special global solution algorithms such as the *modified Riks algorithm* [136, 144], used here. The flexure considered here is 100 mm in length, 10.6 mm in width, is 0.40 mm thick, and has a circular arc cross-section spanning 40°. The cantilevered flexure is oriented such that the circular arc cross-section is concave down and a downward deflection is enforced at the free end such that a total tip deflection of 50 mm is realized. It is modeled assuming half symmetry (along its length) and a total of 2880 second-order reduced integration quadrilateral elements were used, with four elements though the thickness.

Four analyses are considered with material properties defined as given in Table V, and each begins with the beams in the austenitic state. The analysis cases are: *i*) loading of elastic beam with austenitic properties (geometrically nonlinear analysis), *ii*) loading of SMA beam at $T = M_s + 7\,^{\circ}\mathrm{C}$ (geometrically *linear* analysis), *iii*) loading of SMA beam at $T = M_s + 7\,^{\circ}\mathrm{C}$, heating, and unloading at $T = A_f + 5\,^{\circ}\mathrm{C}$ (geometrically nonlinear analysis), and *iv*) loading and unloading of SMA beam at constant $T = A_f + 5\,^{\circ}\mathrm{C}$ (geometrically nonlinear analysis). The tip force-displacement response for each analysis case is illustrated in Fig. 42 where the forward loading results in particular are shown in Fig. 42a. The three geometrically nonlinear analyses

predict a marked decrease in stiffness as local buckling occurs in the flexure, while the geometrically linear (small rotation) analysis is unable to capture this effect, though the stress-induced transformation is captured.[11]

To better compare the two geometrically nonlinear analyses of SMA flexures, Fig. 42b showing loading and unloading is provided. For loading at $M_s + 7\,^{\circ}\mathrm{C}$, the initiation of martensitic transformation at lower stress triggers the local buckling behavior, resulting in a lower stiffness overall. A temperature of $A_f + 5\,^{\circ}\mathrm{C}$, however, is sufficient to drive the transformation stress above the plastic yield stress, leading to delayed buckling, a stiffer response, local irrecoverable deformations in the buckling regions, and a small irrecoverable tip deflection. For these same geometrically nonlinear SMA analyses, Fig. 43 provides detailed results including an illustration of the local buckling behavior, the equivalent stress distribution, and the generation of martensite in the buckling region. Plastic yielding in this region during loading at $T = A_f + 5\,^{\circ}\mathrm{C}$ leads to irrecoverable martensite, which can be observed at the end of unloading in Fig. 43b (right-hand side).

[11]The geometrically linear analysis also predicted a non-physical element expansion of 15% at the free end of the flexure.

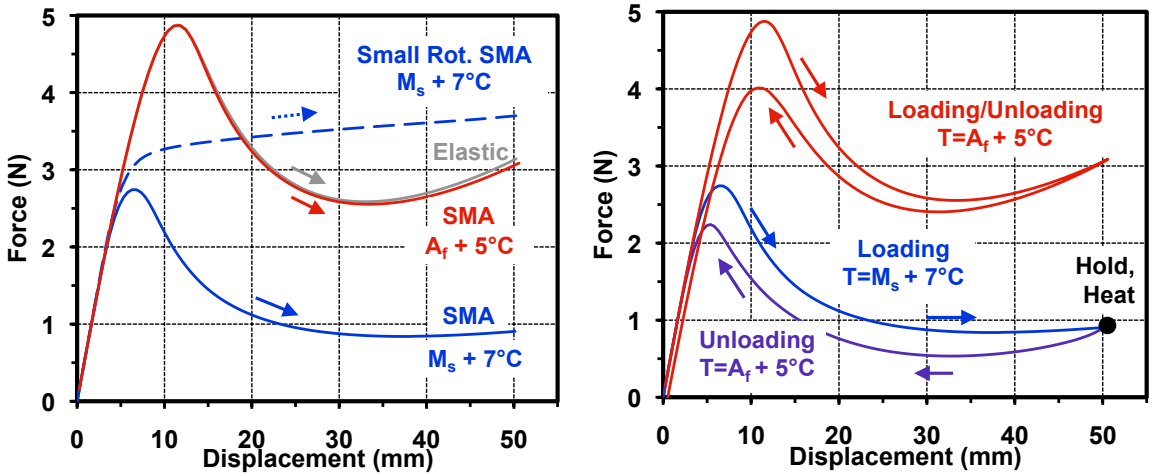

(a) Loading responses for all analysis cases

(b) Full cyclic response for SMA flexures (geometrically nonlinear analyses)

Fig. 42. Force-deflection response at the free end of a cantilevered flexture with circular arc cross-section subjected to tip loading (elastic and SMA beams, geometrically linear and nonlinear analyses).

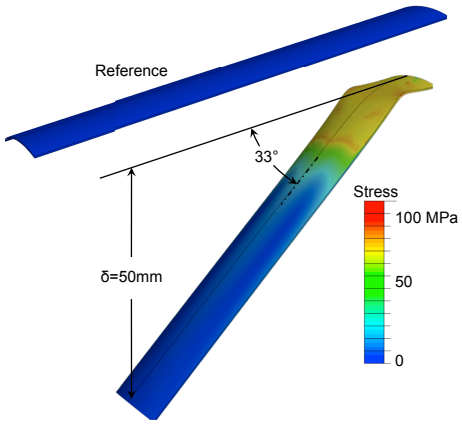

(a) Global flexure deformation and Mises equivalent stress ($\overline{\sigma}$) distribution during loading at $T = M_s + 7\,^{\circ}\mathrm{C}$

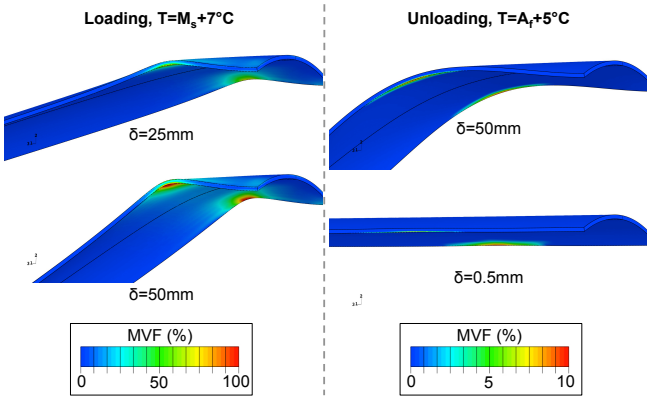

(b) Local flexure buckling deformation and martensitic volume fraction (MVF) distribution during: *i*) loading at $T = M_s + 7\,^{\circ}\mathrm{C}$ (left side), and *ii*) loading/unloading at $T = A_f + 5\,^{\circ}\mathrm{C}$ (right side)

Fig. 43. Geometrically nonlinear analysis predictions for the deformation, stress distribution, and martensitic volume fraction distribution during loading at $T = M_s + 7\,^{\circ}\mathrm{C}$ and loading/unloading at $T = A_f + 5\,^{\circ}\mathrm{C}$.

CHAPTER V

RATE-DEPENDENT VISCOPLASTIC DEFORMATIONS IN SMAS

After the extended effort to model the effects of rate-indpendent plasticity in SMAs, the research focus shifted to the rate-*dependent* deformations observed in HTSMAs and in conventional SMAs at high temperature (i.e., during shape setting). This chapter describes the modeling methods used to account for these effects by again extending both the constitutive model and numerical implementation methods described in Chapter II and Chapter III. This is accomplished by additionally considering the generation and evolution of both transformation-induced plastic (TRIP) strains and rate-dependent viscoplastic strains, as each of these have been observed in experimental studies [155]. Additional motivations have been discussed in Chapter I.

This chapter is organized as follows: Section A describes the derivation of the SMA transformation-viscoplastic yield constitutive model using continuum thermodynamics and various assumptions about the evolution of transformation and viscoplastic deformation processes; Section B introduces several options for the integration of the constitutive equations and then focuses on the numerical implementation of the model in an FEA framework that accounts for large rotations in SMA bodies; Section C includes model calibration and simulation of experiments on an HTSMA exhibiting thermally-induced actuation cycles. This last section also includes five distinct three-dimensional analysis examples to demonstrate the effectiveness of the new modeling tool.

A. Derivation of Coupled Constitutive Model

The model derived in this work considers two distinct dissipative processes: the martensitic phase transformation and rate-dependent viscoplastic yielding. Regarding the phase transformation, we consider both the recoverable and irrecoverable deformations resulting from this process. While the recoverable strain forms the basis for the unique shape memory behaviors observed in SMAs, the transformation-induced irrecoverable (TRIP) strain also becomes prominent in HTSMAs, where high temperatures serve to exacerbate these effects [155]. Note that the relations and assumptions for modeling TRIP considered in this chapter (motivated by [59]) could also be amended to other SMA models such as that described in Chapter IV.

Regarding viscoplasticity, we consider the rate-dependent evolution of an additional inelastic irrecoverable strain. This effect is not observed in conventional SMAs at conventional temperatures; it is observed when these materials are subjected to high temperatures (during processing or shape-setting). Further, these strains can be generated during thermally-induced actuation of HTSMA bodies due to the high temperatures needed to initiate transformation. It is worth mentioning that rate-independent (conventional) plasticity (of the type considered in Chapter II) could also be added to the model of this work. In fact, a large class of "unified theories for viscoplasticity" exist [103, 84] that are suitable for capturing both the rate-independent and rate-dependent irrecoverable inelastic deformations. However, such a complex model and the complicated calibration it would require is beyond the current work.

When comparing the model of this chapter to that in the last, it will become evident that the current viscoplastic model formulation assumes a weaker coupling between phase transformation and irrecoverable deformation (viscoplasticity). There are two reasons for this. The first is that the experimental studies reviewed for this

work do not indicate a need for a viscoplastic back stress, and thus there is no *direct* coupling between the transformation and viscoplastic yield criteria (as compared to the effects of $\boldsymbol{\beta}$ in Chapter IV). Secondly, the viscoplastic evolution equations and flow criteria are formulated so as to be independent of phase (i.e., they are so strongly dependent on temperature that ξ dependence becomes negligible.) But while these two assumptions serve to simplify the derivation slightly, the additional consideration of TRIP strains adds an alternative complexity to both the mathematical model and its implementation.

For materials where the influence of a viscoplastic back stress cannot be neglected, Appendix G has been provided. In this extended discussion, the modifications required to model the evolution and influence of this additional internal variable are made to the relations presented in this chapter. This includes both the constitutive equations and the algorithmic relations for the numerical implementation.

1. Formulation of specific Gibbs free energy potential

The derivation of the current constitutive model for a shape memory alloy undergoing viscoplastic deformations progresses in a manner similar to that used in the previous chapter; it is based on considering the evolution of internal variables (scalar and tensorial) subject to the constraints of thermodynamics. To that end, we again propose[1]:

Assumption 1: The current state of the material is described by a Gibbs free energy thermodynamic potential, which is decomposed into an austenitic, martensitic, and

[1]As it is unclear to what extent the viscoplastic strain is an appropriate internal variable in the Gibbs free energy (i.e., to what level it meaningfully tracks the state of the material), the discussion of Appendix E is especially applicable to the current derivation.

mixing contribution, and which is dependent on particular external and internal state variables.

As in the two models preceding this one (i.e., the transformation-only model of Chapter II and the transformation-plastic model of Chapter IV), the Gibbs energy is chosen as the energy potential with stress and temperature as the external state variables. The internally-evolving state variables are again divided in two categories, and the set of transformation internal state variables is amended by the addition of the irrecoverable *TRIP strain tensor* $\boldsymbol{\varepsilon}^{tp}$ [59]. On the other hand, the viscoplastic mechanisms considered have not been previously addressed in the context of shape memory alloys. The effects of viscoplasticity are characterized by the *viscoplastic strain tensor* $\boldsymbol{\varepsilon}^{vp}$, and the *viscoplastic hardening energy* g^{vp}, which measures the increase in the free energy due to isotropic viscoplastic hardening. The proposed Gibbs free energy potential, dependent on each of these state variables, is decomposed into three contributions and written as (cf. (4.1))[2]

$$\begin{aligned} G(\boldsymbol{\sigma}, T, \boldsymbol{\varepsilon}^t, \boldsymbol{\varepsilon}^{tp}, \xi, g^t, \boldsymbol{\varepsilon}^{vp}, g^{vp}) &= (1-\xi) G^A(\boldsymbol{\sigma}, T, \boldsymbol{\varepsilon}^{vp}, g^{vp}) \\ &+ \quad \xi \; G^M(\boldsymbol{\sigma}, T, \boldsymbol{\varepsilon}^{vp}, g^{vp}) \\ &+ \quad G^{mix}(\boldsymbol{\sigma}, \boldsymbol{\varepsilon}^t, \boldsymbol{\varepsilon}^{tp}, g^t), \end{aligned} \tag{5.1}$$

[2]The following derivation relies on two assumptions that are subject to debate: *i*) that the total strain should be additively decomposed into parts, where each inelastic mechanism is represented by a different inelastic strain, and *ii*) that the free energy potential should admit as internal variables even those quantities that track irrecoverable processes and thus do not contribute to work upon unloading (e.g., $\boldsymbol{\varepsilon}^{tp}$ and $\boldsymbol{\varepsilon}^{vp}$). Appendix E provides an alternative derivation methodology that includes neither of these assumptions and proposed an additive decomposition of the *rates* of irrecoverable strain measures.

where (cf. (2.6) and (4.2))

$$G^{\gamma}(\boldsymbol{\sigma}, T, \boldsymbol{\varepsilon}^{vp}, g^{vp}) = -\frac{1}{2\rho}\boldsymbol{\sigma} : \boldsymbol{\mathcal{S}}^{\gamma}\boldsymbol{\sigma} - \frac{1}{\rho}\boldsymbol{\sigma} : \boldsymbol{\varepsilon}^{vp} + \frac{1}{\rho}g^{vp} - \frac{1}{\rho}\boldsymbol{\sigma} : \boldsymbol{\alpha}(T - T_0) + c\left[(T - T_0) - T\ln\left(\frac{T}{T_0}\right)\right] - s_0^{\gamma}T + u_0^{\gamma} \tag{5.2}$$

for $\gamma = A, M$. Each G^{γ} represents the Gibbs energy of a conventional viscoplastic material (e.g., viscoplastic austenite). The process of transformation from one pure phase to the other is accounted for by the form of (5.1) and the energy of mixing, which includes the contributions of the transformation-induced strains (recoverable and irrecoverable); it is modified from (2.7) and given as:

$$G^{mix}(\boldsymbol{\sigma}, \boldsymbol{\varepsilon}^{t}, \boldsymbol{\varepsilon}^{tp}, g^{t}) = -\frac{1}{\rho}\boldsymbol{\sigma} : (\boldsymbol{\varepsilon}^{t} + \boldsymbol{\varepsilon}^{tp}) + \frac{1}{\rho}g^{t}. \tag{5.3}$$

The material constants are unchanged from previous chapters.

2. Application of the laws of thermodynamics

Application of the first and second laws of thermodynamics via the Coleman-Noll procedure (see Chapter II, Section C.2) then gives the following for the total infinitesimal strain (the relation for entropy being identical to (2.16)):

$$\boldsymbol{\varepsilon} = \boldsymbol{\mathcal{S}}\boldsymbol{\sigma} + \boldsymbol{\alpha}(T - T_0) + \boldsymbol{\varepsilon}^{t} + \boldsymbol{\varepsilon}^{tp} + \boldsymbol{\varepsilon}^{vp}, \tag{5.4}$$

Again rewriting this in terms of stress, we have for Hooke's law:

$$\boldsymbol{\sigma} = \boldsymbol{\mathcal{C}}\left[\boldsymbol{\varepsilon} - \boldsymbol{\alpha}(T - T_0) - \boldsymbol{\varepsilon}^{t} - \boldsymbol{\varepsilon}^{tp} - \boldsymbol{\varepsilon}^{vp}\right] = \boldsymbol{\mathcal{C}}\left[\boldsymbol{\varepsilon} - \boldsymbol{\varepsilon}^{th} - \boldsymbol{\varepsilon}^{t} - \boldsymbol{\varepsilon}^{tp} - \boldsymbol{\varepsilon}^{vp}\right]. \tag{5.5}$$

The remaining dissipative terms resulting from application of the second law (Clausius-Planck inequality), separated into transformation and viscoplastic yield contributions,

are written

$$\begin{aligned} &- \quad \rho\left[\partial_{\xi}G\ \dot{\xi} + \partial_{\boldsymbol{\mathcal{E}}^{t}}G^{mix} : \dot{\boldsymbol{\varepsilon}}^{t} + \partial_{\boldsymbol{\mathcal{E}}^{tp}}G^{mix} : \dot{\boldsymbol{\varepsilon}}^{tp} + \partial_{g^{t}}G^{mix}\dot{g}^{t}\right] \\ &- \quad \rho\left[(1-\xi)\partial_{\boldsymbol{\mathcal{E}}^{vp}}G^{A} + \xi\partial_{\boldsymbol{\mathcal{E}}^{vp}}G^{M}\right] : \dot{\boldsymbol{\varepsilon}}^{vp} \\ &- \quad \rho\left[(1-\xi)\partial_{g^{vp}}G^{A} + \xi\partial_{g^{vp}}G^{M}\right]\dot{g}^{vp} \geq 0. \end{aligned} \tag{5.6}$$

3. Evolution of internal variables

Assumption 2: The rate of evolution of the transformation-induced strains is proportional to the rate of the martensitic volume fraction, $\dot{\xi}$, and this rate alone. Likewise, the rate of evolution of the viscoplastic strain is proportional to the rate of the effective viscoplastic strain, $\dot{p}$, and this rate alone.

Per the form employed in various transformation-plastic models [59, 156], the 3-D evolutions of the TRIP and viscoplastic strains are given as

$$\dot{\boldsymbol{\varepsilon}}^{tp} = \dot{\xi}\boldsymbol{\Lambda}^{tp}; \qquad \dot{\boldsymbol{\varepsilon}}^{vp} = \dot{p}\boldsymbol{\Lambda}^{vp}. \tag{5.7}$$

The flow law for the transformation strain is given in (2.20). Here, p denotes the *effective viscoplastic strain*, whose rate is given from the second invariant of the viscoplastic strain rate per $\dot{p} = \sqrt{2/3\ (\dot{\boldsymbol{\varepsilon}}^{vp} : \dot{\boldsymbol{\varepsilon}}^{vp})}$. The directions of the evolutions for the irrecoverable strains are given as

$$\boldsymbol{\Lambda}^{tp} = \begin{cases} f^{tp}(\bar{\sigma})\boldsymbol{\Lambda}^{vp} & ; \quad \dot{\xi} > 0 \\ -f^{tp}(\bar{\sigma})\boldsymbol{\Lambda}^{vp} & ; \quad \dot{\xi} < 0 \end{cases}; \qquad \boldsymbol{\Lambda}^{vp} = \frac{3}{2}\frac{\boldsymbol{\sigma}'}{\bar{\sigma}},$$

where the transformation direction tensor is given in (2.21). The form of $\boldsymbol{\Lambda}^{vp}$, which has a norm of one, results from classical Mises plasticity. The scalar-valued function $f^{tp}(\bar{\sigma})$ describes the magnitude of the TRIP strain generation rate at at a given stress,

and is calibrated from experimental results.[3]

The evolution equation for the transformation hardening energy is unchanged from Chapter II. We postulate a new evolution equation for the viscoplastic hardening energy, given as

$$\dot{g}^{vp} = \dot{p} f^{vp}(T, p). \tag{5.8}$$

During viscoplastic deformation, the rate of increase in the viscoplastic hardening energy is proportional to the rate of the effective viscoplastic strain by the factor $f^{vp}(T, p)$.

4. Criteria for transformation and viscoplastic yield

Substituting the proposed evolution equations into the dissipative inequality (5.6), we arrive at

$$\left[\boldsymbol{\sigma} : (\boldsymbol{\Lambda}^t + \boldsymbol{\Lambda}^{tp}) - \rho \partial_\xi G - f^t(\xi)\right] \dot{\xi} + \left[\boldsymbol{\sigma} : \boldsymbol{\Lambda}^{vp} - f^{vp}(T, p)\right] \dot{p} \geq 0. \tag{5.9}$$

Assumption 3: The two processes of phase transformation and viscoplasticity are independently strongly dissipative. The Clausius-Duhem inequality is decomposed into two contributions, each being strictly positive during evolution of the associated internal variable.

This assumption follows from that made in the derivation of the model of Chapter IV and the references mentioned therein, and it leads to the following set of two

[3]Note that in past works (i.e., in [59]), the TRIP strain was postulated to stabilize and its evolution cease as the number of transformation cycles increased. This stabilization is not considered in the current work as the high temperatures experienced by HTSMAs during transformation can annihilate dislocations in each cycle, resulting in a constant (non-decreasing) rate of TRIP strain generation [155].

conditions:

$$\begin{gathered}\left[\boldsymbol{\sigma} : \left(\boldsymbol{\Lambda}^{t} + \boldsymbol{\Lambda}^{tp}\right) - \rho\partial_{\xi}G - f^{t}(\xi)\right]\dot{\xi} = \pi^{t}\dot{\xi} > 0 \quad \forall \quad \dot{\xi} \neq 0, \\ \left[\boldsymbol{\sigma} : \boldsymbol{\Lambda}^{vp} - f^{vp}(T,p)\right]\dot{p} = \pi^{vp}\dot{p} > 0 \quad \forall \quad \dot{p} > 0.\end{gathered} \tag{5.10}$$

From $(5.10)_1$ it follows that π^t must be non-zero whenever ξ is evolving, and further, that π^t must change sign as $\dot{\xi}$ changes sign. Considering these constraints and postulating a limit value for π^t during transformation, we arrive at the Kuhn-Tucker conditions given in (2.32) where π^t and $Y^t(\boldsymbol{\sigma})$ are slightly modified to include the effects of the TRIP strain, giving

$$\pi^{t} = \boldsymbol{\sigma} : \boldsymbol{\Lambda}^{t} + \boldsymbol{\sigma} : \boldsymbol{\Lambda}^{tp} + \frac{1}{2}\boldsymbol{\sigma} : \widetilde{\boldsymbol{\mathcal{S}}}\boldsymbol{\sigma} + \rho\tilde{s}_0 T - \rho\tilde{u}_0 - f^{t}, \tag{5.11}$$

$$Y^{t}(\boldsymbol{\sigma}) = Y_0^{t} + D\boldsymbol{\sigma} : (\boldsymbol{\Lambda}^{t} + \boldsymbol{\Lambda}^{tp}). \tag{5.12}$$

Similarly, constraints on the evolution of $\boldsymbol{\varepsilon}^{vp}$ (and thus p) result from $(5.10)_2$. In rate-independent plasticity, these are satisfied by a plastic consistency condition similar to (2.32) (cf. (4.19)). In the current rate-dependent model, however, we satisfy $(5.10)_2$ by explicitly postulating a functional form for p [83, 103] that guarantees positive dissipation (and the satisfaction of the second law). Specifically, we choose a form appropriate for the consideration of primary and secondary creep, and the evolution of effective viscoplastic strain is then given as

$$\dot{p} = \lambda^{vp}(\boldsymbol{\sigma}, T, p) = \left(\frac{\langle \boldsymbol{\sigma} : \boldsymbol{\Lambda}^{vp} - f^{vp}(T,p)\rangle}{K_a(T)}\right)^{N_a(T)}, \tag{5.13}$$

where K_a and N_a are generally temperature-dependent functions and the $\langle\cdot\rangle$ denote the Macaulay brackets.[4] Note that this form, being non-homogeneous in time,

[4]The Macauley brackets are defined such that $\langle x\rangle = \begin{cases} x; & x \geq 0 \\ 0; & x < 0 \end{cases} = \dfrac{x + |x|}{2}$.

introduces rate-dependence into the mathematical model.[5] In the special case that the critical stress for creep is at all times zero (i.e., $f^{vp}(T,p) = 0$ and creep occurs at all stresses), $\dot{p}$ is commonly given explicitly by combining power law creep with Arrhenius' equation (see [157]):

$$\lambda^{vp}(\boldsymbol{\sigma}, T) = A \exp\left(\frac{-Q}{RT}\right) (\boldsymbol{\sigma} : \boldsymbol{\Lambda}^{vp})^{N_a}, \tag{5.14}$$

where Q is the *activation energy*, R is the *gas constant*, and A is an additional fitting parameter (known as the *pre-exponential factor*). Combining (5.13) and (5.14) for the case of $f^{vp}(T,p) = 0$, we find

$$K_a(T) = \left[A \exp\left(\frac{-Q}{RT}\right)\right]^{-1/N_a}. \tag{5.15}$$

5. Reduction to 1-D form and calibration of parameters

To model an SMA material experiencing viscoplastic deformations, six of the above relations are needed. These are as follows: Hooke's law (5.5), the evolution of transformation strain (2.20), the evolution of TRIP strain $(5.7)_1$, the evolution of viscoplastic strain $(5.7)_2$, the evolution of transformation hardening energy (2.26), the Kuhn-Tucker type conditions on transformation (2.32), and the explicit form for the rate of viscoplastic deformation (5.13). These together result in a set of 27 total equations that can be solved for the 27 total unknowns ($\boldsymbol{\sigma}$, $\boldsymbol{\varepsilon}^t$, $\boldsymbol{\varepsilon}^{tp}$, ξ, g^t,$\boldsymbol{\varepsilon}^{vp}$, $\dot{p}$).

Here, as in Chapter IV, Section B.6, we briefly consider the calibration of the proposed model. To begin, the new model is reduced to its 1-D form. The considerations of TRIP and viscoplastic strains only slightly alter the transformation relations

[5] This is distinct from a true *time* dependence as time does not appear as a variable in any of the relations. Truly time-dependent phenomena such as recovery, aging, etc. [84] could be considered provided that the proper time-dependent terms were included.

from their original 1-D form in Chapter II. The 1-D reductions unique to this chapter are as follows:[6]

$$\boldsymbol{\varepsilon}^{tp} \rightarrow \varepsilon_{11}^{tp} = \varepsilon^{tp}, \quad \boldsymbol{\varepsilon}^{vp} \rightarrow \varepsilon_{11}^{vp} = \varepsilon^{vp}.$$

The relation between the current stress and strains is written in 1-D as

$$\sigma = E(\xi)\left[\varepsilon - \alpha(T - T_0) - \varepsilon^t - \varepsilon^{tp} - \varepsilon^{vp}\right], \tag{5.16}$$

where the current Young's modulus is given in (2.34). The evolution equation for the transformation strain is given by (2.20), while for the TRIP and viscoplastic strains, the evolutions are given as

$$\dot{\varepsilon^{tp}} = \dot{\xi} f^{tp}(\sigma)\,\mathrm{sgn}\,(\sigma). \tag{5.17}$$

$$\dot{\varepsilon^{vp}} = \dot{p}\,\mathrm{sgn}\,(\sigma). \tag{5.18}$$

The evolution of the transformation hardening energy is given by (2.26).

To write out the transformation functions, we first write out the form of $Y^t(\sigma)$ in 1-D. For the coupled transformation-viscoplastic model, this is given as

$$Y^t(\sigma) = Y_0^t + D\sigma(\Lambda^t + \Lambda^{tp}). \tag{5.19}$$

We then write out the transformation function during forward transformation as

$$\begin{aligned} \Phi_{fwd}^t(\sigma, T, \xi) &= |\sigma|\left(H^{cur}(\sigma) + f^{tp}(\sigma)\right) + \frac{1}{2}\left(\frac{1}{E^M} - \frac{1}{E^A}\right)\sigma^2 + \rho\tilde{s}_0 T - \rho\tilde{u}_0 \\ &- f_{fwd}^t(\xi) - Y^t(\sigma) = 0 \end{aligned} \tag{5.20}$$

[6] In the special case of non-cyclic tensile loading, $\varepsilon^{vp} = p$. Similarly, in the case of non-cyclic compressive loading, $\varepsilon^{vp} = -p$.

while for reverse transformation it is given as

$$\begin{aligned}\Phi^t_{rev}(\sigma,T,\xi) &= -\sigma\left(\frac{\varepsilon^{t-r}}{\xi^r} - f^{tp}(\sigma)\mathrm{sgn}\,(\sigma)\right) - \frac{1}{2}\left(\frac{1}{E^M} - \frac{1}{E^A}\right)\sigma^2 - \rho\tilde{s}_0 T + \rho\tilde{u}_0 \\ &+ f^t_{rev}(\xi) - Y^t(\sigma) = 0. \end{aligned} \tag{5.21}$$

Finally, the function describing the rate of viscoplastic strain is written as

$$\dot{p} = \left(\frac{\langle|\sigma| - f^{vp}(T,p)\rangle}{K_a(T)}\right)^{N_a(T)}. \tag{5.22}$$

The calibration of the following model parameters follows exactly from the discussion of Chapter II, Section C.5, regardless of the presence of viscoplastic strains in the material:

- the elastic moduli of martensite and austenite (E^M and E^A),
- five additional phase diagram-related parameters ($\rho\tilde{u}_0$, a_1, a_2, a_3, Y^t_0).

The maximum transformation strain $H^{cur}(\sigma)$ is also easily calibrated using the methods of Chapter II, though the modeler must also consider the effects of viscoplastic and TRIP strain when calibrating using the isobaric hysteresis height, for example, as $H^{cur}(\sigma)$ is associated only with fully recoverable strain. If viscoplastic strains are negligible (i.e., if the rate of actuation is sufficiently fast), then only the amount of irrecoverable strain generated by the chosen form of f^{tp} need be considered.

Due to the effects of TRIP strain, the calibration of $\rho\tilde{s}_0$ and D in terms of phase diagram properties must be derived once more. Calibration of these parameters is again performed by considering the slope of the transformation surface in a uniaxial stress-temperature space as measured at reference stress level σ^*. The Kuhn-Tucker conditions (2.32) imply that both the transformation function Φ^t and its rate are zero-valued during transformation. However, for the current model that includes TRIP strain, the functional form of Φ^t contains a new $\mathbf{\Lambda}^{tp}$ (or $\Lambda^{tp} = \pm f^{tp}(\sigma)\mathrm{sgn}\,(\sigma)$

in 1-D). We then proceed by employing the calibration methods from Chapter II, Section C.5, beginning at (2.40). As with (2.47) and (2.48), we consider the slopes of the transformation surfaces for forward and reverse transformation, denoting these slopes at the reference stress σ^* by C^M and C^A, respectively. Solving the these two equations for the two unknowns $(\rho\tilde{s}_0, D)$, we find (where $\Delta\mathcal{S} = \frac{1}{E^M} - \frac{1}{E^A}$)

$$\rho\tilde{s}_0 = -2\left(C^M C^A\right) \left.\frac{\left(H^{cur} + \sigma\partial_\sigma H^{cur} + \sigma\Delta\mathcal{S}\right)\left(H^{cur} + \sigma\partial_\sigma H^{cur}\right) - \left(f^{tp} + \sigma\partial_\sigma f^{tp}\right)^2}{\left(C^M + C^A\right)\left(H^{cur} + \sigma\partial_\sigma H^{cur}\right) + \left(C^M - C^A\right)\left(f^{tp} + \sigma\partial_\sigma f^{tp}\right)}\right|_{\sigma=\sigma^*},$$

$$D = \left.\frac{\left(C^M - C^A\right)\left(H^{cur} + \sigma\partial_\sigma H^{cur} + \sigma\Delta\mathcal{S}\right) + \left(C^M + C^A\right)\left(f^{tp} + \sigma\partial_\sigma f^{tp}\right)}{\left(C^M + C^A\right)\left(H^{cur} + \sigma\partial_\sigma H^{cur}\right) + \left(C^M - C^A\right)\left(f^{tp} + \sigma\partial_\sigma f^{tp}\right)}\right|_{\sigma=\sigma^*}. \tag{5.23}$$

The TRIP function f^{tp} must also be calibrated by measuring the amount of irrecoverable strain generated at several different constant applied stress levels. Note that it is essential that the observed irrecoverable strains be due to transformation alone, and not due to viscoplastic creep. Therefore, temperature levels should be as low as possible while temperature rates should be as high as possible. As will be discussed in the following section, a quadratic form for f^{tp} was assumed in the current research effort.

In addition to the material properties related to the phase transformation, the following functions relating to viscoplastic behavior must also be calibrated. Each can be derived from experimental data as follows:

- $K_a(T)$: calibrated by measuring the change in viscoplastic creep rate at a given constant stress with a change in test temperature. Can be given the form of (5.15), for example.

- $N_a(T)$: in the case that this function is assigned a constant value (as is considered in the remainder of this dissertation), it is calibrated by measuring the change in viscoplastic creep rate with a change in applied stress level at a con-

stant testing temperature.

- $f^{vp}(T,p)$: calibrated by performing constant strain rate monotonic loading experiments at various temperatures and noting the hardening in the yielding response; could take a linear or decaying exponential form, for example.

B. Numerical Implementation of Coupled Model

Here the coupled phase transformation-viscoplastic yield constitutive model of Section A is numerically implemented in an FEA framework. The algorithm follows from the derivations discussed previously in Chapter III, Section A, and also considers the evolution of simultaneous processes as was addressed in Chapter IV, Section C. However, small differences arise due to the rate-dependent nature of the viscoplastic strain. Further, because the transformation and viscoplastic yield are less strongly coupled in the current model (compared to that of Chapter IV), the forms of many of the equations in the algorithm are simplified.

We first focus on the most immediate contribution of this work: the consideration of rate-dependent irrecoverable strains. Several options exist for the integration of the associated evolution equation (cf. Chapter III, Section A.2), and we seek one that is compatible with the chosen methods of solving the transformation constitutive equations.

1. Integration of viscoplastic evolution equation

Here we revisit the discussion of Chapter III, Section A.2 as we now focus on the accurate integration of the evolution equation for the viscoplastic strain, which is non-homogeneous in time (i.e., it is rate-dependent). Therefore, it it worth describing how such an evolution equation can be integrated in time. Of course, we use the same

incremented loading methodology as was previously introduced.

Discretizing a general form for the evolution of the viscoplastic strain in time using the general trapezoidal rule [138], we have for a single loading step

$$\boldsymbol{\varepsilon}^{vp}{}_{n+1} = \boldsymbol{\varepsilon}^{vp}{}_{n} + \Delta t \left[(1-\gamma)\dot{p}_n \boldsymbol{\Lambda}^{vp}_n + \gamma \dot{p}_{n+1} \boldsymbol{\Lambda}^{vp}_{n+1}\right]. \tag{5.24}$$

where, for the remainder of this chapter, we use $\Delta t = \Delta t_{n+1} = t_{n+1} - t_n$. We again consider two options for the value of the algorithmic parameter γ (i.e., $\gamma = 0$ and $\gamma = 1$).

Option 1: Forward Euler integration

A straightforward option is to assume that $\gamma = 1$ and thus that the rate of the viscoplastic strain in the current time step can be approximated explicitly using the solution from the last. To implement this, we use $(5.8)_2$ and (5.13) evaluated at the previous time step, giving

$$\boldsymbol{\varepsilon}^{vp}{}_{n+1} = \boldsymbol{\varepsilon}^{vp}{}_{n} + \Delta t \lambda^{vp}(\boldsymbol{\sigma}_n, T_{n+1}, p_n) \boldsymbol{\Lambda}^{vp}(\boldsymbol{\sigma}_n). \tag{5.25}$$

Some commercial FEA packages employ this most simple option for materials where the rate of creep is slow compared to the time scale of the analysis and time steps are sufficiently small [144]. For higher creep rates, however, very small time steps are required to achieve accuracy and convergence is not guaranteed [138]. As in Chapter III, we consider backward Euler methods as a more robust option.

Option 2: Backward Euler integration (direct iteration)

The method of backward Euler integration assumes $\gamma = 1$ in the discretized evolution

equation (5.24), giving

$$\boldsymbol{\varepsilon}^{vp}{}_{n+1} = \boldsymbol{\varepsilon}^{vp}{}_{n} + \Delta t\ \dot{p}_{n+1}\boldsymbol{\Lambda}^{vp}(\boldsymbol{\sigma}_{n+1}). \tag{5.26}$$

This must be solved implicitly. The most straightforward scheme uses (5.13) to define $\dot{p}$ and then directly iterates over this equation, where k again denotes the iteration counter. The direct iteration formulation is given as

$$\boldsymbol{\varepsilon}^{vp(k+1)}_{n+1} = \boldsymbol{\varepsilon}^{vp}{}_{n} + \Delta t\lambda^{vp}(\boldsymbol{\sigma}^{(k)}_{n+1}, T_{n+1}, p^{(k)}_{n+1})\boldsymbol{\Lambda}^{vp}(\boldsymbol{\sigma}^{(k)}_{n+1}), \tag{5.27}$$

where $\boldsymbol{\sigma}$ in a given iteration is calculated from $\boldsymbol{\varepsilon}^{vp}$ per Hooke's law (5.5). To determine the accuracy of the solution (and thus the cessation of iteration), we introduce the *viscoplastic strain residual*

$$\mathbf{R}^{(k)}_{n+1} = \boldsymbol{\varepsilon}^{vp(k)}_{n+1} - \boldsymbol{\varepsilon}^{vp}{}_{n} - \lambda^{vp}(\boldsymbol{\sigma}^{(k)}_{n+1}, T_{n+1}, p^{(k)}_{n+1})\boldsymbol{\Lambda}^{vp}(\boldsymbol{\sigma}^{(k)}_{n+1})\Delta t, \tag{5.28}$$

and iterate until $\|\mathbf{R}^{(k)}_{n+1}\|$ is less than some tolerance. As discussed in Chapter III, this approach exhibits poor convergence qualities, thus we require a more rigorous method.

Option 3: Backward Euler integration (return mapping algorithms)

Another approach to the integration of (5.26) is to rewrite this relation such that the resulting form is implicit with respect to both time steps and iterations. Such methods are common for the integration of rate-independent inelastic strains (see Chapter III, Section A.2). These can be readily applied to the current problem of rate-dependent viscoplasticity [105, 140], and this is made evident by recasting the numerical equations in a form analogous to the rate-independent relations of Chapter III. To that end, we first consider the unknown $\dot{p}$ as analogous to the conventional "plastic multiplier", and then use (5.13) to form a relation constraining

the value of this unknown (see [105], for example, especially Section 2.3). This new relation is given as

$$\Phi^{vp}(\boldsymbol{\sigma}, T, p, \dot{p}) = \lambda^{vp}(\boldsymbol{\sigma}, T, p) - \dot{p} = 0. \tag{5.29}$$

This relation (5.29) acts as a constraint on $\dot{p}$ and as such is analogous to the conventional (rate-independent) consistency condition (i.e., $\Phi^p = 0$). Given this, a number of integration methodologies can now be applied to the viscoplastic problem. Here, we consider two forms in particular.

Closest point projection:

This method solves the discretized viscoplastic evolution equation (5.26) with all unknowns implicit both in time and in iteration. Note that, for the case of viscoplasticity only (as is considered currently), the current stress is known in terms of $\boldsymbol{\varepsilon}$, T, and $\boldsymbol{\varepsilon}^{vp}$, per Hooke's law (5.5) (where $\boldsymbol{\varepsilon}$ and T are known values provided by the global FEA solver). Thus the two unknown variables to be solved for implicitly are $\{\boldsymbol{\varepsilon}^{vp}, \dot{p}\}$, and the discretized (incremental and iterative) viscoplastic evolution equation (5.26) becomes

$$\boldsymbol{\varepsilon}^{vp}{}_{n+1}^{(k+1)} = \boldsymbol{\varepsilon}^{vp}{}_n + \Delta t\ \dot{p}_{n+1}^{(k+1)} \boldsymbol{\Lambda}^{vp}(\boldsymbol{\sigma}_{n+1}^{(k+1)}). \tag{5.30}$$

To find solutions for the unknown scalar $\dot{p}_{n+1}^{(k+1)}$ and the unknown tensor $\boldsymbol{\varepsilon}^{vp}{}_{n+1}^{(k+1)}$, we first introduce an iterative update of these two variables per

$$\boldsymbol{\varepsilon}^{vp}{}_{n+1}^{(k+1)} = \boldsymbol{\varepsilon}^{vp}{}_{n+1}^{(k)} + \Delta\boldsymbol{\varepsilon}^{vp}{}_{n+1}^{(k)}; \quad \dot{p}_{n+1}^{(k+1)} = \dot{p}_{n+1}^{(k)} + \Delta\dot{p}_{n+1}^{(k)}, \tag{5.31}$$

where the unknowns in the next iteration $k+1$ are now $\Delta\boldsymbol{\varepsilon}^{vp}{}_{n+1}^{(k)}$ and $\Delta\dot{p}_{n+1}^{(k)}$. Linearizing the tensor-valued viscoplastic strain residual $\mathbf{R}$ and the scalar-valued constraint

function Φ^{vp} about their roots gives

$$\begin{aligned} \mathbf{R}_{n+1}^{(k+1)} &= \mathbf{R}_{n+1}^{(k)} + \Delta\mathbf{R}_{n+1}^{(k)} \simeq \mathbf{0}, \\ \Phi^{vp}{}_{n+1}^{(k+1)} &= \Phi^{vp}{}_{n+1}^{(k)} + \Delta\Phi^{vp}{}_{n+1}^{(k)} \simeq 0. \end{aligned} \tag{5.32}$$

where $\Delta\mathbf{R}_{n+1}^{(k)}$ and $\Delta\Phi^{vp}{}_{n+1}^{(k)}$ are expanded via the chain rule [129]. The closest point projection algorithm then relies on the solution of the system of equations (5.32) for the set of unknowns $\{\Delta\boldsymbol{\varepsilon}^{vp}{}_{n+1}^{(k)}, \Delta\dot{p}_{n+1}^{(k)}\}$, which are then used in (5.31). The resulting algorithm is unconditionally convergent provided that the constraint equation is convex. However, as described in Chapter III, several disadvantages reduce its attractiveness for the current implementation. Most importantly, the simultaneous consideration of the transformation equations (including a separate "constraint" equation Φ^t and residual $\mathbf{R}^t$) doubles the size of the system of equations and any coupling complicates its derivation and coding. For these reasons, we explore the simplified form of the return mapping algorithm successfully utilized in the previous two chapters: the convex cutting plane algorithm.

Convex cutting plane:

Again, this method simplifies the closest point projection algorithm by solving for the scalar unknown (in this case $\dot{p}$) implicitly while updating the direction of inelastic deformation from the solution of the last iteration. According to an original source for this algorithm, it "readily extends to viscoplastic materials." [140] The incremental-iterative form of the discretized evolution equation is then given as

$$\boldsymbol{\varepsilon}^{vp}{}_{n+1}^{(k+1)} = \boldsymbol{\varepsilon}^{vp}{}_{n} + \Delta t\ \dot{p}_{n+1}^{(k+1)} \boldsymbol{\Lambda}^{vp}(\boldsymbol{\sigma}_{n+1}^{(k)}). \tag{5.33}$$

The tensor $\boldsymbol{\Lambda}^{vp}$ is calculated from the solution of the last iteration, but a current

solution for $\dot{p}$ must be found. For this we use $(5.31)_2$ and $(5.32)_2$. Considering (5.29) and Hooke's law (5.5) where the total strain is provided by the global FEA solver, we then apply the chain rule. Rearranging terms, this gives

$$\Delta\dot{p}_{n+1}^{(k)} = \frac{-\Phi^{vp}{}_{n+1}^{(k)}}{\left(-\partial_{\boldsymbol{\sigma}}\lambda^{vp}{}_{n+1}^{(k)} : \boldsymbol{\mathcal{C}}\boldsymbol{\Lambda}^{vp} + \partial_p\lambda^{vp}{}_{n+1}^{(k)}\right)\Delta t - 1}. \tag{5.34}$$

This convex cutting plane algorithm has been successfully implemented for the integration of the phase transformation evolution equations (Chapter III) and the rate-independent plastic evolution equations (Chapter IV), therefore it will be used once again for the coupled SMA phase transformation-viscoplastic yield problem.

Figure 44 has been provided to illustrate the convergence differences between the direct iteration method of (5.27) and convex cutting plane method of (5.33) in integrating the viscoplastic relations.[7] Note that, in this case, the direct iteration integration method does converge, though linearly and thus slowly. The convex cutting plane algorithm converges much faster with only a moderate increase in the complexity of the implementation (i.e., the coding).

2. Implementation using convex cutting plane algorithm

In the previous section, we reviewed possible methods for integrating the viscoplastic equations, and the relations for integrating the rate-dependent irrecoverable strain using the convex cutting plane form of the return mapping algorithm were provided. Here we choose this algorithm for the integration of the coupled equations, and the detailed derivation of the needed numerical relations is provided.

To begin, we rewrite (5.5) in the incremental-iterative form such that the stress

[7] The results were obtained during analysis of an HTSMA under 200 MPa load at 520 °C (see Section C.1 for the material properties, etc.). The constant time increment Δt was 63 s (or 1% of the total step time).

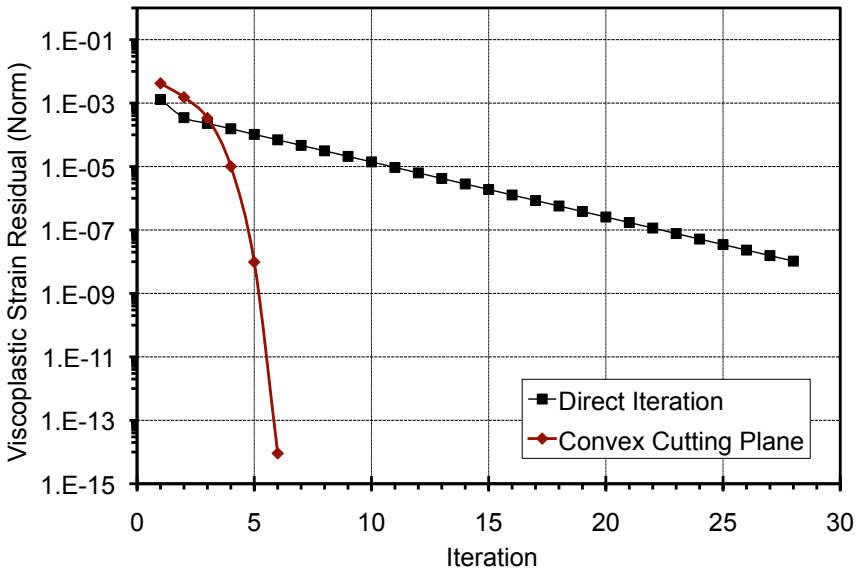

Fig. 44. Comparison of convergence for the direct iteration and convex cutting plane methods applied to the integration of viscoplastic evolution equations (from the simulation of Chapter V, Section C.1; $\|\mathbf{R}\|$ tolerance of 1.0E-8).

during the current loading increment $n+1$ at the end of each iteration k is given as

$$\boldsymbol{\sigma}_{n+1}^{(k)} = \boldsymbol{\mathcal{C}}_{n+1}^{(k)} : [\boldsymbol{\varepsilon}_{n+1} - \boldsymbol{\varepsilon}^{th}{}_{n+1} - \boldsymbol{\varepsilon}^{t(k)}_{n+1} - \boldsymbol{\varepsilon}^{tp(k)}_{n+1} - \boldsymbol{\varepsilon}^{vp(k)}_{n+1}], \tag{5.35}$$

where the total strain increment and temperature increment are supplied by the global solver and are thus known. The current stress, and therefore the current values of $\boldsymbol{\varepsilon}^t$, $\boldsymbol{\varepsilon}^{tp}$, and $\boldsymbol{\varepsilon}^{vp}$, must be found.

In the predictor step, we have

$$\boldsymbol{\varepsilon}^{t(0)}_{n+1} = \boldsymbol{\varepsilon}^{t}{}_{n}, \qquad \boldsymbol{\varepsilon}^{tp(0)}_{n+1} = \boldsymbol{\varepsilon}^{tp}{}_{n}, \qquad \boldsymbol{\varepsilon}^{vp(0)}_{n+1} = \boldsymbol{\varepsilon}^{vp}{}_{n}. \tag{5.36}$$

The transformation function (2.32) and viscoplastic strain rate (5.13) are then calculated based on this prediction. If the transformation criteria are not violated (i.e., if $\Phi^{t(0)}_{n+1} \leq 0$) and if the effective strain rate (5.13) is null, the elastic solution is

accepted as correct and is returned to the global solver. However, if one or both of these functions Φ^t or λ^{vp} is found to have a positive value based on the prediction, the corrective iterations begin. The process completes when Φ^t and Φ^{vp} are sufficiently close to zero.

During iterative correction, we hold the total current strain and temperature constant and the inelastic strains are updated using (5.33) in addition to the following for the transformation-related strains (cf. (2.20) and (5.7)):

$$\begin{aligned} \boldsymbol{\varepsilon}^{t}{}_{n+1}^{(k+1)} &= \boldsymbol{\varepsilon}^{t}{}_{n} + \left(\xi_{n+1}^{(k+1)} - \xi_n\right) \boldsymbol{\Lambda}^{t}(\boldsymbol{\sigma}_{n+1}^{(k)}), \\ \boldsymbol{\varepsilon}^{tp}{}_{n+1}^{(k+1)} &= \boldsymbol{\varepsilon}^{tp}{}_{n} + \left(\xi_{n+1}^{(k+1)} - \xi_n\right) \boldsymbol{\Lambda}^{tp}(\boldsymbol{\sigma}_{n+1}^{(k)}). \end{aligned} \tag{5.37}$$

The scalar-valued internal variables upon which the convex cutting plane algorithm is based are iteratively written as

$$\xi_{n+1}^{(k+1)} = \xi_{n+1}^{(k)} + \Delta\xi_{n+1}^{(k)}, \qquad \dot{p}_{n+1}^{(k+1)} = \dot{p}_{n+1}^{(k)} + \Delta\dot{p}_{n+1}^{(k)}, \tag{5.38}$$

where we now seek the unknowns $\Delta\xi_{n+1}^{(k)}$ and $\Delta\dot{p}_{n+1}^{(k)}$.

It can be shown using (2.32), (5.33), (5.35), (5.37), and (5.38) that the iterative change in stress during correction is

$$\Delta\boldsymbol{\sigma}_{n+1}^{(k)} = \boldsymbol{\mathcal{C}}_{n+1}^{(k)} \left[\mp \left(\partial_{\boldsymbol{\sigma}} \Phi^{t}{}_{n+1}^{(k)} + D(\boldsymbol{\Lambda}^{t}{}_{n+1}^{(k)} + \boldsymbol{\Lambda}^{tp}{}_{n+1}^{(k)}) \right) \Delta\xi_{n+1}^{(k)} - \boldsymbol{\Lambda}^{vp}{}_{n+1}^{(k)} \Delta\dot{p}_{n+1}^{(k)} \Delta t \right], \tag{5.39}$$

where the "$\mp$" corresponds to forward/reverse transformation, respectively.

To clearly illustrate their dependence on the solution-dependent variables, the transformation function given in (2.32) (considering also (5.11)) and the viscoplastic strain rate constraint equation (5.29) are written out as

$$\begin{aligned} \Phi^t(\boldsymbol{\sigma}, T, \xi) = \;& \pm \left[\boldsymbol{\sigma} : \left(\boldsymbol{\Lambda}^t(\boldsymbol{\sigma}) + \boldsymbol{\Lambda}^{tp}(\boldsymbol{\sigma}) \right) + \frac{1}{2} \boldsymbol{\sigma} : \widetilde{\boldsymbol{\mathcal{S}}} \boldsymbol{\sigma} + \rho \tilde{s}_0 T - \rho \tilde{u}_0 - f^t(\xi) \right] \\ & - \; Y_0^t - D\boldsymbol{\sigma} : \left(\boldsymbol{\Lambda}^t(\boldsymbol{\sigma}) + \boldsymbol{\Lambda}^{tp}(\boldsymbol{\sigma}) \right) = 0, \end{aligned} \tag{5.40}$$

$$\Phi^{vp}(\boldsymbol{\sigma}, T, p, \dot{p}) = \left(\frac{\langle \boldsymbol{\sigma} : \boldsymbol{\Lambda}^{vp}(\boldsymbol{\sigma}) - f^{vp}(T,p) \rangle}{K_a(T)} \right)^{N_a(T)} - \dot{p} = 0. \tag{5.41}$$

Linearizing the transformation function $\Phi^t(\boldsymbol{\sigma}, T, \xi)$ and the viscoplastic strain rate constraint equation $\Phi^{vp}(\boldsymbol{\sigma}, T, p, \dot{p})$ about their roots, we find

$$\Phi^{t(k+1)}_{n+1} = \Phi^{t(k)}_{n+1} + \Delta\Phi^{t(k)}_{n+1} \simeq 0, \quad \Phi^{vp(k+1)}_{n+1} = \Phi^{vp(k)}_{n+1} + \Delta\Phi^{vp(k)}_{n+1} \simeq 0. \tag{5.42}$$

Application of the chain rule to these two relations (at a given temperature) implies

$$\Phi^{t(k)}_{n+1} + \partial_{\boldsymbol{\sigma}}\Phi^{t(k)}_{n+1} : \Delta\boldsymbol{\sigma}^{(k)}_{n+1} + \partial_{\xi}\Phi^{t(k)}_{n+1}\Delta\xi^{(k)}_{n+1} \simeq 0 \tag{5.43}$$

$$\Phi^{vp(k)}_{n+1} + \partial_{\boldsymbol{\sigma}}\Phi^{vp(k)}_{n+1} : \Delta\boldsymbol{\sigma}^{(k)}_{n+1} + \partial_{p}\Phi^{vp(k)}_{n+1}\Delta p^{(k)}_{n+1} + \partial_{\dot{p}}\Phi^{vp(k)}_{n+1}\Delta\dot{p}^{(k)}_{n+1} \simeq 0, \tag{5.44}$$

where we note that $\Delta p^{(k)}_{n+1} = \Delta\dot{p}^{(k)}_{n+1}\Delta t$ for a specified constant time increment Δt. Substituting the stress increment (5.39) into (5.43), we find

$$\begin{aligned} \Phi^{t(k)}_{n+1} \;-\; & \partial_{\boldsymbol{\sigma}}\Phi^{t(k)}_{n+1} : \boldsymbol{\mathcal{C}}^{(k)}_{n+1}\Big[\pm\left(\partial_{\boldsymbol{\sigma}}\Phi^{t(k)}_{n+1} + D(\boldsymbol{\Lambda}^{t(k)}_{n+1} + \boldsymbol{\Lambda}^{tp(k)}_{n+1})\right)\Delta\xi^{(k)}_{n+1} \\ + \; & \boldsymbol{\Lambda}^{vp(k)}_{n+1}\Delta t\Delta\dot{p}^{(k)}_{n+1}\Big] + \partial_{\xi}\Phi^{t(k)}_{n+1}\Delta\xi^{(k)}_{n+1} \simeq 0. \end{aligned} \tag{5.45}$$

Likewise, substituting the stress increment (5.39) into (5.44) while further considering the form of (5.29), we find

$$\begin{aligned} \Phi^{vp(k)}_{n+1} \;-\; & \partial_{\boldsymbol{\sigma}}\lambda^{vp(k)}_{n+1} : \boldsymbol{\mathcal{C}}^{(k)}_{n+1}\Big[\pm\left(\partial_{\boldsymbol{\sigma}}\Phi^{t(k)}_{n+1} + D(\boldsymbol{\Lambda}^{t(k)}_{n+1} + \boldsymbol{\Lambda}^{tp(k)}_{n+1})\right)\Delta\xi^{(k)}_{n+1} \\ + \; & \boldsymbol{\Lambda}^{vp(k)}_{n+1}\Delta t\Delta\dot{p}^{(k)}_{n+1}\Big] + \Big[\partial_{p}\lambda^{vp(k)}_{n+1}\Delta t - 1\Big]\Delta\dot{p}^{(k)}_{n+1} \simeq 0. \end{aligned} \tag{5.46}$$

The required partial derivatives of the transformation function can be evaluated using (5.40) while considering the definitions provided in Section A, resulting in the following for Φ^t:

$$\partial_{\boldsymbol{\sigma}}\Phi^t = \pm\left(\boldsymbol{\Lambda}^t + \boldsymbol{\Lambda}^{tp} + \frac{1}{2}\widetilde{\boldsymbol{\mathcal{S}}}\boldsymbol{\sigma}\right) - D(\boldsymbol{\Lambda}^t + \boldsymbol{\Lambda}^{tp}); \qquad \partial_{\xi}\Phi^t = \mp\partial_{\xi}f^t(\xi).$$

Likewise, for Φ^{vp} we use (5.41) and the definitions of Section A to obtain the following:

$$\partial_{\boldsymbol{\sigma}} \lambda^{vp} = N_a(T) \left(\frac{\left\langle \boldsymbol{\sigma} : \boldsymbol{\Lambda}^{vp}(\boldsymbol{\sigma}) - f^{vp}(T,p) \right\rangle}{K_a(T)} \right)^{N_a(T)-1} \boldsymbol{\Lambda}^{vp};$$

$$\partial_p \Phi^{vp} = -N_a(T) \left(\frac{\left\langle \boldsymbol{\sigma} : \boldsymbol{\Lambda}^{vp}(\boldsymbol{\sigma}) - f^{vp}(T,p) \right\rangle}{K_a(T)} \right)^{N_a(T)-1} \partial_p f^{vp}(T,p).$$

Solving (5.45) for the correction in ξ at the given iteration yields

$$\Delta\xi_{n+1}^{(k)} = \frac{-\Phi^{t(k)}_{\ n+1} + A_1^t \Delta\dot{p}_{n+1}^{(k)}}{A_2^t}, \tag{5.47}$$

where

$$\begin{aligned} A_1^t &= \partial_{\boldsymbol{\sigma}} \Phi^{t(k)}_{\ n+1} : \boldsymbol{\mathcal{C}}_{n+1}^{(k)} \boldsymbol{\Lambda}^{vp(k)}_{\ n+1} \Delta t; \\ A_2^t &= \partial_\xi \Phi^{t(k)}_{\ n+1} \mp \partial_{\boldsymbol{\sigma}} \Phi^{t(k)}_{\ n+1} : \boldsymbol{\mathcal{C}}_{n+1}^{(k)} \left(\partial_{\boldsymbol{\sigma}} \Phi^{t(k)}_{\ n+1} + D(\boldsymbol{\Lambda}^{t(k)}_{\ n+1} + \boldsymbol{\Lambda}^{tp(k)}_{\ n+1}) \right). \end{aligned} \tag{5.48}$$

Note that if viscoplastic yield is not occuring ($\lambda^{vp} = 0$), equation (5.47) with $\Delta\dot{p}_{n+1}^{(k)} = \dot{p}_{n+1}^{(k)} = 0$ is used to apply the RMA to the evolution of $\{\xi, \boldsymbol{\varepsilon}^t, \boldsymbol{\varepsilon}^{tp}\}$ while $\{\dot{p}, p, \boldsymbol{\varepsilon}^{vp}\}$ remain constant. Likewise rearranging (5.46) to find the viscoplastic increment gives

$$\Delta\dot{p}_{n+1}^{(k)} = \frac{-\Phi^{vp(k)}_{\ n+1} + A_1^{vp} \Delta\xi_{n+1}^{(k)}}{A_2^{vp}}. \tag{5.49}$$

where

$$\begin{aligned} A_1^{vp} &= \pm \partial_{\boldsymbol{\sigma}} \lambda^{vp(k)}_{\ n+1} : \boldsymbol{\mathcal{C}}_{n+1}^{(k)} \left(\partial_{\boldsymbol{\sigma}} \Phi^{t(k)}_{\ n+1} + D(\boldsymbol{\Lambda}^{t(k)}_{\ n+1} + \boldsymbol{\Lambda}^{tp(k)}_{\ n+1}) \right); \\ A_2^{vp} &= \partial_p \lambda^{vp(k)}_{\ n+1} \Delta t - \partial_{\boldsymbol{\sigma}} \lambda^{vp(k)}_{\ n+1} : \boldsymbol{\mathcal{C}}_{n+1}^{(k)} \boldsymbol{\Lambda}^{vp(k)}_{\ n+1} \Delta t - 1. \end{aligned} \tag{5.50}$$

The relation (5.49) with $\Delta\xi_{n+1}^{(k)} = 0$ is used directly when only viscoplastic yield is occurring ($\Phi^t \leq 0$).

Solving the two equations (5.47) and (5.49) for the two unknowns $\Delta\xi_{n+1}^{(k)}$ and $\Delta\dot{p}_{n+1}^{(k)}$, we arrive at the final form for calculating the simultaneous inelastic corrections for the transformation and viscoplastic deformation processes. This is given for

transformation as

$$\Delta\xi_{n+1}^{(k)} = \frac{-\Phi^{t(k)}_{\ n+1} A_2^{vp} - \Phi^{vp(k)}_{\ n+1} A_1^t}{A_2^t A_2^{vp} - A_1^t A_1^{vp}}, \tag{5.51}$$

while for the viscoplastic phenomena, the simultaneous correction is given as

$$\Delta\dot{p}_{n+1}^{(k)} = \frac{-\Phi^{vp(k)}_{\ n+1} A_2^t - \Phi^{t(k)}_{\ n+1} A_1^{vp}}{A_2^t A_2^{vp} - A_1^t A_1^{vp}}. \tag{5.52}$$

Transformation ends when $\xi_{n+1}^{(k+1)}$ reaches one of two limits given in (3.25). A given bound, if reached, will be reached during the iterative scheme within a single loading increment. Therefore, the implemented algorithm must allow a switch from (5.52) to (5.49) when $\xi_{n+1}^{(k)}$ reaches a bound, implying $\Delta\xi_{n+1}^{(k)} = 0$.

Substituting (5.38) into (5.37) and (5.33), it can be seen that the inelastic strains can be iteratively updated as follows:

$$\boldsymbol{\varepsilon}^{t(k+1)}_{\ n+1} = \boldsymbol{\varepsilon}^{t(k)}_{\ n+1} + \Delta\xi_{n+1}^{(k)} \boldsymbol{\Lambda}^{t(k)}_{\ n+1}, \quad \boldsymbol{\varepsilon}^{tp(k+1)}_{\ n+1} = \boldsymbol{\varepsilon}^{tp(k)}_{\ n+1} + \Delta\xi_{n+1}^{(k)} \boldsymbol{\Lambda}^{tp(k)}_{\ n+1},$$

$$\boldsymbol{\varepsilon}^{vp(k+1)}_{\ n+1} = \boldsymbol{\varepsilon}^{vp(k)}_{\ n+1} + \Delta\dot{p}_{n+1}^{(k)} \Delta t \boldsymbol{\Lambda}^{vp(k)}_{\ n+1}.$$

These three inelastic strains and the updated elastic stiffness are used in (5.35) to calculate an updated stress, which is itself used to calculate the updated transformation and yield functions. The iterative scheme then continues until $\Phi^{t(k+1)}_{\ n+1}$ and $\Phi^{vp(k+1)}_{\ n+1}$ are smaller than some tolerance.

3. Continuum tangent modulus

As in Chapter III, Section A.4 and Chapter IV, Section C.2, we again derive the continuum tangent moduli required by the global FEA solver. Note that the derivation and results for this coupled transformation-viscoplasticity model appear almost identical to those for the coupled transformation-plasticity model of Chapter IV. To begin, the constitutive relation (5.4) is rewritten in differential form and the evolution equations (2.20) and (5.7) are substituted. Note that the increment in time is a

user-specified solution parameter and is not subject to local algorithmic determination, although global (e.g., Abaqus) algorithms may adjust this time increment from loading step to loading step. Rewriting in terms of stress, this gives the following (cf. (5.39))

$$\mathrm{d}\boldsymbol{\sigma} = \boldsymbol{\mathcal{C}} : \left[\mathrm{d}\boldsymbol{\varepsilon} - \boldsymbol{\alpha}\, \mathrm{d}T \mp \mathrm{d}\xi \left(\partial_{\boldsymbol{\sigma}} \Phi^t + D(\boldsymbol{\Lambda}^t + \boldsymbol{\Lambda}^{tp}) \right) - \mathrm{d}\dot{p}\, \boldsymbol{\Lambda}^{vp} \Delta t \right]. \tag{5.53}$$

Both the transformation function (2.32) and the viscoplastic constraint equation (5.29) must be satisfied for all acceptable solutions, and taking the differential of these relations at a specified constant temperature ($\mathrm{d}T = 0$) results in two relations (analogous to the classical "consistency conditions")

$$\begin{aligned} \mathrm{d}\Phi^t &= \partial_{\boldsymbol{\sigma}} \Phi^t : \mathrm{d}\boldsymbol{\sigma} + \partial_\xi \Phi^t \, \mathrm{d}\xi = 0, \\ \mathrm{d}\Phi^{vp} &= \partial_{\boldsymbol{\sigma}} \Phi^{vp} : \mathrm{d}\boldsymbol{\sigma} + \partial_p \Phi^{vp} \, \mathrm{d}p + \partial_{\dot{p}} \Phi^{vp} \, \mathrm{d}\dot{p} = 0, \end{aligned} \tag{5.54}$$

where we note that $\mathrm{d}p = \mathrm{d}\dot{p}\, \Delta t$ for a specified constant time increment Δt. Expressions for the differential of the rate of effective viscoplastic strain $\mathrm{d}\dot{p}$ and the martensitic volume fraction $\mathrm{d}\xi$ are obtained by substituting $\mathrm{d}\boldsymbol{\sigma}$ from (5.53) into (5.54). Noting the form of Φ^{vp} and the definitions of A_1^t and A_2^t as given in (5.48) and of A_1^{vp} and A_2^{vp} as given in (5.50), this gives

$$\mathrm{d}\xi = \frac{-\partial_{\boldsymbol{\sigma}} \Phi^t : \boldsymbol{\mathcal{C}}\, \mathrm{d}\boldsymbol{\varepsilon} + A_1^t \, \mathrm{d}\dot{p}}{A_2^t}. \tag{5.55}$$

$$\mathrm{d}\dot{p} = \frac{-\partial_{\boldsymbol{\sigma}} \lambda^{vp} : \boldsymbol{\mathcal{C}}\, \mathrm{d}\boldsymbol{\varepsilon} + A_1^{vp} \, \mathrm{d}\xi}{A_2^{vp}}. \tag{5.56}$$

Solving the two equations (5.55) and (5.56) for the two unknowns $\mathrm{d}\xi$ and $\mathrm{d}\dot{p}$, we find for transformation

$$\mathrm{d}\xi = \frac{-A_2^{vp} \partial_{\boldsymbol{\sigma}} \Phi^t : \boldsymbol{\mathcal{C}}\, \mathrm{d}\boldsymbol{\varepsilon} - A_1^t \partial_{\boldsymbol{\sigma}} \lambda^{vp} : \boldsymbol{\mathcal{C}}\, \mathrm{d}\boldsymbol{\varepsilon}}{A_2^t A_2^{vp} - A_1^t A_1^{vp}}, \tag{5.57}$$

while for plastic yielding, the differential is given as

$$\mathrm{d}\dot{p} = \frac{-A_2^t \partial_{\boldsymbol{\sigma}} \lambda^{vp} : \boldsymbol{\mathcal{C}}\, \mathrm{d}\boldsymbol{\varepsilon} \; - A_1^{vp} \partial_{\boldsymbol{\sigma}} \Phi^t : \boldsymbol{\mathcal{C}}\, \mathrm{d}\boldsymbol{\varepsilon}}{A_2^t A_2^{vp} - A_1^t A_1^{vp}}. \tag{5.58}$$

Now (5.57) and (5.58) can be used to eliminate $\mathrm{d}\xi$ and $\mathrm{d}\dot{p}$, respectively, in (5.53), giving

$$\begin{aligned} \mathrm{d}\boldsymbol{\sigma} = \boldsymbol{\mathcal{C}}\, \mathrm{d}\boldsymbol{\varepsilon} \quad &\pm \quad \boldsymbol{\mathcal{C}} \left[\frac{A_2^{vp} \partial_{\boldsymbol{\sigma}} \Phi^t : \boldsymbol{\mathcal{C}}\, \mathrm{d}\boldsymbol{\varepsilon} \; + A_1^t \partial_{\boldsymbol{\sigma}} \lambda^{vp} : \boldsymbol{\mathcal{C}}\, \mathrm{d}\boldsymbol{\varepsilon}}{A_2^t A_2^{vp} - A_1^t A_1^{vp}} \; \left(\partial_{\boldsymbol{\sigma}} \Phi^t + D(\boldsymbol{\Lambda}^t + \boldsymbol{\Lambda}^{tp}) \right) \right] \\ &+ \quad \boldsymbol{\mathcal{C}} \left[\frac{A_2^t \partial_{\boldsymbol{\sigma}} \lambda^{vp} : \boldsymbol{\mathcal{C}}\, \mathrm{d}\boldsymbol{\varepsilon} \; + A_1^{vp} \partial_{\boldsymbol{\sigma}} \Phi^t : \boldsymbol{\mathcal{C}}\, \mathrm{d}\boldsymbol{\varepsilon}}{A_2^t A_2^{vp} - A_1^t A_1^{vp}} \; \boldsymbol{\Lambda}^{vp} \Delta t \right]. \end{aligned} \tag{5.59}$$

By applying the definition and identities related to the tensor product (see footnote in Chapter III, Section A.4), this can be rearranged to find the continuum tangent modulus, given by $\boldsymbol{\mathcal{L}}$ per

$$\begin{aligned} \mathrm{d}\boldsymbol{\sigma} &= \left\{ \boldsymbol{\mathcal{C}} + \frac{A_2^t \mathbf{B}_1^{vp} \otimes \mathbf{B}_2^{vp} + A_1^{vp} \mathbf{B}_1^{vp} \otimes \mathbf{B}_2^t \pm [A_2^{vp} \mathbf{B}_1^t \otimes \mathbf{B}_2^t + A_1^t \mathbf{B}_1^t \otimes \mathbf{B}_2^{vp}]}{A_2^t A_2^{vp} - A_1^t A_1^{vp}} \right\} \mathrm{d}\boldsymbol{\varepsilon} \\ &= \boldsymbol{\mathcal{L}}\, \mathrm{d}\boldsymbol{\varepsilon}\,, \end{aligned} \tag{5.60}$$

where the second-order tensors $\mathbf{B}_1^t$, $\mathbf{B}_2^t$, $\mathbf{B}_1^{vp}$, and $\mathbf{B}_2^{vp}$ are defined as

$$\begin{gathered} \mathbf{B}_1^t = \boldsymbol{\mathcal{C}} \left(\partial_{\boldsymbol{\sigma}} \Phi^t + D(\boldsymbol{\Lambda}^t + \boldsymbol{\Lambda}^{tp}) \right); \quad \mathbf{B}_2^t = \boldsymbol{\mathcal{C}} \partial_{\boldsymbol{\sigma}} \Phi^t; \\ \mathbf{B}_1^{vp} = \boldsymbol{\mathcal{C}} \boldsymbol{\Lambda}^{vp} \Delta t; \quad \mathbf{B}_2^{vp} = \boldsymbol{\mathcal{C}} \partial_{\boldsymbol{\sigma}} \lambda^{vp}. \end{gathered} \tag{5.61}$$

In the case of phase transformation only (i.e., $\lambda^{vp} = \dot{p} = 0$), the continuum tangent modulus $\boldsymbol{\mathcal{L}}$ is given by (cf. Chapter III, Section A.4):

$$\boldsymbol{\mathcal{L}} = \boldsymbol{\mathcal{C}} + \frac{\mathbf{B}_1^t \otimes \mathbf{B}_2^t}{A_2^t}. \tag{5.62}$$

Likewise, in the case of viscoplastic yielding only (i.e., $\Phi^t \leq 0$), the tangent modulus is given by

$$\boldsymbol{\mathcal{L}} = \boldsymbol{\mathcal{C}} + \frac{\mathbf{B}_1^{vp} \otimes \mathbf{B}_2^{vp}}{A_2^{vp}}. \tag{5.63}$$

4. Summary of implementation

Table VII provides a summary of the full RMA (convex cutting plane) needed to integrate the constitutive relations for the transformation-viscoplastic yield model in an FEA framework while considering large rotations.

Table VII. RMA for modeling of transformation and viscoplastic phenomena in SMAs.

1. Initialize

a. Rotate all tensors from last increment n by $\boldsymbol{\mathcal{Q}}_{n+1}$

b. Let $k = 0$, $\mathbf{x}_{n+1}^{(0)} = \mathbf{x}_n$ where $\mathbf{x} = \{\xi, \boldsymbol{\varepsilon}^t, \boldsymbol{\varepsilon}^{tp}, \dot{p}, p, \boldsymbol{\varepsilon}^{vp}, \boldsymbol{\mathcal{C}}, \boldsymbol{\alpha}\}$

2. Elastic Prediction

a. $\boldsymbol{\sigma}_{n+1}^{(0)} = \boldsymbol{\mathcal{C}}_{n+1}^{(0)} \left[\boldsymbol{\varepsilon}_{n+1} - \boldsymbol{\alpha}(T_{n+1} - T_0) - \boldsymbol{\varepsilon}^{t\,(0)}_{n+1} - \boldsymbol{\varepsilon}^{tp\,(0)}_{n+1} - \boldsymbol{\varepsilon}^{vp\,(0)}_{n+1}\right]$

b. Find $\Phi^{t\,(0)}_{n+1}$ and $\lambda^{vp\,(0)}_{n+1}$.

c. IF $\Phi^{t\,(0)}_{n+1} \leq 0$ AND $\lambda^{vp\,(0)}_{n+1} = 0$ THEN EXIT (response elastic).

3. Transformation Correction (no viscoplastic deformation)

a. IF $\Phi^{t\,(0)}_{n+1} > 0$ AND $f^{p\,(0)}_{n+1} = 0$ THEN CONTINUE ELSE GOTO 4.

b. Find $\Delta\xi_{n+1}^{(k)}$ via (5.47) with $\Delta\dot{p}_{n+1}^{(k)} = 0$.

c. Find $\xi_{n+1}^{(k+1)}$ per $(5.38)_1$ and $\boldsymbol{\varepsilon}^{t\,(k+1)}_{n+1}$ and $\boldsymbol{\varepsilon}^{tp\,(k+1)}_{n+1}$ per (5.53).

d. IF $\xi_{n+1}^{(k+1)}$ within bounds per (3.25) THEN CONTINUE ELSE set $\xi_{n+1}^{(k+1)}$ to violated bound and set $\Delta\xi_{n+1}^{(k)} = 0$.

e. $\boldsymbol{\sigma}_{n+1}^{(k+1)} = \boldsymbol{\mathcal{C}}_{n+1}^{(k+1)} \left[\boldsymbol{\varepsilon}_{n+1} - \boldsymbol{\alpha}(T_{n+1} - T_0) - \boldsymbol{\varepsilon}^{t\,(k+1)}_{n+1} - \boldsymbol{\varepsilon}^{tp\,(k+1)}_{n+1} - \boldsymbol{\varepsilon}^{vp}{}_{n}\right]$

f. IF $\Phi^{t\,(k+1)}_{n+1} > TOL^t$ per (2.32) THEN CONTINUE ELSE EXIT

g. Increment k and GOTO 3b

4. Viscoplastic Correction (no transformation)

a. IF $\lambda^{vp\,(0)}_{n+1} > 0$ AND $\Phi^{t\,(0)}_{n+1} \leq 0$ THEN CONTINUE ELSE GOTO 5.

b.–g.: Analogous to 3 above, where $\Phi^{vp} < TOL^{vp}$ indicates convergence

5. Transformation-Viscoplastic Correction

a. IF $\lambda^{vp\,(0)}_{n+1} > 0$ AND $\Phi^{t\,(0)}_{n+1} > 0$ THEN CONTINUE ELSE EXIT.

b. Find $\Delta\xi_{n+1}^{(k)}$ and $\Delta\dot{p}_{n+1}^{(k)}$ via (5.51) and (5.52).

c. Find $\xi_{n+1}^{(k+1)}$ and $\dot{p}_{n+1}^{(k+1)}$ per (5.38), while $p_{n+1}^{(k+1)} = p_n + \Delta t \dot{p}_{n+1}^{(k+1)}$;
find $\boldsymbol{\varepsilon}^{t\,(k+1)}_{n+1}$, $\boldsymbol{\varepsilon}^{tp\,(k+1)}_{n+1}$, and $\boldsymbol{\varepsilon}^{vp\,(k+1)}_{n+1}$ per (5.53).

d. IF $\xi_{n+1}^{(k+1)}$ within bounds per (3.25) THEN CONTINUE ELSE set $\xi_{n+1}^{(k+1)}$ to violated bound and set $\Delta\xi_{n+1}^{(k)} = 0$.

e. $\boldsymbol{\sigma}_{n+1}^{(k+1)} = \boldsymbol{\mathcal{C}}_{n+1}^{(k+1)} \left[\boldsymbol{\varepsilon}_{n+1} - \boldsymbol{\alpha}(T_{n+1} - T_0) - \boldsymbol{\varepsilon}^{t\,(k+1)}_{n+1} - \boldsymbol{\varepsilon}^{tp\,(k+1)}_{n+1} - \boldsymbol{\varepsilon}^{vp\,(k+1)}_{n+1}\right]$

f. IF $\Phi^{t\,(k)}_{n+1} > TOL^t$ OR $\Phi^{vp\,(k)}_{n+1} > TOL^{vp}$ THEN GOTO 5i

g. IF $\Delta\xi_{n+1} = \xi_{n+1}^{(k+1)} - \xi_n$ has wrong sign, set $k = 0$ and GOTO 4b ELSE
IF $\Delta p_{n+1} = p_{n+1}^{(k+1)} - p_n \leq 0$, set $k = 0$ and GOTO 3b ELSE EXIT

h. Find $\Phi^{t\,(k+1)}_{n+1}$, $\Phi^{vp\,(k+1)}_{n+1}$ per (2.32), (5.29), increment k, and GOTO 5b

C. Model Calibration and Three-Dimensional Structural Analysis

To demonstrate the capabilities of this new tool, the implemented model of Section B is used to predict the response of four different bodies subjected to varying thermal and mechanical inputs for a total of five analysis cases. The Abaqus Unified Finite Element framework [136] is again used as the FEA solver where the implementation is coded in a new UMAT.

The first analysis considers the response at a single material point and is associated with experimental compression results taken from a cylindrical specimen, demonstrating the ability of the model and implementation to capture a known data set and then to predict the evolution of an unknown one. Following this, the first three-dimensional analysis considers this same material specimen loaded in the same way, and the effects of the 3-D loading applied during the experimentation are assessed, including specimen-grip interaction. The second 3-D analysis considers this same body (cylindrical compression specimen) and assesses the ability of the model to predict its response under *transverse* loading. The third analysis, using the material properties from the first two, considers the coupled transformation-viscoplastic yield response at a stress concentration, specifically a circumferential notch in a cylindrical tensile specimen. The fourth continues to assume the same HTSMA properties, and examines the response of a spring undergoing large deflections. Finally, a fifth example considers a conventional SMA (transformation temperatures below $100\,^{\circ}\mathrm{C}$). It is provided to demonstrate the utility of this new model in capturing the shape-setting behavior in a material such as near-equiatomic NiTi.

1. Model calibration and simulation of experiments

To begin, the results from an experimental study of an HTSMA with a composition of $Ti_{50}Pd_{40}Ni_{10}$ (at%) [96] are used to calibrate the 3-D model. The results from conventional creep tests and isobaric actuation experiments are both used. For each experiment type, the nominal strain data is derived from the change in length of a cylindrical specimen normalized by specimen length (6 mm in diameter, 12 mm in length), and the nominal stress is taken from the total applied force normalized by specimen cross-sectional area. During isobaric loading, these specimens were subjected to constant compressive nominal stresses (100 MPa and 200 MPa), where the temperature rate during cooling and heating was 2 °C/min. The derived properties are given in Table VIII. The conventional SMA elastic and transformation parameters were calibrated per the methods described in earlier chapters.

The new parameters introduced in this chapter are those dealing with the TRIP strain (i.e., the functional form of f^{tp}) and the creep rate (i.e., the parameters needed in the functional form of λ^{vp}). The calibration of these was discussed in Section A.5 Examining the experiments (see [96]), It was observed that, for the thermomechanical paths applied, consideration of an elastic domain was not necessary and the material hardening was negligible ($f^{vp}(T,p) = 0$). This implies that a suitable form for $K_a(T)$ is that given by (5.15). Further, no temperature dependence was observed in the parameter N_a.

The calibrated model is used to simulate the calibration experiments by analyzing a two-element prismatic bar under compressive loading, where the boundary conditions are chosen to provide a homogenous response throughout the body. The results can be seen in Fig. 45a. Note how the ability to capture smooth transformation hardening increases the fidelity of the simulation. Fig. 45b illustrates the predictive

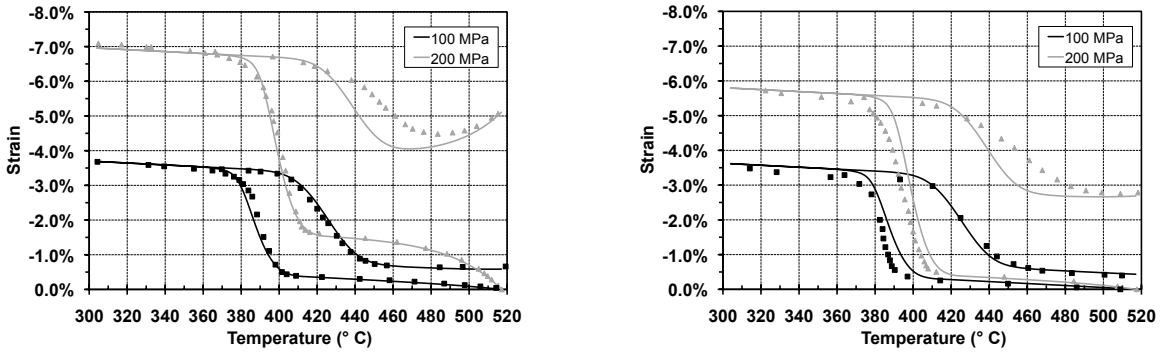

(a) Experimental results and analytical *simulation* (2 °C/min)

(b) Experimental results and analytical *prediction* (20 °C/min)

Fig. 45. Compressive strain/temperature response of a $Ti_{50}Pd_{40}Ni_{10}$ (at%) HTSMA under constant applied stresses given two applied temperature rates.

capabilities of the model and implementation by considering additional experiments performed at a higher thermal rate (20 °C/min), where creep is less pronounced. Recall that the model was calibrated using only 2 °C/min data.

Table VIII. Material properties for $Ti_{50}Pd_{40}Ni_{10}$ (at%) used to calibrate the SMA transformation-viscoplastic yield model (derived from isobaric compressive experiments, $|\dot{T}| = 2\,^{\circ}\mathrm{C}/\mathrm{min}$).

Parameter(s)	**Value(s) or Functional Form(s)**
(Thermoelastic Behavior)	
E^A, E^M	32 GPa, 57 GPa
$\nu^A = \nu^M$	0.33
α	2.8E-5 / °C
(Phase Diagram)	
M_s, M_f, A_s, A_f	407 °C, 350 °C, 372 °C, 456 °C
$C^M\big\|_{\bar{\sigma}=150\,MPa}$, $C^A\big\|_{\bar{\sigma}=150\,MPa}$	12.0 MPa/ °C, 6.0 MPa/ °C
(Maximum Transformation Strain and Smooth Hardening)	
$H^{cur}(\bar{\sigma})$	$= 0.0042 + (0.052 - 0.0042)\left(1 - \exp(240\bar{\sigma}/E^A)\right)$
n_1, n_2, n_3, n_4	0.30, 0.10, 0.20, 0.25
(Transformation-Induced Plastic Strain)	
$f^{tp}(\bar{\sigma})$	$=$9.00E-5$-(0.640/E^A)\bar{\sigma} + (410/{E^A}^2)\bar{\sigma}^2$
(Viscoplastic Modeling Constants)	
$K_a(T)^*$	$= [0.1368 \exp(-197.7/(0.00831T))]^{-1/N_a}$
N_a	4

* taken from the form of (5.15)

2. Actuation response of HTSMA compression specimen

The experiments and subsequent calibration described in Section C.1 are dependent on the assumption that the averaged structural response of the compressive testing specimen is representative of the constitutive response of the material itself. Such an assumption is especially suitable for tensile testing because common wire or "dog-bone" specimens provide a geometrically homogeneous gauge section sufficiently distanced from stress concentrations at the grips. Compression testing, however, does not allow for long gauge sections as high aspect ratio specimens buckle more easily than those with a low aspect ratio. A minimum recommended aspect ratio is 2:1 (length to diameter) [158], as was used in the currently considered experimental effort [96]. In this example, the same compressive testing specimen is analyzed given the same thermomechanical loading path applied during experimentation to investigate the effects that 3-D loading conditions (end effects due to gripping, etc.) have on the internal and averaged responses. This allows one to assess the accuracy of the properties derived from the low AR specimen in describing *constitutive* response.

The boundary value problem consists of loading a solid cylinder in compression where the cylinder dimensions match those of the experimental specimen. The specimen is modeled assuming both axisymmetry and a symmetric bisection of the specimen length. The compression grip is modeled as a rigid planar surface. Abaqus contact algorithms were utilized to account for the grip-specimen interface [136], and a coefficient of friction of 0.2 was used, determined from simple experiments. A 200 MPa nominal constant stress is applied by specifying a 5655 N total downward force on the reference point of the rigid grip surface. With this force held constant, a spatially homogenous temperature evolution was then applied with the same average rate as was used during the calibration experiments (2 °C/min).

The results of this analysis are shown in Fig. 46 and Fig. 47. The predicted evolution in grip displacement is illustrated in Fig. 46a. The distribution of equivalent (or Mises) stress $\bar{\sigma}$ and martensitic volume fraction ξ during forward and reverse transformation are shown in Fig. 46b and Fig. 46c, while the stress and effective viscoplastic strain (p) distributions are shown in Fig. 46d (reverse transformation completed). Clearly the solution fields are not spatially homogeneous, indicating that the average response of the specimen may not be representative of the constitutive response of the material. In Fig. 47, the predicted deformation response of the compressive specimen (grey line) is compared to the original experimental results. A small error is observed in the amount of recoverable transformation strain observed. This deviation from the results of Fig. 45 indicates that the model and FEA analysis tool are useful not only in the prediction of structural behavior in proposed applications, but that they may also have a role in the proper interpretation of some experimental results. This example in particular shows that the analysis tool can provide insight into assumptions regarding the relationship between local material behavior and overall structural response.

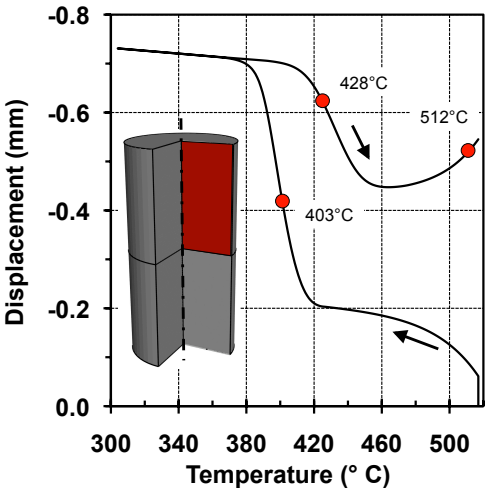

(a) Thermomechanical loading cycle and cylinder reference configuration (axisymmetric computational domain highlighted)

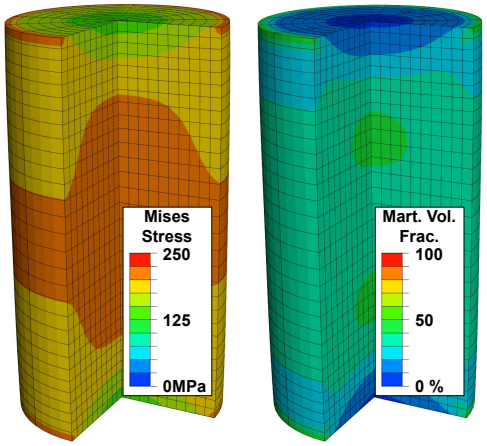

(b) Mises stress and martensitic volume fraction distributions at 403 °C during cooling

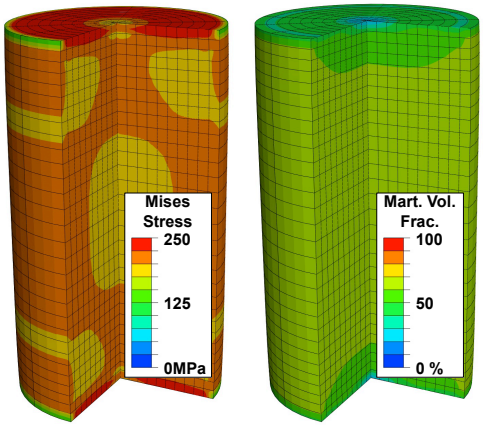

(c) Mises stress and martensitic volume fraction distributions at 428 °C during heating

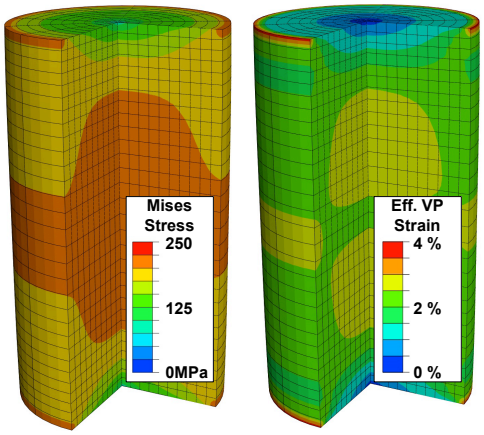

(d) Mises stress and effective viscoplastic strain distributions at 512 °C during heating

Fig. 46. Analytical results for isobaric thermal cycling of an HTSMA compression specimen illustrating non-homogeneous distribution of solution fields.

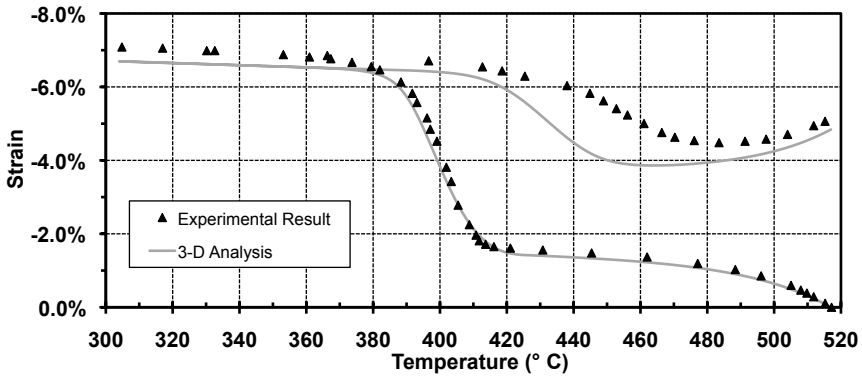

Fig. 47. Comparison of experimental compression testing results for $Ti_{50}Pd_{40}Ni_{10}$ (at%) to results of 3-D analysis applied to the same specimen given the original parameters of Table VIII (grey line).

3. Response of HTSMA cylindrical specimen under transverse loading

The second computational FEA example considers the structural analysis of the same cylindrical compression specimen previously discussed (nominal dimensions and material unchanged). Relative to the previous analysis, however, we rotate the specimen by 90° and analyze the thermally-induced displacements and internal state evolution given a constant applied *transverse* load (2500 N). The rate of heating and cooling is again 2 °C/min. To validate the analysis predictions, we then apply this same thermomechanical loading path to the physical specimen in an experimental setup and compare the results.

Material parameters for the analysis are taken directly from the calibration discussion above, and no additional recalibration is performed. For the experimental study, a portion of the specimen was polished away to provide a flat surface to mate with the lower compression grip, and this is accounted for in the FEA model. Generalized plane strain kinematics and a spatially homogeneous temperature distribution are assumed, and the model takes advantage of the symmetric specimen cross section. The experimental specimen and associated FEA model are shown in Fig. 48. A total of 2540 linear (4-node) elements (Abaqus designation `CPEG4`) are used to construct the mesh, and Abaqus contact algorithms are used to account for the interaction between the rigid upper grip and the lateral surface of the cylinder.

The thermomechanical loading path for the analysis consists of the following steps:

1. apply a 2500 N load to the specimen via a rigid plane surface at $T = 525\,^{\circ}\mathrm{C} > A_f$ (10 s elapsed time),

2. cool the specimen to $T = 300\,^{\circ}\mathrm{C} < M_f$ at 2°C/min,

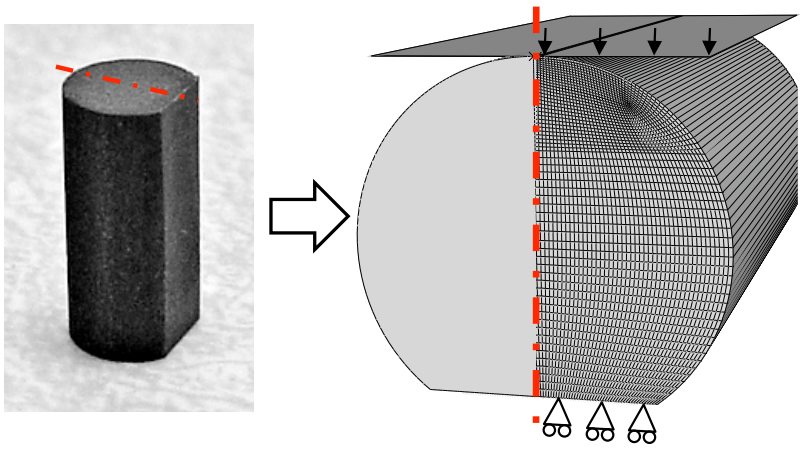

Fig. 48. HTSMA cylindrical specimen prepared for transverse loading and corresponding FEA model.

3. heat the specimen to $T = 525\,^{\circ}\mathrm{C} > A_f$ at $2^{\circ}\mathrm{C}/\mathrm{min}$.

The analysis predictions and experimental results for the transverse displacement of the specimen with respect to the applied temperature are shown in Figure 49. Considering that the analysis utilizes only material properties from standard compression testing [96] and that significant stress concentrations result from transverse loading, the predictive capabilities of the model and its implementation are quite good. Notice that the relative actuation deformation is closely captured while the creep trends, especially during heating, are also accounted for. In fact, it appears that the majority of the error is associated with the predictions of the TRIP strain due to the assumed strong dependence of this deformation on local stress level (regardless of temperatures, see Table VIII).

Examining the internal state of the transversely loaded cylinder throughout the thermal actuation cycle, we observe the interplay between the rate-dependent irrecoverable viscoplastic strain and the rate-independent recoverable transformation

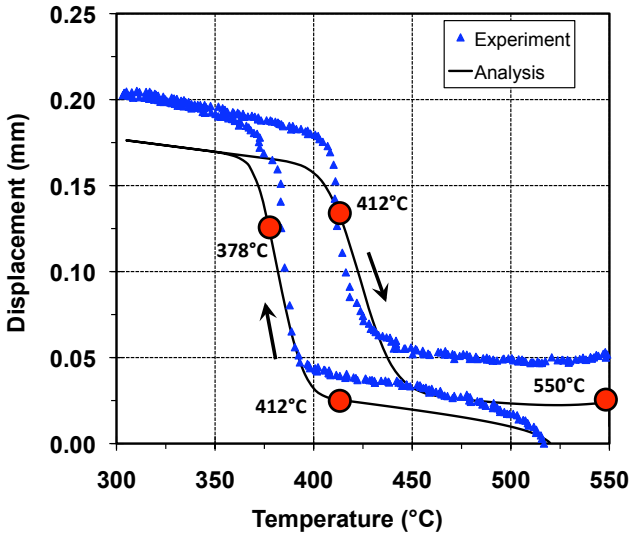

Fig. 49. Analysis predictions and experimental results for grip displacement vs. temperature for a transversely loaded HTSMA cylindrical specimen (2 °C/min temperature rates).

strains. Contour plots illustrating the distribution of two internal variables, effective viscoplastic strain p and martensitic volume fraction ξ, are shown in Fig. 50. The temperature states considered have been highlighted in Fig. 49. To begin, high stresses are generated in the regions nearest the compression grip during loading. Cooling at 2° C/min then allows sufficient time for these regions to generate viscoplastic strains, which can be observed in Fig. 50a. This relaxes the local stresses, transferring the load away from the centerline of the cross-section. As the martensitic transformation begins, the new regions of highest stress transform into martensite first (per the phase diagram [159]), and this can be seen in Fig. 50b. Conversely, during heating the regions of highest stress remain martensitic the longest, and this is seen in Fig. 50c. Finally, continued heating initiates further viscoplastic creep, and this is seen in Fig. 50d.

4. Viscoplastic deformation at circumferential notch

In the next analysis, the effects of loading rate on the response at a stress concentration are considered, where the material is the same HTSMA previously discussed. A *compact notched tensile* (CNT) specimen is analyzed [160]. The specimen consists of a long cylindrical bar (length of 40 mm, diameter of 9.5 mm) with a circumferential filleted notch at its midsection. This choice of geometry is inspired by the development of HTSMA wire actuators [161], which have a cylindrical shape and may be subject to stress concentrations due to fastening (e.g., clamping), damage, or other effects. Here the circumferential notch has a fillet radius and depth of 0.72 mm. This SMA component is modeled by assuming axisymmetry and further by taking advantage of symmetry about the midsection. This is shown in Fig. 51.

Loading is performed by application of a defined displacement (0.3 mm) at the end of the initially austenitic bar. The temperature was globally defined to be a constant 420 °C, which was 13 °C above the martensitic start temperature. The time to complete loading was varied from 0.1 hr to 10 hr, and the stresses generated were sufficient to initiate stress-induced transformation of austenite into martensite at some regions while also causing localized creep in the material.

The results of this analysis can be seen in Fig. 52, Fig. 53, and Fig. 54. Increased loading times (slower loading rates) allow the generation of greater amounts of viscoplastic strain, especially in the 10 hr case. This can be seen in Fig. 52. Because of the constant defined displacement, more viscoplastic strain leads to lower stress levels overall, per Fig. 53. This in turn reduces the amount of stress-induced martensite that can be formed from the original austenitic material, as shown in Fig. 54. Thus the rate of loading affects both the generation and evolution of recoverable and irrecoverable strains in the specimen.

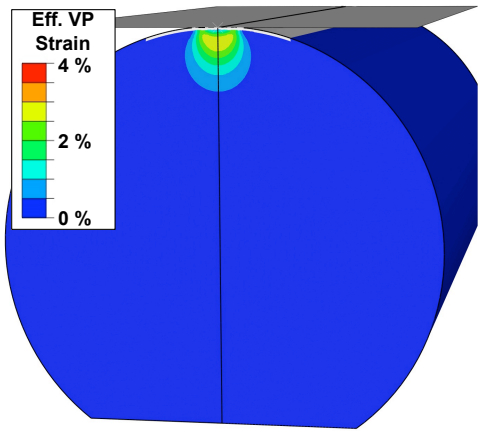

(a) Effective viscoplastic strain (Cooling, $T = 412\,^{\circ}\mathrm{C}$)

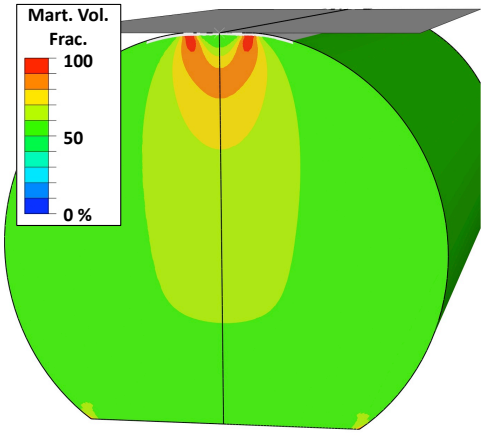

(b) Martensitic volume fraction (Cooling, $T = 378\,^{\circ}\mathrm{C}$)

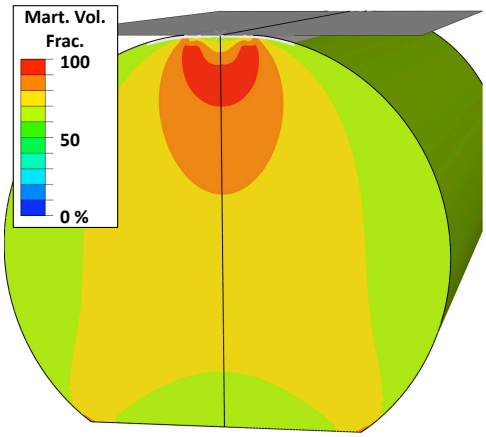

(c) Martensitic volume fraction (Heating, $T = 412\,^{\circ}\mathrm{C}$)

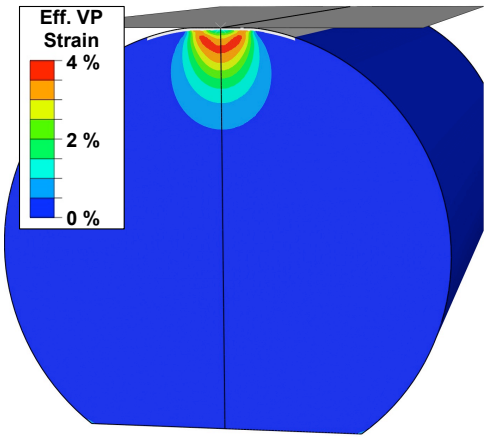

(d) Effective viscoplastic strain (Heating, $T = 550\,^{\circ}\mathrm{C}$)

Fig. 50. Viscoplastic strain and martensitic volume fraction contours for HTSMA cylinder under constant transverse load.

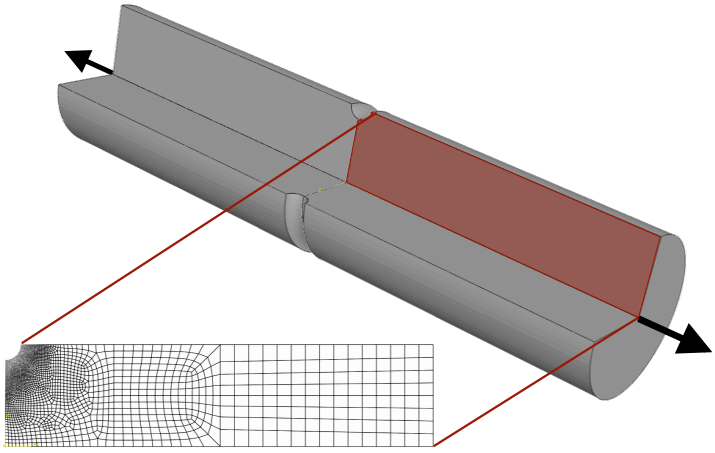

Fig. 51. Configuration of the *compact notched tensile* (CNT) specimen and associated computational domain.

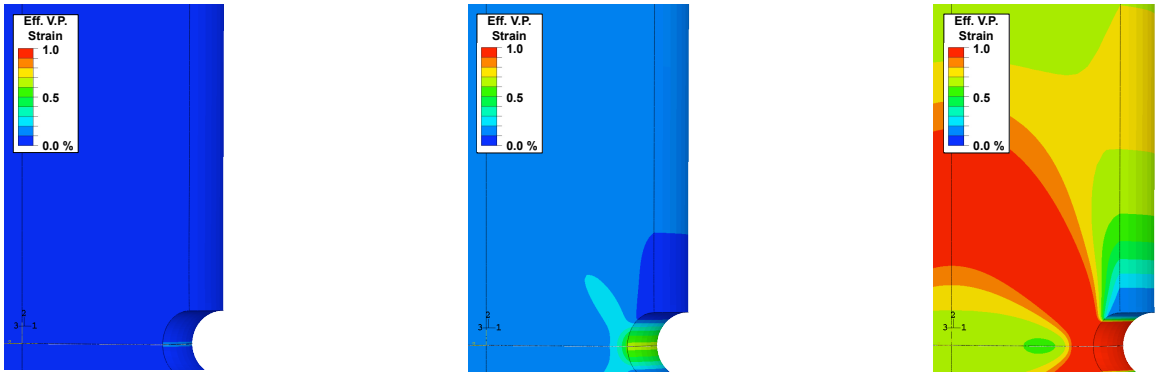

(a) Time to load: 0.1 hr

(b) Time to load: 1.0 hr

(c) Time to load: 10 hr

Fig. 52. Dependence of effective viscoplastic strain (p) distribution on rate of loading applied to the CNT specimen.

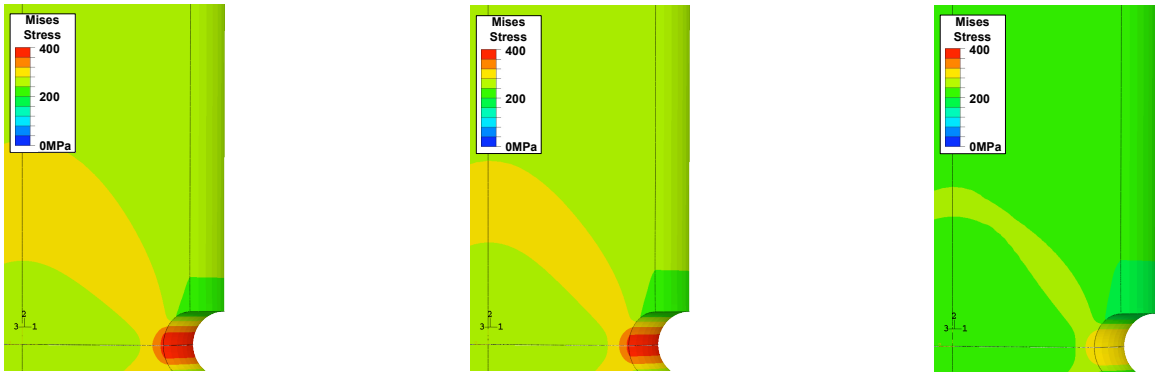

(a) Time to load: 0.1 hr

(b) Time to load: 1.0 hr

(c) Time to load: 10 hr

Fig. 53. Dependence of Mises equivalent stress ($\overline{\sigma}$) distribution on rate of loading applied to the CNT specimen.

5. Actuation response of HTSMA spring

Here we expand on the previous analysis by considering the same HTSMA material ($Ti_{50}Pd_{40}Ni_{10}$) utilized in a different, more structurally complex application: a helical spring providing thermally-induced actuation. It is described in a work on such HTSMA springs [162] that methods such as drawing or precision grinding can be

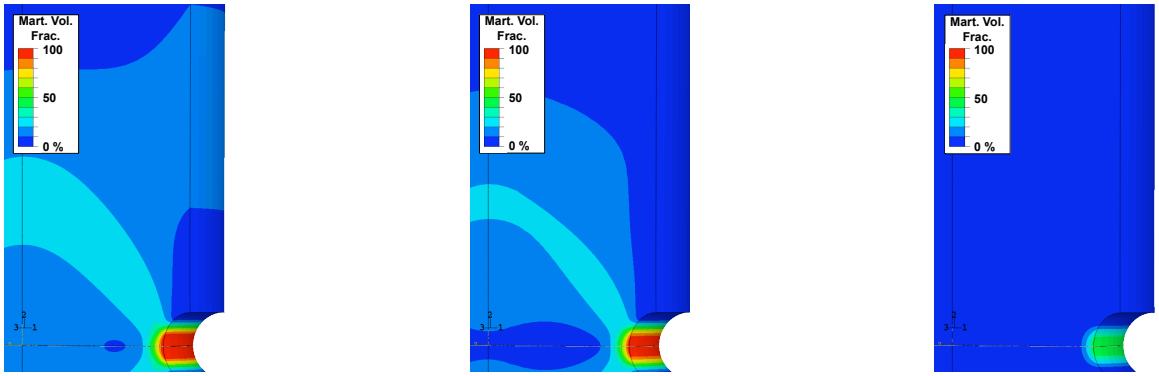

(a) Time to load: 0.1 hr

(b) Time to load: 1.0 hr

(c) Time to load: 10 hr

Fig. 54. Dependence of martensitic volume fraction (ξ) distribution on rate of loading applied to the CNT specimen.

used to reduce HTSMA rods to wire form, which can then be formed into springs. Helical springs, like beams, provide a structural method of maximizing the deflections attainable from even moderate transformation strains. However, in the case of HTSMAs, the effects of rate-dependent irrecoverable strains are also magnified and must be considered. The analysis of conventional SMA springs has been performed by other researchers, and large deformation formulations have been employed [163, 164], though rate-dependent irrecoverable strains have not been considered to date.

Motivated by published experimental work [162], the spring modeled here has a coil diameter of 12.7 mm and a wire diameter of 0.5 mm. One full coil (or "turn") is modeled in a three-dimensional space using second-order hexahedral elements with reduced integration (Abaqus designation `C3D20R`). The single coil is discretized such that its length is divided into 150 uniform segments while 32 elements make up the cross section, resulting in 4800 total elements. The boundary conditions consist of fixing the nodes at one end of the spring wire while applying a downward biasing force (parallel to the axis of the spring) to the other end of the spring wire. The reference geometry, the mesh through the cross-section, and the applied boundary conditions

are shown in Fig. 55a. The full thermomechanical loading path proceeds as follows:

1. Apply 0.25 N biasing load at $T = 517\,^{\circ}\mathrm{C}$ (material is austenitic, length of step is 1 sec).

2. Maintaining the biasing load, cool spring uniformly to $T = 380\,^{\circ}\mathrm{C}$ at constant rate,

3. Maintaining the biasing load, heat spring uniformly to $T = 517\,^{\circ}\mathrm{C}$ at constant rate.

In agreement with observed SMA spring behavior, this analysis predicts substantial deformation of the spring during actuation from an initially coiled shape towards a straight wire configuration. The total elongation of the single-coil spring is over 1000%. Though the local strains never exceed 2.6% at any point, non-linear geometric effects are important, especially the local rotations undergone by each material point. These rotations are accounted for by ensuring that the algorithm of Section B is implemented in an "incrementally objective" manner.[8]

The analysis results for the extension of the single-coil HTSMA spring given this loading path are shown in Fig. 55b for temperature rates of $2\,^{\circ}\mathrm{C}$/min and $20\,^{\circ}\mathrm{C}$/min (cf. Section C.2). As with the analysis of the compression specimen, the $2\,^{\circ}\mathrm{C}$/min rate is sufficiently slow to allow the spring to viscoplastically creep during cooling at $T > 450\,^{\circ}\mathrm{C}$. Additional creep is observed during heating back to $517\,^{\circ}\mathrm{C}$. The $20\,^{\circ}\mathrm{C}$/min rate results in less creep and thus less overall loss in recoverable actuation.

Another more interesting result highlights the coupling that exist between the transformation-induced strains and the viscoplastic strain. By examining the "gap"

[8]This is accomplished by using the method of Chapter III, Section A.5 and [50] and activating the non-linear geometry flag in the global solver (option `NLGEOM=YES` in Abaqus).

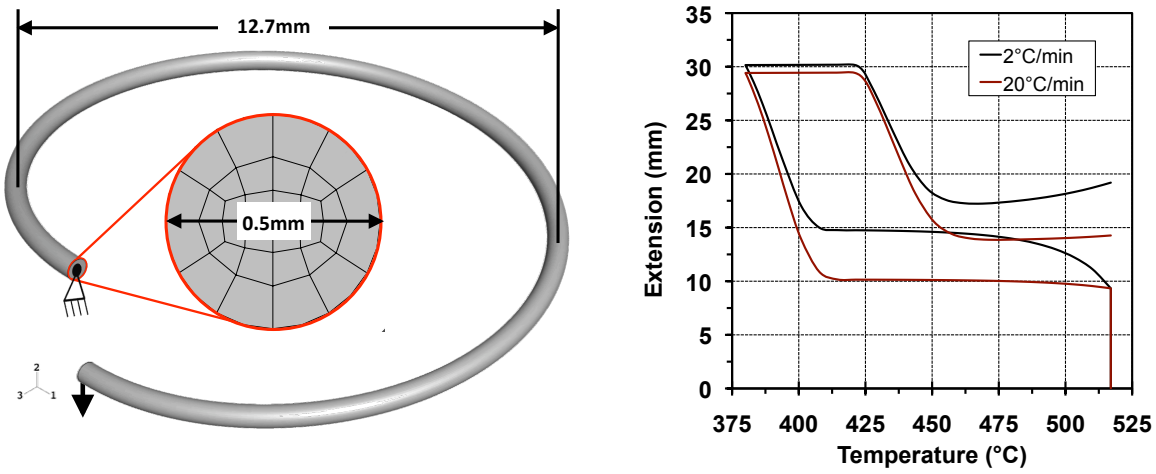

(a) Initial geometric configuration (including cross-sectional mesh) and applied boundary conditions

(b) Spring extension over thermal cycle (2 °C/min and 20 °C/min heating/cooling rates)

Fig. 55. Reference geometry, boundary conditions, and thermally-induced actuation results for the analysis of an HTSMA extensional spring under 0.25 N biasing load.

in the hysteresis at $T \approx 470\,^{\circ}\mathrm{C}$, it is clear that the slower thermal rate, which leads to more creep overall, results in *less* irrecoverable strain due to TRIP. In other words, less transformation-induced plastic strain has been generated due to an increase in generated viscoplastic strain. This is because the viscoplastic strain serves to relax the stresses where they are at their highest, homogenizing the stress state through the cross-section. Because the magnitude of TRIP strain is related to the square of the local stress magnitude (see the form of f^{tp} in Table VIII), viscoplastic relaxation of the stress near the wires surface results in decreased TRIP strain generation.

Detailed analysis results for the case of 2 °C/min cooling and heating are provided in Fig. 56. Here the deformation of the single-coil spring is shown at various points along the loading path (highlighted in Fig. 56a). The slow cooling at high

temperatures ($T > 450\,^{\circ}\mathrm{C}$) leads to the generation of viscoplastic strains throughout the spring, especially at the wire mid-length where torsional loads are the highest. Examining the cross-section at this point shows that the highest viscoplastic strains are generated on the surface of the wire as expected, where stresses are maximized. The same trend is observed in the distribution of martensitic volume fraction as the spring begins to transform (Fig. 56b). Substantial extension is observed during spring actuation although full forward transformation is not completed. As the spring is heated and reverse transformation begins, we see that the viscoplastic strains have not evolved appreciably but that the martensitic volume fraction at the wire surface has reached $\approx 50\%$ (Fig. 56c). Finally, as the spring is heated back toward its initial temperature, all martensite is transformed once again into austenite and a substantial portion of the deformation is recovered. However, additional viscoplastic strains are generated (exceeding 1% in some local material regions); The combination of viscoplastic and TRIP strains results in irrecoverable spring deformation (Fig. 56d).

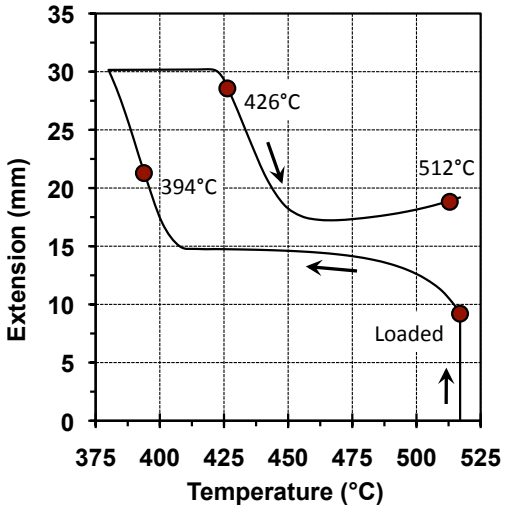

(a) Extension throughout thermal cycle applied to spring

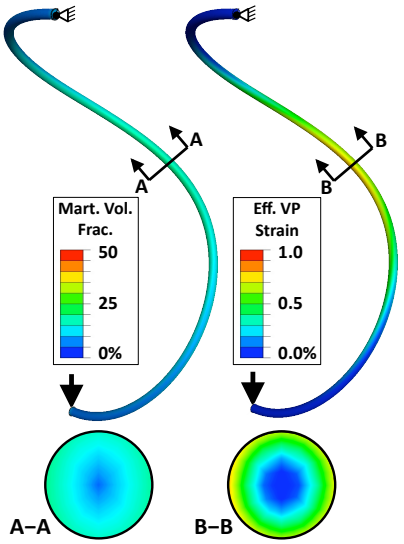

(b) Cooled to 394 °C

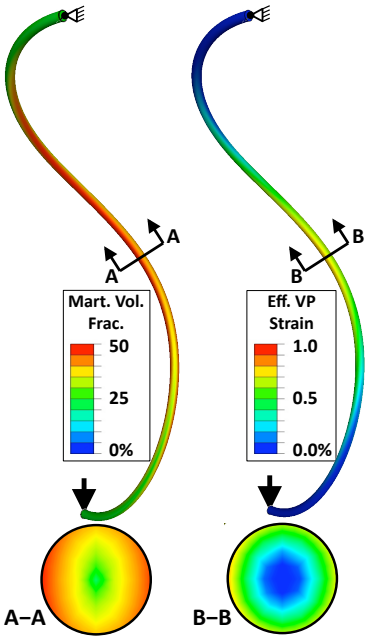

(c) Heated to 426 °C

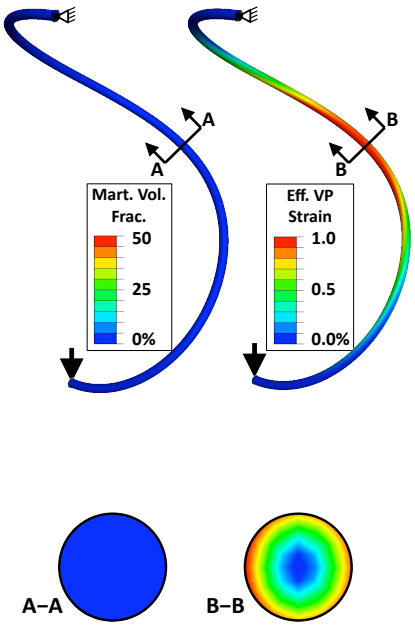

(d) Heated to 512 °C

Fig. 56. Evolution of martensitic volume fraction (ξ) and effective viscoplastic strain (p) for HTSMA spring heated and cooled at 2 °C/min (contour/deformation plots all of equal scale; deformation is *not* magnified).

6. Shape-setting of pseudoelastic SMA stent

For the last of the analyses considered herein, we shift our focus away from HTSMAs and consider instead the behavior of a near-equiatomic NiTi pseudoelastic medical stent during device processing. These devices represent the most common application of SMAs in the medical industry and are among one of the most well-known SMA applications [9, 10]. Some stent configurations are formed by first laser-cutting the complex structural forms from solid tubes of relatively small diameter [165]. An expansion step increases the stent diameter, which is then constrained in this expanded configuration. Exposure to high temperatures for some span of time relaxes the stresses generated during expansion, and, upon cooling and removal of the diameter constraints, a new unconstrained diameter is observed. This process of altering the force-free reference shape of an SMA structure by constraint and exposure to elevated temperatures is known as *shape setting* [165].

For the current analysis, nominal NiTi properties have been used to describe the conventional (i.e., fully recoverable) transformation behavior of the material (see [114], Table 2.4). The effects of TRIP, which can be minor in high quality medical-grade NiTi, are not considered. The viscoplastic model parameters were taken from conventional creep tests performed on nickel-rich NiTi and described in [166] (where the interpretation of [93] was most helpful; see Table 2 and Fig. 2 in the cited work). Of the viscoplastic studies performed on NiTi, the work of [166] considers temperatures and stress levels most applicable to common shape-setting conditions (i.e., $T \approx 500\,^{\circ}\mathrm{C}$). Specifically, if we consider the forms of (5.13) and (5.15), the viscoplastic material properties are described by

$$A = 1.0E11\ \mathrm{MPa}^{-N_a}\ \mathrm{s}^{-1}; \quad Q = 421.0\ \mathrm{kJ\ mol}^{-1};$$

$$R = 0.00831 \text{ kJ K}^{-1} \text{ mol}^{-1}; \qquad N_a = 5.$$

The full 3-D FEA model for the medical stent was obtained from Dassault Systèmes, who distribute Abaqus, and is available to the public as a benchmarking problem [167]. Here we consider the periodic axisymmetry of the structure and model two "legs" only; the model is meshed with 672 quadratic hexahedral elements with reduced integration (Abaqus designation `C3D20R`). Four elements are used through the bending thickness. The initial reference mesh is shown in Fig. 57a, where the computational domain (two legs) is highlighted. The large rotations experienced by the stent legs are accounted for by considering the same non-linear geometric effects as the previous analysis.

The thermomechanical loading path considered here is based on the common NiTi shape-setting process previously described. After shape setting, the device is taken through an additional crimp-release cycle to demonstrate the usefulness of the numerical tool in capturing both the shape setting and stress-induced transformation in a single multi-step analysis. The overall thermomechanical loading path is shown in Fig. 57b, where the temperature and outer diameter (OD) are plotted vs. time. The imposed thermal and boundary conditions applied during this one analysis are as follows:

I. Shape-setting

1. Increase stent outer diameter from $D = 1.47\,\text{mm}$ to $D = 6.04\,\text{mm}$ at $T = 22\,^{\circ}\text{C}$ (length of step: $1\,\text{min}$),
2. With diameter constrained, heat stent uniformly to $T = 500\,^{\circ}\text{C}$ (length of step: $5\,\text{min}$),
3. Maintain $T = 500\,^{\circ}\text{C}$ (length of step: $5\,\text{min}$),

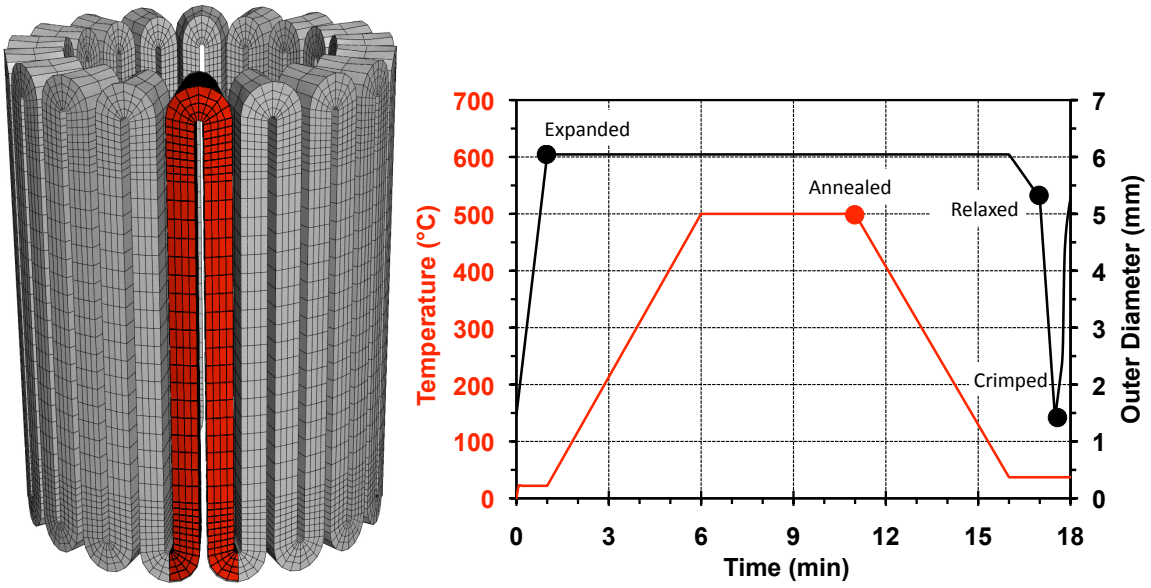

(a) Initial geometric configuration (computational domain highlighted)

(b) Thermomechanical loading path applied

Fig. 57. Reference geometry and thermomechanical loading path for the analysis of shape setting in an NiTi medical stent.

4. Cool uniformly to $T = 37\,^{\circ}\mathrm{C}$ (length of step: 5 min),

5. Release diameter constraints at $T = 37\,^{\circ}\mathrm{C}$ (length of step: 1 min).

II. Crimping and free deployment

6. Decrease stent outer diameter to $D = 1.47\,\mathrm{mm}$ at $T = 37\,^{\circ}\mathrm{C}$ (length of step: 30 sec),

7. Release diameter constraints at $T = 37\,^{\circ}\mathrm{C}$ (length of step: 30 sec).

The results of the NiTi stent shape-setting analysis are shown in Fig. 58 for four different solution states in the loading path. These four states are highlighted in Fig. 57b. For each state, the deformations of single leg and of the annular array

of stent legs are illustrated in addition to the stress, martensitic volume fraction, and effective viscoplastic strain contours. These results are useful in illustrating the qualitative evolution in the state of the SMA stent during shape-setting.

The initial expansion from the reference configuration causes local stresses sufficient to initiate and, in some regions, complete the transformation into martensite (Fig. 58a). Subsequent heating then transforms these regions back into austenite. The process of heating to and holding at 500 °C over the span of 10 min provides enough thermal energy and elapsed time to allow the generation of viscoplastic strains in the regions of highest stress. This relaxes stresses throughout the stent (Fig. 58b). After cooling, the diameter constraint is removed, reducing the stresses even further. Little additional viscoplastic strain generation occurs during cooling, and the elastic unloading causes a small decrease in the diameter (Fig. 58c). Finally, crimping the stent back toward its reference configuration results in internal effects analogous to the original expansion step: local regions reach high stress levels, inducing (but not quite completing) the stress induced martensitic transformation (Fig. 58d).

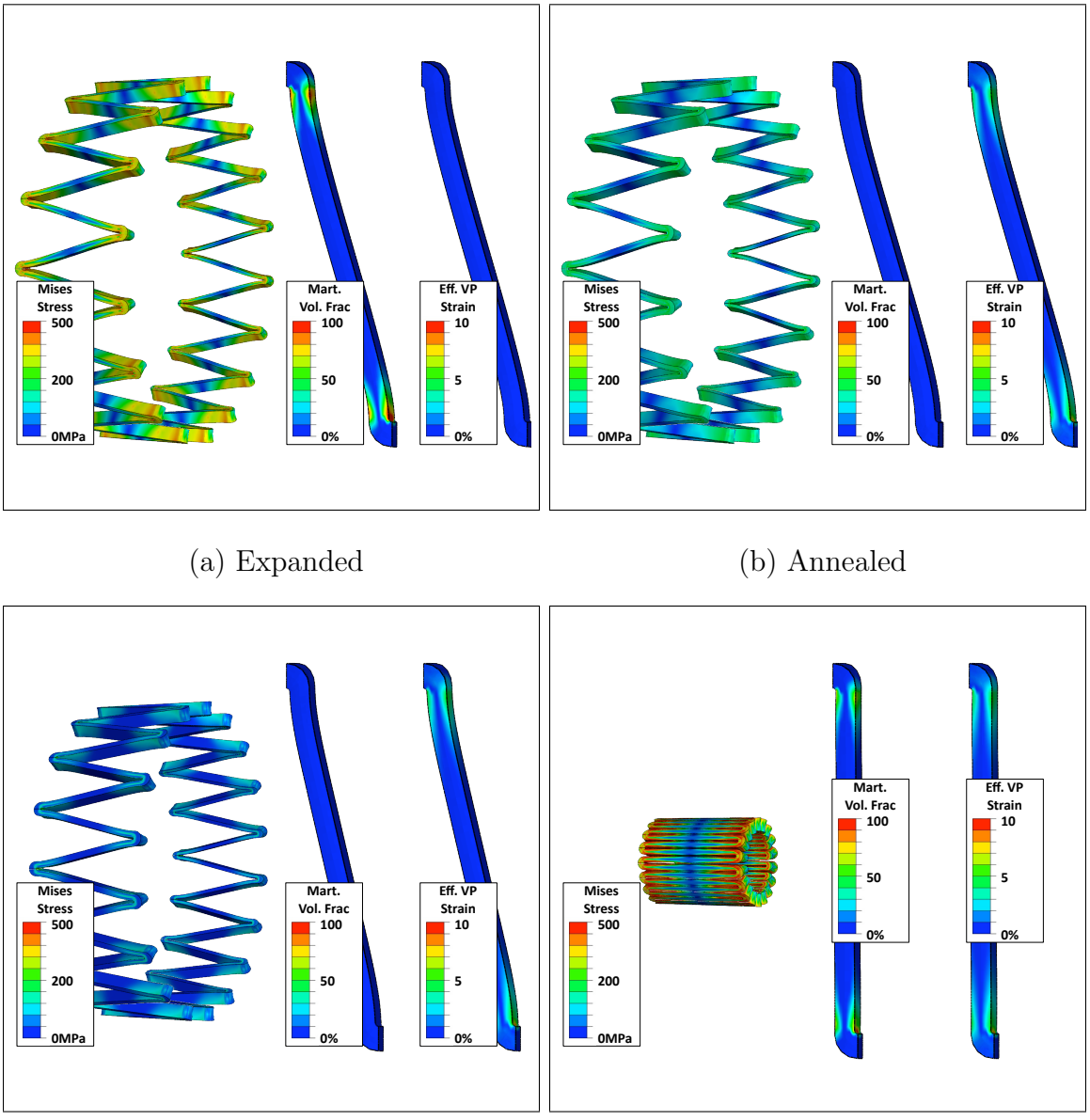

(a) Expanded (b) Annealed

(c) Relaxed (d) Crimped

Fig. 58. Analysis results for the shape-setting and subsequent crimping of an NiTi SMA stent. Contours indicate Mises equivalent stress ($\bar{\sigma}$), martensitic volume fraction (ξ), and effective viscoplastic strain (p) distributions.

CHAPTER VI

CONCLUSIONS AND FUTURE WORK

To conclude this dissertation, the key points presented in each of the previous chapters are summarized, and future research tasks pertaining to these are suggested.

A. Improved SMA Model for Analysis of Complex Applications

The first two technical chapters demonstrated that, despite their many inherent complexities, shape memory alloy materials and the structures composed of them can be accurately modeled, and this accuracy can be validated by comparison with independent experimental data. The derivation of an improved constitutive model was described where the proposed extensions were based on the particular behaviors of a new SMA composition for aerospace applications: Ni60Ti. It was shown that the needed model parameters can be calibrated by careful, standardized experimentation. The required experimentation was shown to be straightforward and constant stress tests alone were sufficient to fully and accurately calibrate the constitutive model.

The numerical implementation was described in detail, including a review of the options available for integrating the constitutive equations. It was concluded that the convex cutting plane form of the return mapping algorithm provided the best balance of cost and benefit. The analysis of large structural rotations in SMA bodies was also considered; "incrementally objective" algorithms used in conjunction with the return mapping algorithm allow small strain constitutive models to be applied to material points undergoing large rotations. The analysis of active structures undergoing large deformations (with moderate strains) is rare in the SMA modeling community.

The FEA implementation of the model was then used to analyze a smart struc-

ture, specifically a variable geometry jet engine chevron composed of an elastic composite substrate onto which active SMA flexures are installed. The predictions of the FEA for the active beam subcomponents and for the multi-component VGC structure were compared directly to experimental results. The predictions for the actuated deflection of the active VGC centerline had an average error of less than 6%. The ability to model multi-component smart structures including contact is important as engineers and designers in more industrial sectors continue to discover the benefits of SMA utilization as an enabling technology. By incorporating these tools, the legacy method of arriving at final smart structure designs based solely on design-build-test cycles can be augmented, and analytical results can be used to both improve and expedite the overall design process.

As modelers continue to develop new and improved constitutive models for conventional SMA transformation behaviors, several challenges remain. For one, the modeling problem discussed in Chapter IV, Section D.4 must be addressed. Specifically, the existing models are unable to accurately capture the behavior of an SMA material point that has undergone forward transformation given a biasing load in one direction and must then undergo reverse transformation given a new biasing load in the opposite direction. Though this problem was discussed in the context of transformation and plastic yield, it applies in general to all phase transformation models. The effects of non-homogenous plastic deformations and the internal stresses they cause only highlights the problem. To study this issue, careful experimentation needs to be undertaken, and the mathematical formulations of the transformation direction tensor and transformation function must be assessed. Special attention must be paid to the numerical implementation, as any correction that leads to material "softening", especially during the correction step of an algorithm, will lead to convergence difficulties.

The currently proposed model (with variable maximum transformation strain and smooth hardening) should also be numerically implemented in *fully* coupled thermomechanical framework, where the latent heat effects of transformation and heat transfer are also considered. This will be important as engineers continue to design actuation applications that utilize localized heating (i.e., via the installation of heaters). Augmentation of this improved model to also consider a transformation surface with tension-compression asymmetry could be beneficial. Some materials, especially those that have undergone processing to induce texturing, may exhibit this behavior. The analysis of some SMA applications, such as active beams, may need to account for it.

B. Rate-Independent Plastic Deformations in SMAs

A new design and analysis tool for SMAs subjected to high stresses was presented in Chapter IV. The theoretical model considers the two processes of martensitic transformation and plastic yielding and follows directly from the derivation of the transformation-only model that preceded it. The transformation and yield processes can progress independently or simultaneously in a coupled manner, depending on the thermomechanical loading path applied to the material. Coupling has been accounted for by the evolution of plastic hardening parameters with phase transformation, by the introduction of kinematic plastic hardening which also modifies the martensitic transformation surfaces, and by the dependence of the irrecoverable martensitic volume fraction on plastic deformation. The model is implemented using the same FEA framework and same convex cutting plane form of return mapping algorithm used for the transformation-only model, but the evolution of two inelastic processes requires the adaptation of methods for multisurface plasticity.

Experimental results were provided and were used to calibrate the model, and simulations of the experiments showed a close fit, validating the ability of the model to capture experimental material behavior. Several additional numerical analysis examples were provided based on the FEA implementation proposed. Analysis predictions were presented for a bending member experiencing simultaneous forward transformation and plastic yield while undergoing significant local rotations. The accuracy of the results was made evident by comparison with independently-obtained experimental data, and the fidelity of these predictions demonstrates the usefulness of the model and implementation as a tool for future engineering application design and analysis. A crack tip under mode I loading and SMA indentation were also analyzed, each being an example of stress concentrations leading to local yielding. Finally, local structural buckling behavior in an SMA component was analyzed for the first time, where plastic yielding was also observed. Such analysis was made possible by the geometrically nonlinear implementation of the model.

As research on plasticity in SMAs moves forward, several additional features of the yielding behavior should be experimentally investigated more closely. First, the conventional cyclic kinematic hardening response of a pure phase (i.e., of austenite) was not examined in this work (nor elsewhere in the literature), but is important in the calibration of any plastic model for a conventional material. Standardized kinematic hardening characterization methods should be applied for the pure phases. Also, a microstructural investigation of the effects of plasticity on the creation, the evolution, and the recovery of martensite could help in supporting some of the modeling assumptions in this dissertation. The error in capturing the peculiar hardening of the reverse transformation (unloading) plateau should also be addressed.

Perhaps the most important improvement, however, would be the consideration of large strains in an SMA undergoing transformation and plastic yielding, where

the total strains exceed 10%. Given that transformation strains alone can exceed 6%, it is not difficult to imagine engineering problems where this might occur (i.e., when local plastic strains of $> 5\%$ are observed). A new finite strain formulation of the constitutive model would be required, thus a parallel but altogether different derivation than the one considered in Chapter IV would be needed. This potential improvement would be most useful in the analysis of material processing such as cold working, where large plastic strains are induced in a material body.

C. Rate-Dependent Viscoplastic Deformations in SMAs

To account for the effects of viscoplastic deformation on the actuation characteristics of 3-D SMA and HTSMA structural elements, a third phenomenological constitutive model was both derived and implemented for the first time in Chapter V. The new model not only captures rate-dependent viscoplastic yielding in the pure SMA phases (i.e., austenite or martensite); it also considers simultaneous transformation/viscoplastic behavior. This ability is important to those in the smart structures engineering community considering HTSMA materials, where the transformation and creep phenomena are often observed concurrently. The interpretation of HTSMA characterization experiments and especially the analysis of SMA and HTSMA components subjected to high temperatures can each be improved by the use of the modeling methods of Chapter V.

The numerical implementation of the new model was described in detail, where the numerical integration options for the evolution equations were revisited, focusing this time on the rate-dependent viscoplastic behavior (where the evolution equation is non-homogeneous in time). It was found that the same methods that have been used to integrate the constitutive equations of Chapter II and the coupled SMA

transformation-plastic yield constitutive equations of Chapter IV could also be used when transformation is coupled with rate-dependent viscoplastic yield (i.e., the convex cutting plane algorithm). It was shown that the implemented model could be accurately calibrated and experimental results from an HTSMA study were predicted.

The new modeling tool was used to perform five 3-D analyses. The first considered the 3-D HTSMA cylindrical compressive specimen used to calibrate the model and showed that the internal state of such a low aspect ratio specimen is not homogenous along the length or throughout the cross-section. The second considered the same specimen subjected to transverse loading, where the values for the model calibration parameters where unchanged from the previous analysis. The force-deflection predictions where compared to independent experimental data, and a good match was observed. The third considered the coupled transformation-viscoplastic response at a stress concentration. Specifically, a circumferentially notched cylindrical specimen was analyzed, and it was observed that the rate-independent transformation can become structurally rate-dependent when coupled with viscoplastic deformations. Fourth, an HTSMA spring was analyzed, where simultaneous creep and forward transformation combined to cause substantial deformation (extension) of the spring, only some of which was recovered during transformation back into austenite. Finally, to highlight the uses of the new model with regards to conventional SMAs, the shape setting of an NiTi stent was considered. It was shown that, using creep data for NiTi found in the literature, the salient effects of conventional shape-setting processes can be predicted.

As with the plastic model of Chapter IV, perhaps the most important future extension of this work is the consideration of large strains. Given some processes (i.e., *equal channel angular extrusion* (ECAE) [168]), it is not unexpected that the total strains in an HTSMA or conventional SMA subjected to high temperature processing

might exceed 10%. Of course, the discussion in this work about the equivalence of considering plasticity and viscoplasticity in SMAs could be beneficial in that the efforts to extend one coupled model would apply directly to the extension of the other. A more in-depth study of coupled creep-reverse transformation might provide the means to correct any errors observed in the predictions of Fig. 45. The ability to capture the effects of time and elevated temperature on the material properties themselves would also be a welcome addition to the current modeling effort. Such changes might result from the processes of aging and annealing and their effects on grain size, precipitate growth, etc. An informed fusion of mechanics and fundamental materials science, especially metallurgy, would be important to the success of such research and would help to improve an already promising analysis tool.

REFERENCES

[1] D. Lagoudas (Ed.), Shape Memory Alloys: Modeling and Engineering Applications, Springer-Verlag, New York, 2008.

[2] A. V. Srinivasan, D. Michael McFarland, Smart Structures: Analysis and Design, Cambridge University Press, Cambridge, U.K., 2000.

[3] J. Perkins, Shape Memory Effects in Alloys, Plenum Press, New York, 1975.

[4] K. Otsuka, C. M. Wayman (Eds.), Shape Memory Materials, Cambridge University Press, Cambridge, 1999.

[5] V. Birman, Review of mechanics of shape memory alloy structures, Applied Mechanics Reviews 50 (11) (1997) 629–645.

[6] O. Godard, M. Lagoudas, D. Lagoudas, Design of space systems using shape memory alloys, in: Proceedings of SPIE, Smart Structures and Materials, Vol. 5056, San Diego, CA, 2003, pp. 545–558.

[7] D. J. Hartl, D. Lagoudas, Aerospace applications of shape memory alloys, Proceedings of the Institution of Mechanical Engineers, Part G: Journal of Aerospace Engineering 221 (Special Issue) (2007) 535–552.

[8] S. Miyazaki, Medical and dental applications of shape memory alloys, in: K. Otsuka, C. M. Wayman (Eds.), Shape Memory Materials, Cambridge University Press, Cambridge, 1999, Ch. 12, pp. 267–281.

[9] D. Mantovani, Shape memory alloys: Properties and biomedical applications, Journal of the Minerals, Metals and Materials Society 52 (2000) 36–44.

[10] L. Machado, M. Savi, Medical applications of shape memory alloys, Brazilian Journal of Medical and Biological Research 36 (2003) 683–691.

[11] K. Otsuka, T. Kakeshita, Science and technology of shape-memory alloys: New developments, MRS Bulletin 27 (2) (2002) 91–100.

[12] J. Kudva, Overview of the DARPA smart wing project, Journal of Intelligent Material Systems and Structures 15 (2004) 261–267.

[13] D. Hartl, D. Lagoudas, J. Mabe, F. Calkins, Use of Ni60Ti shape memory alloy for active jet engine chevron application, Part I: Thermomechanical characterization, Smart Materials and Structures (Accepted for publication).

[14] D. Hartl, D. Lagoudas, J. Mabe, F. Calkins, J. Mooney, Use of Ni60Ti shape memory alloy for active jet engine chevron application, Part II: Experimentally validated numerical analysis, Smart Materials and Structures (Accepted for publication).

[15] B. Carpenter, J. Lyons, EO-1 technology validation report: Lightweight flexible solar array experiment, Tech. rep., NASA Godard Space Flight Center, Greenbelt, MD (8 August 2001).

[16] K. R. Melton, General applications of shape memory alloys and smart materials, in: K. Otsuka, C. M. Wayman (Eds.), Shape Memory Materials, Cambridge University Press, Cambridge, 1999, Ch. 10, pp. 220–239.

[17] P. Jardine, J. Flanigan, C. Martin, Smart wing shape memory alloy actuator design and performance, in: Proceedings of SPIE, Smart Structures and Materials, Vol. 3044, San Diego, CA, 1997, pp. 48–55.

[18] D. Pitt, J. Dunne, E. White, E. Garcia, SAMPSON smart inlet SMA powered adaptive lip design and static test, Proceedings of the 42nd AIAA Structures, Structrual Dynamics, and Materials Conference, Seattle, WA, 16–20 April 2001 (2001) 1–11.

[19] K. Singh, I. Chopra, Design of an imporoved shape memory alloy actuator for rotor blade tracking, in: Proceedings of SPIE, Smart Structures and Materials, Vol. 4701, San Diego, CA, 2002, pp. 244–266.

[20] N. Caldwell, A. Glaser, E. Gutmark, R. Ruggeri, Heat transfer model for blade twist actuator system, in: Proceedings of 44th AIAA Aerospace Sciences Meeting and Exhibit, 2006, pp. 1–22.

[21] C. Willey, B. Huettl, S. Hill, Design and development of a miniature mechanisms tool-kit for micro spacecraft, in: Proceedings of the 35th Aerospace Mechanisms Symposium, Ames Research Center, 9–11 May, 2001, pp. 1–14.

[22] J. Roh, J. Han, I. Lee, Finite element analysis of adaptive inflatable structures with SMA strip actuator, in: Proceedings of SPIE, Smart Structures and Materials, Vol. 5764, San Diego, CA, 2005, pp. 460–471.

[23] F. Calkins, J. Mabe, R. Ruggeri, Overview of Boeing's shape memory alloy based morphing aerostructures, Proceedings of SMASIS08: ASME Conference on Smart Materials, Adaptive Structures and Intelligent Systems, October 28–30, 2008, Ellicott City, MD (2008) 1–11.

[24] F. Calkins, G. Butler, J. Mabe, Variable geometry chevrons for jet noise reduction, Proceedings of the 27th Annual AIAA Aeroacoustics Conference (2006) 1–11.

[25] J. H. Mabe, F. Calkins, G. Butler, Boeing's variable geometry chevron, morphing aerostructure for jet noise reduction, in: 47th AIAA/ ASME / ASCE / AHS / ASC Structures, Structural Dynamics and Materials Conference, Newport, Rhode Island, 2006, pp. 1–19.

[26] W. Buehler, R. Wiley, The properties of TiNi and associated phases, Tech. rep., U.S. Naval Ordnance Laboratory (1961).

[27] E. Patoor, D. C. Lagoudas, P. B. Entchev, L. C. Brinson, X. Gao, Shape memory alloys, Part I: General properties and modeling of single crystals, Mechanics of Materials 38 (5–6) (2006) 391–429.

[28] D. C. Lagoudas, P. B. Entchev, P. Popov, E. Patoor, L. C. Brinson, X. Gao, Shape memory alloys, Part II: Modeling of polycrystals, Mechanics of Materials 38 (5–6) (2006) 430–462.

[29] K. Bhattacharya, Microstructure of Martensite: Why it Forms and How it Gives Rise to the Shape-Memory Effect, Oxford University Press, Oxford, 2003.

[30] A. Bertram, Thermo-mechanical constitutive equations for the description of shape memory effects in alloys, Nuclear Engineering and Design 74 (1982) 173–182.

[31] K. Tanaka, A thermomechanical sketch of shape memory effect: One-dimensional tensile behavior, Res Mechanica 18 (1986) 251–263.

[32] M. Fremond, Matériaux à mémoire de forme, CRAS 304 (7) (1987) 239–244.

[33] C. Liang, C. A. Rogers, One-dimensional thermomechanical constitutive relations for shape memory materials, Journal of Intelligent Material Systems and Structures 1 (1990) 207–234.

[34] L. C. Brinson, One-dimensional constitutive behavior of shape memory alloys: Thermomechanical derivation with non-constant material functions and redefined martensite internal variable, Journal of Intelligent Material Systems and Structures 4 (1993) 229–242.

[35] X. Gao, R. Qiao, L. Brinson, Phase diagram kinetics for shape memory alloys: A robust finite element implementation, Smart Materials and Structures 16 (2007) 2102–2115.

[36] C. Liang, C. A. Rogers, A multi-dimensional constitutive model for shape memory alloys, Journal of Engineering Mathematics 26 (1992) 429–443.

[37] J. G. Boyd, D. C. Lagoudas, A thermodynamical constitutive model for shape memory materials. Part I. The monolithic shape memory alloy, International Journal of Plasticity 12 (6) (1996) 805–842.

[38] D. C. Lagoudas, Z. Bo, M. A. Qidwai, A unified thermodynamic constitutive model for SMA and finite element analysis of active metal matrix composites, Mechanics of Composite Materials and Structures 3 (1996) 153–179.

[39] D. Helm, P. Haupt, Shape memory behaviour: Modelling within continuum thermomechancs, International Journal of Solids and Structures 40 (2003) 827–849.

[40] B. Raniecki, C. Lexcellent, Thermodynamics of isotropic pseudoelasticity in shape memory alloys, European Journal of Mechanics - A/Solids 17 (2) (1998) 185–205.

[41] P. Popov, D. C. Lagoudas, A 3-D constitutive model for shape memory alloys incorporating pseudoelasticity and detwinning of self-accommodated martensite, International Journal of Plasticity 23 (10–11) (2007) 1679–1720.

[42] M. Panico, L. Brinson, A three-dimensional phenomenological model for martensite reorientation in shape memory alloys, Journal of the Mechanics and Physics of Solids 55 (2007) 2491–2511.

[43] S. Seelecke, I. Müller, Shape memory alloy actuators in smart structures: Modeling and simulation, Applied Mechanics Reviews 57 (1) (2004) 23–46.

[44] F. Auricchio, R. L. Taylor, Shape-memory alloys: Modelling and numerical simulation of the finite-strain superelastic behavior., Computer Methods in Applied Mechanics and Engineering 143 (1–2) (1997) 175–194.

[45] S. Moyne, M. Boubakar, C. Lexcellent, Extension of a linear behaviour model of shape memory alloys for finite strain studies, Journal of Physique IV 7 (5) (1997) C5.83–C5.88.

[46] L. Anand, M. E. Gurtin, Thermal effects in the superelasticity of crystalline shape-memory materials, Journal of the Mechanics and Physics of Solids 51 (2003) 1015–1058.

[47] A. Ziolkowski, Three-dimensional phenomenological thermodynamic model of pseudoelasticity of shape memory alloys at finite strains, Continuum Mechanics and Thermodynamcis 19 (2007) 379–398.

[48] S. Reese, D. Christ, Finite deformation pseudo-elasticity of shape memory alloys - Constitutive modelling and finite element implementation, International Journal of Plasticity 24 (2008) 455–482.

[49] K. Rajagopal, A. R. Srinivasa, On the thermomechanics of shape memory wires, Z. angew. Math. Phys. 50 (1999) 459–496.

[50] T. J. R. Hughes, J. Winget, Finite rotation effects in numerical integration of rate constitutive equations arising in large-deformation analysis, International Journal for Numerical Methods in Engineering 15 (12) (1980) 1862–1867.

[51] M. Jaber, H. Smaoui, P. Terriault, Finite element analysis of a shape memory alloy three-dimensional beam based on a finite strain description, Smart Materials and Structures 17 (2008) 1–11.

[52] W. S. Slaughter, The Linearized Theory of Elasticity, Birkhäuser, Boston, 2002.

[53] F. Auricchio, D. Fugazza, R. DesRoches, Rate-dependent thermo-mechanical modelling of superelastic shape-memory alloys for seismic applications, Journal of Intelligent Material Systems and Structures 19 (2008) 47–61.

[54] Z. Bo, D. C. Lagoudas, Thermomechanical modeling of polycrystalline SMAs under cyclic loading, Part I: Theoretical Derivations, International Journal of Engineering Science 37 (1999) 1089–1140.

[55] Z. Bo, D. C. Lagoudas, D. Miller, Material characterization of SMA actuators under nonproportional thermomechanical loading, Journal of Engineering Materials and Technology 121 (1999) 75–85.

[56] L. M. Machado, P. Popov, D. C. Lagoudas, Constitutive model for pollycrystalline shape memory alloys with smooth transformation hardening, International Journal of Engineering Science (Submitted, in review).

[57] Z. Bo, D. C. Lagoudas, Thermomechanical modeling of polycrystalline SMAs under cyclic loading, Part III: Evolution of plastic strains and two-way shape memory effect, International Journal of Engineering Science 37 (1999) 1175–1203.

[58] F. Fischer, E. Oberaigner, K. Tanaka, F. Nishimura, Transformation induced plasticity revised an updated formulation, International Journal of Solids and Structures 35 (18) (1998) 2209–2227.

[59] D. Lagoudas, P. Entchev, Modeling of transformation-induced plasticity and its effect on the behavior of porous shape memory alloys: Part I: Constitutive model for fully dense SMAs, Mechanics of Materials 36 (9) (2004) 865–892.

[60] A. Paiva, M. A. Savi, A. M. B. Bragra, P. M. C. L. Pacheco, A constitutive model for shape memory alloys considering tensile-compressive asymmetry and plasticity, International Journal of Solids and Structures 42 (11–12) (2005) 3439–3457.

[61] X. Feng, Q. Sun, Shakedown analysis of shape memory alloy structures, International Journal of Plasticity 23 (2007) 183–206.

[62] W. Yan, C. Wang, X. Zhang, Y. Mai, Theoretical modeling of the effect of plasticity on reverse transformation in superelastic shape memory alloys, Material Science & Engineering A A354 (2003) 146–157.

[63] X. Wang, B. X. Xu, Z. Yue, Micromechanical modelling of the effect of plastic deformation on the mechanical behavior in pseudoelastic shape memory alloys, International Journal of Plasticity 24 (2008) 1307–1332.

[64] Y. Zhang, Y. Cheng, D. Grummon, Finite element modeling of indentation-induced superelastic effect using a three-dimensional constitutive model for shape memory materials with plasticity, Journal of Applied Physics 101 (053507) (2007) 1–6.

[65] F. Jemal, T. Bouraoui, T. Zineb, E. Patoor, C. Brada, Modelling of martensitic transformation and plastic slip effects on the thermo-mechanical behaviour of fe-based shape memory alloys, Mechanics of Materials 41 (2009) 849–856.

[66] M. Ahlers, Martensitic transformation and plastic deformation: A comparison, Smart Materials and Structures 16 (2007) S115–S125.

[67] S. Miyazaki, K. Otsuka, Y. Suzuki, Transformation pseudoelasticity and deformation behavior in a Ti-50.6at%Ni alloy, Scripta Materialia 15 (1981) 287–292.

[68] J. Shaw, S. Kyriakides, Thermomechanical aspects of NiTi, Journal of the Mechanics and Physics of Solids 43 (8) (1995) 1243–1281.

[69] I. Khmelevskaya, S. Prokoshkin, Recovery stress, in: V. Brailovski, S. Prokoshkin, P. Terriault, F. Trochu (Eds.), Shape Memory Alloys: Funedementals, Modeling and Applications, University of Quebec, Quebec, 2003, Ch. 8, pp. 233–258.

[70] S. Saadat, J. Salichs, M. Noori, Z. Hou, H. Davoodi, I. Bar-on, An overview of vibration and seismic applications of NiTi shape memory alloy, Smart Materials and Structures 11 (2002) 218–229.

[71] T. Duerig, A. Pelton, Ti-Ni shape memory alloys, in: Material Properties Handbook: Titanium Alloys, ASM International, 1994, pp. 1035–1048.

[72] Y. Liu, S. Galvin, Criteria for pseudoelasticity in near-equiatomic NiTi shape memory alloys, Acta Metallurgica 45 (11) (1997) 4431–4439.

[73] W. D. Callister, Jr., Materials Science and Engineering: An Introduction, 5th Edition, John Wiley & Sons, New York, 1999.

[74] Y. Zhang, Y. Cheng, D. Grummon, Novel tribological systems using shape memory alloys and thin films, Surface and Coatings Technology 202 (2007) 998–1002.

[75] L. Qian, Q. Sun, Z. Zhou, The role of martensite reorientation in the fretting behaviour of nickel titanium shape memory alloy, Proceedings of the Institution of Mechanical Engineers Part J: Journal of Engineering Tribology 222 (2008) 887–897.

[76] W. Ni, Y. Cheng, D. Grummon, Recovery of microindents in a nickel-titanium shape memory alloy: A self-healing effect, Applied Physics Letters 80 (18) (2002) 3310–3312.

[77] K. Gall, K. Juntunen, H. Maier, H. Sehitoglu, Y. Chumlyakov, Instrumented micro-indentation of NiTi shape memory alloys, Acta Materialia 49 (2001) 3205–3217.

[78] G. Shaw, D. Stone, A. Johnson, A. Ellis, W. Crone, Shape memory effect in nanoindentation of nickel-titanium thin films, Applied Physics Letters 83 (2) (2003) 257–259.

[79] Y. Zhang, Y. Cheng, D. Grummon, Two-way indent depth recovery in a NiTi shape memory alloy, Applied Physics Letters 88 (2006) 131904–1–131904–3.

[80] P. G. McCormick, Y. Liu, Thermodynamic analysis of the martensitic transformation in TiNi—II. Effect of transformation cycling, Acta Metallurgica et Materialia 42 (7) (1994) 2407–2413.

[81] A. McKelvey, R. Ritchie, Fatigue-crack growth behavior in the superelastic and shape-memory alloy nitinol, Metallurgical and Material Transactions A 32 (13) (2001) 731–743.

[82] Y. Liu, D. Favier, Stabilization of martensite due to shear deformation via variant reorientation in polycrystalline NiTi, Acta Materialia 48 (2000) 3489–3499.

[83] J. Lemaitre, J.-L. Chaboche, Mechanics of Solid Materials, Cambridge University Press, Cambridge, UK, 1990.

[84] A. Miller, Unified Constitutive Equations for Creep and Plasticity, Springer-Verlag, New York, 1987.

[85] R. Noebe, T. R. Quackenbush, S. Padula, Benchtop demonstration of an adaptive chevron completed using a new high-temperature shape-memory alloy, Tech. Rep. 20060054078, NASA, Glenn Research Center (May 2006).

[86] J. Escobar, R. Clifton, On pressure-shear plate impact for studying the kinetics of stress-induced phase transformations, Material Science & Engineering A 170 (1993) 125–142.

[87] P. Popov, K. Ravi-Chandar, D. Lagoudas, Dynamic loading of polycrystalline shape memory alloy rods, Mechanics of Materials 35 (7) (2003) 689–716.

[88] Y. Liu, Y. Li, K. Ramesh, Rate dependence of deformation mechanisms in a shape memory alloy, Philosophical Magazine A 82 (12) (2002) 2461–2473.

[89] A. Keefe, G. Carman, Thermo-mechanical characterization of shape memory alloy torque tube actuators, Smart Materials and Structures 9 (2000) 665–672.

[90] A. Mukherjee, High-temperature -creep mechanisms of TiNi, Journal of Applied Physics 39 (5) (1968) 2201–2204.

[91] G. Eggeler, J. Khalil-Allafi, K. Neuking, A. Dlouhy, Creep of binary Ni-rich NiTi shape memory alloys and the influence of pre-creep on martensitic transformations, Z. Metallkd. 93 (2002) 654–660.

[92] C. Lexcellent, P. Robinet, J. Bernardini, D. Beke, P. Olier, High temperature creep measurements in equiatomic Ni-Ti shape memory alloy, Mat.-wiss. u. Werkstofftech 36 (10) (2005) 509–512.

[93] S. Oppenheimer, A. Yung, D. Dunand, Power-law creep in near-equiatomic nickel-titanium alloys, Acta Materialia 57 (2007) 377–380.

[94] S. Padula, G. Bigelow, R. Noebe, D. Gaydosh, A. Garg, Challenges and progress in the development of high-temperature shape memory alloys based on NiTiX compositions for high-force actuator applications., in: Proceedings of the International Conference on Shape Memory and Superelastic Technologies, ASM International, Metals Park, OH, 2006.

[95] P. K. Kumar, D. C. Lagoudas, K. J. Zanca, M. Z. Lagoudas, Thermomechanical characterization of high temperature SMA actuators, in: Proceedings of SPIE, Vol. 6170, 2006, pp. 306–312.

[96] P. Kumar, D. Lagoudas, Creep behavior in TiPdNi high temperature shape memory alloy, Proceedings of SPIE, Smart Structures and Materials: Behavior and Mechanics of Multifunctional Materials and Composites III, San Diego, CA, 8–12 March 7289 (2009) 1–6.

[97] C. Lexcellent, J. Rejzner, Modeling of the strain rate effect, creep, and relaxation of a Ni-Ti shape memory alloy under tension (compression)-torsional proportional loading in the pseudoelastic range, Smart Materials and Structures 9 (2000) 613–621.

[98] P. Monteiro, M. Savi, T. Netto, P. Pacheco, A phenomenological description of the thermomechanical coupling and the rate-dependent behavior of shape memory alloys, Journal of Intelligent Material Systems and Structures 10.1177/1045389X09341199 (2009) 1–13.

[99] E. J. Graesser, F. A. Cozzarelli, Shape memory alloys as new materials for aseismic isolation, Journal of Engineering Mechanics 117 (11) (1991) 2590–2608.

[100] E. Graesser, F. Cozzarelli, A proposed three-dimensional constitutive model for shape memory alloys, Journal of Intelligent Material Systems and Structures 5 (1994) 78–89.

[101] C. Făciu, M. Mihăilescu-Suliciu, On a rate-type thermomechancial model for shape memory bars. Stress-controlled problems, Z. angew. Math. Phys. 53 (2002) 1014–1025.

[102] J. Chaboche, Thermodynamic formulation of constitutive equations and application to the viscoplasticity and viscoelasticity of metals and polymers, International Journal of Solids and Structures 34 (18) (1997) 2239–2254.

[103] J. Chaboche, A review of some plasticity and viscoplasticity constitutive theories, International Journal of Plasticity 24 (2008) 1642–1693.

[104] S. Arnold, A. Saleeb, M. Castelli, A fully associative, nonlinear, kinematic, unified viscoplastic model for titanium-based matrices, in: W. Johnson, J. Larson, B. Cox (Eds.), Life Prediction Methodology for Titanium Matrix Composites, ASTM STP 1253, ASTM, 1996.

[105] P. Nukala, A return mapping algorithm for cyclic viscoplastic constitutive models, Computer Methods in Applied Mechanics and Engineering 195 (2006) 148–178.

[106] J. Mabe, R. Ruggeri, F. T. Calkins, Characterization of nickel-rich nitinol alloys for actuator development, in: Proceedings of the International Conference on Shape Memory and Superelasticity Technology, 2006.

[107] T. Tadaki, Y. Nakata, K. Shimizu, K. Otsuka, Crystal structure, composition and morphology of a precipitate in an aged Ti-51 at%Ni shape memory alloy, Trans. of Japan Institute of Metals 27 (10) (1986) 731.

[108] T. Tadaki, Y. Nakata, K. Shimizu, Thermal cycling effects in an aged Ni-rich Ti-Ni shape memory alloy, Trans. of Japan Institute of Metals 28 (11) (1987) 883–890.

[109] G. Julien, Manufacturing of nitinol parts and forms, U.S. Patent 6,422,010 (July 2002).

[110] C. Wojcik, Shape memory properties of nickel rich Ni-Ti alloys, in: A. Pelton, T. Duerig (Eds.), SMST-2003: Proceedings of the International Conference on Shape Memory and Superelastic Technologies, Pacific Grove, CA, 2003, pp. 43–52.

[111] C. Wojcik, Aging effects in nickel rich NiTi alloys, in: M. Mertmann (Ed.), SMST-2004: Proceedings of the International Conference on Shape Memory and Superelastic Technologies, Baden-Baden, Germany, 2004, pp. 229–236.

[112] D. J. Clingman, F. T. Calkins, J. P. Smith, Thermomechanical properties of 60-Nitinol, in: Proceedings of the SPIE, Smart Structures and Materials: Active Materials: Behavior and Mechanics, Vol. 5053, 2003, pp. 219–229.

[113] ASTM, Standard Test Method for Tension Testing of Metallic Materials, ASTM International (2004).

[114] D. Hartl, D. Lagoudas, Thermomechanical chracterization of shape memory alloy materials, in: D. Lagoudas (Ed.), Shape Memory Alloys: Modeling and Engineering Applications, Springer-Verlag, New York, 2008, Ch. 2, pp. 53–119.

[115] D. Lagoudas, Z. Bo, M. Qidwai, P. Entchev, Manual for SMA_UM: User Material Subroutine for Thermomechanical Constitutive Model of Shape Memory Alloys, Texas A&M University, College Station, TX (March 2003).

[116] K. Otsuka, X. Ren, Physical metallurgy of Ti–Ni-based shape memory alloys, Progress in Materials Science 50 (2005) 511–678.

[117] D. C. Lagoudas, Z. Bo, Thermomechanical modeling of polycrystalline SMAs under cyclic loading, Part II: Material characterization and experimental results for a stable transformation cycle, International Journal of Engineering Science 37 (1999) 1141–1173.

[118] B. Chang, J. Shaw, M. Iadicola, Thermodynamics of shape memory alloy wire: Modeling, experiments, and application, Continuum Mechanics and Thermodynamics 18 (1–2) (2006) 83–118.

[119] R. Hamilton, H. Sehitoglu, Y. Chumlyakov, H. Maier, Stress dependence of the hysteresis in single crystal NiTi alloys, Acta Materialia 52 (2004) 3383–3402.

[120] P. Šittner, P. Lukáš, V. Novák, M. Daymond, G. Swallowe, In situ neutron diffraction studies of martensitic transformations in NiTi polycrystals under tension and compression stress, Material Science & Engineering A 378 (2004) 91–104.

[121] K. Tanaka, S. Kobayashi, Y. Sato, Thermomechanics of transformation pseudoelasticity and shape memory effect in alloys, International Journal of Plasticity 2 (1986) 59–72.

[122] L. Machado, D. Lagoudas, Thermomechanical constitutive modeling of SMAs, in: D. Lagoudas (Ed.), Shape Memory Alloys: Modeling and Engineering Applications, Springer-Verlag, New York, 2008, Ch. 3, pp. 122–187.

[123] L. Machado, D. Lagoudas, M. Savi, Lyapunov exponents estimation for hysteretic systems, submitted (2007).

[124] M. A. Qidwai, D. C. Lagoudas, Numerical implementation of a shape memory alloy thermomechanical constitutive model using return mapping algorithms, International Journal for Numerical Methods in Engineering 47 (2000) 1123–1168.

[125] F. Mollica, K. Rajagopal, A. Srinivasa, The inelastic behavior of metals subject to loading reversal, International Journal of Plasticity 17 (8) (2001) 1119–1146.

[126] B. D. Coleman, W. Noll, Material symmetry and thermostatic inequalities in finite elastic deformations, Archive for Rational Mechanics and Analysis 15 (1964) 87–111.

[127] B. D. Coleman, Thermodynamics of materials with memory, Archive for Rational Mechanics and Analysis 17 (1964) 1–46.

[128] B. D. Coleman, M. E. Gurtin, Thermodynamics with internal state variables, The Journal of Chemical Physics 47 (2) (1967) 597–613.

[129] J. C. Simo, T. J. R. Hughes, Computational Inelasticity, Vol. 7 of Interdisciplinary Applied Mathematics, Springer-Verlag, New York, 1998.

[130] M. A. Qidwai, D. C. Lagoudas, On the thermodynamics and transformation surfaces of polycrystalline NiTi shape memory alloy material, International Journal of Plasticity 16 (2000) 1309–1343.

[131] J. Lubliner, Plasticity Theory, Macmillan Publishing Company, New York, 1990.

[132] A. S. Khan, S. Huang, Continuum Theory of Plasticity, John Wiley & Sons, New York, 1995.

[133] G. Stachowiak, P. McCormick, Two stage yielding in a NiTi alloy, Scripta Metallurgica 21 (1987) 403–406.

[134] G. Stachowiak, P. McCormick, Shape memory behaviour associated with the R and martensitic transformations in a NiTi alloy, Acta Materialia 36 (2) (1988) 291–297.

[135] M. Qidwai, D. Hartl, D. Lagoudas, Numerical implementation of an SMA thermomechanical constitutive model using return mapping algorithms, in: D. Lagoudas (Ed.), Shape Memory Alloys: Modeling and Engineering Applications, Springer-Verlag, New York, 2008, Ch. 4, pp. 189–231.

[136] Abaqus, Analysis User's Manual, Dassault Systèmes of America Corp., Woodlands Hills, CA (2007).

[137] J. N. Reddy, Introduction to the Finite Element Method, 2nd Edition, McGraw-Hill, Boston, 1993.

[138] M. Ortiz, E. P. Popov, Accuracy and stability of integration algorithms for elastoplastic constitutive relations, International Journal for Numerical Methods in Engineering 21 (1985) 1561–1576.

[139] J. Reddy, An Introduction to Nonlinear Finite Element Analysis, Oxford University Press, Oxford, UK, 2004.

[140] M. Ortiz, J. Simo, An analysis of a new class of integration algorithms for elastoplastic constitutive relations, International Journal for Numerical Methods in Engineering 23 (1986) 353–366.

[141] M. E. Gurtin, An Introduction to Continuum Mechanics, Vol. 158 of Mathematics in Science and Engineering, Academic Press, San Diego, 1981.

[142] K. Rajagopal, Class notes (2009).

[143] Swanson Analysis Systems, Inc, Houston, PA, ANSYS Engineering Analysis System Users Manual.

[144] Abaqus, Theory Manual, Dassault Systèmes of America Corp., Woodlands Hills, CA (2007).

[145] B. Van West, C. Capps, M. Voth, J. Saint Clair, Instrumentation and emperical assessment of post-buckling response in grid-stiffened structures, in: 43rd AIAA/ASME/ASCE/AHS/ASC Structures, Structural Dynamics, and Materials Conference, Denver, CO, 2002, pp. 1–7.

[146] F. Calkins, J. Mabe, Shape memory alloy based morphing chevrons: full scale static engine test, in: Proceedings of the 28th Annual AIAA Aeroacoustics Conference, No. 3438 in AIAA 2007, Rome, Italy, 2007, pp. 1–12.

[147] J. Shaw, S. Kyriakides, On the nucleation and propagation of phase transformation fronts in a NiTi alloy, Acta Metallurgica 45 (2) (1997) 683–700.

[148] P. Germain, Cours de Mécanique des Miliex Continus: Tome I-Théorie Général, Masson Et Cie, Paris, 1973.

[149] G. Houlsby, A. Puzrin, Principles of Hyperplasticity, Springer-Verlag, 2006.

[150] ASTM International, Standard Test Method for Linear-Elastic Plane-Strain Fracture Toughness KIc of Metallic Materials (2008).

[151] X. Wang, Y. Wang, A. Baruj, G. Eggeler, Z. Yue, On the formation of martnsite in front of cracks in pseudoelastic shape memory alloys, Material Science & Engineering A 394 (2005) 393–398.

[152] A. Fisher-Cripps, Nanoindentation, Mechanical Engineering Series, Springer-Verlag, New York, 2004.

[153] A. Birnbaum, Personal email communications (2008).

[154] W. Francis, M. Lake, K. Mallick, G. Freebury, A. Maji, Development and testing of a hinge/actuator incorporating elastic memory composites, in: 44th AIAA Structures, Structural Dynamics, and Materials Conference, Norfolk, VA, 2003.

[155] P. Kumar, D. Lagoudas, Thermomechanical characterization of a tipdni high temperature sma under tension, Proceedings of SPIE, Smart Structures and Materials: Behavior and Mechanics of Multifunctional Materials and Composites, San Diego, CA, 19–24 March 6526 (2007) 1–10.

[156] G. Chatzigeorgiou, D. Lagoudas, A constitutive model for high temperature SMAs exhibiting viscoplastic behavior, Proceedings of SPIE, Smart Structures and Materials: Behavior and Mechanics of Multifunctional Materials and Composites III, San Diego, CA, 8–12 March 7289 (2009) 1–7.

[157] F. Odqvist, Mathematical Theory of Creep and Creep Rupture, Clarendon Press, Oxford, UK, 1966.

[158] ASTM, Standard Test Methods of Compression Testing of Metallic Materials at Room Temperature, ASTM International (2000).

[159] G. Chatzigeorgiou, D. Lagoudas, A constitutive model for high temperature SMAs exhibiting viscoplastic behavior, Proceedings of SPIE, Smart Structures and Materials: Behavior and Mechanics of Multifunctional Materials and Composites III, San Diego, CA, 8–12 March 7289 (2009) 1–7.

[160] R. Rihan, R. Singh Raman, R. Ibrahim, Circumferential notched tensile (CNT) testing of cast iron for determination of threshold (KISCC) for caustic crack propagation, Material Science & Engineering A 407 (2005) 207–212.

[161] S. Padula, R. Noebe, G. Bigelow, D. Culley, M. Stevens, N. Penney, D. Gaydosh, T. Quackenbush, B. Carpenter, Development of a HTSMA-actuated surge control rod for high-temperature turbomachinery applications, In proceedings of 48th AIAA/ASME/ASCE/AHS/ASC Structures, Structural Dynamics, and Materials Conference, April 2007, Honolulu, Hawaii.

[162] A. Stebner, S. Padula, R. Noebe, B. Lerch, D. Quinn, Development, characterization, and design considerations of Ni19.5Ti50.5Pd25Pt5 high-temperature shape memory alloy helical actuators, Journal of Intelligent Material Systems and Structures,Accepted, in press.

[163] Y. Toi, J.-B. Lee, M. Taya, Finite element analysis of superelastic, large deformation behavior of shape memory alloy helical springs, Computers and Structures 82 (2004) 1685–1693.

[164] F. Auricchio, L. Petrini, A three-dimensional model describing stress-temperature induced solid phase transformations: solution algorithm and boundary value problems, International Journal for Numerical Methods in Engineering 61 (2004) 807–836.

[165] N. Morgan, Medical shape memory alloy applications – the market and its products, Material Science & Engineering A 378 (2004) 16–23.

[166] E. Kobus, K. Neuking, G. Eggeler, The creep behavior of a NiTi-alloy and the effect of creep deformation on its shape-memory properties, Praktische Metallographie - Practical Metallography 39 (2002) 177.

[167] D. Systèms, Abaqus version 6.7 performance data, Website, `http://www.simulia.com/support/v67/v67_performance.html` (2009).

[168] B. Kockar, I. Karaman, J. Kim, Y. Chumlyakov, A method to enhance cyclic reversibility of nitihf high temperature shape memory alloys, Acta Materialia 54 (12) (2006) 2203–2208.

[169] P. Jardine, J. Kudva, C. Martin, K. Appa, Shape memory alloy NiTi actuators for twist control of smart designs, in: Proceedings of SPIE Smart Materials and Structures, Vol. 2717, San Diego, CA, 1996, pp. 160–165.

[170] A. Srinivasa, S. Srinivasan, Inelasticity of Materials: An Engineering Approach and a Practical Guide, 1st Edition, World Scientific, Singapore, 2000.

APPENDIX A

EQUIVALENCE OF CONSTITUTIVE MODELS DERIVED FROM HELMHOLTZ AND GIBBS POTENTIALS

In this appendix, it is shown that the constitutive model of Chapter II (phase transformation only) can be derived from a Helmholtz free energy potential just as it was from a Gibbs free energy potential provided that the Helmholtz free energy is given the proper functional form.

To begin, we motivate this proper form by substituting the entire Gibbs energy of (2.5), (2.6), and (2.7) into the Legendre transformation for ψ [122], given as

$$\psi = \frac{1}{\rho}\boldsymbol{\sigma} : \boldsymbol{\varepsilon} + G. \tag{A.1}$$

Thus, for the transformation-only model of Chapter II, this gives

$$\begin{aligned}\psi = \frac{1}{\rho}\boldsymbol{\sigma} : \boldsymbol{\varepsilon} \quad &- \quad \frac{1}{2\rho}\boldsymbol{\sigma} : \boldsymbol{\mathcal{S}}(\xi)\boldsymbol{\sigma} - \frac{1}{\rho}\boldsymbol{\sigma} : \left[\boldsymbol{\varepsilon}^{th} + \boldsymbol{\varepsilon}^{t}\right] \\ &+ \quad c\left[(T - T_0) - T\ln\left(\frac{T}{T_0}\right)\right] - s_0(\xi)T + u_0(\xi) + \frac{1}{\rho}g^t,\end{aligned} \tag{A.2}$$

where $\boldsymbol{\varepsilon}^{th} = \boldsymbol{\alpha}(T - T_0)$. Also, the material properties $\boldsymbol{\mathcal{S}}(\xi)$, $s_0(\xi)$, and $u_0(\xi)$ are assumed to vary linearly with ξ per the discussion of Chapter II, Section C.2.

Assuming the relationships between stress, the total strain, and the strains due to thermal expansion and transformation gives

$$\boldsymbol{\sigma} = \boldsymbol{\mathcal{C}}(\xi)\boldsymbol{\varepsilon}^{el}; \qquad \boldsymbol{\mathcal{C}}(\xi) = [\boldsymbol{\mathcal{S}}(\xi)]^{-1}; \qquad \boldsymbol{\varepsilon}^{el} = \boldsymbol{\varepsilon} - \boldsymbol{\varepsilon}^{th} - \boldsymbol{\varepsilon}^{t}. \tag{A.3}$$

This allows us to write

$$\begin{aligned}\psi \quad &= \quad \frac{1}{\rho}\left[\boldsymbol{\mathcal{C}}(\xi)\boldsymbol{\varepsilon}^{el}\right] : \left[\boldsymbol{\varepsilon}^{el} + \boldsymbol{\varepsilon}^{th} + \boldsymbol{\varepsilon}^{t}\right] - \frac{1}{2\rho}\boldsymbol{\varepsilon}^{el} : \boldsymbol{\mathcal{C}}(\xi)\boldsymbol{\varepsilon}^{el} - \frac{1}{\rho}\left[\boldsymbol{\mathcal{C}}(\xi)\boldsymbol{\varepsilon}^{el}\right] : \left[\boldsymbol{\varepsilon}^{th} + \boldsymbol{\varepsilon}^{t}\right] \\ &+ \quad c\left[(T - T_0) - T\ln\left(\frac{T}{T_0}\right)\right] - s_0(\xi)T + u_0(\xi) + \frac{1}{\rho}g^t.\end{aligned} \tag{A.4}$$

Canceling out the $\boldsymbol{\varepsilon}^{th}$ and $\boldsymbol{\varepsilon}^{t}$ terms and simplifying, we have

$$\psi = \frac{1}{2\rho}\boldsymbol{\varepsilon}^{el} : \boldsymbol{\mathcal{C}}(\xi)\boldsymbol{\varepsilon}^{el} + c\left[(T - T_0) - T\ln\left(\frac{T}{T_0}\right)\right] - s_0(\xi)T + u_0(\xi) + \frac{1}{\rho}g^t. \tag{A.5}$$

Substituting in the definition of $\boldsymbol{\varepsilon}^{el}$ once again gives the final needed form of the Helmholtz free energy potential, written in terms of the conventional state variables

(i.e., strain-type variables) as

$$\begin{aligned}\psi\left(\boldsymbol{\varepsilon}, T, \boldsymbol{\varepsilon}^t, \xi, g^t\right) &= \frac{1}{2\rho}\left[\boldsymbol{\varepsilon} - \boldsymbol{\varepsilon}^{th} - \boldsymbol{\varepsilon}^t\right] : \boldsymbol{\mathcal{C}}(\xi)\left[\boldsymbol{\varepsilon} - \boldsymbol{\varepsilon}^{th} - \boldsymbol{\varepsilon}^t\right] \\ &+ c\left[(T - T_0) - T\ln\left(\frac{T}{T_0}\right)\right] - s_0(\xi)T + u_0(\xi) + \frac{1}{\rho}g^t. \quad \text{(A.6)}\end{aligned}$$

To continue with the derivation of the constitutive model, we apply the first and second laws of thermodynamics via the Coleman-Noll procedure (see Chapter II, Section C.2 and also [122]). For the entropy-temperature relation, this methodology and (A.3) gives

$$s = -\partial_T \psi = \frac{1}{\rho}\boldsymbol{\sigma} : \boldsymbol{\alpha} + c\ln\left(\frac{T}{T_0}\right) + s_0(\xi), \quad \text{(A.7)}$$

which is identical to (2.16). Thus, the constitutive relation relating to entropy is unchanged from Chapter II despite being derived from a Helmholtz potential. This is expected given the form of the Legendre transformation (A.1). Further, we have

$$\boldsymbol{\sigma} = \rho\partial_{\boldsymbol{\varepsilon}}\psi = \boldsymbol{\mathcal{C}}(\xi)\left[\boldsymbol{\varepsilon} - \boldsymbol{\varepsilon}^{th} - \boldsymbol{\varepsilon}^t\right], \quad \text{(A.8)}$$

which agrees with (A.3) and (2.18). The remainder of the Clausius-Duhem inequality gives

$$-\rho\left[\partial_{\boldsymbol{\varepsilon}^t}\psi : \dot{\boldsymbol{\varepsilon}^t} + \partial_\xi\psi\ \dot{\xi} + \partial_{g^t}\psi\dot{g^t}\right] \geq 0. \quad \text{(A.9)}$$

Evaluating two of the partial derivatives gives

$$\left[\boldsymbol{\mathcal{C}}(\xi)\left[\boldsymbol{\varepsilon} - \boldsymbol{\varepsilon}^{th} - \boldsymbol{\varepsilon}^t\right] : \dot{\boldsymbol{\varepsilon}^t} - \rho\partial_\xi\psi\ \dot{\xi} - \dot{g^t}\right] \geq 0. \quad \text{(A.10)}$$

Further, substituting the stress from (A.8), the assumed evolution of $\boldsymbol{\varepsilon}^t$ from (2.20), and the assumed evolution of g^t from (2.26) gives

$$\left[\boldsymbol{\sigma} : \boldsymbol{\Lambda}^t - \rho\partial_\xi\psi - f^t\right]\dot{\xi} \geq 0. \quad \text{(A.11)}$$

This can be shown to be identical to the constraint given in (2.28), which is central to the formulation of the transformation function. To demonstrate equivalence of (A.11) and (2.28), we need only show that $\partial_\xi\psi = \partial_\xi G$ to prove equivalence of the resulting constitutive models. Comparing $\partial_\xi\psi$ (while considering (A.6)) to $\partial_\xi G$ given in (2.29), we have

$$\begin{aligned}\partial_\xi\psi &= \partial_\xi G - \left(-\frac{1}{2\rho}\boldsymbol{\sigma} : \widetilde{\boldsymbol{\mathcal{S}}}\boldsymbol{\sigma}\right) + \partial_\xi\left(\frac{1}{2\rho}\boldsymbol{\varepsilon}^{el} : \boldsymbol{\mathcal{C}}\boldsymbol{\varepsilon}^{el}\right) \\ &= \partial_\xi G + \left(\frac{1}{2\rho}\boldsymbol{\sigma} : \widetilde{\boldsymbol{\mathcal{S}}}\boldsymbol{\sigma}\right) + \frac{1}{2\rho}\boldsymbol{\varepsilon}^{el} : \partial_\xi\boldsymbol{\mathcal{C}}\boldsymbol{\varepsilon}^{el}. \quad \text{(A.12)}\end{aligned}$$

Using $(\text{A.3})_2$, the definition $\boldsymbol{\mathcal{S}}(\xi) := \boldsymbol{\mathcal{S}}^A + \xi\widetilde{\boldsymbol{\mathcal{S}}}$ (from Chapter II, Section C.2), the properties of tensor differentiation, and the symmetries of the tensors involved, we

can then write

$$\begin{aligned}
\partial_\xi \psi &= \partial_\xi G + \left(\frac{1}{2\rho}\boldsymbol{\sigma} : \widetilde{\boldsymbol{\mathcal{S}}}\boldsymbol{\sigma}\right) - \frac{1}{2\rho}\boldsymbol{\varepsilon}^{el} : \left[\boldsymbol{\mathcal{C}}\widetilde{\boldsymbol{\mathcal{S}}}\boldsymbol{\mathcal{C}}\boldsymbol{\varepsilon}^{el}\right] \\
&= \partial_\xi G + \left(\frac{1}{2\rho}\boldsymbol{\sigma} : \widetilde{\boldsymbol{\mathcal{S}}}\boldsymbol{\sigma}\right) - \left(\frac{1}{2\rho}\boldsymbol{\sigma} : \widetilde{\boldsymbol{\mathcal{S}}}\boldsymbol{\sigma}\right) \\
&= \partial_\xi G. \qquad \text{(A.13)}
\end{aligned}$$

Thus, (A.11) is identical to (2.28), and the final form of the constitutive model (practically consisting of the elastic relations, the evolution equations, and the transformation function formed from these constraints) does not depend on whether the Gibbs or Helmholtz free energy is chosen as the free energy potential. As expected, this is a result of the Legendre transformation.

APPENDIX B

PROOF OF BOYD-LAGOUDAS / SMOOTH HARDENING EQUIVALENCE

Here the one-dimensional form of the model derived in Chapter II, Section C is considered, where this model of SMA transformation is formulated to provide smooth transitions from a thermoelastic response to the transformation response, or "smooth hardening." It is shown that, although the smooth hardening capability is an important extension, the derived model of Chapter II and the established model of Boyd and Lagoudas [37] are equivalent in both required model parameters and predicted results in the special case that: *i*) all of the hardening function exponents n_i $(i = 1, 2, 3, 4)$ are unity, and *ii*) the phase diagram transformation slopes for forward and reverse transformation are identical ($C^M = C^A$).

One-Dimensional Form of Boyd-Lagoudas Model

The one-dimensional form of the strain equation for the Boyd-Lagoudas model [37] is given by

$$\varepsilon = \mathcal{S}\sigma + \alpha\left(T - T_0\right) + H\mathrm{sgn}(\sigma)\dot{\xi}, \tag{B.1}$$

where the effective property $\mathcal{S}$ is given by

$$\mathcal{S}\left(\xi\right) = \mathcal{S}^A + \xi\left(\mathcal{S}^M - \mathcal{S}^A\right); \quad \mathcal{S}^A = \frac{1}{E^A}; \quad \mathcal{S}^M = \frac{1}{E^M} \tag{B.2}$$

Therefore, for a given stress level and temperature, the total strain can be computed via (B.1) if the martensitic volume fraction is known. To compute the martensitic volume fraction, one utilizes the transformation function (here denoted Φ^t_{BL}, cf. (2.32)) and solves it for ξ. Assuming that the coefficients of thermal expansion and the latent heats of the two phases are identical (a common assumption), the transformation function for the Boyd-Lagoudas model has the following one-dimensional form:

$$\Phi^t_{BL} = \left|\sigma\right| H + \frac{1}{2}\sigma^2\widetilde{S} + \rho\tilde{s}_0 T - \rho\tilde{u}_0 - f^t \mp Y^t_{BL} = 0, \tag{B.3}$$

where the $\mp$ denotes forward/reverse transformation, respectively.

The hardening function of the Boyd and Lagoudas model is of the form:

$$f^t_{BL}\left(\xi\right) = \begin{cases} b_1\xi + b_2 \quad ; & \dot{\xi} > 0 \\ \\ b_3\xi + b_4 \quad ; & \dot{\xi} < 0 \end{cases} \tag{B.4}$$

According to the original source [37], the parameters of the Boyd-Lagoudas model can be calculated from known material properties per the relations provided in Table IX.

Table IX. Model parameters used in the Boyd-Lagoudas Model.

$Y^t_{BL} = \frac{1}{4}\rho\tilde{s}_0\left(M_s + M_f - A_f - A_s\right)$
$b_1 = \rho\tilde{s}_0\left(M_f - M_s\right)$
$b_2 = \frac{1}{4}\rho\tilde{s}_0\left(A_s + A_f + 3M_s - M_f\right) - \rho\tilde{u}_0$
$b_3 = \rho\tilde{s}_0\left(A_s - A_f\right)$
$b_4 = \frac{1}{4}\rho\tilde{s}_0\left(-A_s + 3A_f + M_s + M_f\right) - \rho\tilde{u}_0$

Therefore, after substituting the values of the model parameters given by Table IX into equation (B.3) and (B.4), the transformation function Φ^t_{BL} can be rewritten for *forward transformation* as

$$\begin{aligned}\Phi^t_{BL} = |\sigma|\, H + \frac{1}{2}\sigma^2\widetilde{\mathcal{S}} + \rho\tilde{s}_0\left(T - M_s\right) \\ - \rho\tilde{s}_0\left(M_f - M_s\right)\xi = 0, \quad \dot{\xi} > 0.\end{aligned} \tag{B.5}$$

By solving equation (B.5) for ξ, one gets:

$$\xi = \frac{1}{\rho\tilde{s}_0\left(M_f - M_s\right)}\left[|\sigma|\, H + \frac{1}{2}\sigma^2\widetilde{\mathcal{S}} + \rho\tilde{s}_0\left(T - M_s\right)\right], \quad \dot{\xi} > 0. \tag{B.6}$$

The same procedure can be use to derive the following closed-form solution for ξ during reverse phase transformation:

$$\xi = \frac{1}{\rho\tilde{s}_0\left(A_s - A_f\right)}\left[|\sigma|\, H + \frac{1}{2}\sigma^2\widetilde{\mathcal{S}} + \rho\tilde{s}_0\left(T - A_f\right)\right], \quad \dot{\xi} < 0. \tag{B.7}$$

One-Dimensional Form of Current Model with Smooth Hardening

Now we consider the analytical 1-D form of the current model of Chapter II in the case that all exponents n_i of the smooth hardening function are equal to one. Assuming $H^{cur}(\sigma) = H$, the smooth hardening function (2.26) reduces to

$$f^t_{smooth}\left(\xi\right) = \begin{cases} a_1\xi + a_3 \quad ; & \dot{\xi} > 0 \\ \\ a_2\xi - a_3 \quad ; & \dot{\xi} < 0 \end{cases} \tag{B.8}$$

The model parameters for the current model are calculated from the material properties per Table II. Given the assumption of $n_i = 1$ $(i = 1...4)$ and $C^A = C^M$, these relations take on the forms given in Table X.

Table X. Model parameters used in the model of Chapter II.

$$Y^t_{smooth} = \tfrac{1}{4}\rho\tilde{s}_0\left(M_s + M_f - A_f - A_s\right) + DH|\sigma|$$

$$D = 0$$

$$a_1 = \rho\tilde{s}_0\left(M_f - M_s\right)$$

$$a_2 = \rho\tilde{s}_0\left(A_s - A_f\right)$$

$$a_3 = \tfrac{1}{4}\rho\tilde{s}_0\left(M_s - M_f - A_f + A_s\right)$$

$$\rho\tilde{u}_0 = \tfrac{1}{2}\rho\tilde{s}_0\left(M_s + A_f\right)$$

As before, we substitute these model parameter relations into the 1-D form of the transformation function for *forward transformation*, given here by (2.36). This yields

$$\begin{aligned}\Phi^t_{smooth} = &|\sigma|\,H + \frac{1}{2}\sigma^2\widetilde{\mathcal{S}} + \rho\tilde{s}_0 T - \frac{1}{2}\rho\tilde{s}_0\left(A_f + M_s\right) \\ &- \rho\tilde{s}_0\left(M_f - M_s\right)\xi - \frac{1}{2}\rho\tilde{s}_0\left(M_s - A_f\right) = 0, \quad \dot{\xi} > 0.\end{aligned} \tag{B.9}$$

Solving equation (B.9) for ξ gives

$$\xi = \frac{1}{\rho\tilde{s}_0\left(M_f - M_s\right)}\left[|\sigma|\,H + \frac{1}{2}\sigma^2\tilde{\mathcal{S}} + \rho\tilde{s}_0\left(T - M_s\right)\right], \quad \dot{\xi} > 0. \tag{B.10}$$

Now using the same methodology and (2.37) (where $\varepsilon^{t-r}/\xi^r = H$ for isobaric loading), ξ during reverse transformation can be computed as:

$$\xi = \frac{1}{\rho\tilde{s}_0\left(A_s - A_f\right)}\left[|\sigma|\,H + \frac{1}{2}\sigma^2\tilde{\mathcal{S}} + \rho\tilde{s}_0\left(T - A_f\right)\right], \quad \dot{\xi} < 0. \tag{B.11}$$

Because the total strain is obtained through equation (B.1), and because equations (B.6) and (B.7) are equivalent to their counterparts (B.10) and (B.11), it is clear that the model of Chapter II in the current dissertation produces the same result as the Boyd-Lagoudas model in the case that $n_1 = n_2 = n_3 = n_4 = 1$.

This same conclusion can be reached by examining the calibrated model parameters of the Boyd-Lagoudas model and the current model of Chapter II. Comparing

Table IX and Table X, clearly

$$Y^t_{BL} = Y^t_{smooth}. \tag{B.12}$$

Per (B.4) and (B.8), b_1 and a_1 have identical roles in their respective models (and likewise for b_3 and a_2). Again comparing Table IX and Table X, we see

$$b_1 = a_1; \qquad b_3 = a_2. \tag{B.13}$$

Finally, if we consider the substitution of b_1 and b_2 into (B.4) and this into (B.3) (forward transformation form), we notice that we arrive at an identical transformation function as would result if we substituted a_1 and a_3 into (B.8) and this into (2.36). The same is found for the reverse transformation. Thus, the two models are clearly identical when the smooth hardening exponents n_i are set to unity and the phase diagram transformation slopes C^A and C^M are identical.

APPENDIX C

1-D NUMERICAL IMPLEMENTATION OF SMA CONSTITUTIVE MODEL (TRANSFORMATION ONLY)

The purpose of this appendix is to provide the mathematical relations and numerical algorithm needed to implement the SMA thermomechanical constitutive model of Chapter II, Section C in one dimension, specifically for actuator applications. The implementation considers the thermomechanical response of a 1-D uniaxial SMA component undergoing thermally-induced transformation and opposed to some biasing force that may vary linearly with actuator deflection (i.e., biasing spring load).

Three important constitutive relations are needed to model this behavior; discussions and derivations of these can be found in Chapter II, especially Section C. The new contributions of this dissertation are also considered, including a variable maximum transformation strain $H^{cur}(\sigma)$ and "smooth" material hardening during transformation.

The first of the three required relations is derived from the consistency condition that requires the transformation function remain zero-valued during transformation ($0 < \xi < 1, \quad \dot{\xi} \neq 0$). The form of this constraint varies whether the transformation is forward ($\dot{\xi} > 0$) or reverse ($\dot{\xi} < 0$), and here we solve for the temperature T in terms of the other state variables during forward (T^{fwd}) and reverse (T^{rev}) transformation:

$$T^{fwd}(\sigma,\xi) = \frac{(D-1)H^{cur}(\sigma)|\sigma| - \frac{1}{2}\left(\frac{1}{E^M} - \frac{1}{E^A}\right)\sigma^2 + \rho\tilde{u}_0 + f^t_{fwd}(\xi) + Y^t_0}{\rho\tilde{s}_0}, \quad \text{(C.1a)}$$

$$T^{rev}(\sigma,\xi) = \frac{-(D+1)\frac{\varepsilon^{t-r}}{\xi^r}\sigma - \frac{1}{2}\left(\frac{1}{E^M} - \frac{1}{E^A}\right)\sigma^2 + \rho\tilde{u}_0 + f^t_{rev}(\xi) - Y^t_0}{\rho\tilde{s}_0}. \quad \text{(C.1b)}$$

The material parameters $\rho\tilde{u}_0$, $\rho\tilde{s}_0$, Y^t_0, and D are calibrated from the phase diagram per Chapter II, Section C using equations (2.35), (2.40), (2.44), and (2.50).

The second relation describes the evolution of the total strain as additively decomposed into a thermoelastic part $\dot{\varepsilon}^{te}$ and a transformation part $\dot{\varepsilon}^t$, where the change in elastic compliance between phases has been accounted for and the evolution of transformation strain has been discussed in Chapter II, Section C per (2.35). This is given as

$$\begin{aligned} \dot{\varepsilon} &= \dot{\varepsilon}^{te} + \dot{\varepsilon}^t \\ &= \left[\widetilde{\mathcal{S}}\sigma\dot{\xi} + \mathcal{S}(\xi)\dot{\sigma} + \alpha(\dot{T} - T_0)\right] + \Lambda^t\dot{\xi}. \end{aligned} \quad \text{(C.2)}$$

where the effective property $\mathcal{S}$ is given by

$$\mathcal{S}(\xi) = \mathcal{S}^A + \xi\left(\mathcal{S}^M - \mathcal{S}^A\right); \quad \mathcal{S}^A = \frac{1}{E^A}; \quad \mathcal{S}^M = \frac{1}{E^M} \quad \text{(C.3)}$$

The third and final relation allows for the consideration of an external variable biasing force, such as a bias spring or other elastic structural member, and directly links the evolution of applied stress and total strain:

$$\dot{\sigma} = -K\dot{\varepsilon} = -\frac{k_{spring}L_0}{A}\dot{\varepsilon}, \quad K \geq 0. \tag{C.4}$$

where A and L_0 describe the reference area and length of the SMA wire or rod, for example, and k_{spring} describes the variable force opposing actuation (in units force/distance).

The implementation of these relations considers an incremental approach to the evolution of the state variables. Such a method is straightforward and effective considering the form of the evolution equation for transformation strain (2.20). The increments in state variables are written in the backward Euler sense as follows, where "Δ" denotes the increment in a quantity from the previous time step to the current:

$$\sigma_{n+1} = \sigma_n + \Delta\sigma_{n+1}; \quad \varepsilon_{n+1} = \varepsilon_n + \Delta\varepsilon_{n+1}; \quad T_{n+1} = T_n + \Delta T_{n+1}; \quad \xi_{n+1} = \xi_n + \Delta\xi_{n+1}.$$

Equations (C.2) and (C.4), being homogenous in time, can be written in the incremental form. For example, (C.4) is written

$$\Delta\sigma_{n+1} = -K\Delta\varepsilon_{n+1},$$

$$(\sigma_{n+1} - \sigma_n) = -K(\varepsilon_{n+1} - \varepsilon_n).$$

For portions of the thermomechanical loading path which do not induce transformation (i.e., ξ is constant), the stress and strain can be incrementally calculated from (C.2) and (C.4) in an implicit manner given a specified evolution in temperature and known initial conditions. These relations form a linear system of equations written as

$$\begin{bmatrix} A_{11} & A_{12} \\ A_{21} & A_{22} \end{bmatrix} \begin{Bmatrix} \sigma_{n+1} \\ \varepsilon_{n+1} \end{Bmatrix} = \begin{Bmatrix} a_1 \\ a_2 \end{Bmatrix}, \tag{C.5}$$

where

$$A_{11} = 1; \qquad A_{12} = K; \qquad A_{21} = S(\xi); \qquad A_{22} = -1$$

$$a_1 = \sigma_n + K\varepsilon_n; \qquad a_2 = S(\xi)\sigma_n - \varepsilon_n - \alpha\Delta T_{n+1}.$$

When transformation is occurring, the consistency condition (C.1a) or (C.1b) must also be accounted for. For the smooth hardening model considered in this dissertation, the consistency condition relations are strongly nonlinear in ξ. Further, the elastic stiffness also varies with ξ. Therefore, the most straightforward and robust method of calculating the value of the state variables during evolution of transformation using the smooth model is to explicitly define the evolution of martensitic volume fraction and then solve for the current stress, strain, and temperature in an

implicit manner. The nonlinear set of equations required is given as

$$\begin{bmatrix} B_{11} & B_{12} & B_{13} \\ B_{21} & B_{22} & B_{23} \\ B_{31} & B_{32} & B_{33} \end{bmatrix} \begin{Bmatrix} \sigma_{n+1} \\ \varepsilon_{n+1} \\ T_{n+1} \end{Bmatrix} = \begin{Bmatrix} b_1 \\ b_2 \\ b_3 \end{Bmatrix} \tag{C.6}$$

where the components of the coefficient matrix and the right hand side vector are not necessarily constant. Specifically,

$$\begin{aligned} B_{11} &= A_{11}; & B_{12} &= A_{12}; & B_{13} &= 0; \\ B_{21} &= A_{21} + \widetilde{\mathcal{S}}\Delta\xi_{n+1}; & B_{22} &= A_{22}; & B_{23} &= \alpha; \\ & & B_{32} &= 0; & B_{33} &= \rho\tilde{s}_0, \end{aligned}$$

and

$$b_1 = a_1; \qquad b_2 = \mathcal{S}\sigma_n - \varepsilon_n + \alpha T_n - H^{cur}(\sigma_n)\Delta\xi_{n+1}.$$

The coefficient B_{31} and the last component of the right hand b_3 side both vary with transformation direction per

$$B_{31} = \begin{cases} (1-D)H^{cur}(\sigma_{n+1})\mathrm{sgn}\,(\sigma_{n+1}) + \frac{1}{2}\widetilde{\mathcal{S}}\sigma_{n+1} & ; \quad \Delta\xi_{n+1} > 0 \\ (1+D)\frac{\varepsilon^{t-r}}{\xi^r} + \frac{1}{2}\widetilde{\mathcal{S}}\sigma_{n+1} & ; \quad \Delta\xi_{n+1} < 0 \end{cases},$$

$$b_3 = \rho\tilde{u}_0 + \begin{cases} f^t_{fwd}(\xi_{n+1}) + Y^t_0 & ; \quad \Delta\xi_{n+1} > 0 \\ f^t_{rev}(\xi_{n+1}) - Y^t_0 & ; \quad \Delta\xi_{n+1} < 0 \end{cases}.$$

The overall numerical calculation algorithms for full forward and subsequent full reverse transformation are summarized in Table XI and Table XII, respectively. The simulation results of Figure 17 in the main text were generated using this algorithmic implementation of the constitutive model.

Table XI. Solution algorithm for one-dimensional modeling of forward transformation given initial conditions in austenite.

1. Initiate algorithm
    a. Specify minimum actuation temperature.
    b. Specify increments $\Delta T_{n+1} < 0$ and $\Delta \xi_{n+1} > 0$.
    c. Specify initial conditions $\sigma_0, \varepsilon_0, T_0$, $\xi_0 = 0$, and $n = 0$.
2. Increment counter ($n = n + 1$).
3. Solve for temperature to begin forward transformation using $T^{Ms} = T^{fwd}(\sigma_n, \xi_n)$.
4. Increment temperature ($T_{n+1} = T_n + \Delta T_{n+1}$).
5. If $T^{Ms} < T_{n+1}$ then
    a. Solve linear equations (C.5) for current values of σ and ε.
    b. Go to 2.

   Else
    c. Increment martensitic volume fraction ($\xi_{n+1} = \xi_n + \Delta \xi_{n+1}$).
    d. If $\xi < 1$ then
        i. Solve nonlinear equations (C.6) for current values of σ, ε, and T.
        ii. Increment counter ($n = n + 1$).
        iii. Go to 5.c.

       Else
        iv. Set $\xi = 1$.
        v. Increment temperature ($T_{n+1} = T_n + \Delta T_{n+1}$).
        vi. Solve linear equations (C.5) for current values of σ and ε.
        vii. Increment counter ($n = n + 1$).
        viii. Go to 5.d.*v*.

Table XII. Solution algorithm for one-dimensional modeling of reverse transformation given conditions at end of forward transformation.

1. Initiate algorithm
    a. Specify maximum actuation temperature.
    b. Specify increments $\Delta T_{n+1} > 0$ and $\Delta \xi_{n+1} < 0$.
    c. Specify initial conditions $\sigma_{n+1}, \varepsilon_{n+1}, T_{n+1}$ using cooling results ($\xi_{n+1} = 1$).
2. Increment counter ($n = n + 1$).
3. Solve for temperature to begin forward transformation using $T^{As} = T^{rev}(\sigma_n, \xi_n)$.
4. Increment temperature ($T_{n+1} = T_n + \Delta T_{n+1}$).
5. If $T^{As} > T_{n+1}$ then
    a. Solve linear equations (C.5) for current values of σ and ε.
    b. Go to 2.

   Else
    c. Increment martensitic volume fraction ($\xi_{n+1} = \xi_n + \Delta \xi_{n+1}$).
    d. If $\xi > 0$ then
        i. Solve nonlinear equations (C.6) for current values of σ, ε, and T.
        ii. Increment counter ($n = n + 1$).
        iii. Go to 5.c.

       Else
        iv. Set $\xi = 0$.
        v. Increment temperature ($T_{n+1} = T_n + \Delta T_{n+1}$).
        vi. Solve linear equations (C.5) for current values of σ and ε.
        vii. Increment counter ($n = n + 1$).
        viii. Go to 5.d.*v.*

APPENDIX D

LARGE ROTATION ANALYSIS EXAMPLES

Example Analysis 1: Rotating Uniaxial Bar

To demonstrate the importance of rotating both the *global* solution tensors ($\overline{\boldsymbol{\varepsilon}}_{n+1}$, $\overline{\boldsymbol{\sigma}}_{n+1}$) and the *internal* state variable $\boldsymbol{\varepsilon}_n^t$ and constant $\boldsymbol{\varepsilon}_n^{t-r}$, a simple objectivity problem is considered. Here a bar is modeled using two linear hexahedral elements (`C3D8` in Abaqus) and is subjected to tensile loading in the local direction of its longitudinal axis while simultaneously rotating in space. The end of the bar is given a defined displacement (relative to the bar center) such that the total rotation of the bar reaches 38°. The total applied strain in the local axial direction is assigned to be 5.8% and the temperature is $T = A_f + 1\,^{\circ}\mathrm{C}$.

Three example cases were analyzed, and the reference mesh and final deformed configurations are shown in Figure 59. The first case considered full geometric linearity where no tensors were rotated into the current frame. The second considered rotation of the global variables only ($\overline{\boldsymbol{\varepsilon}}_n$, $\overline{\boldsymbol{\sigma}}_n$), where the Abaqus `NLGEOM` option was activated but the return mapping algorithm was not consistently augmented to account for the rotations of internal variables. The third considers the consistent implementation of the Hughes-Winget algorithm for both the global and internal variables.

Analysis assuming a small rotation formulation grossly under-predicts the rotation of the bar and results in principle total strains which remain aligned with the original reference axis (as expected). When the global variables are properly rotated, the final model orientation is correctly computed, though the local principle strains at each integration point are inaccurately calculated due to error in the orientations of the transformation strain increments compounded over many loading steps. It should be noted that, upon unloading, this analysis did not converge. Finally, the analysis using the consistent implementation of the return mapping algorithm with the rotation of global variables predicts the correct orientation of principle total strains and converges easily upon unloading. The stress-strain results measured in the local rotated frame for each of these cases are shown in Figure 60.

Example Analysis 2: Torque Tube Actuator

This example analysis considers the rotational actuation of an SMA torque tube component [169, 17]. It is intended to demonstrate the importance of the large rotation implementation of Chapter III, Section A, providing a torsional demonstration to reinforce the bending example found in [48]. It considers a torsional actuator loaded against a biasing torsional spring. The actuator is 124 mm in length, has an outer diameter of 10.2 mm, and a wall thickness of 1.00 mm while the spring provides a biasing force of 34000 N-mm/rad. The tube, initially in austenite, is fixed at one end while the free end is loaded by the spring to a torque of 16500 N-mm. During cooling into martensite, the spring causes a large rotation as transformation shear

strains are generated. These are recovered during heating. The analysis was performed twice, once considering a small-rotation implementation of the infinitesimal strain model (geometrically linear analysis) and once again by activating the Abaqus `NLGEOM` option [136] while also locally utilizing the Hughes-Winget implementation of Chapter III, Section A (geometrically nonlinear analysis). The results at the end of the cooling step are shown in Figure 61 where unreasonable element growth can be seen in the geometrically linear analysis due to large rotations at the end of the tube (47°). The geometrically nonlinear analysis predicts the correct tube diameter at the free end, identical to the reference state.

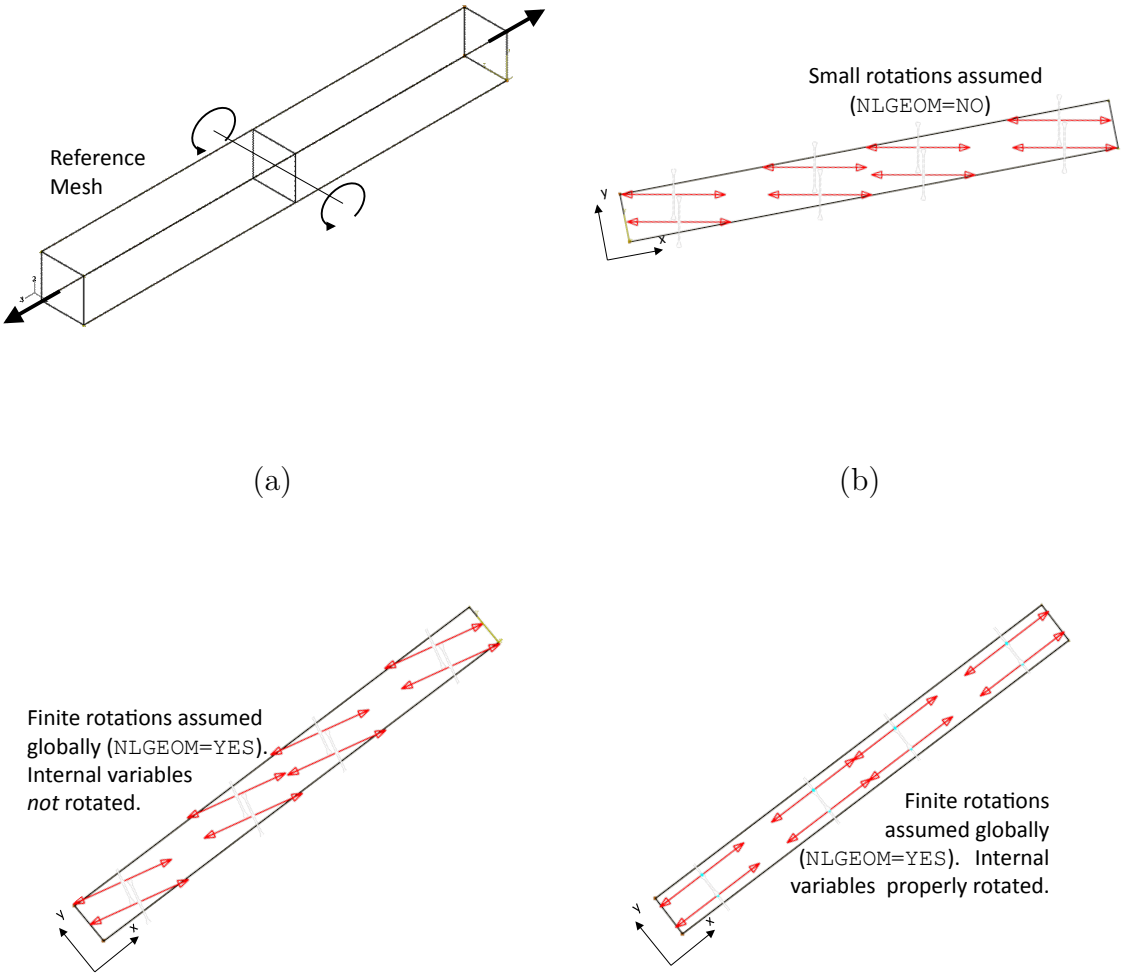

(a) (b)

(c) (d)

Fig. 59. Reference mesh and deformed results, including principle total strains, for three analysis cases of a uniaxial bar simultaneously loaded in tension and rotated in space.

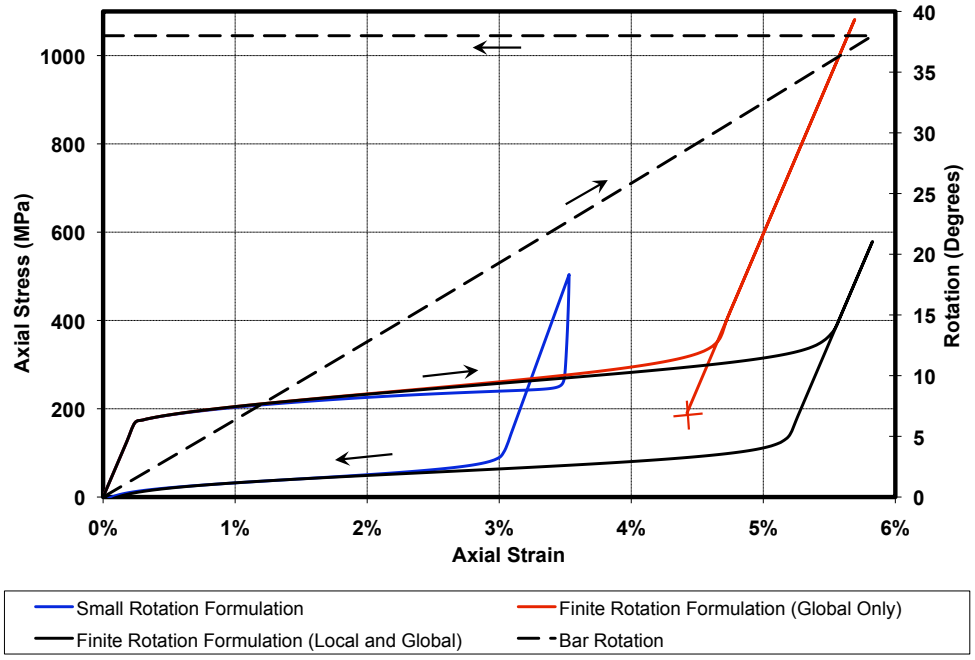

Fig. 60. Stress-strain results measured in local rotating frame for rotating bar problem (three analysis cases).

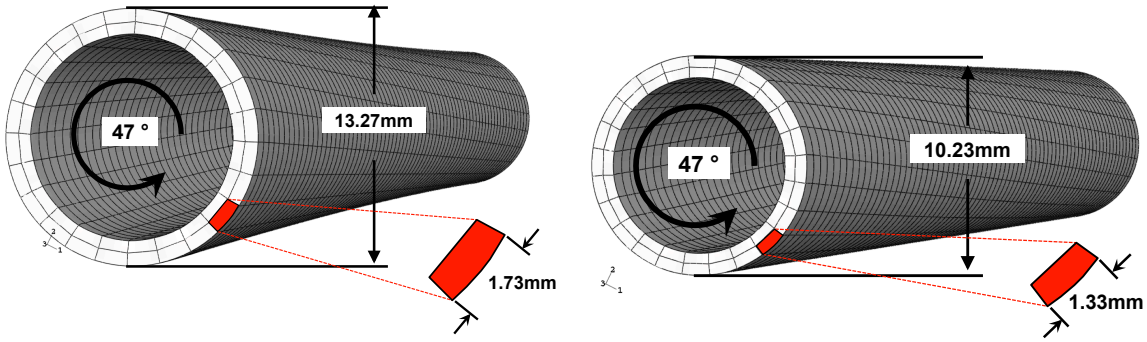

(a) Geometrically linear analysis (b) Geometrically nonlinear analysis

Fig. 61. Change in end diameter during cooling of SMA torque tube actuator assuming both small rotation and finite rotation analysis.

APPENDIX E

ALTERNATIVE DERIVATION OF CONSTITUTIVE MODELS WITH MULTIPLE RECOVERABLE AND IRRECOVERABLE INELASTIC STRAINS

In this appendix, an alternative derivation is proposed for a shape memory alloy constitutive model that considers multiple inelastic irrecoverable deformation mechanisms. The thermodynamic framework used throughout the body of this dissertation always begins with a Gibbs free energy potential that includes as internal variables any strains which are not thermoelastic. These include the transformation strain ($\boldsymbol{\varepsilon}^t$, Chapter II), plastic strain ($\boldsymbol{\varepsilon}^p$, Chapter IV), transformation-induced plastic strain ($\boldsymbol{\varepsilon}^{tp}$, Chapter V), and viscoplastic strain tensors ($\boldsymbol{\varepsilon}^{vp}$, Chapter V). Among these, only the transformation strain is considered fully recoverable. However, legitimate philosophical disagreement exists regarding the inclusion of inelastic *irrecoverable* strains as internal variables for two reasons:

1. Separately listing these strains in the set of internal variables presupposes that the total strain can be additively decomposed, which may not be a suitable assumption;

2. Neither the generation nor the evolution of irrecoverable strains in a material body increases the amount of work that can be performed by that body during unloading, thus a free energy potential should not have a dependence on irrecoverable strains.

In what follows, it is assumed that each of these arguments is valid, and an alternative derivation framework is provided that is compatible with these claims. A Gibbs energy potential is postulated, and the inelastic but *recoverable* transformation strain is included as a valid internal variable. Given this, it is then assumed that the total strain tensor $\boldsymbol{\varepsilon}$ is additively decomposed into recoverable part $\boldsymbol{\varepsilon}^{rec}$ and irrecoverable part $\boldsymbol{\varepsilon}^{irr}$. Regarding the irrecoverable strain, it will be shown that only its *rate* need be additively decomposed to account for various mechanisms. In the example provided in this appendix, the irrecoverable mechanisms are taken to be plastic yielding strain (of the kind considered in Chapter IV), and transformation-induced plastic (TRIP) strain (see Chapter V).

To begin, we propose to use the Gibbs potential described in (2.5)–(2.7) of Chapter II, which is provided here for completeness. Note that, although the resulting constitutive model will capture both yield plasticity and transformation-induced plasticity, neither phenomena is considered in the form of the free energy. Specifically,

$$G(\boldsymbol{\sigma}, T, \boldsymbol{\varepsilon}^t, \xi, g^t) := (1-\xi)G^A(\boldsymbol{\sigma}, T) + \xi G^M(\boldsymbol{\sigma}, T) + G^{mix}(\boldsymbol{\sigma}, \boldsymbol{\varepsilon}^t, g^t),$$

where

$$\begin{aligned} G^\gamma(\boldsymbol{\sigma}, T) &= -\frac{1}{2\rho}\boldsymbol{\sigma} : \boldsymbol{\mathcal{S}}^\gamma \boldsymbol{\sigma} - \frac{1}{\rho}\boldsymbol{\sigma} : \boldsymbol{\alpha}(T - T_0) \\ &+ c\left[(T - T_0) - T\ln\left(\frac{T}{T_0}\right)\right] - s_0^\gamma T + u_0^\gamma, \end{aligned}$$

for $\gamma = A, M$. The energy of mixing is given as:

$$G^{mix}(\boldsymbol{\sigma}, \boldsymbol{\varepsilon}^t, g^t) = -\frac{1}{\rho}\boldsymbol{\sigma} : \boldsymbol{\varepsilon}^t + \frac{1}{\rho} g^t.$$

We then apply the first and second law of thermodynamics as described in Section 2, here altered to account for the two arguments outlined above. Equations (2.8)–(2.10) remain applicable as before, but here we consider an alternative form of the Legendre transformation (2.11). For example, using (9.18) and (9.29) from [170] (and associated discussions), we find

$$G = u - \frac{1}{\rho}\boldsymbol{\sigma} : \boldsymbol{\varepsilon}^{rec} - sT. \tag{E.1}$$

Solving for the internal energy u and taking the time derivative gives

$$\dot{u} = \dot{G} + \frac{1}{\rho}\left(\dot{\boldsymbol{\sigma}} : \boldsymbol{\varepsilon}^{rec} + \boldsymbol{\sigma} : \dot{\boldsymbol{\varepsilon}}^{rec}\right) + \dot{s}T + s\dot{T}. \tag{E.2}$$

Substituting (E.2) into (2.10) while further considering that $\boldsymbol{\varepsilon} = \boldsymbol{\varepsilon}^{rec} + \boldsymbol{\varepsilon}^{irr}$ gives

$$-\rho\dot{G} - \rho s\dot{T} - \dot{\boldsymbol{\sigma}} : \boldsymbol{\varepsilon}^{rec} + \boldsymbol{\sigma} : \dot{\boldsymbol{\varepsilon}}^{irr} \geq 0. \tag{E.3}$$

Applying the chain rule to the state function $G(\boldsymbol{\sigma}, T, \boldsymbol{\varepsilon}^t, \xi, g^t)$ as used in (E.3), we find

$$\begin{aligned} - \quad & \rho\left(\partial_{\boldsymbol{\sigma}} G : \dot{\boldsymbol{\sigma}} + \partial_T G\ \dot{T} + \partial_{\boldsymbol{\varepsilon}^t} G : \dot{\boldsymbol{\varepsilon}}^t + \partial_\xi G\ \dot{\xi} + \partial_{g^t} G\ \dot{g}^t\right) \\ - \quad & \rho s\dot{T} - \dot{\boldsymbol{\sigma}} : \boldsymbol{\varepsilon}^{rec} + \boldsymbol{\sigma} : \dot{\boldsymbol{\varepsilon}}^{irr} \geq 0. \end{aligned} \tag{E.4}$$

Using the methodology of Section 2, we again find (2.16) for the relationship between entropy and the free energy potential. However, examining the terms related with the time rate of change of stress and given the forms assumed above, it is observed that only the recoverable portion of the total strain can be derived from the free energy potential, giving

$$\boldsymbol{\varepsilon}^{rec} = -\rho\partial_{\boldsymbol{\sigma}} G = \boldsymbol{\mathcal{S}}(\xi) : \boldsymbol{\sigma} + \boldsymbol{\alpha}(T - T_0) + \boldsymbol{\varepsilon}^t. \tag{E.5}$$

The dissipation inequality is then given as

$$-\rho\left(\partial_{\boldsymbol{\varepsilon}^t} G : \dot{\boldsymbol{\varepsilon}}^t + \partial_\xi G\ \dot{\xi} + \partial_{g^t} G\ \dot{g}^t\right) + \boldsymbol{\sigma} : \dot{\boldsymbol{\varepsilon}}^{irr} \geq 0. \tag{E.6}$$

The evolution equations for the two irrecoverable phenomena are then proposed using (4.6) and $(5.7)_1$, which are reproduced here for completeness:

$$\dot{\boldsymbol{\varepsilon}}^p = \dot{\bar{\epsilon}}^p \boldsymbol{\Lambda}^p, \qquad \dot{\boldsymbol{\varepsilon}}^{tp} = \dot{\xi}\boldsymbol{\Lambda}^{tp}.$$

The evolution of $\boldsymbol{\varepsilon}^t$ and g^t are as given in (2.20) and (2.26), respectively. Substituting each of these evolution equaitons into (E.6), separating the plastic and transformation phenomena, and assuming strict inequalities for both dissipative processes gives (cf.

(4.14) and (4.15)):

$$\left[\boldsymbol{\sigma} : (\boldsymbol{\Lambda}^t + \boldsymbol{\Lambda}^{tp}) - \rho\partial_\xi G - f^t\right]\dot{\xi} = \pi^t\dot{\xi} > 0 \quad \forall \quad \dot{\xi} \neq 0; \tag{E.7}$$

$$\boldsymbol{\sigma} : \boldsymbol{\Lambda}^p\dot{\epsilon}^p = \pi^p\dot{\bar{\epsilon}}^p > 0 \quad \forall \quad \dot{\bar{\epsilon}}^p > 0. \tag{E.8}$$

Note that, if the TRIP phenomena is disregarded, we arrive once again at (2.28) and that the derivation of a transformation function Φ^t is completed with the assumption of a critical thermodynamic driving force for transformation, Y^t. On the other hand, if TRIP is considered as intended, we arrive at (5.10), and the derivation likewise continues as in the original Chapter V presentation.

It is clear that the plastic dissipation equation is substantially altered from (4.15). The end result for the equation $\Phi^p = 0$ is only preserved if we propose a new Y^p_{new} such that $Y^p_{new} = Y^p + (f^p_A + \xi\tilde{f}^p)$. This has important consequences with respect to the first and second laws of thermodynamics. The amount of energy presumed to be dissipated, which can be measured by

$$\int_{-\infty}^{t} \pi^p\dot{\bar{\epsilon}}^p \,\mathrm{d}\tau \;= \int_{-\infty}^{t} Y^p\dot{\bar{\epsilon}}^p \,\mathrm{d}\tau\,,$$

is changed significantly by the change from Y^p in the original derivation to Y^p_{new} in the current alternative. Specifically, for the new derivation and in the case of plastic hardening, the rate of energy dissipation (and thus heat dissipation) will continue to increase as plastic yield progresses, while in the original model, the rate of dissipation was assumed to be constant for the yielding of a pure phase, regardless of hardening.

APPENDIX F

PROOF FOR THE REQUIREMENT OF INDEPENDENTLY STRONGLY DISSIPATIVE TRANSFORMATION AND PLASTIC YIELD PROCESSES

GOAL:

Given the following constraint representing the coupled dissipation due to SMA transformation ($\pi^t\dot{\xi}$) and plastic yielding ($\pi^p\dot{\bar{\epsilon}}^p$)

$$\pi^t\dot{\xi} + \pi^p\dot{\bar{\epsilon}}^p > 0, \tag{F.1}$$

prove the following:

$$\pi^t\dot{\xi} + \pi^p\dot{\bar{\epsilon}}^p > 0 \iff \pi^t\dot{\xi} > 0, \quad \pi^p\dot{\bar{\epsilon}}^p > 0. \tag{F.2}$$

PROOF:

Note: For the following proof we assume simultaneous *forward* transformation ($\dot{\xi} > 0$) and plastic yield. The same could easily be shown for reverse transformation. It is obvious that

$$\pi^t\dot{\xi} + \pi^p\dot{\bar{\epsilon}}^p > 0 \impliedby \pi^t\dot{\xi} > 0, \quad \pi^p\dot{\bar{\epsilon}}^p > 0.$$

We then aim to prove

$$\pi^t\dot{\xi} + \pi^p\dot{\bar{\epsilon}}^p > 0 \implies \pi^t\dot{\xi} > 0, \quad \pi^p\dot{\bar{\epsilon}}^p > 0. \tag{F.3}$$

To begin, assume that (F.3) is *not* true for simultaneous processes. It is clearly meaningless to assume

$$\pi^t\dot{\xi} < 0, \quad \pi^p\dot{\bar{\epsilon}}^p < 0$$

which violates (F.1). We then consider the case

$$\pi^t\dot{\xi} > 0, \quad \pi^p\dot{\bar{\epsilon}}^p < 0. \tag{F.4}$$

Knowing that $\dot{\bar{\epsilon}}^p > 0$ at all times, we reduce the above to

$$\pi^t\dot{\xi} > 0, \quad \pi^p < 0.$$

For SMAs, there exists a significantly large class of smooth, continuous loading paths inducing simultaneous transformation and plasticity that also pass through some stress-temperature state in the set $\{\boldsymbol{\sigma}, T\}_{M_f}$ such that transformation ends and ($\dot{\xi} > 0$) $\rightarrow$ ($\dot{\xi} = 0$)[1]. Such a path is shown in Fig. 62 and is denoted Path **1**. Per (F.1), at

[1]The set $\{\boldsymbol{\sigma}, T\}_{M_f}$ corresponds to points on the M_f line of the phase diagram

the end of transformation we have

$$\dot{\xi} = 0 \implies \pi^p > 0.$$

Thus, as a loading path crosses through a state included in $\{\boldsymbol{\sigma}, T\}_{M_f}$ causing ξ to approach 1 from below, we have

$$\xi = 1^- \implies \dot{\xi} > 0, \quad \pi^p < 0,$$

$$\xi = 1 \implies \dot{\xi} = 0, \quad \pi^p > 0.$$

But the form of π^p is defined based on the partial derivatives of the Gibbs free energy G, which itself is postulated to be both continuous and *smooth*. Thus π^p is *not* functionally capable of such a jump. Therefore, for all forward transforming and yielding loading paths including a state in the set $\{\boldsymbol{\sigma}, T\}_{M_f}$, we have

$$\pi^t \dot{\xi} + \pi^p \dot{\bar{\epsilon}}^p > 0 \implies \pi^p \dot{\bar{\epsilon}}^p > 0. \tag{F.5}$$

Next, we examine the other contradiction to (F.3) for simultaneous evolutions by considering the complimentary case to (F.4), given as

$$\pi^t \dot{\xi} < 0, \quad \pi^p \dot{\bar{\epsilon}}^p > 0. \tag{F.6}$$

Knowing that $\dot{\xi} > 0$ at all times during forward transformation, we reduce the above to

$$\pi^t < 0, \quad \pi^p \dot{\bar{\epsilon}}^p > 0.$$

For SMAs, there exists a significantly large class of smooth, continuous loading paths inducing simultaneous transformation and plasticity that also reach a stress peak, after which plastic yield ceases although transformation continues. Such a path is shown in Fig. 62 and is denoted Path **2**. Per (F.1), when plastic yield ends, we have

$$\dot{\bar{\epsilon}}^p = 0 \implies \pi^t > 0.$$

Thus, as a loading path of this class approaches a stress peak $\boldsymbol{\sigma}_{peak}$ from below, we have

$$\boldsymbol{\sigma} = \boldsymbol{\sigma}^-_{peak}, \quad \dot{\overline{\boldsymbol{\sigma}_{peak}}} > 0 \implies \dot{\bar{\epsilon}}^p > 0, \quad \pi^t < 0,$$

$$\boldsymbol{\sigma} = \boldsymbol{\sigma}^-_{peak}, \quad \dot{\overline{\boldsymbol{\sigma}_{peak}}} < 0 \implies \dot{\bar{\epsilon}}^p = 0, \quad \pi^t > 0.$$

But the form of π^t, like π^p, is defined based on the partial derivatives of the Gibbs free energy G, and thus π^t is *not* functionally capable of such a jump. Therefore, for all paths during which plastic yield ceases but forward transformation continues, we have

$$\pi^t \dot{\xi} + \pi^p \dot{\bar{\epsilon}}^p > 0 \implies \pi^t \dot{\xi} > 0. \tag{F.7}$$

Because we seek a model for which (F.1) is satisfied for *all* loading paths inducing simultaneous transformation and plastic yield, including those paths discussed here,

we then enforce the following:

$$\pi^t \dot{\xi} > 0 \quad \forall \quad \dot{\xi} > 0; \tag{F.8}$$

$$\pi^p \dot{\bar{\epsilon}}^p > 0 \quad \forall \quad \dot{\bar{\epsilon}}^p > 0. \tag{F.9}$$

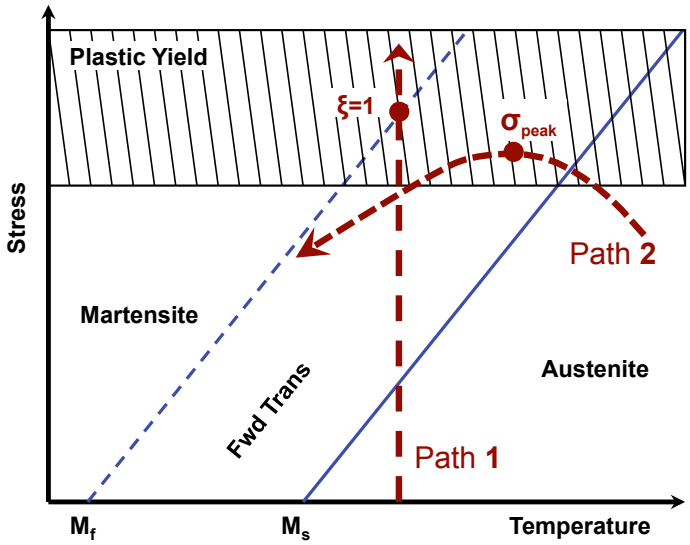

Fig. 62. Schematic illustration of two possible thermomechanical loading paths that lead to the requirement of Eqn. (F.3).

APPENDIX G

REQUIRED MODIFICATIONS TO THE TRANSFORMATION-VISCOPLASTICITY CONSTITUTIVE MODEL FOR THE CONSIDERATION OF VISCOPLASTIC BACK STRESS

This appendix considers the inclusion of a viscoplastic back stress in the formulation of the SMA simultaneous transformation-viscoplasticity constitutive model of Chapter V. Though the material characterization that motivated the development of the original model did not indicate such an internal stress was present, other material systems may exhibit kinematic-type hardening in their viscoplastic response (or a dependence of transformation criteria on viscoplastic strain). Here the modifications to the key constitutive relations are provided followed by the modified algorithmic equations needed for the numerical implementation.

Constitutive Relations

To begin, we define the viscoplastic back stress explicitly in terms of the current viscoplastic strain, the phase-dependent kinematic hardening modulus, and the back stress in the reference configuration (cf. (4.12)). This is given as

$$\boldsymbol{\beta} = K_\beta(\xi)\boldsymbol{\varepsilon}^{vp} + \boldsymbol{\beta}_0. \tag{G.1}$$

Given this new stress-like tensor, we then redefine the direction tensors for transformation, TRIP, and viscoplastic strains. The transformation direction tensor is given by the form of (4.7), while the TRIP and viscoplastic direction tensors are given as

$$\boldsymbol{\Lambda}^{tp} = \begin{cases} f^{tp}(\bar{\sigma}_{vp}^{eff})\boldsymbol{\Lambda}^{vp} & ; \quad \dot{\xi} > 0 \\ -f^{tp}(\bar{\sigma}_{vp}^{eff})\boldsymbol{\Lambda}^{vp} & ; \quad \dot{\xi} < 0 \end{cases} ; \qquad \boldsymbol{\Lambda}^{vp} = \frac{3}{2}\frac{\boldsymbol{\sigma}_{vp}^{eff\prime}}{\bar{\sigma}_{vp}^{eff}}. \tag{G.2}$$

The effective stresses $\boldsymbol{\sigma}_t^{eff\prime}$ and $\boldsymbol{\sigma}_{vp}^{eff\prime}$ used above are defined in (4.9), where $\boldsymbol{\sigma}_p^{eff}$ is replaced by $\boldsymbol{\sigma}_{vp}^{eff}$, etc. The evolution of the transformation hardening energy should take the form given by (4.10), while that for the viscoplastic hardening energy does not require modification.

This new back stress and associated new evolution equations result in a modified form for the dissipation inequality, given for transformation as

$$\left[(\boldsymbol{\sigma} + \boldsymbol{\beta}) : \left(\boldsymbol{\Lambda}^t + \boldsymbol{\Lambda}^{tp}\right) - \rho\partial_\xi G - f^t\right]\dot{\xi} = \pi^t\dot{\xi} > 0 \quad \forall \quad \dot{\xi} \neq 0. \tag{G.3}$$

Considering the additional back stress-related terms of $\rho\partial_\xi G$, the thermodynamic

driving force π^t is written as

$$\pi^t = (\boldsymbol{\sigma} + \boldsymbol{\beta}) : \left(\boldsymbol{\Lambda}^t + \boldsymbol{\Lambda}^{tp}\right) + \frac{1}{2}\boldsymbol{\sigma} : \widetilde{\boldsymbol{\mathcal{S}}}\boldsymbol{\sigma} + \rho\tilde{s}_0 T - \rho\tilde{u}_0 - f^t - \frac{1}{2}\tilde{\boldsymbol{\beta}} : \boldsymbol{\varepsilon}^{vp}. \tag{G.4}$$

In the transformation-viscoplastic creep/yield model, the rate of the effective viscoplastic strain is defined explicitly. If we consider the back stress as a kinematic hardening variable, this relation becomes

$$\dot{p} = \lambda^{vp}(\boldsymbol{\sigma}, T, p, \boldsymbol{\beta}) = \left[\frac{\langle (\boldsymbol{\sigma} - \boldsymbol{\beta}) : \boldsymbol{\Lambda}^{vp} - f^{vp}(T,p)\rangle}{K_a(T)}\right]^{N_a(T)}, \tag{G.5}$$

where, in the special case that $f^{vp}(T,p) = 0$ and the temperature dependence is given by Arrhenius equation alone (i.e., $N_a(T) = N_a$), we have

$$\lambda^{vp}(\boldsymbol{\sigma}, T, \boldsymbol{\beta}) = A \exp\left(\frac{-Q}{RT}\right) \left[(\boldsymbol{\sigma} - \boldsymbol{\beta}) : \boldsymbol{\Lambda}^{vp}\right]^{N_a}. \tag{G.6}$$

This completes the summary of the modifications to key constitutive equations caused by the consideration of a viscoplastic back stress.

Numerical Implementation

The consideration of back stress affects the numerical implementation algorithms through the required reformulation of the phase transformation function Φ^t and explicit form of the effective viscoplastic strain rate λ^{vp}, described above. Specifically, additional partial derivatives must be considered. The transformation function given in (2.32) (considering also (G.4)) and the viscoplastic strain rate constraint equation (5.29) (considering the new form of λ^{vp} given in (G.5)) are written out as

$$\begin{aligned} \Phi^t(\boldsymbol{\sigma}, T, \xi, \boldsymbol{\varepsilon}^{vp}) = \; & \pm \; \Big[(\boldsymbol{\sigma} + K_\beta(\xi)\boldsymbol{\varepsilon}^{vp}) : \left(\boldsymbol{\Lambda}^t(\boldsymbol{\sigma}, \xi, \boldsymbol{\varepsilon}^p) + \boldsymbol{\Lambda}^{tp}(\boldsymbol{\sigma}, \xi, \boldsymbol{\varepsilon}^p)\right) \\ & + \; \frac{1}{2}\boldsymbol{\sigma} : \widetilde{\boldsymbol{\mathcal{S}}}\boldsymbol{\sigma} + \rho\tilde{s}_0 T - \rho\tilde{u}_0 - \frac{1}{2}\tilde{K}_\beta \boldsymbol{\varepsilon}^{vp} : \boldsymbol{\varepsilon}^{vp} - f^t(\xi)\Big] \\ & - \; Y_0^t - D(\boldsymbol{\sigma} + K_\beta(\xi)\boldsymbol{\varepsilon}^{vp}) : \left(\boldsymbol{\Lambda}^t(\boldsymbol{\sigma}, \xi, \boldsymbol{\varepsilon}^p) + \boldsymbol{\Lambda}^{tp}(\boldsymbol{\sigma}, \xi, \boldsymbol{\varepsilon}^p)\right) = 0, \end{aligned} \tag{G.7}$$

$$\begin{aligned} \Phi^{vp}(\boldsymbol{\sigma}, T, \xi, \boldsymbol{\varepsilon}^{vp}, p, \dot{p}) \; & = \; \left(\frac{\langle (\boldsymbol{\sigma} - K_\beta(\xi)\boldsymbol{\varepsilon}^{vp}) : \boldsymbol{\Lambda}^{vp}(\boldsymbol{\sigma}, \xi, \boldsymbol{\varepsilon}^p) - f^{vp}(T,p)\rangle}{K_a(T)}\right)^{N_a(T)} \\ & - \; \dot{p} = 0. \end{aligned} \tag{G.8}$$

The application of the chain rule to these new forms, each of them being functions of new variables, requires new partial derivatives be considered. Specifically,

$$\Phi^{t(k)}_{n+1} + \partial_{\boldsymbol{\sigma}}\Phi^{t(k)}_{n+1} : \Delta\boldsymbol{\sigma}^{(k)}_{n+1} + \partial_\xi \Phi^{t(k)}_{n+1}\Delta\xi^{(k)}_{n+1} + \partial_{\boldsymbol{\varepsilon}^{vp}}\Phi^{t(k)}_{n+1} : \Delta\boldsymbol{\varepsilon}^{vp(k)}_{n+1} \simeq 0 \tag{G.9}$$

$$\begin{aligned}\Phi^{vp(k)}_{n+1} &+ \partial_{\boldsymbol{\sigma}}\lambda^{vp(k)}_{n+1} : \Delta\boldsymbol{\sigma}^{(k)}_{n+1} + \partial_{\xi}\lambda^{vp(k)}_{n+1}\Delta\xi^{(k)}_{n+1} + \partial_{\boldsymbol{\varepsilon}^{vp}}\lambda^{vp(k)}_{n+1} : \Delta\boldsymbol{\varepsilon}^{vp} \\ &+ \partial_{p}\lambda^{vp(k)}_{n+1}\Delta p^{(k)}_{n+1} + \partial_{\dot{p}}\Phi^{vp(k)}_{n+1}\Delta\dot{p}^{(k)}_{n+1} \simeq 0. \end{aligned} \tag{G.10}$$

Substituting the stress increment (5.39) into (G.9), we find

$$\begin{aligned}\Phi^{t(k)}_{n+1} &- \partial_{\boldsymbol{\sigma}}\Phi^{t(k)}_{n+1} : \boldsymbol{\mathcal{C}}^{(k)}_{n+1}\Big[\pm\left(\partial_{\boldsymbol{\sigma}}\Phi^{t(k)}_{n+1} + D(\boldsymbol{\Lambda}^{t(k)}_{n+1} + \boldsymbol{\Lambda}^{tp(k)}_{n+1})\right)\Delta\xi^{(k)}_{n+1} \\ &+ \boldsymbol{\Lambda}^{vp(k)}_{n+1}\Delta t\Delta\dot{p}^{(k)}_{n+1}\Big] + \partial_{\xi}\Phi^{t(k)}_{n+1}\Delta\xi^{(k)}_{n+1} \\ &+ \partial_{\boldsymbol{\varepsilon}^{vp}}\Phi^{t(k)}_{n+1} : \boldsymbol{\Lambda}^{vp(k)}_{n+1}\Delta t\Delta\dot{p}^{(k)}_{n+1} \simeq 0. \end{aligned} \tag{G.11}$$

Likewise, substituting the stress increment (5.39) into (G.10), we find

$$\begin{aligned}\Phi^{vp(k)}_{n+1} &- \partial_{\boldsymbol{\sigma}}\lambda^{vp(k)}_{n+1} : \boldsymbol{\mathcal{C}}^{(k)}_{n+1}\Big[\pm\left(\partial_{\boldsymbol{\sigma}}\Phi^{t(k)}_{n+1} + D(\boldsymbol{\Lambda}^{t(k)}_{n+1} + \boldsymbol{\Lambda}^{tp(k)}_{n+1})\right)\Delta\xi^{(k)}_{n+1} \\ &+ \boldsymbol{\Lambda}^{vp(k)}_{n+1}\Delta t\Delta\dot{p}^{(k)}_{n+1}\Big] + \partial_{\xi}\lambda^{vp(k)}_{n+1}\Delta\xi^{(k)}_{n+1} \\ &+ \Big[\partial_{\boldsymbol{\varepsilon}^{vp}}\lambda^{vp(k)}_{n+1} : \boldsymbol{\Lambda}^{vp(k)}_{n+1}\Delta t + \partial_{p}\lambda^{vp(k)}_{n+1}\Delta t - 1\Big]\Delta\dot{p}^{(k)}_{n+1} \simeq 0. \end{aligned} \tag{G.12}$$

The new partial derivatives for Φ^t are given as

$$\begin{aligned}\partial_{\xi}\Phi^{t} &= (\pm 1 - D)\tilde{K}_{\beta}(\boldsymbol{\Lambda}^{t} + \boldsymbol{\Lambda}^{tp}) : \boldsymbol{\varepsilon}^{vp} \mp \partial_{\xi}f^{t}(\xi), \\ \partial_{\boldsymbol{\varepsilon}^{vp}}\Phi^{t} &= (\pm 1 - D)K_{\beta}(\xi)(\boldsymbol{\Lambda}^{t} + \boldsymbol{\Lambda}^{tp}) \mp \tilde{K}_{\beta}\boldsymbol{\varepsilon}^{vp}, \end{aligned}$$

while for λ^{vp} we have

$$\partial_{\boldsymbol{\sigma}}\lambda^{vp} = N_a(T)\left(\frac{\langle(\boldsymbol{\sigma}-\boldsymbol{\beta}) : \boldsymbol{\Lambda}^{vp} - f^{vp}(T,p)\rangle}{K_a(T)}\right)^{N_a(T)-1}\boldsymbol{\Lambda}^{vp};$$

$$\partial_{\xi}\lambda^{vp} = -N_a(T)\left(\frac{\langle(\boldsymbol{\sigma}-\boldsymbol{\beta}) : \boldsymbol{\Lambda}^{vp} - f^{vp}(T,p)\rangle}{K_a(T)}\right)^{N_a(T)-1}\tilde{K}_{\beta}\boldsymbol{\Lambda}^{vp} : \boldsymbol{\varepsilon}^{vp};$$

$$\partial_{\boldsymbol{\varepsilon}^{vp}}\lambda^{vp} = -N_a(T)\left(\frac{\langle(\boldsymbol{\sigma}-\boldsymbol{\beta}) : \boldsymbol{\Lambda}^{vp} - f^{vp}(T,p)\rangle}{K_a(T)}\right)^{N_a(T)-1}K_{\beta}(\xi)\boldsymbol{\Lambda}^{vp};$$

$$\partial_{p}\Phi^{vp} = -N_a(T)\left(\frac{\langle(\boldsymbol{\sigma}-\boldsymbol{\beta}) : \boldsymbol{\Lambda}^{vp} - f^{vp}(T,p)\rangle}{K_a(T)}\right)^{N_a(T)-1}\partial_{p}f^{vp}(T,p).$$

Finally, we can write the new forms of A_1^t A_1^{vp}, and A_2^{vp} as

$$
\begin{aligned}
A_1^t &= \partial_{\boldsymbol{\sigma}} \Phi^{t(k)}_{\ n+1} : \boldsymbol{\mathcal{C}}^{(k)}_{n+1} \boldsymbol{\Lambda}^{vp(k)}_{\ n+1} \Delta t - \partial_{\boldsymbol{\varepsilon}^{vp}} \Phi^{t(k)}_{\ n+1} : \boldsymbol{\Lambda}^{vp(k)}_{\ n+1}; \\
A_1^{vp} &= \pm \partial_{\boldsymbol{\sigma}} \lambda^{vp(k)}_{\ n+1} : \boldsymbol{\mathcal{C}}^{(k)}_{n+1} \left(\partial_{\boldsymbol{\sigma}} \Phi^{t(k)}_{\ n+1} + D(\boldsymbol{\Lambda}^{t(k)}_{\ n+1} + \boldsymbol{\Lambda}^{tp(k)}_{\ n+1}) \right) - \partial_{\xi} \lambda^{vp(k)}_{\ n+1}; \\
A_2^{vp} &= \partial_p \lambda^{vp(k)}_{\ n+1} \Delta t - \partial_{\boldsymbol{\sigma}} \lambda^{vp(k)}_{\ n+1} : \boldsymbol{\mathcal{C}}^{(k)}_{n+1} \boldsymbol{\Lambda}^{vp(k)}_{\ n+1} \Delta t + \partial_{\boldsymbol{\varepsilon}^{vp}} \lambda^{vp(k)}_{\ n+1} : \boldsymbol{\Lambda}^{vp(k)}_{\ n+1} - 1.
\end{aligned}
\tag{G.13}
$$

VITA

Darren J. Hartl graduated from Texas A&M with a Bachelor of Science degree in Aerospace Engineering in May of 2004. During his time as an undergraduate, he worked as a research assistant for two years and also spent 13 months as a co-op engineer at American Airlines, where he focused on aircraft structural maintenance. He entered the graduate program at Texas A&M in the fall of 2004, where his research interests came to include active materials and applied mechanics. Darren graduated with a Doctor of Philosophy degree in Aerospace Engineering in December of 2009 and has taken the position of Senior Research Associate in the department.

Darren Hartl can be reached at:

Department of Aerospace Engineering
Texas A&M University, 3409 TAMU
College Station, Texas, 77843-3409.

His email address is darren.hartl@tamu.edu.